

KfK 3051
Dezember 1980

Progress Report

Teilinstitut Nukleare Festkörperphysik
des Instituts für
Angewandte Kernphysik
1.6.1979 - 31.5.1980

Editors:
V. Jung, V. Oestreich
Institut für Angewandte Kernphysik

Kernforschungszentrum Karlsruhe

KERNFORSCHUNGSZENTRUM KARLSRUHE

Institut für Angewandte Kernphysik

K f K 3051

PROGRESS REPORT

Teilinstitut Nukleare Festkörperphysik
des Instituts für Angewandte Kernphysik

1.6.1979 - 31.5.1980

Editors:

V. Jung and V. Oestreich

Kernforschungszentrum Karlsruhe GmbH, Karlsruhe

Als Manuskript vervielfältigt
Für diesen Bericht behalten wir uns alle Rechte vor

Kernforschungszentrum Karlsruhe GmbH

ISSN 0303-4003

ISSN 0171-2381

ABSTRACT

This Progress Report of the Teilinstitut Nukleare Festkörperphysik covers the work done at the Institute during the period from June 1st, 1979 to May 31st, 1980.

The main research areas presently under investigation are underlined by the arrangement of the report: structure and dynamics of solids, electronic structure and magnetism of solids, and the development and investigation of novel materials. Some technical developments important in carrying out this research are included as well.

ZUSAMMENFASSUNG

Dieser Progress Report des Teilinstituts Nukleare Festkörperphysik erfaßt den Zeitraum vom 1. Juni 1979 - 31. Mai 1980. Die Darstellung betont die Hauptforschungsgebiete, auf denen das Institut zur Zeit tätig ist. Diese sind: Struktur und Dynamik von Festkörpern, Elektronenstruktur und Magnetismus von Festkörpern und die Entwicklung und Untersuchung neuartiger Materialien. Einige technische Entwicklungen, die für diese Forschungsarbeiten wichtig sind, wurden ebenfalls in den Bericht aufgenommen.

EDITORIAL

This Progress Report of the Teilinstitut Nukleare Festkörperphysik of the Institut für Angewandte Kernphysik (IAK I) covers the main part of the work done during the period from June 1st, 1979 to May 31st, 1980.

The main research areas presently under investigation are underlined by the arrangement of the report: structure and dynamics of solids, electronic structure and magnetism of solids, and the development and investigation of novel materials. A special section is dedicated to theoretical work which is closely related to the experimental research done at our Institute. Some new developments in computer techniques and in instrumentation important for carrying out this research are included as well.

A part of the work submitted for publication or already published is accounted for in a short version or as an abstract. First results of current investigations are described more extensively. Neutron scattering work by guest groups, not related to the research area of this Institute, has not been included in the report. An account of it will be given in a separate report.

The report is supplemented by a list of the Institute's staff members, their publications in the period of reporting, and a list of the neutron spectrometers available in the research reactor FR2.

We are very much indebted to Mrs. M. Müller for her engagement in typing this report.

V. Jung

V. Oestreich

P R E F A C E

The Teilinstitut Nukleare Festkörperphysik of the Institut für Angewandte Kernphysik (IAK I) originated from the use of nuclear methods in solid state research. Its initial methods were elastic and inelastic neutron scattering, Mössbauerspectroscopy, and irradiation of solids with ions from a 3 MV van de Graaff accelerator. With the development of its research program toward specific problems in solid state research, the institute has supplemented its experimental equipment with facilities for ion implantation, thin film preparation by sputtering and evaporation, back-scattering and channeling, magnetization- and T_c -measurements, crystal growing, X-ray diffraction, and recently electron beam annealing. This tendency toward non-nuclear methods will be continued in the coming years, because after the shut-down of the Karlsruhe research reactor FR2 at the end of 1981 only part of the neutron scattering activity will be continued at instruments transferred to the French reactors Orphée in Saclay and Siloe and Melusine at Grenoble.

The construction of the new experimental hall was started at the end of 1979. It will be equipped with the already existing ion implantation facility, an upgraded 2 MV accelerator, common target stations for these two accelerators and the 3 MV accelerator, an electron energy loss spectrometer and a rotating anode X-ray facility.

A considerable part of the research effort of the IAK I is concentrated on materials with high superconducting transition temperatures, T_c . The theoretical investigations on electronic bandstructure, lattice dynamics, electron-phonon coupling and T_c -calculations have been continued. Among the various projects a recent calculation of the electronic bandstructure of $Nb_{0.75}O_{0.75}$ by a self-consistent Gaussian LCAO program may be mentioned. The experimental work on phonons has been complemented by the measurement of the dispersion curves of $NbN_{0.87}$, $Nb_{0.75}O_{0.25}$, and $LaAl_2$, and of the phonon densities of states of $Nb_xV_{1-x}N$ and $Nb_{0.75}Zr_{0.25}$. Also most of the Materials Research Program is concerned with high T_c -superconductors. For bulk sample preparation in addition to RF-heating, arc melting and hot pressing the method of chemical vapor deposition is being applied more extensively. A broad variety of superconducting thin films or layers is produced by sputtering, coevaporation and ion implantation. Rutherford back-scattering, channeling, X-ray analysis, T_c - and electrical resistivity-measurements are at present the major methods for characterization of these samples. As typical examples for this type of investigation the formation of a metastable $A15-Nb_7Si$ phase and the X-ray studies on radiation-damaged Nb_3Al and Nb_3Ge may be cited.

Research work on materials or phenomena outside of the scope of superconductivity is widely dispersed according to the special experimental equipment and know-how of the institute:

The investigations under the heading Electronic Structure and Magnetism are at present focused on alloys of transition and rare-earth metals which allow Mössbauer-spectroscopy with ^{61}Ni , ^{155}Gd , and ^{151}Eu . This work aims at a better understanding of local moment formation and magnetic coupling in metals. The analysis of Mössbauer spectra of ^{155}Gd in amorphous GdNi alloys, i.e. the distribution of electric field gradients and the asymmetry parameter, has revealed a unique possibility of obtaining information about the angular distribution of ionic coordinates. The development of the high-resolution 250 keV electron energy loss spectrometer in collaboration with the IFF at Jülich is proceeding well. The neutron scattering studies on magnetic materials have been continued for some special problems of 3d metal alloys (Fe_3Si , Ni_3Mn , $\text{Ni}_{0.65}\text{Mn}_{0.35}$ and $\text{Y}_6(\text{Fe}_{0.4}\text{Mn}_{0.4})_{23}$).

The neutron scattering group was also concerned with the construction of a practically new triple axis spectrometer for the Orphée-reactor, the preparation of the instrument transfer, measurements of the neutron yield by spallation, general considerations on spallation sources and collaboration with other institutes in the use of the neutron scattering facilities at the FR2. For the latter activity as a typical case among many others the softening of a librational mode in K_2SnCl_6 may be cited.

Theoretical and some experimental effort has been put on the dynamics of superionic conductors. Theoretical investigations on the electronic structure of simple-metal surfaces have been started. They might also lead to an extension of the experimental program. Another example of the broad use of the existing experimental equipment - partly in collaboration with guest scientists - are the implantation studies for Cu in Al, As in Si, Pt in Al_2O_3 and MgO, and Pb and Au in Fe. In all these cases the channeling technique has been proved as an essential tool for analyzing the defect position and average lattice distortion.

The institute has 24 scientists as professional staff. The number of guest scientists, Ph.D. and graduate students fluctuates around 20. IAK I shares with its sister institute IAK II (Teilinstitut Kernphysik) a common infrastructure consisting of a mechanical and an electronic workshop, a maintenance group for the 3 MV accelerator, and a group responsible for experimental computers and data processing. Some development activities of the latter group are included in this report.

In the Research & Development Program and in the Annual Report of the Nuclear Research Center as a whole, the research program of IAK I is subdivided into the following three topics (titles for 1979):

11.02.02 Structure and Dynamics of Solids

11.02.03 Electronic Structure of Solids and Magnetism

10.02.03 Ion Implantation and Channeling

The list of contents of this report differs from the listing above by an extra chapter for Theory and the listing of activities in Ion Implantation and Channeling together with those in materials development under the common title Materials Research. There are also the extra chapters Data Processing and Development of Instruments.

W. Schmatz

CONTENTS

1.	INVESTIGATIONS ON THE DYNAMICS AND STRUCTURE OF SOLIDS	page
1.1	Optical Phonons in $\text{NbN}_{.83}$ <i>W. Reichardt and B. Scheerer</i>	1
1.2	Preparation and Analysis of $\text{Nb}_x\text{V}_{1-x}\text{N}$ Superconducting Polycrystalline Samples <i>C. Geibel</i>	2
1.3	Crystal Structure and Lattice Distortion of $\gamma\text{-NbN}_x$ and $\delta\text{-NbN}_x$ <i>G. Heger and O. Baumgartner</i>	4
1.4	Phonon Dispersion of NbO <i>P. Roedhammer, W. Reichardt, and J. Hufnagl</i>	5
1.5	The Phonon Density of States of $\text{Nb}_{.75}\text{Zr}_{.25}$ <i>F. Gompf and B. Scheerer</i>	8
1.6	Phonons in $\text{Me}_x\text{Mo}_{6-x}\text{X}_8$ Compounds <i>P. Schweiss, B. Renker, and R. Flükiger</i>	10
1.7	Search for Phonon Anomalies in the Intermediate Valence Compound CeSn_3 <i>L. Pintschovius, E. Holland-Moritz, D. Wohlleben, S. Stähr, and J. Liebertz</i>	11
1.8	Neutron Diffraction Study of Brominated $(\text{SN})_x$ <i>L. Pintschovius and M. Kobbelt</i>	12
1.9	Lattice Dynamics of $\text{Pd D}_{.78}$ above and below the Order- Disorder Transition <i>O. Blaschko, H. Klemencic, and L. Pintschovius</i>	14

	page
1.10 Structural Changes in PdD _x in the Temperature Region of the >>50 K-anomaly<<	16
<i>O. Blaschko, R. Klemencic, P. Weinzierl, O.J. Eder, and P.v. Blanckenhagen</i>	
1.11 Lattice Dynamics of the Laves Phase Compounds LaAl ₂ and YAl ₂	16
<i>C.T. Yeh, B. Renker, N. Nücker, and M. Löwenhaupt</i>	
1.12 Comparison of the Phonon Densities of States of the Metallic Glass Fe-40/Zr-60 with 1% and 7% Krypton	19
<i>F. Gompf, B. Renker, and H.-J. Schmidt</i>	
1.13 Study of the Influence of Heavy Doping on the Phonons in Si	20
<i>L. Pintschovius and M. Cardona</i>	
1.14 Phonon Density of States of the Layer Compounds Bi ₂ Te ₃ , Bi ₂ Se ₃ , Sb ₂ Te ₃ , and Bi ₂ (Te _{0.5} Se _{0.5}) ₃ , (Sb _{0.5} Bi _{0.5}) ₂ Te ₃	23
<i>N. Nücker, N. Lehner, H. Rauh, R. Geick, and H. Köhler</i>	
1.15 Scattering Law of the Superionic Conductor CuBr	25
<i>M. Kobbelt, B. Renker, P. Schweiss, and W. Abel</i>	
1.16 Soft Mode and Central Peak in the Cubic High Temperature Phase of K ₂ SnCl ₆	27
<i>K. Vogt, W. Reichardt, and W. Prandl</i>	
1.17 Neutron Scattering Study of Polyacetylene	30
<i>F. Gompf, B. Renker, and G. Wegner</i>	
1.18 Crystal Structure and Lattice Dynamics of Perovskite Type KMe ^{II} F ₃	32
Part I: Structural Investigations of KMnF ₃	
<i>G. Heger and J. Leciejewicz</i>	
1.18 Part II: Phonon Dispersion of KZnF ₃	34
<i>G. Heger, B. Renker, N. Lehner, and R. Geick</i>	
1.19 On the Space Group of MgAl ₂ O ₄ (Spinel)	36
<i>O. Baumgartner and G. Heger</i>	

	page
1.20 Strukturverfeinerung von Harnstoff mit Neutronen- beugungsdaten bei 60, 123 und 293 K und X-N- und X-X(1s ²)-Synthesen bei etwa 100 K <i>H. Guth, G. Heger, S. Klein, W. Treutmann und C. Scheringer</i>	39

2. THEORY

2.1 Electronic Structure of NbO <i>K.-P. Bohnen, W. Weber, and D.R. Hamann</i>	40
2.2 Electronic Structure of Cubic V ₃ Si and Nb ₃ Sn <i>L.F. Mattheiss and W. Weber</i>	43
2.3 Selfconsistent Study of Surfaces of Simple Metals by the Density Matrix Method: (100)- and (110)-surfaces of Na, K, Rb, and Cs* <i>K.-P. Bohnen and S.C. Ying</i>	44
2.4 Recent Calculations of Phonon Spectra of Transition Metals and Compounds <i>W. Weber</i>	44
2.5 A Model Study of the Kohn Anomaly in the Optical Phonon Branch of a Binary Compound <i>C.Y. Fong and W. Weber</i>	45
2.6 Displacement Correlations in Covalent Semiconductors <i>O.H. Nielsen and W. Weber</i>	45
2.7 Strong Depression of Superconductivity in VN by Spin Fluctuations <i>H. Rietschel, H. Winter, and W. Reichardt</i>	46
2.8 Structural and Dynamical Behavior of α -AgI <i>W. Schommers</i>	46

	page
2.9 Structure and Dynamics of Superionic Conductors <i>W. Schommers</i>	47

3. ELECTRONIC STRUCTURE AND MAGNETISM OF SOLIDS

3.1 Muon Spin Rotation Measurements in Paramagnetic <u>Pd</u> Fe and <u>Pd</u> Ni Alloys <i>H. Schmidt, B. Scheerer, V. Oestreich, F. Götz, G. Czjzek, F.N. Gyax, A. Hintermann, W. Rüegg, A. Schenck, and W. Studer</i>	48
3.2 Spin Wave Dispersion Relations in Ordered Fe ₃ Si <i>P.v. Blanckenhagen and C. Lin</i>	50
3.3 Spin Wave Dispersion Relation in Partially Ordered Ni ₃ Mn <i>P.v. Blanckenhagen and B. Scheerer</i>	52
3.4 Antiferromagnetic Long Range Order in Ni _{0.65} Mn _{0.35} <i>P.v. Blanckenhagen and T.J. Hicks</i>	53
3.5 Magnetic Order in Y ₆ (Fe _{0.4} Mn _{0.6}) ₂₃ <i>P.v. Blanckenhagen, C. Lin, and G. Hilscher</i>	55
3.6 The Puzzle of Magnetic Ordering in YbEu Alloys <i>V. Oestreich, G. Czjzek, H. Schmidt, F. Götz, K. Zlatka, K.H. Wienand, and B. Elschner</i>	58
3.7 Magnetization of Dwarf Moments in <u>Pr</u> Gd and <u>Pr</u> Eu Alloys <i>F. Götz, G. Czjzek, H. Schmidt, V. Oestreich, and P. Fulde</i>	61
3.8 Magnetization of UPd ₂ Si ₂ in a Field of 3.7 T <i>J. Leciejewicz and P.v. Blanckenhagen</i>	64

	page
3.9 Atomic Coordination and the Distribution of Electric Field Gradients in Amorphous Solids <i>G. Czjzek, J. Fink, F. Götz, H. Schmidt, J.M.D. Coey, J.-P. Rebouillat, and A. Liénard</i>	65
3.10 Interband Transitions and Core-Level Excitations in 1T-SnS ₂ and 1T-SnSe ₂ by High Energy Electron Loss Spectroscopy and X-Ray Photoelectron Spectroscopy <i>R. Manzke, J. Fink, G. Crecelius, J. Fuggle, R. Schöllhorn, and M. Campagna</i>	66
3.11 The XPS Valence Band Spectra of NbC <i>H. Höchst, P. Steiner, S. Hüfner, and C. Politis</i>	68

4. MATERIALS RESEARCH

4.1 The Influence of Oxygen on the Superconducting Transition Temperature of Quench Condensed Al Films <i>M. Nittmann, P. Ziemann, and G. Linker</i>	69
4.2 Redistribution of Cu in Al Single Crystals after Pulsed Electron Beam Annealing <i>T. Hussain, G. Linker, F. Ratzel, and J. Geerk</i>	71
4.3 Dependence of Defect Structures on Implanted Impurity Species in Al Single Crystals <i>T. Hussain and G. Linker</i>	73
4.4 Low Temperature Self-Ion Irradiation of Pure and Granular Aluminium-Films <i>P. Ziemann, O. Meyer, G. Heim, and W. Buckel</i>	73
4.5 Search for the Solubility Limit of Arsenic in Silicon <i>A. Tuross, J. Geerk, M. Kraatz, and F. Ratzel</i>	74

	page
4.6 Channeling Study of Pt Implanted Al ₂ O ₃ and MgO Single Crystals <i>A. Turos, Hj. Matzke, and O. Meyer</i>	76
4.7 Lattice Location of Pb and Au in Fe Single Crystals <i>H. Alberts, A. Turos, and O. Meyer</i>	78
4.8 Investigation of Structural Distortions in Ion Implanted Molybdenum Layers <i>G. Linker and M. Kraatz</i>	79
4.9 Pulsed Electron Beam Annealing of Ion Implanted Vanadium Single Crystals <i>H.W. Alberts, O. Meyer, J. Geerk, and F. Ratzel</i>	82
4.10 Dechanneling Cross Section for Defect Clusters in Cu Single Crystals <i>O. Meyer and B. Larson</i>	83
4.11 Temperature-Dependant Channeling Studies on NbC-Single Crystals <i>R. Kaufmann and B. Scheerer</i>	85
4.12 On the Effects of ³ He Implantation in NbC Single Crystals <i>R. Kaufmann, A. Turos, and M. Kraatz</i>	88
4.13 Pulsed Laser Beam Treatment of NbN Single Crystals <i>O. Meyer, B.R. Appleton, C.W. White, and B. Scheerer</i>	89
4.14 Preparation of TiN- and ZrN-Single Crystals with Different Nitrogen Content <i>Th. Wolf</i>	91
4.15 Elastic Properties of Polycrystalline TiN, ZrN, and HfN <i>Th. Wolf</i>	92
4.16 The Effect of Temperature and Nitrogen Content on the Electrical Resistivity of Ta(C,N) and U(C,N) <i>H. Matsui, Hj. Matzke, H. Schneider, and C. Politis</i>	94

	page
4.17 Nb ₇ Si - A New Type of High T _c Superconductor <i>Ernst L. Haase, R. Smithey, and O. Meyer</i>	95
4.18 Increase of the Superconducting Critical Temperature of A15 Mo ₃ Ge Thin Films by Heavy Ion Irradiation <i>M. Lehmann, E.L. Haase, and G. Saemann-Ischenko</i>	97
4.19 Investigations of the Defect Structure of Proton-Irradiated Nb ₃ Ge-Layers <i>W. Stocker, G. Linker, M. Kraatz, O. Meyer, B. Krevet, and F. Wüchner</i>	99
4.20 X-Ray Diffraction Studies on He- and Ar-Irradiated Nb ₃ Ge Thin Films <i>J. Pflüger and O. Meyer</i>	102
4.21 The Superconducting Transition Temperature of Bulk Samples of the Niobium-Germanium A15-Phase after Implantation of Ge, Si, O, and Ar Ions <i>J. Geerk</i>	102
4.22 The Defect Structure of Irradiated Nb ₃ Al Films <i>U. Schneider, G. Linker, and M. Kraatz</i>	103
4.23 Superconducting Properties and Structure of Bombarded Nb Layers <i>G. Linker</i>	105
4.24 Channeling Measurements in He-Irradiated V ₃ Ge-Single Crystals <i>O. Meyer, R. Kaufmann, B. Appleton, and M. Chang</i>	106
4.25 The Influence of Light- and Heavy-Ion Irradiation on the Structure, Resistivity, and Superconducting Transition Temperature of V ₃ Si. A Comparativ Study <i>O. Meyer and G. Linker</i>	108
4.26 Pulsed Laser Annealing of V ₃ Si-Single Crystals and Thin Films <i>O. Meyer, J. Thompson, B.R. Appleton, and C.W. White</i>	109

	page
4.27 Preparation of YB ₆ -Powder Samples <i>B. Scheerer and F. Gompf</i>	111
4.28 Mean Free Path of Electrons in Rhenium Films <i>A. ul Haq and O. Meyer</i>	112
4.29 Disorder Analysis in Argon Implanted Rhenium Single Crystals <i>E. Friedland, A. ul Haq, and M. Kraatz</i>	114
4.30 Rhenium Nitride Formation by Nitrogen Implantation in Rhenium <i>A. ul Haq, O. Meyer, and M. Kraatz</i>	116
4.31 Transport Properties, Electronic Density of States and T _c in Disordered A15 Compounds <i>P. Müller, G. Ischenko, H. Adrian, J. Bieger, M. Lehmann, and E.L. Haase</i>	117
4.32 Changes of Superconducting Properties and Electrical Resistivity of Amorphous Compounds by Means of Low Temperature Heavy Ion Irradiation <i>J. Bieger, G. Saemann-Ischenko, H. Adrian, M. Lehmann, P. Müller, L. Söldner, E.L. Haase, and C.C. Tsuei</i>	118
4.33 Single Crystal Preparation of TiN, ZrN, HfN, VN, and NbN by Chemical Vapor Deposition <i>H.-J. Schmidt and Th. Wolf</i>	119
4.34 Determination of Stresses in Materials by Neutron Diffraction <i>L. Pintschovius and V. Jung</i>	120
4.35 Investigation of Stress Induced Phase Transformations in Unstabilized Cr-Ni Steel by the Neutron Diffraction Technique <i>V. Jung</i>	122

	page
5. DATA PROCESSING	
5.1 Interactive Function Minimization <i>W. Abel</i>	127
5.2 Variable Acceleration and Deceleration Profiles for Stepper Motors <i>G. Ehret, H. Hanak, and H. Sobiesiak</i>	129
5.3 A Time-of-Flight Unit for Spallation Source Investigation <i>G. Ehret, H. Hanak, and H. Sobiesiak</i>	131
6. DEVELOPMENT OF INSTRUMENTS	
6.1 Fast Neutron Yields from Spallation Targets <i>F. Gompf and W. Reichardt</i>	133
6.2 Moderator Studies for Spallation Targets <i>F. Gompf, W. Reichardt, M. Kuchle, G. Bauer, and Spitzer</i>	136
6.3 On the Actual State of the 250 keV Electron-Energy- Loss Spectrometer <i>J. Fink, G. Crecelius, R. Manzke, P. Johnen, and F. Schmidt</i>	137
6.4 A Low Temperature UHV Two-Axis-Goniometer for Channeling Experiments <i>R. Kaufmann and F. Ratzel</i>	138
6.5 A Program System for Computer-Controlled Channeling Measurements <i>R. Kaufmann</i>	140

	page	
6.6	Determination of the Superconducting Transition Temperature of Thin Layers by the Inductive Method <i>U. Schneider and J. Geerk</i>	142
7.	PUBLICATIONS , CONFERENCE CONTRIBUTIONS , AND SEMINARS	
7.1	Publications	143
7.2	Conference Contributions and Seminars	148
8.	LIST OF THE NEUTRON SPECTRO - METERS AT THE FR2 AT KARLSRUHE OPERATED BY THE IAK I	155
9.	STAFF MEMBERS	156

1. INVESTIGATIONS ON THE DYNAMICS AND STRUCTURE OF SOLIDS

1.1 Optical Phonons in NbN_{.83}

W. Reichardt and B. Scheerer

We have completed our former investigations on the dispersion curves of δ -NbN_{.83} by measurements of the optical branches. These measurements were performed on the triple axis spectrometer IN8 at the HFR Grenoble. Two single crystals were coaligned to form a sample with a total volume of .4 cm³.

The experimental results are given in Fig. 1 together with our former data of the acoustic branches /1/. Contrary to the acoustic region no anomalous broadening of the phonon groups has been observed.

The full curves in Fig. 1 were obtained by fitting a 6 neighbours-axially symmetric Born von Kármán model to the experimental data. Additional shell interactions between nearest and next nearest Nb-neighbours have been included in the model. Similar calculations on the basis of Weber's double shell model are in progress.

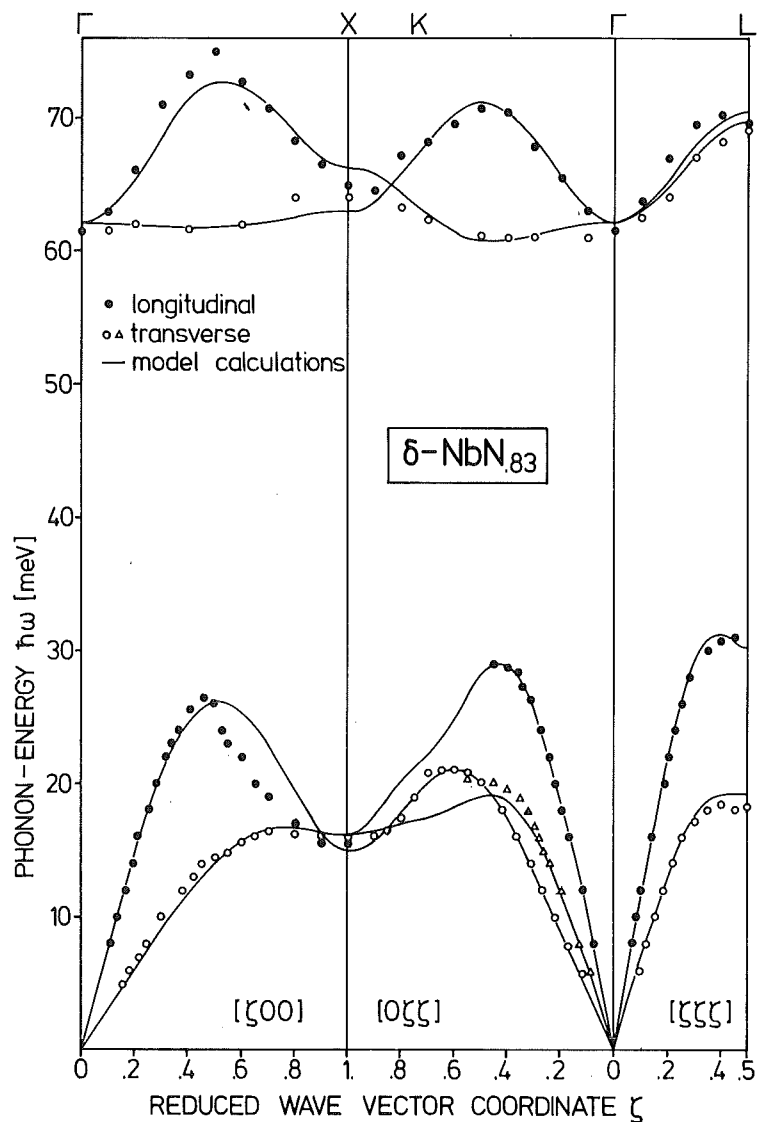


Fig. 1
Dispersion curves of cubic δ -NbN_{.83}

Reference

/1/ W. Reichardt and B. Scheerer, Progr. Rep. IAK I, KfK 2881, 4 (1979)

1.2 Preparation and Analysis of $\text{Nb}_x\text{V}_{1-x}\text{N}$ Superconducting Polycrystalline Samples

C. Geibel

The two refractory compounds NbN and VN, both with rather high T_c (17 K and 9 K) are continuously miscible and form a cubic solid solution with rocksalt structure. The T_c -composition relationship in $\text{Nb}_x\text{V}_{1-x}\text{N}$ has been investigated by Pessal et al. /1/ and by Yen et al., /2/.

Both found that T_c has a pronounced minimum at $x \approx 0.5$, shown in Fig. 1, that could not be explained by nitrogen deficiency. Till now, due to a lack of information about this system, no convincing explanation has been offered for this minimum. Therefore, we decided to extend our investigations of refractory compounds to this pseudobinary system.

The first step was to prepare samples with high nitrogen content. The starting materials were Nb sheets and V slugs with a nominal purity of 99,9 %. The metal mixtures were molten in an electron beam at the Heraeus company (Hanau) (sample C4 and C9) or in an R.F. furnace under argon pressure in our institute (sample C5, C6, C7, C8). The alloys were then loaded with hydrogen and ground into fine powder. Subsequently, the metal-hydrides were nitrated in an alumina-tube furnace under H_2/N_2 atmosphere. The temperature was maintained at 1250°C for 20 hours and then reduced slowly to 1100°C in the following 30 hours. With this preparation method, we obtained single phase $\text{Nb}_x\text{V}_{1-x}\text{N}$ with high nitrogen content and B1 structure. Only in sample C7 and C8 we observe a mixture of δ - $\text{Nb}_x\text{V}_{1-x}\text{N}$ (cubic) and ϵ - $\text{Nb}_x\text{V}_{1-x}\text{N}$ (hexagonal). To transform the ϵ phase into the δ phase, we had to heat the samples till 1350°C in a N_2 atmosphere. At this temperature, we observed a decrease in the nitro-

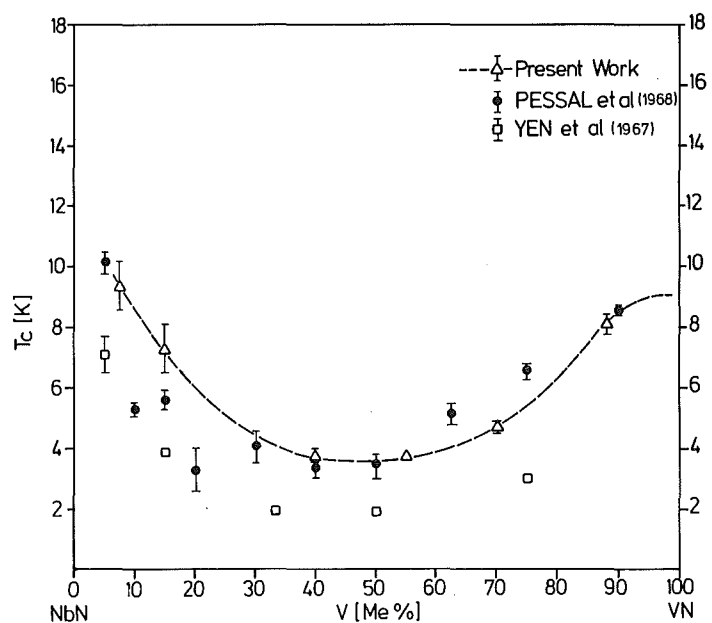


Fig. 1

T_c composition relationship in $\text{Nb}_x\text{V}_{1-x}\text{N}$. The lower T_c in the samples of Yen et al. are due to nitrogen deficiency.

gen content of the sample, due to the rise of the nitrogen dissociation pressure. Thus, after we obtained single phase $\delta\text{-Nb}_x\text{V}_{1-x}\text{N}$, these two samples were annealed again in N_2 at 1250°C (C8) and 1150°C (C7) to increase the nitrogen content.

Table 1 Characterization of Niob-Vanadiumnitrides

Sample Nr.	composition $\text{Nb}_x\text{V}_{1-x}\text{N}_z\text{O}_u$				α_0 [Å]	T_C [midpoint] [K]
	x	1-x	z	u		
C9	0.12	0.88	0.999	0.004	4.1790	8.15
C6	0.30	0.70	0.993	0.005	4.2355	4.70
C4	0.45	0.55	0.996	0.004	4.277	3.73
C5	0.60	0.40	1.001	0.008	4.313	3.76
C7	0.85	0.15	0.991	0.007	4.3665	7.20
C8	0.925	0.075	0.978	0.011	4.3808	9.40

C content : lower than 0.0025 at%

The samples were characterized by chemical analysis, T_C -measurement and x-ray- and neutron-diffraction. The results of these measurements, which are given in Table 1, show that we obtained almost stoichiometric nitrides with pure B1 structure, quite low oxygen and no carbon contamination. Only in sample C5 and C7, we detected 1 % $\epsilon\text{-NbN}$, using neutron diffraction. The T_C -composition relationship we found is shown in Fig. 1, and agrees well with the results previously reported. Especially, we could confirm the deep minimum at the composition $x \approx 0.5$ and it is now established that this minimum is not due to a nitrogen deficiency.

In NbN_x and VN_x , the decrease in T_C at lower nitrogen contents x is correlated with a hardening of the acoustic phonon frequencies. It is interesting to see whether the correlation between phonon frequencies and transition temperatures also holds in

$\text{Nb}_x\text{V}_{1-x}\text{N}$.

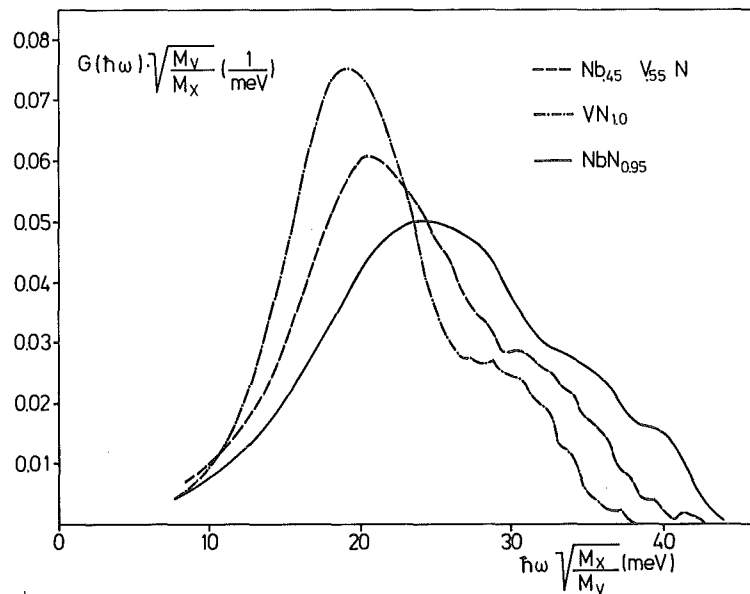


Fig. 2

Comparison of $G(\omega)$ for NbN , VN and $\text{Nb}_{.45}\text{V}_{.55}\text{N}$

We determined the phonon density of states in $\text{Nb}_{.45}\text{V}_{.55}\text{N}_{1.00}$. The experiment was performed on the time of flight spectrometer TOF1 at the FR2. The acoustic part of the generalized phonon density of states $G(\hbar\omega)$ extracted from this experiment is shown in the Fig. 2, together with those in VN and NbN /3/. The frequencies were scaled by a factor $\sqrt{\frac{M_x}{M_V}}$ where M_V is the mass of V and M_x is the mass of the metal atom in the specified compound.

This comparison shows that the general shape of the phonon spectra is almost the same for the three compounds and that the frequency moment $M_i \langle \omega^2 \rangle$ increases almost linearly with the composition. Thus the phonons cannot account for the decrease in T_c . Even if we took the VN_x system as a reference the increase of $M_i \langle \omega^2 \rangle_i$ from VN to $\text{Nb}_{.45}\text{V}_{.55}\text{N}$ would correspond to a decrease in T_c of only 2 K. Therefore we intend to perform additional measurements of the specific heat and the magnetic susceptibility to see whether the decrease in T_c is due to a change in the electronic density of states or to the presence of paramagnons.

References

- /1/ N. Pessal, R.E. Gold, H.A. Johansen, J. Phys. Chem. Solids 29, 19 (1968)
- /2/ C.M. Yen, L.E. Toth, Y.M. Shy, D.E. Anderson, L.G. Rosner, J. Appl. Phys. 38, 2268 (1967)
- /3/ W. Reichardt, F. Gompf, Progr. Rep. IAK I, KfK 2538, 10 (1977)

1.3 Crystal Structure and Lattice Distortion of $\gamma\text{-NbN}_x$ and $\delta\text{-NbN}_x$

G. Heger and O. Baumgartner

J. Phys. C, in print

Abstract

By means of neutron diffraction on single crystals we have studied the γ - and δ -modification of NbN_x using samples with approximately the same $x = \text{N}/\text{Nb} \approx 0.85$. For the ordered $\gamma\text{-NbN}_{0.85}$ we have been able to refine a tetragonal distorted sodium chloride structure model in spite of the occurrence of twinning domains. The

individual mean square displacements of the N and Nb atoms are compared with those of the disordered cubic δ -NbN_{0.84} and the dynamical components out of former inelastic neutron scattering investigations. For the δ -NbN_{0.84} single crystal almost no static distortion of the Nb and N sublattices is found. For γ -NbN_{0.85} large static contributions to the mean square displacements of the N atoms occur whereas the sublattice of the Nb atoms is nearly undistorted. The group theoretical relationship between the structures of the γ - and the δ -phase of NbN_x is discussed.

1.4 Phonon Dispersion of NbO

P. Rödhammer^a, W. Reichardt, and J. Hufnagl^a

^a*Fachbereich Physik, Universität Konstanz, D-7350 Konstanz*

Extensive investigations on the refractory compounds with NaCl (B1)-structure both by experiment and theory have established a close correlation between the number of valence electrons (VE), the superconducting transition temperature (T_c) and the occurrence of anomalous regions in the phonon dispersion curves, where the phonon frequencies are strongly depressed by electron phonon interaction. Compounds with 9VE show pronounced dips in some acoustic branches close to reduced wave vector coordinates $\zeta=0.5$ whereas those with 10VE exhibit a strong reduction of phonon frequencies in the vicinity of the X-point. It seems of interest to extend these investigations to compounds with 11VE.

In contrast to the refractory carbides and nitrides with B1 structure, NbO (nominally 11VE per molecule, $T_c=1.6$ K) contains three formula units in the unit cell. This structure originates from the NaCl lattice by removing the Nb-atoms and the O-atoms from the corners and the centers of the cubic cells, respectively. Thus we may consider NbO as a B1 structure with ordered vacancies both in the metal and non-metal sublattices. The Bravais lattice is simple cubic.

In view of our goal to compare the dispersion curves of NbO with those of the superconducting refractory carbides and nitrides the question arises whether it is possible to distinguish between effects due to the superstructure and those caused by electron-phonon interaction.

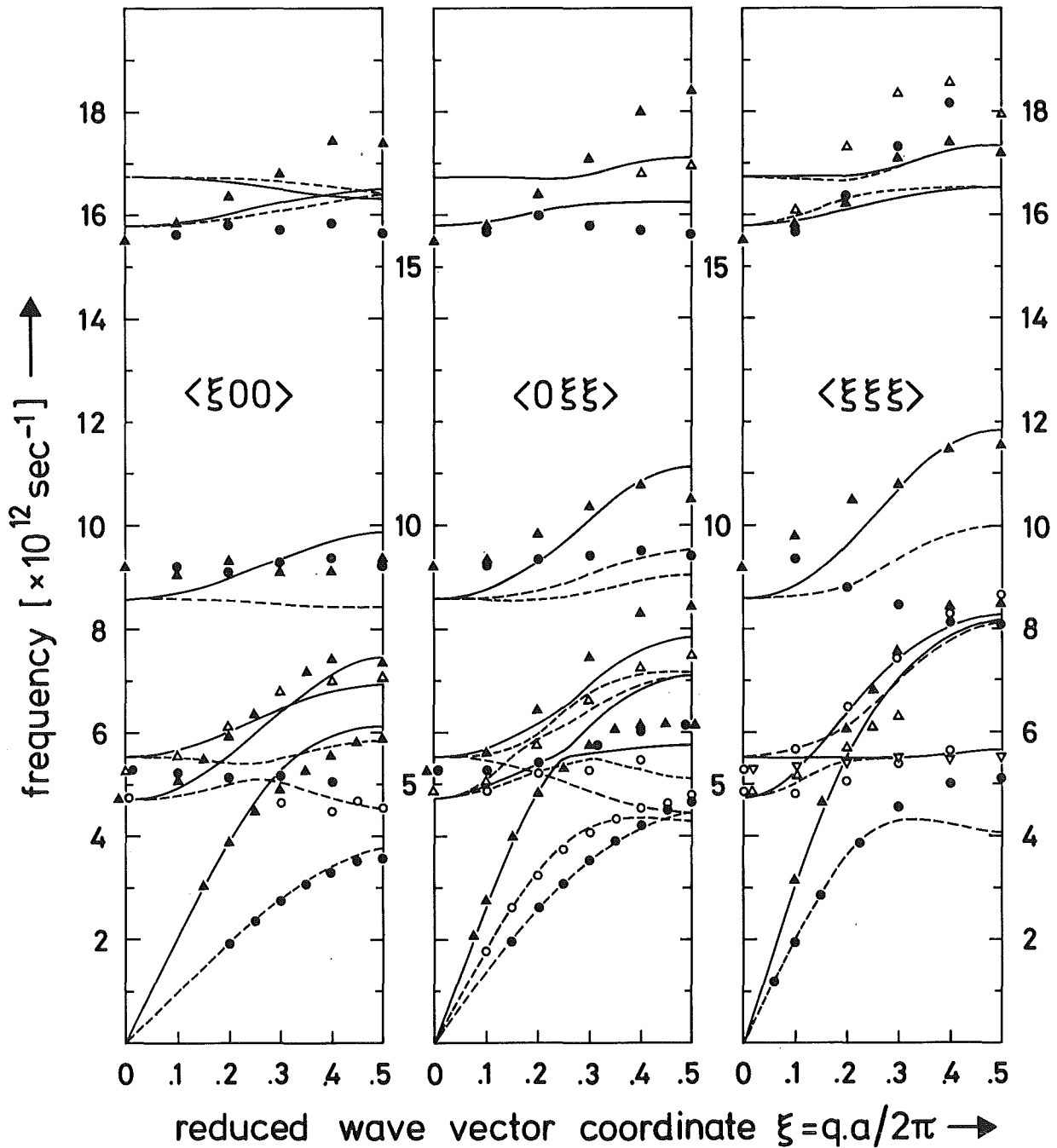


Fig. 1 Dispersion curves of NbO ($\Delta\Delta\nabla$ longitudinal, ∞ transverse). Curves were calculated from a 12 parameter Born von Kármán model (— longitudinal, --- transverse)

Inelastic neutron scattering experiments were performed on the triple axis spectrometers TAS1 at the FR2 Karlsruhe and IN8 at the HFR Grenoble.

The phonon dispersion curves of NbO are presented in Fig. 1. Three phonon bands can be distinguished. The lowest, in the frequency range below 8.5 THz, corresponds to the acoustic branches of refractory compounds with B1 structure. The optic band of the B1 compounds splits into two bands in NbO, the upper and the lower one containing 6 and 3 branches, respectively. The two Γ -point frequencies of the upper band are the same within experimental accuracy. From the existing information

on branches not completely measured we conclude that all of the 6 branches lie in the frequency range 15.5 to 18.5 THz. The lower optic band between 8 and 11.5 THz is due to modes where one or two oxygen atoms of the unit cell vibrate towards the adjacent vacancy positions while the other atoms are essentially at rest.

The curves in Fig. 1 were obtained from a 12 parameter Born von Kármán model fitted to those phonon frequencies where a unique attribution of calculated curves to experimental data was possible. Therefore those data for the $[0\zeta\zeta]$ and $[\zeta\zeta\zeta]$ directions in the region between 5 and 8 THz where there is a large number of densely spaced interacting phonon branches have so far been excluded from the fit. The assignment of the data points to specific branches as indicated by different symbols is based on a comparison of measured intensities to calculated structure factors. In spite of the simplicity of our model the general features of the experimental data are well reproduced. Discrepancies are strongest in the two upper bands; they might be removed by the inclusion of screened Coulomb interactions.

In view of an intercomparison with other refractory compounds experimental data corresponding to acoustic branches of the B1 structure are plotted in Fig. 2a in the appropriate extended zone scheme. In this manner of representation gaps ap-

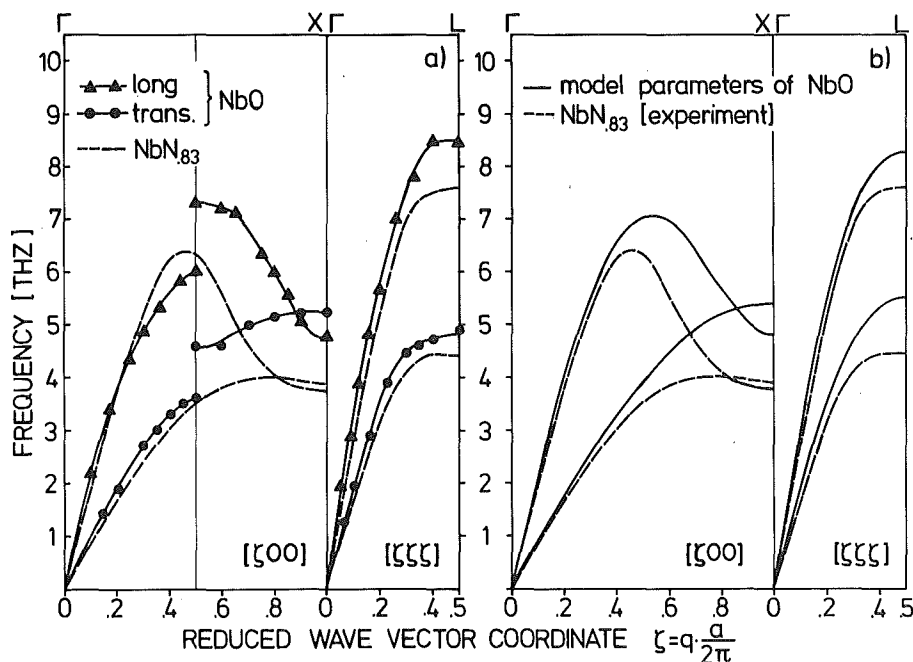


Fig. 2 Acoustic branches of NbO and NbN₈₃ for the $[\zeta 0 0]$ and $[\zeta \zeta \zeta]$ directions plotted in the Brillouin zone of the NaCl structure. a) Experimental data of NbO and NbN₈₃. (— guide to the eye). b) Model calculation for a hypothetical NbO without vacancies.

pear in the dispersion curves at $\zeta=(0.5,0,0)$ due to the vacancy superstructure. There is a striking similarity to the acoustic phonon branches of $\text{NbN}_{.83}$ /1/ which are indicated by the dashed lines. In particular both compounds show an unusual depression of the LA $[\zeta 00]$ -modes in the vicinity of the X-point.

In order to distinguish between 'trivial' effects in the dispersion curves due to the superstructure and anomalies caused by electron-phonon interactions we have used the force constants of our model to calculate the dispersion curves of a hypothetical NbO without vacancies. The result of this calculation is shown in Fig. 2b by the full curves. The frequencies have been divided by $\sqrt{4/3}$ in order to account for the introduction of additional bonds by filling the vacancies. It is seen that these curves reproduce the data for NbO rather well except of course for a small region around the gaps. Especially the depression of the longitudinal branch at the X-point is essentially unaffected. This leads us to the conclusion that it originates from the same mechanism that causes the phonon anomalies in the superconducting refractory compounds with NaCl structure. A comparison with the dispersion curves of $\text{NbN}_{.83}$ (dashed lines in Fig. 2b) suggests that the transverse branches in NbO are not strongly renormalized. A similar behaviour has been observed in two other chalcogenides, YS /2/ and LaS /3/ where phonon anomalies occur only in longitudinal branches.

References

- /1/ W. Reichardt and B. Scheerer, Progr. Rep. IAK I, KfK 2881, 4 (1979)
- /2/ P. Rödhammer, W. Reichardt, and F. Holtzberg, Phys. Rev. Lett. 40, 465 (1978)
- /3/ W. Reichardt, P. Rödhammer, and F. Holtzberg, Progr. Rep. IAK I, KfK 2670, 1 (1978)

1.5 The Phonon Density of States of $\text{Nb}_{.75}\text{Zr}_{.25}$

F. Gompf and B. Scheerer

The bcc structure of the superconducting substitutional alloy $\text{Nb}_{.75}\text{Zr}_{.25}$ is unstable below 1000 K and can only be preserved down to room temperature via rapid quenching. We have prepared bulk samples of $\text{Nb}_{.75}\text{Zr}_{.25}$ by melting Zr (purity > 99.9%,

$T_C = 9.2$ K) and Nb (purity > 99.99 %, $T_C = 9.2$ K) in a RF furnace with a water cooled Cu crucible and letting a rather small sample drop into the cold crucible by turning off the RF. This procedure was repeated several times, until we had a sufficiently large amount of material to perform a neutron inelastic scattering experiment. A typical superconducting transition curve of our material with a T_C of 11.2 K is shown in Fig. 1.

Like the NbTi system $Nb_{1-x}Zr_x$ exhibits a marked increase of the upper critical fields H_{C2} compared to pure Nb which gives such superconducting transition metal alloys great technical importance. Recently Wolf et al. /1/ were able to determine the Eliashberg function $\alpha^2F(\omega)$ of $Nb_{.75}Zr_{.25}$ from tunnelling experiments. They observed a marked enhancement of $\alpha^2F(\omega)$ in the region below about 15 meV compared to pure Nb (see Fig.2a).

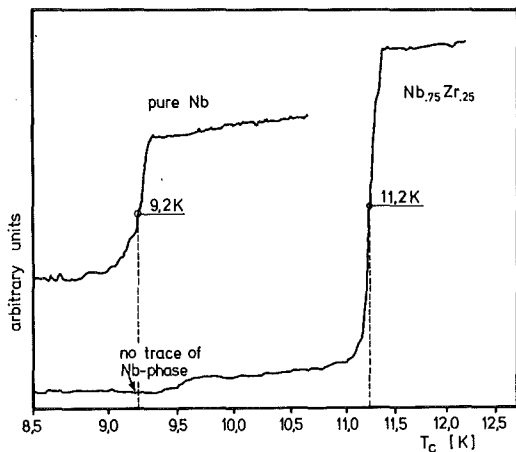


Fig. 1
 T_C of Nb and $Nb_{.75}Zr_{.25}$

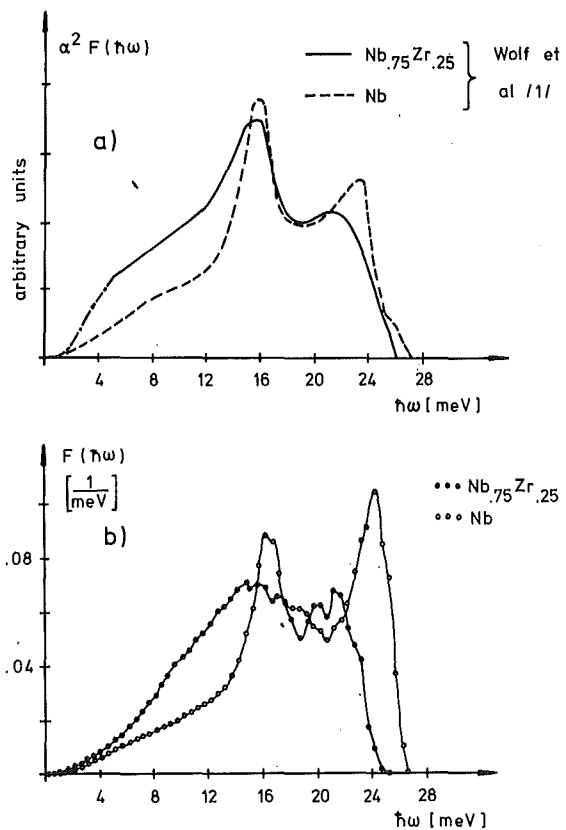


Fig. 2
Comparison of Nb with $Nb_{.75}Zr_{.25}$
a) $F(\hbar\omega)$ b) $\alpha^2F(\hbar\omega)$

The question arises whether this effect is due to a strong softening of the phonon frequencies in this alloy or caused by an enhancement of the electron phonon coupling. This question can be answered by a comparison with the phonon density of states $F(\omega)$ obtained from a neutron scattering experiment. Due to the fact that the scattering factors $\frac{\sigma}{M}$ (σ =scattering cross-section, M =atomic mass) of Nb and Zr differ only by about 2 % such an experiment directly yields $F(\omega)$ to a very good approximation.

The neutron measurements were carried out on the time of flight spectrometer TOF1 at the FR2 using an incident neutron energy of 37.5 meV. A preliminary result for $F(\omega)$ of $\text{Nb}_{.75}\text{Zr}_{.25}$ as deduced from our neutron data is shown in Fig.2b together with $F(\omega)$ of Nb obtained from an earlier experiment /2/.

The neutron data show the same characteristic changes as was observed in $\alpha^2 F(\omega)$ when going from Nb to $\text{Nb}_{.75}\text{Zr}_{.25}$: A shift of the longitudinal peak downward by about 3 meV combined with a reduction in intensity and a marked increase of the intensity between 10 and 15 meV by about the same magnitude. Below about 8 meV the changes in the neutron results are less drastic than in $\alpha^2 F(\omega)$.

This comparison unequally shows that the differences in the $\alpha^2 F(\omega)$ functions of $\text{Nb}_{.75}\text{Zr}_{.25}$ and Nb originate mainly from a strong phonon softening in the alloy whereas the changes in the electron phonon coupling are of much less importance. This is in accordance with the discussion of Wolf et al. /1/ which agree that the increase of the superconducting transition temperature T_c in the alloy is caused by a strong phonon softening.

References

- /1/ E.L. Wolf and R.I. Noer, Solid State Commun. 30, 391 (1979)
 /2/ F. Gompf, Progr. Rep. IAK I, KfK 2538, 30 (1977)

1.6 Phonons in $\text{Me}_x\text{Mo}_6\text{X}_8$ Compounds

P. Schweiss^a, B. Renker, and R. Flükiger^b

^a*Institut für Kristallographie und Mineralogie der Universität Frankfurt a.M.*

^b*Institut für Technische Physik, Kernforschungszentrum Karlsruhe*

Proc. Intern. Conf. on Ternary Superconductors, Lake Geneva, Wisconsin, Sept. 1980, in press.

Abstract

The phonon density of states has been measured by inelastic neutron scattering for PbMo_6S_8 , SnMo_6S_8 , $\text{Cu}_2\text{Mo}_6\text{S}_8$, Mo_6S_8 , PbMo_6Se_8 , and Mo_6Se_8 both at 297 K and 5 K. The data are compared and discussed in view of the superconducting pro-

erties of the compounds. Our previous finding that the superconducting compounds exhibit a pronounced phonon softening at frequencies below ~ 2.5 THz on cooling /1/ is confirmed on the basis of these more comprehensive data for those compounds which do not perform a phase transition (all except $\text{Cu}_2\text{Mo}_6\text{S}_8$).

Our investigations on polycrystalline materials are supplemented by measurements of the dispersion of acoustical phonons on Mo_6Se_8 and $\text{Cu}_2\text{Mo}_6\text{S}_8$ single crystals. For superconducting Mo_6Se_8 a softening has been observed in the TA $1\bar{1}0$ branch.

Reference

/1/ P. Schweiss, B. Renker, and J.-B. Suck, J. Phys. (Paris) C6, 356 (1978)

1.7 Search for Phonon Anomalies in the Intermediate Valence Compound CeSn_3

L. Pintschovius, E. Holland-Moritz^a, D. Wohlleben^a, S. Stähr^b, and J. Liebertz^b

^aII. Physikalisches Institut der Universität zu Köln

^bInstitut für Kristallographie der Universität zu Köln

Solid State Comm. 34, 953 (1980)

Abstract

The phonon dispersion relations of the intermediate valence compound CeSn_3 and the integral valence reference compound LaSn_3 were measured by inelastic neutron scattering. They are quite similar and no phonon anomalies due to valence fluctuations in CeSn_3 were detected. Likewise no line broadening was observed. Model calculations revealed, that the influence of the 'breathing' deformability of the rare earth ions on the lattice dynamics is only moderate; moreover the breathing force constant turned out to be equal for both CeSn_3 and LaSn_3 .

1.8 Neutron Diffraction Study of Brominated $(\text{SN})_x$

L. Pintschovius and M. Kobbelt

Since some years it is known that the physical properties of $(\text{SN})_x$ can be largely modified by reaction with bromine or other halogens /1-3/. In particular the electrical conductivity is increased by an order of magnitude /2,4/. So far the origin of these changes is not well understood, mainly because of the lack of structural data of halogenated $(\text{SN})_x$. Structural investigations are very difficult because of the poor crystallinity of the reaction products. So even for the best investigated compound, i.e. $(\text{SNBr}_{.4})_x$, it remains still unclear to what extent the bromine atoms enter into the $(\text{SN})_x$ lattice or stay outside in the interfiber regions.

The results of our previous investigations of the phonon dispersion of brominated $(\text{SN})_x$ were compatible with the assumption that the bromine is not incorporated into the $(\text{SN})_x$ lattice. However, conclusions concerning the structure from inelastic studies are rather indirect, and therefore we tried to get additional information by neutron diffraction experiments.

Two single crystals were used as samples with a volume of 0.03 cm^3 and 0.08 cm^3 , respectively. They were encapsulated in a quartz glass container under vacuum. This was filled with bromine vapor for about 15 minutes and then evacuated again. The bromine content was deduced from the increase in weight to be $(\text{SNBr}_{.35})_x$ for the larger and $(\text{SNBr}_{.4})_x$ for the smaller crystal. Both crystals have been investigated before and after bromination; in particular the smaller crystal has been studied intensively to check the structure factors given in the literature /5/. This test revealed some minor discrepancies between the measured and the predicted values of the Bragg intensities which are possibly due to the different amount of disorder present in the various samples.

Because of the pronounced broadening and low peak intensity of the diffraction maxima of the brominated samples it is necessary to perform the experiment on an instrument with low background. Therefore we used a triple-axis-spectrometer (TAS 2 at FR2 Karlsruhe) instead of a standard four-circle diffractometer. The measurements were carried out in the $hk0$ and $h0l$ -planes. In the case of the brominated samples mesh-type scans covered the whole area within the limits $2k_I \sin \theta_{\text{max}}$, whereas for the unbrominated samples only the Bragg spots were scanned.

A preliminary evaluation of the data yields the following results: the integrated intensities and because of the strong broadening even more the peak intensities of the Bragg spots are considerably reduced, but the ratios of intensities are not substantially altered. Consequently all peaks which are weak for the pristine $(\text{SN})_x$ were not observable for the brominated samples. An attempt to deduce lattice parameters from the position of the diffraction maxima did not lead to clear results, except for the b-axis which is apparently not changed after bromination: judging from the position of reflections with large indices h and l , the length of the a- and c-axis and the monoclinic angle seem to be modified by not more than 2 %. However, starting from the position of the basis reflections 100 and 002, the length of the a-axis seems to have decreased and the length of the c-axis and the monoclinic angle seem to have increased by about 4 %. This ambiguity is probably the reason for the discrepancies concerning the lattice parameters of brominated $(\text{SN})_x$ given by different authors.

The mosaic spread in the chain direction increased only slightly, but for directions perpendicular to the chains it increased from about 6° to 10° for the sample with the lower and to more than 15° for the sample with the higher bromine content. As is commonly observed for $(\text{SN})_x$ crystals our samples were twinned with 100 as the twin axis. The volume ratio of the twinning components was not changed after bromination. This indicates that, in contrast to the findings of Geiss et al. /6/, bromination does not lead to a higher degree of microtwinning than is incident in the parent crystal.

Gill et al. and Geiss et al. reported the occurrence of superlattice streaks intersecting b^* at $0\ k/2\ 0$ for all k /2,6/ as observed in electron diffraction patterns. These lines are rather weak at $T = 145\ \text{K}$, but strong at ambient or higher temperature. They were interpreted as arising from linear chains of Br_3^- molecules arranged parallel to, but irregularly arrayed about, the $(\text{SN})_x$ backbone.

Though special care was taken to detect these lines in the neutron diffraction pattern we could not find a trace of them. Instead some sharp additional diffraction maxima $hk0$ with non integral values of h , but integral values of k were observed. This indicates that an appreciable amount of bromine is regularly incorporated into the host lattice.

Taking the elastic and inelastic neutron data of brominated $(\text{SN})_x$ together, the most probable picture emerges as follows: the bromine enters into the $(\text{SN})_x$ lattice, starting from the fiber surfaces and gradually advancing to the cores, thereby severely increasing the amount of disorder. Diffraction patterns seem to arise from thin fibers of unbrominated $(\text{SN})_x$ with diameters of a few lattice constants only, and of domains with regularly packed bromine atoms.

References

- /1/ C. Bernard, A. Herold, M. LeLaurain, and G. Robert, C.R. Acad. Sc. 26, 612 (1976)
- /2/ W.D. Gill, W. Bludau, R.H. Geiss, P.M. Grant, R.L. Greene, J.J. Mayerle, and G.B. Street, Phys. Rev. Lett. 38, 1305, (1977)
- /3/ M. Akhtar, J. Kleppinger, A.G. MacDiarmid, J. Milliken, M.J. Moran, C.K. Chiang, M.J. Cohen, A.J. Heeger, and D.L. Peebus, Chem. Commun. 473 (1977)
- /4/ C.K. Chiang, M.J. Cohen, D.L. Peebus, A.J. Heeger, M. Akhtar, J. Kleppinger, A.G. MacDiarmid, S. Milliken, and M.S. Moran, Solid State Commun. 23, 607 (1977)
- /5/ G. Heger, S. Klein, L. Pintschovius, and H. Kahlert, J. Solid State Chem. 23, 341 (1978)
- /6/ R.H. Geiss, J. Thomas, and G.B. Street, Synthetic Metals 1, 257 (1979/80)

1.9 Lattice Dynamics of Pd D_{0.78} above and below the Order-Disorder Transition

O. Blaschko^a, H. Klemencic^a, and L. Pintschovius

^aInstitut für Physik, Forschungszentrum Seibersdorf, Österreich

The first detailed information on the metal-hydrogen and hydrogen-hydrogen forces in Palladium hydride has been obtained from measurements of the phonon dispersion curves of Pd D_{0.63} by Rowe et al. /1/. These results can be summarized as follows: (i) The frequencies in the acoustic region are lowered by about 20 % as compared to pure Pd. (ii) The optic branches show a strong dispersion. The mean optic frequency is remarkably low. (iii) Because of the large number of vacancies the longitudinal optic branches exhibit very large linewidths, whereas the other branches remain fairly sharp.

Recently we were able to produce PdD_x single crystals with a Deuterium content appreciably higher than that of Rowe et al., i.e. PdD_{0.78}. These crystals show an order-disorder transition at 78 K /2/; Below that temperature the vacancies are no longer randomly distributed, but form a nearly ideal tetragonal superlattice (complete ordering is achieved for PdD_{0.80}). Such a crystal was investigated on the

C3 triple axis spectrometer at the FR2 Karlsruhe to answer two questions: (i) Is there a further softening of acoustic and optic frequencies, as is commonly assumed, when going from PdD_{.63} to PdD_{.78}? (ii) What changes in position and linewidth of the phonons are caused by the ordering of the vacancies? The measurements are not yet finished, but the following results are already settled: In the acoustic region the frequencies of PdD_{.78} are higher than those of PdD_{.63} (but still lower than those of pure Pd). In the optic region the center of gravity and the lineshape of the phonon groups in PdD_{.78} above 80 K are almost identical to those of PdD_{.63}. When cooling a few degrees below the transition temperature no change was observed in the acoustic region. In the optic region sharp structures show up in scans which above 80 K gave very broad intensity distributions. The analysis is complicated by the fact that the crystal consists of different domains, because the tetragonal axis of the ordered phase can be parallel to each of the three cubic axis of the unordered phase. In most cases the center of gravity of the phonon groups did not change upon the ordering, except for the TO branch in the 110-direction, where it was shifted by a few percent to higher frequencies.

References

- /1/ J.M. Rowe, J.J. Rush, H.G. Smith, M. Mostoller, and H.E. Flotow, Phys. Rev. Lett. 33, 1297 (1974)
- /2/ O. Blaschko, R. Klemencic, P. Weinzierl, O.J. Eder, and P.v. Blanckenhagen, Acta Cryst. (1980), in press; for the abstract see this report, following contribution

1.10 Structural Changes in PdD_x in the Temperature Region of the 50 K Anomaly

O. Blaschko^{a,b}, R. Klemencic^{a,b}, P. Weinzierl^{a,b}, O.J. Eder^b, and
P.v. Blanckenhagen

^aInstitut für Experimentalphysik, Universität Wien

^bPhysikinstitut, Forschungszentrum Seibersdorf, Österreich

Acta Crystallogr. A36, 605 (1980)

Abstract

Diffuse neutron scattering in β -PdD_x (for $x = 0.710, 0.742, 0.754,$ and 0.780) was observed around the $(1, 1/2, 0)$ point in reciprocal space in the temperature range between 50 and 150 K. The detailed shape of the diffuse pattern is dependent on the deuterium concentration for x between 0.71 and 0.742 and nearly independent for higher concentrations. An increase of the diffuse intensities was found when cooling down the samples to 50 K and was associated with the anomaly of the resistivity.

During an annealing treatment in PdD_{0.780} at 70 K and 75 K $\{4/5, 2/5, 0\}$ superlattice reflections appeared whose intensity after 53 hours was 2 % of the intensity of the $(2, 0, 0)$ fundamental reflection.

1.11 Lattice Dynamics of the Laves Phase Compounds LaAl₂ and YAl₂

C.T. Yeh^a, B. Renker, N. Nücker, and M. Löwenhaupt^b

^aInstitute of Atomic Energy, Academia Sinica, Peking, China
(Fellow of Alexander von Humboldt Foundation).

^bKFA, Jülich

In the present work we report investigations of the lattice dynamics of the two Laves phase compounds LaAl₂ and YAl₂. The point lattice can be described by 6 intersecting fcc lattices.

La and Y have no 4f electrons and both compounds are non magnetic. In contrast to YAl₂, LaAl₂ seems to have a considerably higher N(0) (density of states at

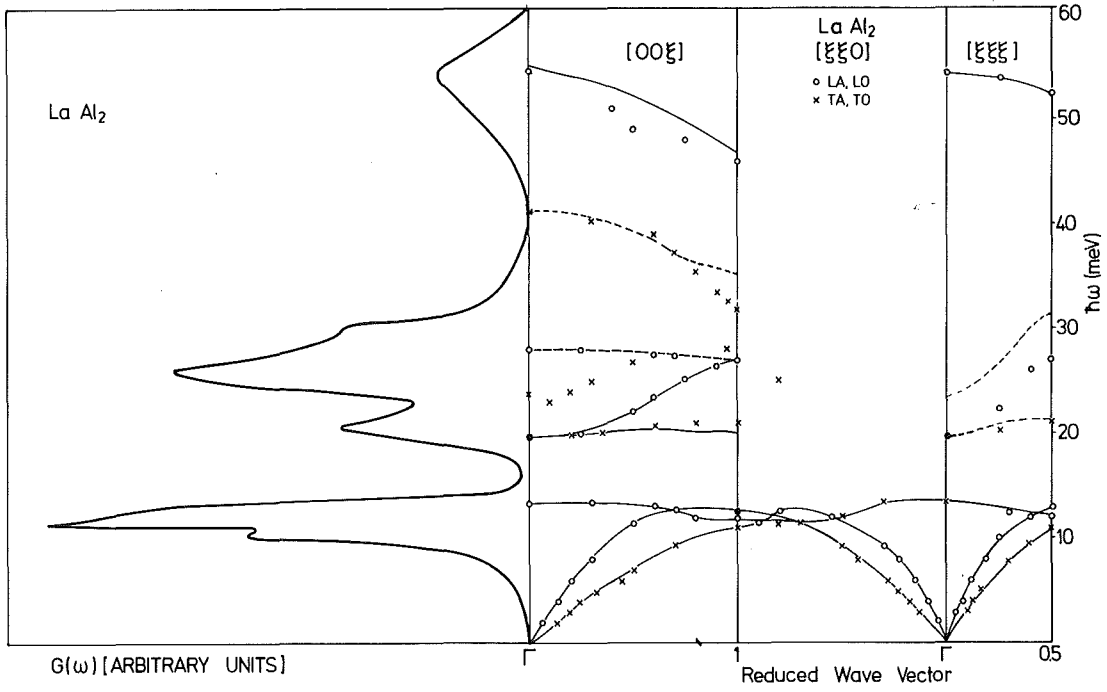


Fig. 1 Phonon dispersion curves for LaAl_2 together with the phonon density of states $G(\omega)$.

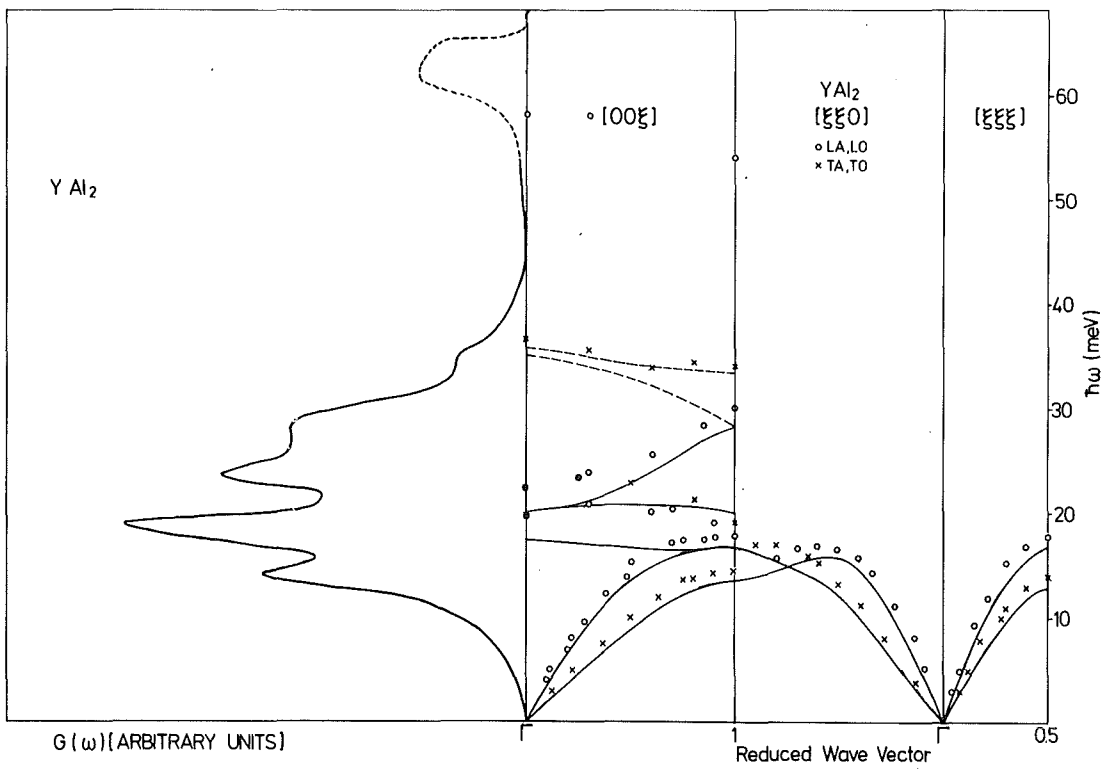


Fig. 2 Phonon dispersion curves for YAl_2 together with the phonon density of states $G(\omega)$.

the Fermi level) and is a superconductor. The electronic contribution to the specific heat γ is about twice as high for LaAl_2 than for YAl_2 : $\gamma^{\text{LaAl}_2} = 3.65 \text{ mJ}/(\text{g.at. K}^2)$, $\gamma^{\text{YAl}_2} = 1.81 \text{ mJ}/(\text{g.at. K}^2)$.

In the present work the phonon dispersion of both Laves phase compounds has been studied in order to investigate whether these different electronic properties are reflected in the phonon spectrum.

Fig. 1 shows the present results for phonon branches in LaAl_2 together with the measured generalized phonon density of states $G(\hbar\omega)$ /2/. Phonons have been measured in the 110 scattering plane and it can be seen that there is a good correspondence between maxima in $G(\hbar\omega)$ and the measured zone boundary frequencies. Parallel to the measurements model calculations have been performed with a force field of axially symmetry. These calculations have essentially been used to determine inelastic structure factors for the phonon measurements. In particular in the frequency region between 20 and 40 meV no satisfactory fit of the measured phonon frequencies could be obtained (dashed lines in Fig. 1).

Therefore a more general tensor force field will be applied in future. Since the ratio of the atomic radius is close to 1.255 - the value for ideal packing in the Laves phase structure - the distance between atoms of the same species of atoms (A-A, B-B) is rather short, which is not the case for the A-B distance. Thus - especially in view of the A-B interaction - we expect that the fit can be considerably improved with the new model.

Fig. 2 shows the corresponding results for YAl_2 . The theoretical curves have been calculated with the mass of Y but the force constants of LaAl_2 have been maintained. Thus, if we exclude those parts of the spectrum in Fig. 1, which are not well fitted by the model, the differences between the calculated and the measured curves should reflect peculiarities of LaAl_2 . It can be seen that the experimental points for YAl_2 are generally well above the calculated curves. Such a result is to be expected: the higher $N(0)$ for LaAl_2 causes a stronger screening and lower phonon frequencies. In conclusion, the present results seem to show a stronger electron phonon coupling for LaAl_2 than for YAl_2 . This result is in line with the specific heat measurement and the fact that LaAl_2 is a superconductor.

References

- /1/ R.E. Hungsberg and K.A. Gschneidner, J. Phys. Chem. Solids 33, 401 (1972)
- /2/ N. Nücker and M. Löwenhaupt, Progr. Rep. IAK I, KfK 2881, 31 (1979)

1.12 Comparison of the Phonon Densities of States of the Metallic Glass
 $\text{Fe}_{40}\text{Zr}_{60}$ with 1 % and with 7 % Krypton

F. Gompf, B. Renker, and H.-J. Schmidt

In recent years much interest has been focussed on metallic glasses since they are promising materials for a wide field of technical applications. Many of their physical properties, however, are not well understood.

Our investigations had two aspects:

- (i) It seemed of interest to learn more about the lattice dynamics of amorphous metallic compounds, since only a few investigations have been published so far.
- (ii) Researchers have looked for ways to store the radioactive Kr-85 a reactor fission product. Loading metallic glass is a promising possibility since 250 dm^3 of Kr-gas can be stored in $1 \text{ dm}^3 \text{ Fe}_{40}\text{Zr}_{60}$.

We have produced $\text{Fe}_{40}\text{Zr}_{60}$ loaded with up to 7 % Kr with the help of a triode sputtering system described in /1/. We checked the structure of our samples by measuring the structure factor $S(Q,0)$ by neutron diffraction. No Bragg lines were observed showing that the materials were totally amorphous. In order to determine the frequency spectrum of such a metallic glass we performed neutron inelastic scattering experiments with TOF II at the cold source of the FR2 with an incident energy of 5 meV. The time-of-flight spectra obtained for $\text{Fe}_{40}\text{Zr}_{60}$ with 1 % and with 7 % Kr are shown in Fig. 1a. The sample containing 7 % Kr exhibits a strong increase of intensity of scattered neutrons in the region of 1 to 18 meV. From a preliminary evaluation of the data we extracted the generalized phonon densities states $G(h\nu)$ as shown in Fig. 2 (with $G(h\nu)$ for 1 % Kr normalized to 1). We get a triangular distribution which peaks around 22 meV

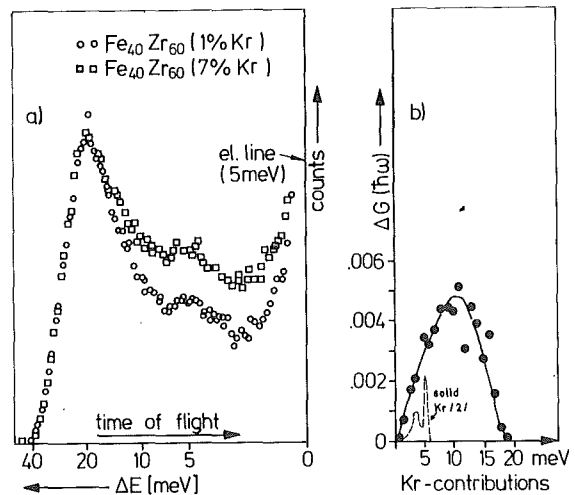


Fig. 1a Time-of-flight spectra for $\text{Fe}_{40}\text{Zr}_{60}$ doped with 1 % and 7 % Kr.

1b Difference in the phonon densities of states

and has a cut-off frequency of about 40 meV. The krypton contributions are again found in the lower part of the spectra, the difference of which has a peak at 10 meV and is shown in Fig. 1b. The integrated intensities gain below 20 meV agrees well with what we expect as contribution to $G(\hbar\omega)$ from 6 % Kr.

The question arises whether the 7 atomic percent of Kr is embedded in the form of bubbles or as single atoms distributed in the amorphous host matrix. As bubbles Kr would have to be in the liquid state since it can easily be

shown that the pressure necessary to hold such amounts of Kr is far above its critical pressure. For solid Kr the frequency spectrum peaks around 4 meV and ends at 6 meV /2/ whereas we obtained a much harder Kr spectrum which makes the dynamical forces larger by a factor of ten. For the liquid state the dynamical forces should be rather weak being of the Van de Waals type. These results rule out that Kr is embedded in form of bubbles and suggest that the Kr-atoms are sitting on single sites in the amorphous host lattice.

References

- /1/ H.-J. Schmidt, E. Henrich, T. Fritsch, F. Gompf, B. Renker, E. Mohs; Proc. of the Int. Conf. on Liquid and Amorphous Metals, Grenoble (1980), to be published
 /2/ J. Skalyo, Y. Erdoh, and G. Shirane, Phys. Rev. B9, 1797 (1974)

1.13 Study of the Influence of Heavy Doping on the Phonons in Si

L. Pintschovius and M. Cardona^a

^a*MPI für Festkörperforschung, Stuttgart*

It was first shown by Keyes /1/ that the free carriers can produce significant changes in the elastic constants of heavily doped semiconductors. This has

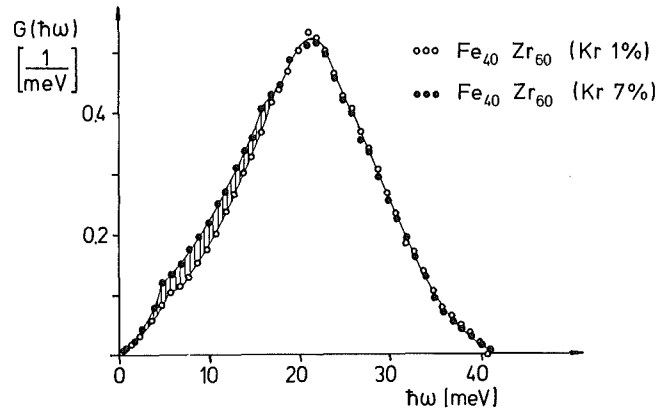


Fig. 2
 Comparison of the phonon densities of states for $\text{Fe}_{40}\text{Zr}_{60}$ doped with 1 % and 7 % Kr.

been confirmed by ultrasonic measurements on n-type Si by Hall /2/ and on p-type Si by Fjeldly et al. /3/. Moreover Cerdeira et al. /4/ investigated the effect of doping on the zone center optical modes by Raman scattering which suggested an intimate relationship between the effects of doping on the acoustical and the optical modes.

The experiments mentioned above were all restricted to very small wave numbers. Neutron scattering experiments in principle allow to extend these investigations throughout the whole Brillouin zone. However, the effects of doping are small ($\sim 1\%$) and hence data of high precision are required which forces to restrict the investigations to a very limited range in q-space.

The measurements were performed on the triple axis spectrometer TAS 1 at the FR2 Karlsruhe. Instrument parameters were chosen to get a high resolution (e.g. $\Delta h\omega=0.65$ meV for $h\omega=14$ meV). Three single crystals of doped Si were used as a sample, each of a volume of about 30 cm^3 :

An n-type crystal doped with As with a dopant concentration of $n=5\cdot 10^{19}\text{ cm}^{-3}$, p-type crystal doped with B with $n=17\cdot 10^{19}\text{ cm}^{-3}$, and an n-type crystal with a very low dopant concentration which was used as a reference.

The results are shown in Figs. 1-2. In the region of small q-values reasonable agreement exists between the ultrasonic and the neutron data. The rapid decrease of the effects of doping for increasing q-values are caused by the small size of the Fermi surfaces. There is only one case where the plot $\Delta v/v$ versus q shows a peak, i.e. for the LA branch in the 100 direction in n-type Si: This peak is presumably due to intervalley scattering. Theoretical predictions of large frequency shifts for the TA branch in the 111 direction in p-type silicon /6/ could not be confirmed.

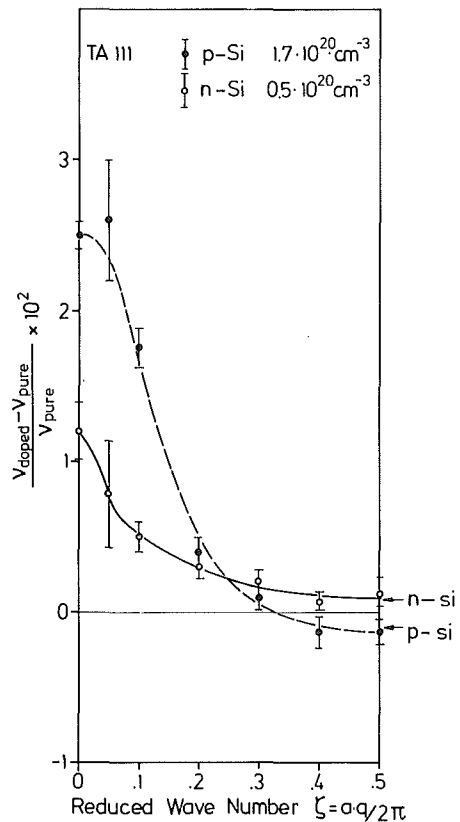


Fig. 1
Relative frequency shifts for the TA branch in the 111-direction in n-type ($c=5\cdot 10^{19}\text{ cm}^{-3}$) and p-type ($c=17\cdot 10^{19}\text{ cm}^{-3}$) silicon. Data for $q=0$ (ultrasonic measurements) after Ref. /5/. The arrows denote those shifts which are expected from the change in the average atomic mass.

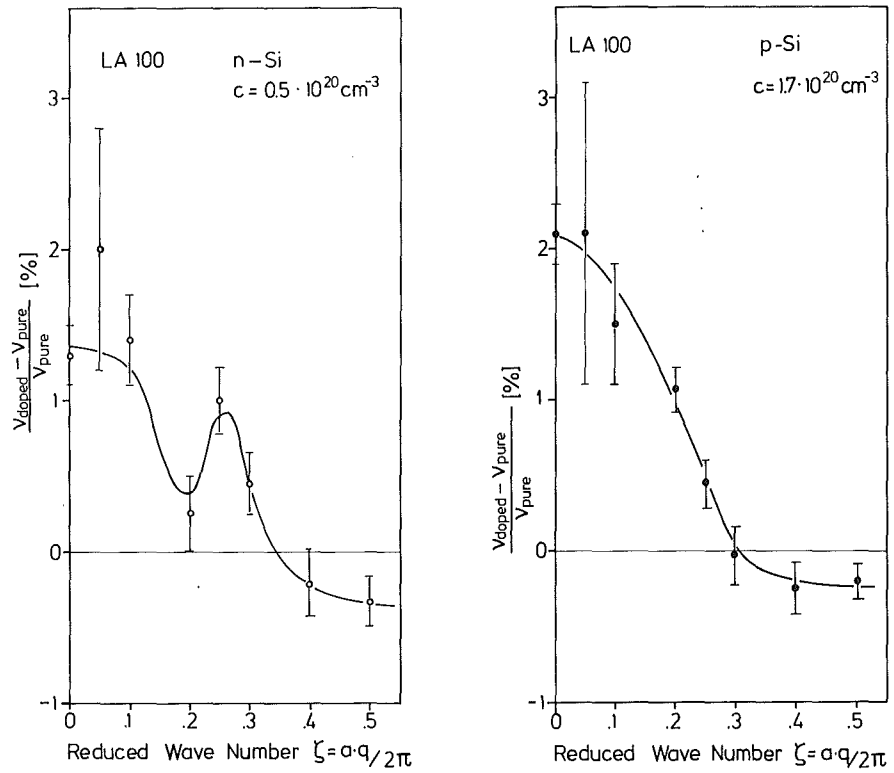


Fig. 2
Relative frequency shifts for the LA branch in the 100-direction in heavily doped silicon.
Left: n-type Si ($c=5 \cdot 10^{19} \text{cm}^{-3}$),
right: p-type Si ($c=17 \cdot 10^{19} \text{cm}^{-3}$)

References

- /1/ R.W. Keyes, IBM, J. Res. Dev. 5, 266 (1961),
R.W. Keyes, in Solid State Physics, ed. by F. Seitz, and
D. Turnbull, Academic Press, New York, 20, 37 (1967)
- /2/ J.J. Hall, Phys. Rev. 161, 756 (1967)
- /3/ T.A. Fjeldly, F. Cerdeira, and M. Cardona, Phys. Rev. B8, 4723 (1973)
- /4/ F. Cerdeira, T.A. Fjeldly, and M. Cardona, Phys. Rev. B8, 4734 (1973)
- /5/ M. Kobbelt, private communication
- /6/ P.H. Allen, private communication

1.14 Phonon Density of States of the Layer Compounds Bi_2Te_3 , Bi_2Se_3 , Sb_2Te_3 , and $\text{Bi}_2(\text{Te}_{0.5}\text{Se}_{0.5})_3$, $(\text{Sb}_{0.5}\text{Bi}_{0.5})_2\text{Te}_3$.

N. Nücker, N. Lehner^a, H. Rauh^b, R. Geick^b, and H. Köhler^b

^aILL, Grenoble

^bUniversität Würzburg

The compounds A_2B_3 with $\text{A}=\text{Bi}$ or Sb and $\text{B}=\text{Te}$ or Se crystallize in sandwich-like layer structures of rhombohedral symmetry (D_{3d}^5) with one formula unit per primitive cell. The sequence of layers in a sandwich is $\text{B}_1 - \text{A} - \text{B}_2 - \text{A} - \text{B}_1$. The binding within one sandwich is assumed to be mainly covalent. The easy cleavage of these materials indicates weak forces between sandwiches. The knowledge of the lattice dynamics of these materials is rather limited; apart from ultrasonic and light scattering¹⁾ experiments, the phonon dispersion curves of Bi_2Te_3 ²⁾ and Sb_2Te_3 ³⁾ have been measured along the (001) direction (perpendicular to the layers) and to some extent along the $(11\bar{2})$ direction in Bi_2Te_3 .

In order to get further information on the lattice dynamics we have performed inelastic neutron scattering experiments on powder samples using the TOF 3 time-of-flight spectrometer at the FR2. The experiments were performed at 77 K sample temperature. Some results from samples at 300 K showed considerable contributions from multiphonon processes which were difficult to correct for.

Fig. 1 shows the generalized phonon density of states (GDOS) of Bi_2Se_3 compared to that of Bi_2Te_3 . The latter is almost identical to the true phonon density of states since the scattering powers σ/m of Bi and Te are nearly equal. We note that the GDOS curves of Bi_2Te_3 and Bi_2Se_3 agree quite well in both the high and the low frequency range, when they are scaled by $(m_{\text{Te}}/m_{\text{Se}})^{1/2}$. The GDOS curves span the same frequency range as the optical data of Richter et al. and the phonon dispersions of Wagner et al.. Furthermore, peaks in the GDOS are observed in those frequency regions where the dispersion curves are rather flat (at 4, 11, 13, and 15 meV). The observed mass scaling in the GDOS is also observed in the Raman and infrared data of the two materials. It would indicate that the modes in these regions have mainly chalcogenide character, and that both the intra and inter sandwich force constants are the same.

Fig. 1
The phonon density of states of Bi_2Te_3 compared to phonon dispersion curves for (001) direction and to Raman and Infrared frequencies¹ as well as to the phonon density of states of Bi_2Se_3 (upper energy scale, dashed curve).

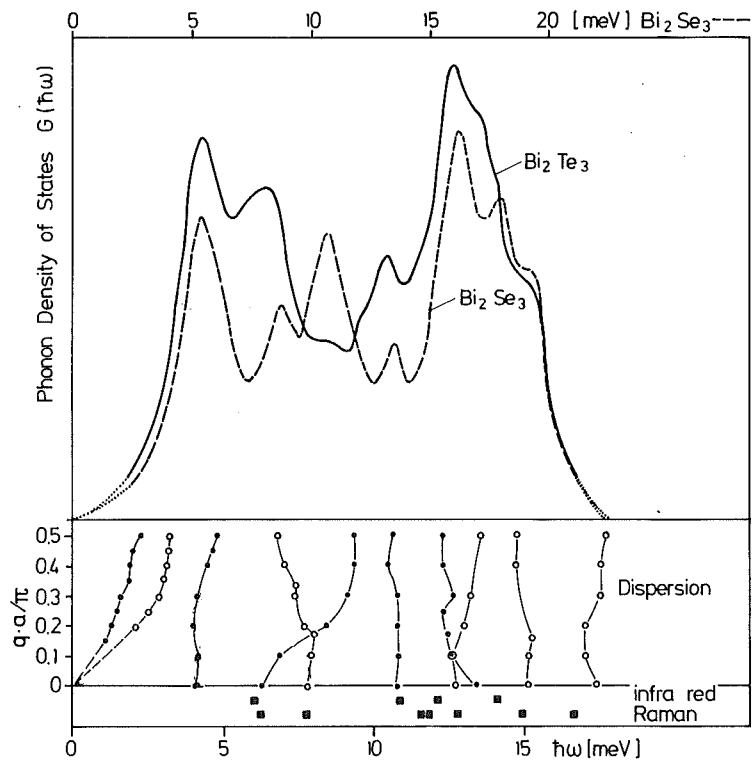


Fig. 2
Phonon density of states of Bi_2Te_3 , Sb_2Te_3 , and $(\text{Sb}_{.5}\text{Bi}_{.5})_2\text{Te}_3$.

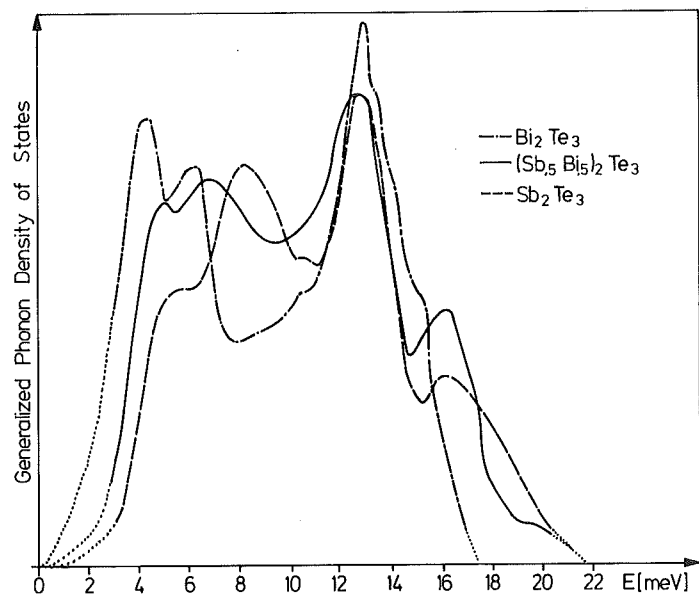


Fig. 2 shows the GDOS curves for the tellurides. With the Bi to Sb replacements, we observe - apart from an unaffected peak at 13 meV - shifts both in the low and the high frequency regions, which indicate considerable Bi or Sb contributions in those modes. Therefore the success of the chalcogenide mass scaling model may be fortuitous. Instead we suspect that nonnegligible force constant changes occur.

References

- /1/ W. Richter, H. Köhler, C.R. Becker, Phys. Stat. Sol. (b)84, 619 (1977)
- /2/ V. Wagner, G. Dolling, B.M. Powell, G. Landwehr, Phys. Stat. Sol. (b)85, 311 (1978)
- /3/ H. Burkhard, P. Grosse, and V. Wagner; ILL Progress Report Annex 1977, p. 80 Experiment No. 04-01-044)

1.15 Scattering Law of the Superionic Conductor CuBr

M. Kobbelt, B. Renker, P. Schweiss^a, and W. Abel

^a*Institut für Kristallographie und Mineralogie der Universität Frankfurt, 6000 Frankfurt a. M. 1*

CuBr has been referred as a superionic conductor because its maximum conductivity ($\approx 3 \Omega^{-1} \text{cm}^{-1}$ at 760 K) exceeds that of the best liquid electrolytes. The table below shows the different phases together with the ionic conductivities.

Table 1 Structural and Conductivity Data of CuBr

	structure of Br-lattice	conductivity [$\Omega^{-1} \text{cm}^{-1}$]	stability range
γ -phase	f.c.c.	$< 10^{-4}$ at room temp. ≈ 0.1 at 664 K	0-664 K
β -phase	h.c.p.	≈ 0.3	664-744 K
α -phase	b.c.c.	$\approx 3.$	744-765 K
melt			> 765 K

We have investigated CuBr by means of neutron scattering with the time-of-flight spectrometer TOF 2 at the FR2 using an incident neutron energy of 5.06 meV. The sample consisted of 40g CuBr powder encased in eight V2A-tubes (\varnothing 6mm) mounted side by side on a copper plate with a heating device.

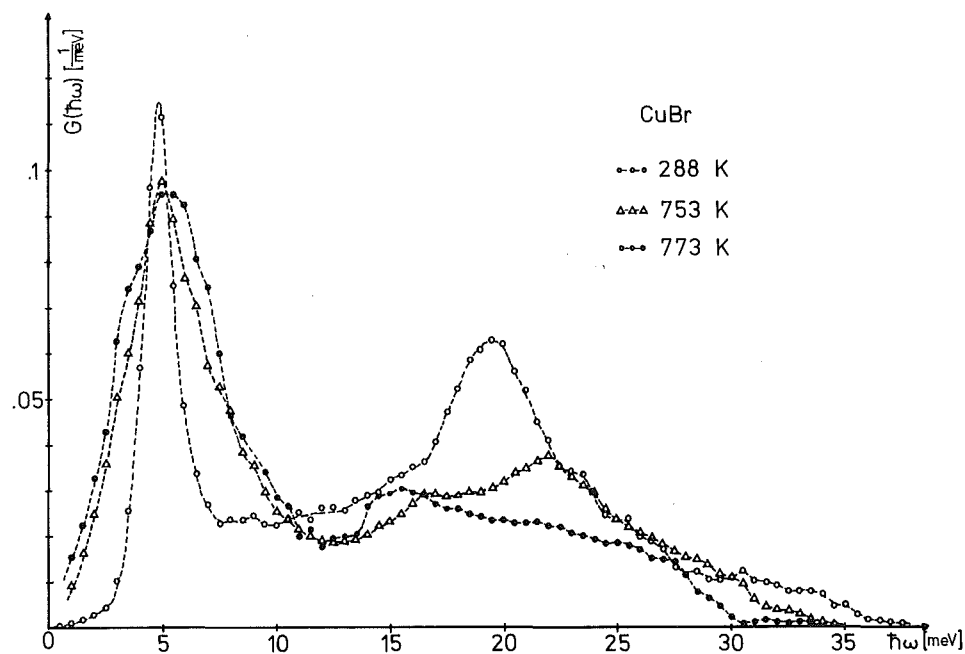


Fig. 1
Generalized phonon density of states $G(\hbar\omega)$ of CuBr for various temperatures, corresponding to γ -phase, α -phase and melt.

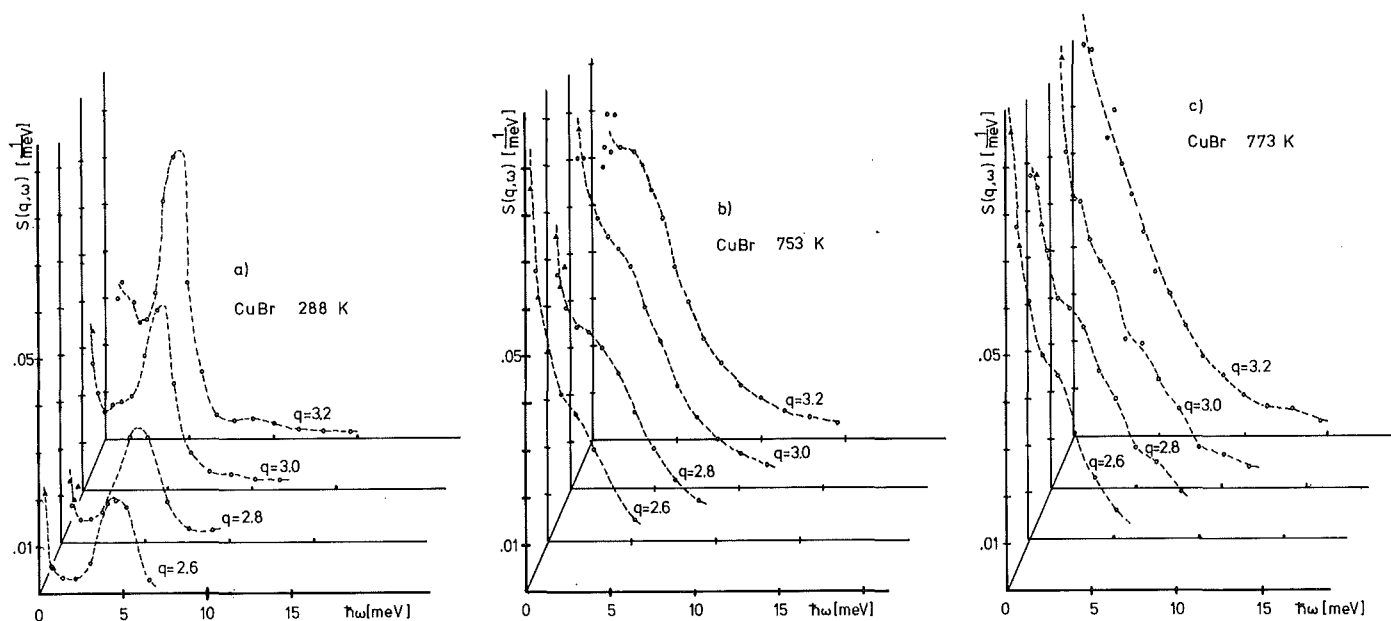


Fig. 2 a,b,c Examples for the symmetrized scattering law $S(q=\text{const.}, \omega)$ at different temperatures. Triangles and circles indicate the results measured in energy loss and energy gain, respectively. Lines are a guide to the eye.

Fig. 1 shows the generalized phonon density of states at three characteristic temperatures. The room temperature data correspond well to the measured phonon dispersion /1/. On heating a broadening of the first peak which corresponds to the TA zone boundary phonons can be seen. The high frequency peak caused by optical vibrations almost disappears.

For a more detailed discussion we show the line shapes of the scattering law $S(q, \omega)$ (Fig. 2). It can be seen that the strong TA phonon peak at ≈ 5 meV in the room temperature spectrum broadens at higher temperatures and merges with the elastic line. This spectrum is typical for super ionic conductors. The structure of the high temperature scattering laws reflects the movement of the mobile ion which is usually described by a jump diffusion model /2/. A study of α -CuBr on the basis of molecular dynamics is in progress.

References

- /1/ B. Prevat, C. Carabatos, and C. Schwab, *Solid State Commun.* **13**, 1726 (1973)
/2/ K. Funke, *Progress in Solid State Chemistry*, (Ed. J. Mc Caldin, G. Somorjai), Pergamon Press, (1976), Vol II, Part 4, p. 345

1.16 Soft Mode and Central Peak in the Cubic High Temperature Phase of K_2SnCl_6

K. Vogt^a, W. Reichardt, and W. Prandl^a

^a*Institut für Kristallographie der Universität Tübingen, D-7400-Tübingen*

The room temperature neutron inelastic measurements on the diffuse streak system in cubic (Fm3m) K_2SnCl_6 have been reported in an earlier paper /1/.

These streaks originate from librations of the $SnCl_6$ -octahedra (Fig. 1) which are strongly correlated in planes perpendicular to the rotation axes whereas the correlation between the planes is weak.

In a simple model we assumed rigid octahedra and torsional springs acting on the individual octahedra (spring strength E), between nearest neighbours in the

plane (D), and in adjacent planes (F). For a streak along \underline{c}^* we obtain

$$\hbar^2 \omega^2(\mathbf{q}) = \frac{4D}{\Theta} \left\{ 1 - \frac{1}{2} \left(\cos \frac{q_x + q_y}{2} + \cos \frac{q_x - q_y}{2} \right) \right. \\ \left. + \frac{E}{4D} + \frac{F}{D} \left(\cos \frac{q_x}{2} + \cos \frac{q_y}{2} \right) \cos \frac{q_z}{2} \right\}$$

where Θ is the moment of inertia.

From the measured profile of the dispersion surface we get

$$E = 673 \pm 55 \text{ meV}$$

$$D = 1018 \pm 11 \text{ meV}$$

$$F = -25.5 \pm 3.9 \text{ meV}$$

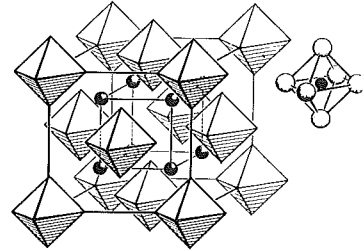


Fig. 1
The structure of K_2SnCl_6

The negative sign of F indicates that an antiphase rotation of adjacent planes is favoured. The correlations between the planes is weaker by a factor of forty than within the planes.

Further neutron inelastic measurements were performed at temperatures between 293 K and 513 K to verify the soft mode behaviour of the librational A_2 mode.

Fig. 2 shows constant- Q -scans at the X point of the Brillouin zone. The incoherent elastic scattering has been subtracted. The solid curves represent least squares fits of the theoretical function described below. At 170 degrees above the phase transition ($T_{C1}=261.5$ K) the mode is still overdamped. At 513 K we observe distinct phonon maxima in energy gain and loss.

Superimposed on the phonon scattering is a maximum centered at $E=0$ with a FWHM given by the instrumental resolution and an intensity that increases in approaching the phase transition - the central peak.

Whereas an energy width of this central peak is not detectable its extension along the streak is quite considerable (Fig. 3).

For a quantitative analysis of the measurements we used essentially the same scattering law as Shapiro et al. /2/:

$$S(\mathbf{q}, \omega) = \frac{k_B T}{\pi} \frac{\Gamma_0}{(\omega_\infty^2(\mathbf{q}, T) - \omega^2)^2 + \omega^2 \Gamma_0^2} + \frac{\delta^2(T)}{(\omega_\infty^2(\mathbf{q}, T) - \delta^2(T)) \omega_\infty^2(\mathbf{q}, T)} \frac{\gamma'^2}{\omega^2 + \gamma'^2}$$

where the second term represents the central peak scattering and $\frac{\gamma'^2}{\omega^2 + \gamma'^2} \approx \pi \delta(\omega)$.

From the 433 K and 513 K scans we obtained the scaling factor A and the damping constant $\Gamma_0 = 2.75$ meV. These values were kept fixed during the fits of the scans taken at lower temperatures.

The results of the least squares fits for the central peak strength $\delta(T)$ and the quasi-harmonic frequency of the mode $\omega_\infty(O,T)$ are shown in Fig. 4. Here $\omega_\infty(O,T)$ has been corrected for resolution effects by numerically folding the scattering function and the resolution function $R(Q-Q_0, \omega-\omega_0) / 3, 4/$.

The temperature dependence of the corrected frequency is given to a good approximation by

$$\hbar^2 \omega_\infty^2(O,T) = a(T-T_c)$$

with $a = 0.026 \text{ meV}^2/\text{K}$.

This work was supported by the Bundesministerium für Forschung und Technologie (BMFT project Nr. O3-41AO3P/I).

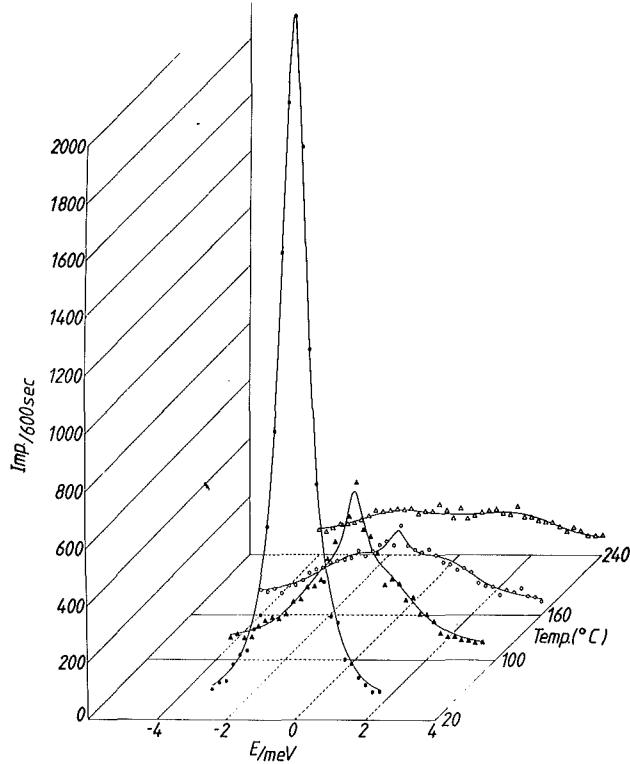


Fig. 2
Constant-Q-scans at the zone boundary (X point)

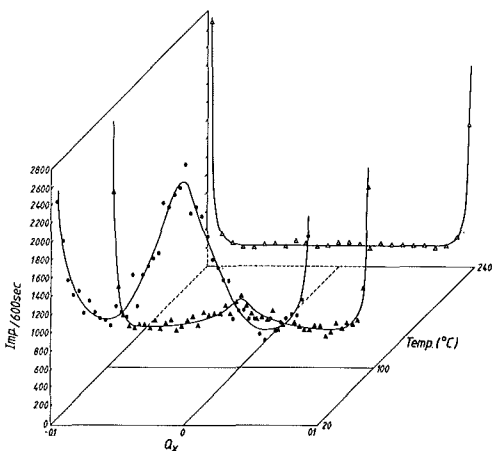


Fig. 3
Scans along the streak at $E = 0$

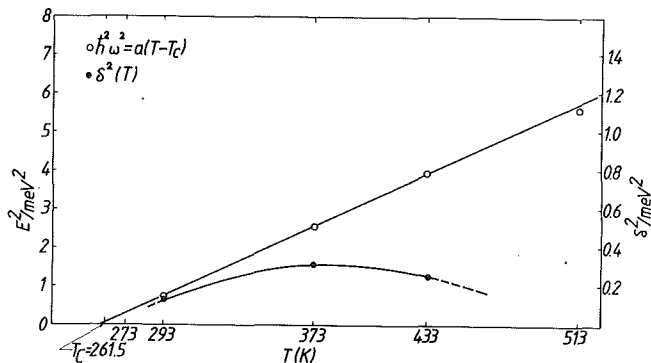


Fig. 4
Resolution corrected $\hbar^2 \omega_\infty^2$ and central peak strength δ^2 vs temperature

References

- /1/ K. Vogt, W. Reichardt, W. Prandl, Progr. Rep. IAK I, KfK 2881, 46 (1979)
 /2/ S.M. Shapiro, J.D. Axe, G. Shirane, and T. Riste, Phys. Rev. B6, 4332 (1972)
 /3/ M.J. Cooper and R. Nathans, Acta Cryst. 23, 357 (1967)
 /4/ B. Dorner, Acta Cryst. A28, 319 (1972)

1.17 Neutron Scattering Study of Polyacetylene

F. Gompf, B. Renker, and G. Wegner^a

^aInstitut für Makromolekulare Chemie, Universität Freiburg

Polyacetylene (CH) shows an electrical conductivity which can be varied between $\sigma \sim 10^{-9} \Omega^{-1}$ and $\sigma \sim 10^{-3} \Omega^{-1} \text{ cm}^{-1}$ by chemical doping /1/. A structure has been proposed on the basis of x-ray diffraction and crystal packing analysis /2/. Since the diffraction measurements are limited to polycrystalline samples the results were rather poor and consist of the measurement of very few and broad lines only. We have augmented these data by neutron diffraction measurements (Fig. 1) which due to the different cross sections might give some additional information. Our results are in good agreement with the x-ray data. One additional line at 78 degrees is observed in the neutron spectrum.

Structure factors have been calculated for the ortho-

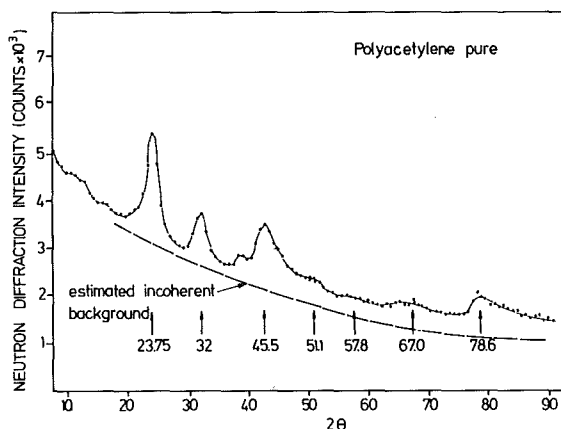


Fig. 1
Neutron diffraction pattern of pure polyacetylene

rhombic space group Pnm_a and the fractional coordinates of Ref. 2. We find rough agreement in view of the limited experimental accuracy (see Table 1).

Finally the generalized phonon densities of states have been deduced from inelastic neutron scattering data for the undoped and I_2 -doped material (Fig. 2). The measurements were performed with an incident energy of 5 meV.

The doped sample was obtained by storing pure polyacetylene powder in a I_2 atmosphere for about 30 hours which should be sufficient to obtain a saturation concentration. Fig. 2 shows that upon doping frequencies are shifted in the region between 20 to 90 meV. For better understanding we want to

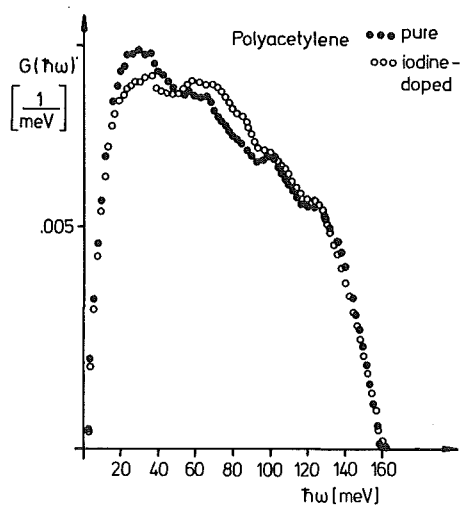


Fig. 2
Comparison of the generalized phonon densities of states of pure with iodine-doped polyacetylene.

h k l	$2\theta_{Br.}$	$I_{calc.}^0$	$I_{calc.} = \sum e^{-2W} I_{calc.}^0$	h k l	$2\theta_{Br.}$	$I_{calc.}^0$	$I_{calc.} = \sum e^{-2W} I_{calc.}^0$
2 0 0	23.37	0.88	1.54	3 0 2	55.32	0.21	0.11
1 0 1	23.38	1.00		4 1 1	56.57	0.13	
2 1 0	30.84	0.25		3 2 1	58.92	0.12	
1 1 1	30.86	0.31	0.62	0 2 2	58.95	0.49	0.25
2 0 1	31.09	0.32		3 1 2	59.36	0.22	
2 1 1	37.16	0.9	0.55	0 3 1	66.20	0.75	
3 0 1	41.07	0.14		0 1 3	67.29	0.12	
0 0 2	41.10	0.38	0.34	2 3 0	67.47	0.32	
1 0 2	42.86	0.10		1 3 1	67.48	0.10	
3 1 1	46.02	0.27		4 2 1	68.12	0.30	0.62
2 2 0	47.13	0.10		5 1 1	68.51	0.21	
1 2 1	47.14	0.25	0.71	4 1 2	68.53	0.26	
1 1 2	47.65	0.42		2 0 3	68.68	0.90	
4 0 0	47.78	0.33		1 3 2	78.57	0.53	
2 0 2	47.81	0.20		4 2 2	79.17	0.68	
2 2 1	51.78	0.86		4 3 0	82.12	0.54	0.44
4 1 0	52.23	0.13	0.69	2 2 3	82.77	1.38	
2 1 2	52.26	0.40		4 0 3	83.25	0.51	
4 0 1	52.39	0.39					

point out that $G(\omega)$ represents a sum of partial density of states functions each of which contains a weighting factor (σ/M σ =neutron cross section M : atomic mass). In this case the hydrogen value for σ/M dominates so much that in the neutron measurement we observe the spectrum of lattice vibrations only by the hydrogen atoms. This may be the reason that two Raman-lines at ~ 13 and 18.7 meV which are attributed stretching vibrations of I_3^- do not show up in the neutron spectra. Our results reflect a frequency hardening in a medium range of energies which probably contains an essential part of the C vibrations. We think that the additional 'springs' to I atoms (the saturation concentration is rather high: $(CHI_{0.3})_n$) is responsible for this effect, which would mean that the iodine is bound rather strong in the doped compound.

References

- /1/ S.L. HSU, A.J. Signorelli, G.P. Pezand, and R.H. Banghman, J. Chem. Phys. 69, 106 (1978)
- /2/ P.H. Banghman, S.L. HSU, G.P. Pez, and A.J. Signorelli, J. Chem. Phys. 68, 5405 (1978)

1.18 Crystal Structure and Lattice Dynamics of Perovskite Type $KMe^{II}F_3$

Part I: Structural Investigations of $KMnF_3$

G. Heger and J. Leciejewicz^a

^a*Institute of Nuclear Research, Otwock, Poland*

Perovskite type $KMnF_3$ is one of the best known examples where structural phase transitions occur caused by lattice dynamical instabilities. In addition to its antiferromagnetic Néel temperature $T_N=88$ K, two successive structural phase transformations were observed at 186 K and 91 K which are combined with the condensation of the Γ_{25} mode at the boundary of the cubic Brillouin zone in [111] direction (R-point) and of the M_3 mode at the [110] zone boundary (M-point), respectively /1/. These two modes correspond to a rotation of the fluorine octahedra around one of the [100] axes.

Low temperature X-ray crystal structure analyses of KMnF_3 have been performed at 145 K /2/ and at 50 K /3/ leading to the following sequence of structural modifications:

space groups:	$P4/\text{mbm} \leftarrow k_2 \rightarrow I4/\text{micm} \leftarrow k_2 \rightarrow (P4/\text{mmm}) \leftarrow t_3 \rightarrow \text{Pm}3\text{m}$
lattice constants:	$a_t \approx a_c/2$ $a_t \approx a_c/2$ $a_t \approx a_c$ $a_c = 4.186 \text{ \AA}$
	$c_t = 2a_c$ $c_t = 2a_c$ $c_t \approx a_c$
	virtual

experiment temperature:	50 K	145 K	295 K
-------------------------	------	-------	-------

The type of group-subgroup relationship is given by t_3 or k_2 /4/. But there still exist discrepancies in literature, especially concerning the crystal structure in the temperature range between about 80 and 125 K. We have started neutron diffraction experiments in order to check the former findings and to study the complicated situation around the onset of magnetic ordering in between 80 and 100 K.

On the four-circle diffractometer P110/FR2 a first data set of integral intensities was taken at 195(1) K, i.e. still in the region of the cubic high temperature modification of KMnF_3 ($T - T_{c1} \approx 9 \text{ K}$). At this temperature the lattice parameter a was determined to $4.182(2) \text{ \AA}$. A structure model refinement including anisotropic temperature factors yields a reliability factor $R(F) = \frac{\sum ||F_o| - |F_c||}{\sum |F_o|} = 0.038$. In Fig. 1 there is shown the atomic density distribution of the MnF_6 octahedron. In the representation of 50 % probability ellipsoids the anisotropic thermal vibrations of fluorines with dominant amplitudes perpendicular to the Mn-F bondings (due to the soft mode behaviour) are clearly visible.

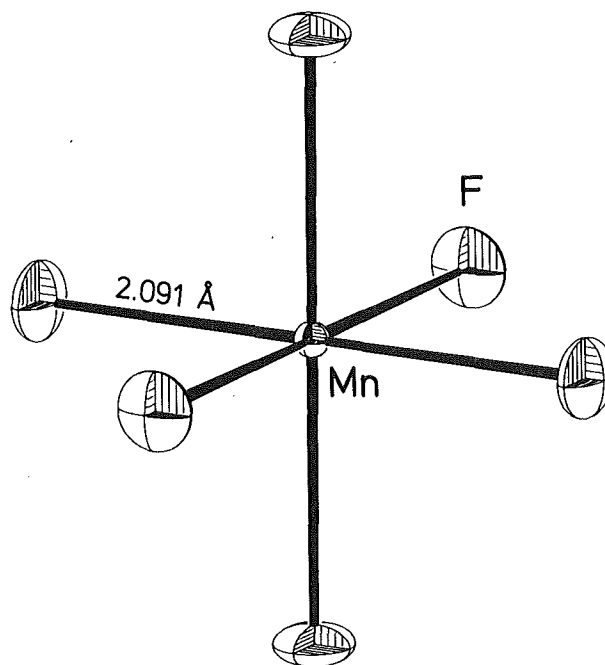


Fig. 1
 MnF_6 octahedron with ellipsoids of thermal vibrations at 195(1) K

At the phase transition between the cubic high temperature

modification and the body-centered tetragonal phase below 186 K in the group-subgroup scheme ($Pm\bar{3}m \xrightarrow{t3} P4/m\bar{3}m \xrightarrow{k2} 14/m\bar{3}m$) a virtual phase of space group type $P4/m\bar{3}m$ is by-passed. Due to the translationally equivalent symmetry reduction of index 3 ($Pm\bar{3}m \xrightarrow{t3} P4/m\bar{3}m$) this phase transition is combined with the occurrence of twinning domains with three different orientations. In spite of experimental difficulties in using a multidomain sample crystal, a structure analysis of the body centered tetragonal modification of $KMnF_3$ at about 100 K is in progress.

References

- /1/ G. Shirane, Rev. Modern Phys. 46, 437 (1974)
- /2/ V.J. Minkiewicz, Y. Fujii, and Y. Yamada, J. Phys. Soc. Japan 28, 443 (1970)
- /3/ M. Hidaka, J. Phys. Soc. Japan 39, 180 (1975)
- /4/ H. Bärnighausen, X. Int. Congr. Crystallography (Amsterdam, 1975), Acta Cryst. A31, p. S3 (1975)

1.18 Part II: Phonon Dispersion of $KZnF_3$

G. Heger, B. Renker, N. Lehner^a, and R. Geick^b

^a*Institut Laue-Langevin, Grenoble*

^b*Physikalisches Institut der Universität Würzburg*

Whereas the perovskite type $KMnF_3$ shows structural phase transitions caused by lattice dynamical instabilities (see preceding contribution: part I) $KZnF_3$ remains cubic (space group: $Pm\bar{3}m$) down to lowest temperatures. In order to clarify the difference in the behaviour of these two closely related substances we performed measurements of the phonon dispersion curves of $KZnF_3$ on the triple-axis spectrometers TAS 1 and TAS 2 at the FR2. The room temperature data, mainly of the acoustic branches, are plotted in Fig. 1. A comparison with the corresponding low-energy phonon dispersion curves of $KMnF_3$ /1/ shows no qualitative discrepancies. The softening of the TA modes at the M (M_3 phonon) and R points (Γ_{25} phonon) of the boundary of the cubic Brillouin zone is well established in $KZnF_3$ but less pronounced than in $KMnF_3$. An investigation of the temperature dependence of the M_3 and Γ_{25} modes of $KZnF_3$ shows a li-

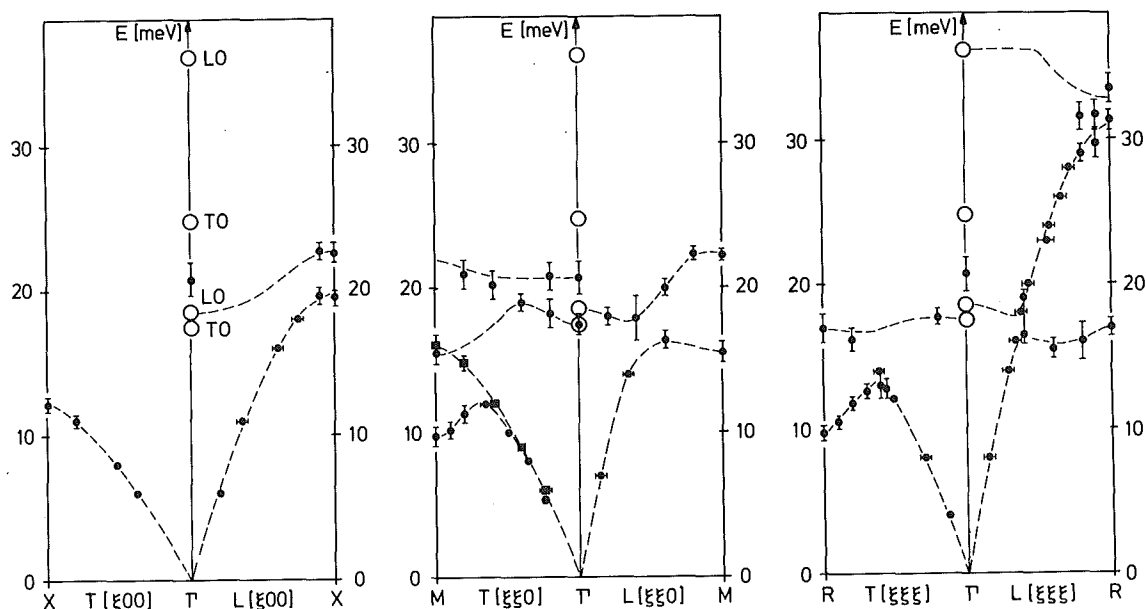


Fig. 1 Phonon dispersion of KZnF_3 at room temperature. The dotted lines result from preliminary shell model calculations. The open circles give the positions of the IR active modes.

near decrease of the squared phonon frequencies as a function of temperature (see Fig.2).

At finite temperatures no lattice dynamical instability - and therefore no structural phase transition - occurs.

From our experiments we have learned that the lattice dynamics of the fluoperovskites $\text{KMe}^{\text{II}}\text{F}_3$ with $\text{Me}^{\text{II}} = \text{Mn}$ and Zn are rather similar. Especially the softening of the Γ_{25} and M_3 modes with decreasing

temperature was observed for both substances. The quantitative differences - and hence the reduced stability of the cubic KMnF_3 - can be explained by geometrical arguments. The ionic radius of Mn^{2+} ($r(\text{Mn}^{2+}) = 0.80 \text{ \AA}$) is larger than that of Zn^{2+} ($r(\text{Zn}^{2+}) = 0.71 \text{ \AA}$) leading to a smaller Goldschmidt factor of 0.91 for KMnF_3 (compared with 0.95 for KZnF_3) near the limit of stability for the cubic perovskite structure (0.90) /2/.

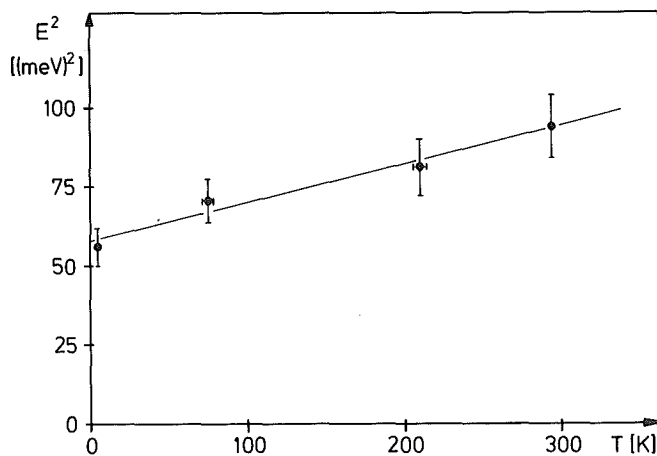


Fig. 2 Temperature dependence of $h^2 E^2$ for the Γ_{25} mode of KZnF_3

References

- /1/ K. Gesi, J.D. Axe, G. Shirane, and A. Linz, Phys. Rev. B5, 1933 (1972)
 /2/ D. Babel, Structure and Bondings 3, 1 (1967)

1.19 On the Space Group of MgAl_2O_4 (Spinel)

O. Baumgartner and G. Heger

We have started investigations of MgAl_2O_4 (spinel) in order to study its structural phase transition at about 800°C in more detail. The high temperature modification of spinel is of special interest due to the diffusion of Mg^{2+} and Al^{3+} ions (enhanced ionic conductivity).

Over many years - the first structural investigations of MgAl_2O_4 date back to 1915 /1,2/ - there are still controversies in literature concerning the space group of spinel. We want to specify the open questions:

- (1) the space group of natural spinel (grown at low temperature below the phase transition)
- (2) the space group of spinel in the high temperature modification
- (3) the space group of spinel at room temperature after a thermal treatment above 800°C .

Up to now the space groups $Fd\bar{3}m$ and $F\bar{4}3m$ are discussed for spinel at room temperature. According to the d glide plane symmetry, (hko) reflections are systematically absent when $1/2(h+k)=\text{odd}$ for the space group $Fd\bar{3}m$ in contrast to $F\bar{4}3m$. To decide between the two space groups under consideration by means of diffraction methods it is sufficient to check the systematic extinction conditions for (hko) reflections.

We used natural MgAl_2O_4 crystals from China (Cr^{3+} content $\leq 0.4\%$, Fe content $\ll 1\%$) for neutron diffraction measurements. An experimental check of the interesting (hko) reflections is complicated by very low intensities, multiple diffraction effects (Umweganregung), and higher order contamination. By rotation about the scattering vector (ψ -scan technique) we studied the influence of Umweganregung. ψ -scan measurements of the (200) and (600) reflections using a mean neutron wave-

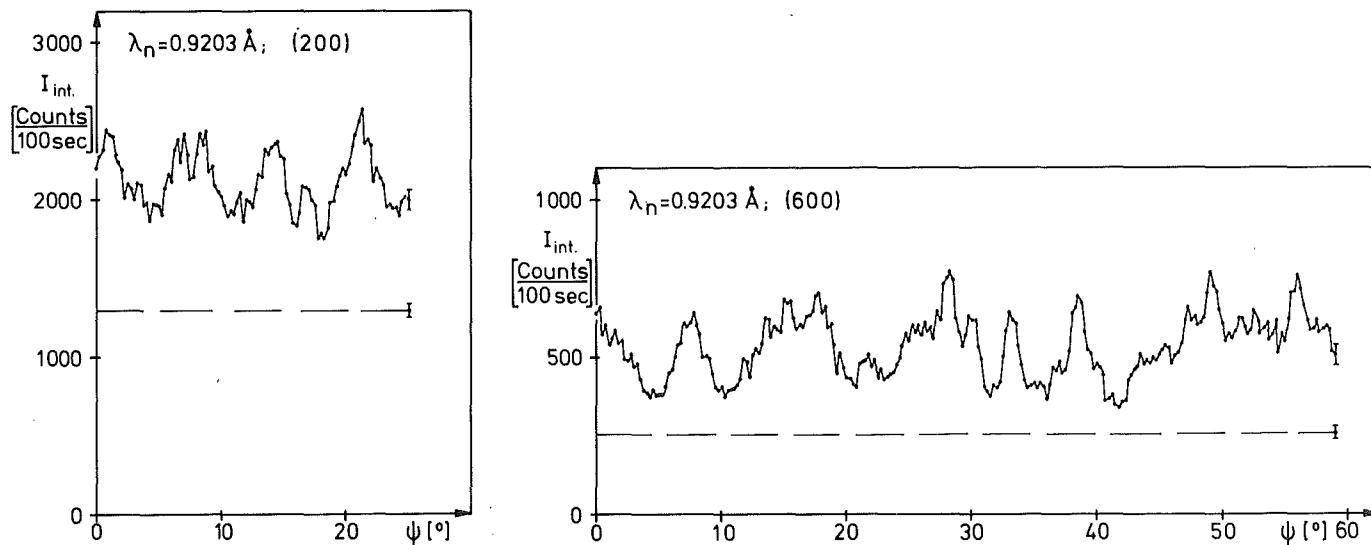


Fig. 1 ψ -scan measurements of the (200) and (600) reflections ($\lambda_n=0.9203 \text{ \AA}$)

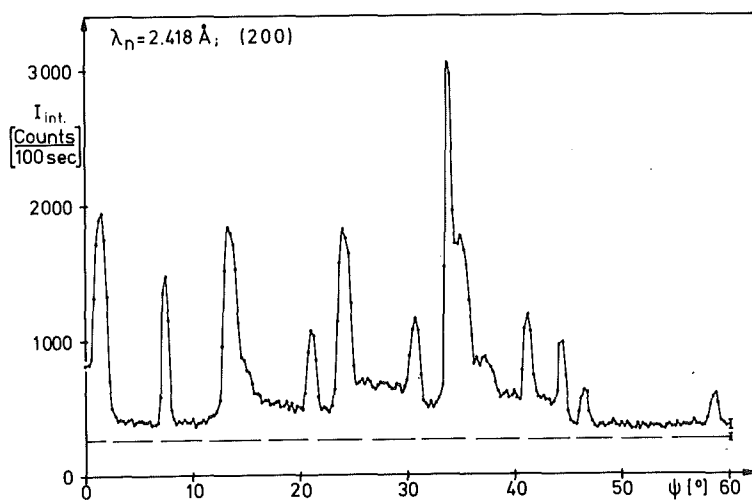


Fig. 2
 ψ -scan measurements of the (200) reflection ($\lambda_n=2.418 \text{ \AA}$). The broken straight line represents the accumulated intensity of measured background and estimated higher order contamination



Fig. 3 Diverse ω -scans (fixed ω -scan range $\Delta\Omega=1.2^\circ$) for different ψ -values out of the Umweganregung - free region

length of 0.9203 \AA are shown in Fig. 1. Instead of a plateau peaks of Umweganregung are observed nearly at any ψ angle. We repeated these ψ -scan measurements with a mean neutron wave length of 2.418 \AA . In this way we reduced the number of possible reflections by a factor of about 18, and thus the probability of multiple diffraction. Fig. 2 shows the results for the (200) reflection. Beside some high peaks we have clear evidence of ψ -regions without contributions of Umweganregung. Every point in Fig. 1 and Fig. 2 represents the integrated intensity of an ω -scan. The reflection profiles of these ω -scans are shown in Fig. 3 for the ψ -region between 47° and 58° where there is no Umweganregung. These small peaks have the shape of Bragg reflections. With these experiments we were able to confirm the existence of the (200) reflection. Our result indicate definitely an infraction of the d glide plane symmetry of space group Fd3m. Therefore, at least for natural $\text{MgAl}_2\text{O}_4(\text{Cr})$ at room temperature, the proper space group is $\overline{\text{F}}43\text{m}$. The resulting structure factors of "d-forbidden" reflections are so small that there is practically no deviation of atomic parameters between model calculations in Fd3m and $\overline{\text{F}}43\text{m}$. The origin of the symmetry reduction yielding the "d-forbidden" reflections is not yet understood.

Recent high temperature measurements at 830°C (see point (2) of the introduction) gave no indication of (hko) reflections with $1/2(h+k)=\text{odd}$. Therefore, we assume for the high temperature modification of spinel the space group Fd3m. Anharmonic structure model calculations are in progress.

References

- /1/ W.H. Bragg, Phil. Mag. 30, 305 (1915)
- /2/ S. Nishikawa, Proc. Tokyo Math. Phys. Soc. 8, 199 (1915)

1.20 Strukturverfeinerung von Harnstoff mit Neutronenbeugungsdaten bei 60, 123 und 293 K und X-N- und X-X($1s^2$)-Synthesen bei etwa 100 K

H. Guth^a, G. Heger, S. Klein^a, W. Treutmann^a, und C. Scheringer^a

^aSFB 127 Kristallstruktur und Chemische Bindung, Institut für Mineralogie der Universität Marburg

Z. Kristallogr. (in print)

Abstract

Neutron diffraction data were collected on urea at 60, 123, and 293 K, and the nuclear parameters were determined [$R(F)=0.034, 0.033, \text{ and } 0.043$ respectively]. The parameters at 293 K are compared with the neutron parameters of Pryor and Sanger by means of half normal plots and χ^2 tests, and the low-temperature parameters with the $1s^2$ -core parameters which were determined by Mullen and Hellner with x-ray data. Significant differences of 0.0030 \AA , on average, were found between the U_{33} components from our low-temperature determination and from the $1s^2$ -core refinement. X-N and X-X($1s^2$) maps are calculated for about 100 K with two different scale factors and, after an assessment of all parameters, a "best" experimental deformation density is calculated. The effect of large librations of the N atom about the C-O axis (4.2 rms degrees) on the density distribution, and the effect of using not fully correct phases are discussed. The errors in the density distribution which are caused by errors in the x-ray data, in the scale factor and in the neutron parameters, are assessed to be 0.07 e\AA^{-3} at the bond peaks, and 0.45 e\AA^{-3} at the nuclear positions. The "best" experimental deformation density has higher bond peaks (except for the C-O bond) than a (published) theoretical difference density (4-31 G basis), but lower peaks in the lone-pair regions of the oxygen atom and no polarization minimum at the oxygen atom.

2. THEORY

2.1 Electronic Structure of NbO

K.-P. Bohnen, W. Weber, and D.R. Hamann^a

^a*Bell Laboratories, Murray Hill, N.J., USA*

All rocksalt structure refractory compounds exhibit a strong tendency towards the formation of vacancies. With increasing number of valence electrons (VE), e.g. going from ZrC over NbC to NbN, there is a trend that not only the nonmetal sites, but also the metal sites become more and more unoccupied. In NbO, there exist about 25 % vacancies in both sublattices which form a simple cubic superstructure. The size of the unit cell-hosting three Nb and three O atoms plus two vacant atomic sites - is small enough to allow first principles electronic bandstructure calculations.

Two reasons have stimulated our interest in such a calculation: i) the influence of vacancies on the bandstructure of refractory compounds and ii) the phonon dispersion curves of $\text{Nb}_{0.75}\text{O}_{0.75}$ have been measured recently /1/. They show a deep minimum of the longitudinal acoustic (LA) branch, which is very similar to the LA anomaly of VN and NbN at the X point, when the NbO dispersion curves are unfolded into a fcc Brillouin zone. This similarity seems to be very surprising when looked at from a rigid-band point of view: $\text{Nb}_{0.75}\text{O}_{0.75}$ (8.25 VE) should have about the same dispersion curves as ZrC (8 VE), but not as NbN (10 VE).

For the bandstructure calculation we have used a selfconsistent Gaussian linear-combination-of-atomic-orbitals (LCAO) program developed by Hamann and Appelbaum /2/. In the program, the crystal charge density and the crystal potential are also expanded in terms of Gaussian exponentials centered at arbitrary positions in the unit cell. This allows to describe the crystal potential very accurately. All "non-muffin-tin" corrections can be included automatically. As the size of the valence orbital basis is governing the amount of computer time required for the calculation, we have studied various basis sets in calculations of perfect NbO with the rocksalt structure. We found that a basis set of 9 valence orbitals for the Nb atom (s + p + d) and 4 for the O atom (s + p) was sufficient there. Thus, for $\text{Nb}_{0.75}\text{O}_{0.75}$ we used these orbitals for Nb and O plus some s and p orbitals at the

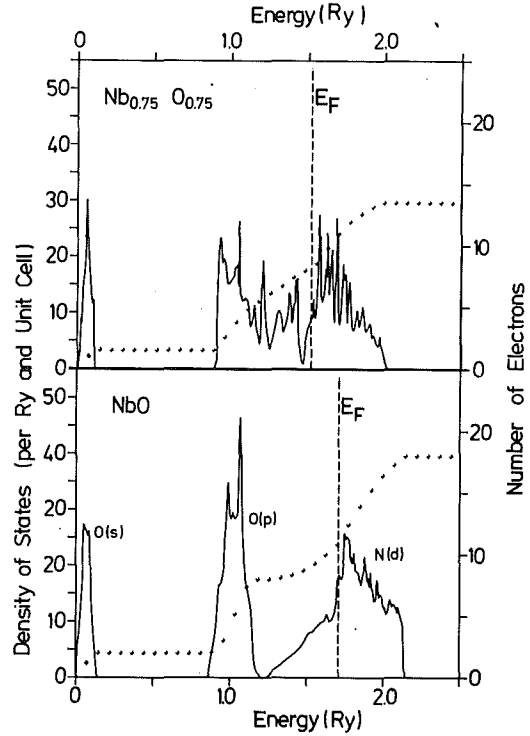


Fig. 1
Electronic density of states for $\text{Nb}_{0.75}\text{O}_{0.75}$ and NbO , both normalized on a fcc unit cell. Dotted lines show corresponding number of electrons.

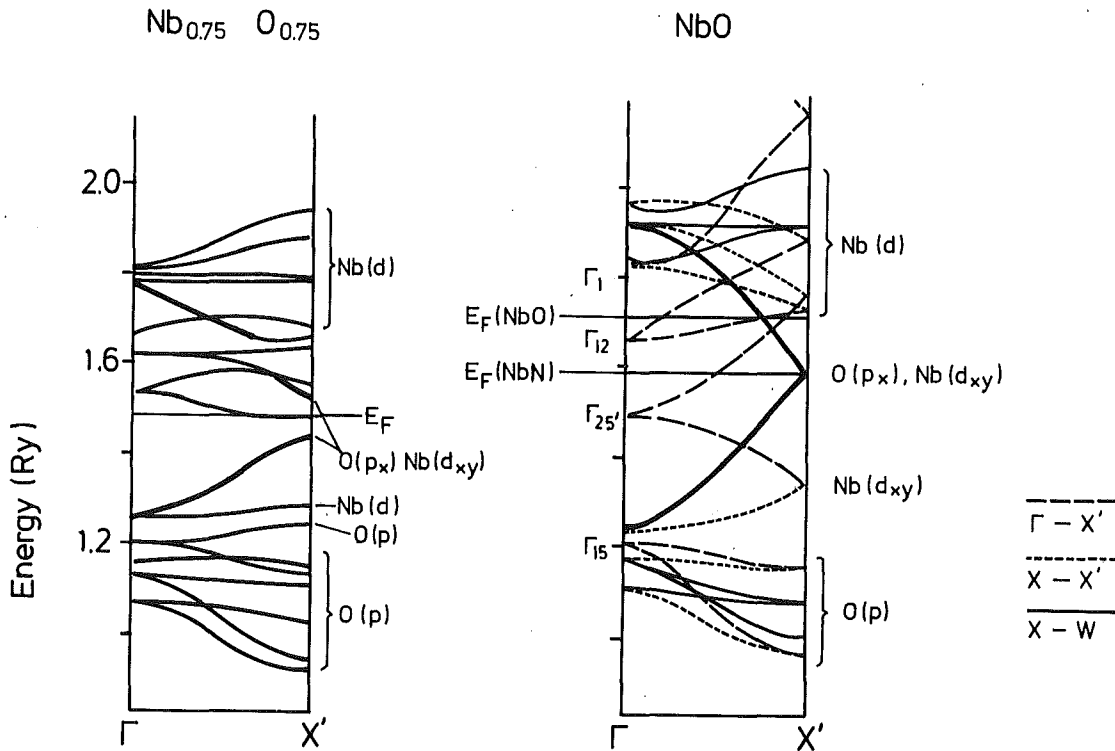


Fig. 2 Electronic bandstructure for $\text{Nb}_{0.75}\text{O}_{0.75}$ and NbO for the Γ - X' direction of the simple cubic Brillouin zone. The low-lying O s bands are omitted. For NbO , we have indicated the origin of the back-folded bands in the fcc zone. The fat solid lines denote the X-W bands which cause the LA (X) anomaly in NbN .

vacancy sites. For the potential centers we chose the atomic and vacancy sites and in addition positions on the body diagonals halfway between Nb and O.

Results of our calculations both for $\text{Nb}_{0.75}\text{O}_{0.75}$ and for hypothetical fcc NbO are shown in Fig. 1 and 2. The density of states curves are displayed in Fig. 1. For fcc NbO we find the typical three-peak-structure of all cubic refractory compounds, very similar to results of the Vienna group /3/.

However, in $\text{Nb}_{0.75}\text{O}_{0.75}$ a large number of new states appears in the gap between the O p and the Nb d peaks. These states are obviously associated with the vacancies. They are partly split off the O p bands and partly shifted down from the Nb d bands. This result is similar to that of Ries and Winter /4/ who studied the electronic structure of a vacancy in NbC using a cluster method.

In Fig. 2, the energy bands for $\text{Nb}_{0.75}\text{O}_{0.75}$ and for fcc NbO are compared along the Γ -X' direction (X' denotes the simple cubic X point). We note that the O - p bands of $\text{Nb}_{0.75}\text{O}_{0.75}$ have not been altered much. In contrast, the higher lying bands changed quite drastically. However, among those bands are some which have not been altered too much. Two of those bands have been especially marked in Fig. 2. The LA big anomaly at the X point in the phonon dispersion curves of VN and NbN originates from these bands. It is caused by particularly strong coupling between states of these bands due to large and opposite band dispersion and strong O(p)-Nb(d) hybridisation /5/. In $\text{Nb}_{0.75}\text{O}_{0.25}$ these two bands have maintained their basic features, in addition, the Fermi energy lies between the two bands, very similar to NbN. These analogies in the electronic bands should explain why the LA anomalies are so similar in $\text{Nb}_{0.75}\text{O}_{0.75}$ and NbN.

References

- /1/ P. Rödhammer, W. Reichardt, and J. Hufnagl, this volume
- /2/ J.A. Appelbaum and D.R. Hamann, in Transition Metals (Eds., M.J.G. Lee, J.M. Perz, E. Fawcett), 1977, Conference Series No. 39, The Institute of Physics, Bristol and London
- /3/ K. Schwarz, J. Phys. C8, 809 (1975), A. Neckel, et al., J. Phys. C9, 579 (1976)
- /4/ G. Ries and H. Winter, J. Phys. F10, 1 (1980)
- /5/ W. Weber et al., Phys. Rev. Lett. 43, 868 (1979)

2.2 Electronic Structure of Cubic V_3Si and Nb_3Sn

L.F. Mattheiss^a and W. Weber

^a*Bell Laboratories, Murray Hill, New Jersey 07974, USA*

Phys. Rev. B, to be published

Abstract

The results of self-consistent augmented-plane-wave (APW) energy-band calculations by Klein et al. for V_3Si and Nb_3Sn have been fitted using a nonorthogonal-tight-binding (NTB) interpolation scheme. The NTB basis functions include Bloch sums formed from s,p,d orbitals at the V(Nb) sites and s,p orbitals at the Si(Sn) sites, respectively. The resulting 62x62 secular equation contains approximately 80-100 independent two-center energy and overlap parameters which have been determined by means of a nonlinear-least-squares fitting procedure. Highly accurate fits have been obtained for the lowest 40 bands at 35 k-points in the Brillouin zone; the corresponding rms errors are 3 mRy and 2 mRy for V_3Si and Nb_3Sn , respectively. The accuracy of this NTB fit has allowed the calculation of high-resolution density-of-states curves $N(E)$, including the decomposition into angular-momentum and subband components $N_\alpha(E)$. The results of these studies provide new and interesting insight regarding the orbital character of the extremely flat Γ_{12} bands which lie near E_F in both V_3Si and Nb_3Sn . The present results show that the principal orbital component of this subband is transition-metal (TM) σ -bonding d orbitals with $(3z^2-r^2)$ symmetry along the TM-atom chains parallel to the Z-1c axis. It is also shown that the small dispersion of the Γ_{12} subbands over a large fraction of the Brillouin zone (2 mRy) is due to strong hybridization effects with TM p orbitals which are also oriented along the chain axes. We believe that this novel combination of strong but compensating d-d and p-d interactions within the Γ_{12} subband near E_F is the principal source of the anomalous electronic properties which have long been associated with both V_3Si and Nb_3Sn .

2.3 Selfconsistent Study of Surfaces of Simple Metals by the Density Matrix Method: (100)- and (110)-surfaces of Na, K, Rb and Cs*

K.-P. Bohnen and S.C. Ying^a

^aBrown University, Providence, R.J. 02912, USA

Phys. Rev. B 22, 1806 (1980)

Abstract

The electronic structure of surfaces of simple metals has been studied by a direct determination of the density matrix in a local orbital basis. The method is based on a variational treatment of the ground state energy applying the Hohenberg-Kohn-Sham functional formalism. We present here results for low index surfaces of a series of alkali metals for which the ionic pseudo potential is treated non-perturbatively. The results for surface charge density, work function and surface energy are compared with other self-consistent calculations and experimental values.

2.4 Recent Calculations of Phonon Spectra of Transition Metals and Compounds

W. Weber

Proc. 3rd Conference on Superconductivity in d- and f-Band Metals, San Diego (1979)

Abstract

A new formulation of the lattice dynamics is presented, based on the non-orthogonal tight binding scheme. The method is applied for calculations of the phonon dispersion curves in various transition metals and compounds. All anomalous features in the phonon spectra of these crystals are reproduced. The physical origin of the anomalies and their relation to superconductivity are elucidated.

2.5 A Model Study of the Kohn Anomaly in the Optical Phonon Branch of a Binary Compound

C.Y. Fong^a and W. Weber

^aDepartment of Physics, University of California, Davis,
California 95616, USA

Phys. Status Solidi B 99, 689 (1980)

Abstract

We have generalized Labbé's tight binding method and applied it to a linear chain with two atoms/unit cell to study the Kohn anomaly in the optical phonon branch. The effects of various tight binding matrix elements on the anomaly have been explored. The enhancement of anomaly can be effectively obtained by increasing the electron-phonon interactions.

2.6 Displacement Correlations in Covalent Semiconductors

O.H. Nielsen^a and W. Weber

^aInstitute of Physics, University of Aarhus, DK-8000 Aarhus C, Denmark

*J. Phys. C*13, 2449 (1980)

Abstract

Displacement-displacement correlation functions as well as vibrational amplitudes and Debye temperatures, are calculated for covalent semiconductors using the adiabatic bond charge model. The results are compared with the shell model and heat capacity as well as x-ray and Mössbauer data. Radial and transverse correlations are computed. Good agreement is found with recent EXAFS results. Values for the mean square dynamic deformations of the bond length and bond angles are presented. The dynamical disorder of crystalline germanium is compared with the static disorder of amorphous germanium.

2.7 Strong Depression of Superconductivity in VN by Spin Fluctuations

H. Rietschel, H. Winter, and W. Reichardt

Phys. Rev. B 22, 4284 (1980)

Abstract

In this paper we argue that spin fluctuations prevent VN from being a superconductor with a transition temperature of about 30 K instead of the experimental value of 8.6 K. Thus, besides V and Nb for which similar results have been reported recently, VN provides a further and even more pronounced example for spin fluctuations limited high T_c superconductivity. Our results are obtained from microscopic calculations of T_c for the refractory compounds TiN, ZrN, VN and NbN and from magnetic susceptibility data. Among these four compounds VN is exceptional in exhibiting both a large theoretical overestimate of T_c , if spin fluctuations are omitted, and a high magnetic susceptibility. Incorporating spin fluctuations within the theory of Berk and Schrieffer, the theoretical value of T_c can be brought in agreement with experiment. Calculations of the magnetic susceptibility and of T_c in nonstoichiometric VN_x ($0.75 \leq x \leq 1.0$) and their comparison to experimental results of Ajami and MacCrone provide further support for our ideas.

2.8 Structural and Dynamical Behavior of α -AgI

W. Schommers

In: "Proceedings of the Conference on Fast Ion Transport in Solids", ed. by P. Vashishta et al. (Elsevier, North Holland, New York, 1979)

Abstract

We have performed molecular-dynamics calculations for α -AgI at 585 K using a two-dimensional model of 256 particles. It turned out that the structure of the I^- subsystem is distinctly reflected in the Ag^+ subsystem, in particular,

the Ag^+ subsystem forms a quasi-lattice and we have to distinguish between quasi-lattice positions and interstitial positions; this behavior is supported by the observed jump-diffusion processes. Furthermore, we have found (i) that there is a strong coupling between individual motions of the Ag^+ ions and the collective behavior of the system and, (ii) that a pronounced collisionless motion takes place. Our results agree well with various experimental data.

2.9 Structure and Dynamics of Superionic Conductors

W. Schommers

Phys. Rev. B 21, 847 (1980)

Abstract

Within a two-dimensional molecular-dynamics model of superionics, the following effects were observed: (i) the silver subsystem tends to form a Wigner lattice, (ii) a pronounced collisionless motion takes place within an important frequency range, and (iii) the individual motions of the ions are strongly coupled to the collective modes of the system. Although we had to restrict ourselves to a two-dimensional model, the results for the main dynamical properties of the system agree well with various experimental data for $\alpha\text{-AgI}$.

3. ELECTRONIC STRUCTURE AND MAGNETISM OF SOLIDS

3.1 Muon Spin Rotation Measurements in Paramagnetic PdFe and PdNi Alloys

H. Schmidt, B. Scheerer, V. Oestreich, F. Götz, G. Czjzek, F.N. Gygax^a, A. Hintermann^a, W. Rüegg^a, A. Schenck^a, and W. Studer^a

^a*Laboratory for High Energy Physics, ETH Zürich*

The asymmetric intensity distribution of positrons emerging from the decay of positive muons can be used to detect the precession of the muon spin in a magnetic field (muon spin rotation, μ SR). For muons implanted into solids this provides a possibility for determining the internal magnetic field acting on the muons at interstitial sites since positive muons are repelled by the charges of the ion cores. This yields information about the distribution of fields in solids complementary to that obtained by measurements of nuclear hyperfine fields which are generally dominated by the polarization of core electrons.

Measurements of μ SR can be carried out by observing in a counter at some fixed position directly the oscillations of the positron count rate with time due to the precession of the muon spin (time-differential method) /1/ or by the stroboscopic method /2/ using the pulse structure of the accelerator beam which generates the muons. In homogeneous materials and if relaxation effects are unimportant, the field acting on the muons can be determined to a much higher precision by the stroboscopic method than by time-differential measurements. If these conditions are not met, the stroboscopic signal becomes broadened, and then the observation of the damping of the oscillations by the time differential method often yields more significant information.

We have investigated the magnetic fields at interstitial sites in dilute PdFe (0.3, 3, and 10 at% Fe) and PdNi (1.5 and 10 at% Ni) alloys over a large temperature range. The Knight shift $K_{\mu} = (v_{\mu} - v_0) / v_0$ of the muon precession frequency v_{μ} relative to the frequency corresponding to the applied field was measured by the stroboscopic method at temperatures ranging from the respective Curie temperatures T_c of the samples up to 775 K (for PdNi (1.5 at%) for $25 \text{ K} \leq T \leq 775 \text{ K}$). The applied field of 7.38 kG was measured and stabilized by proton NMR to a precision of 1 ppm.

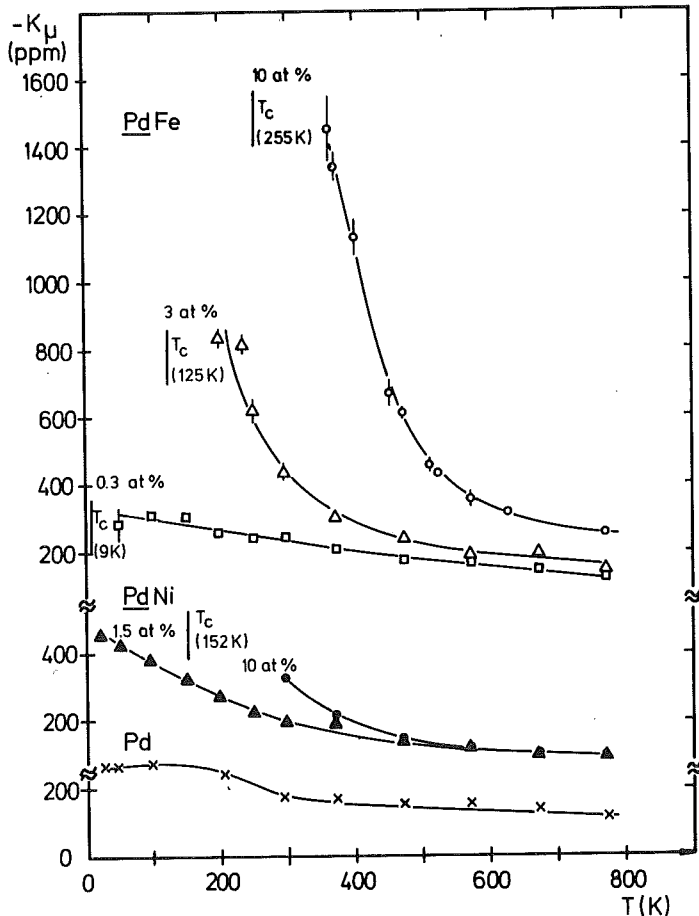


Fig. 1 Knight shifts of PdFe and PdNi alloys as a function of temperature. Knight shifts of pure Pd measured at the same temperatures as the alloys are shown for comparison.

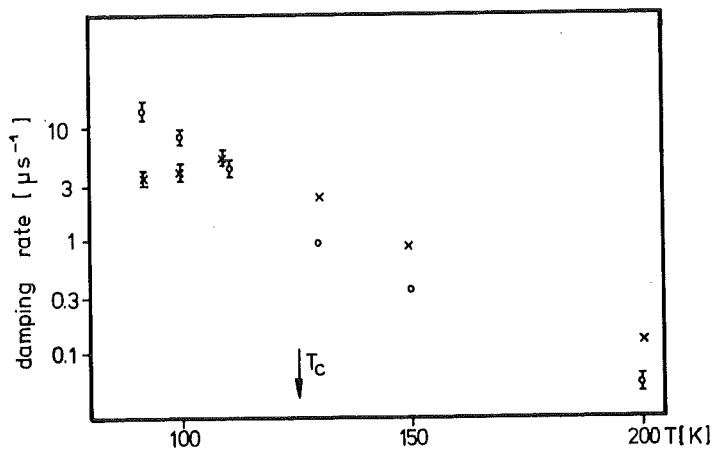


Fig. 2 Damping rates observed in time differential measurements for $\text{Pd}_{0.97}\text{Fe}_{0.03}$ in applied fields of 2 kOe (O) and 4 kOe (x)

The results obtained for the alloy samples and for pure Pd (containing less than 6 ppm of magnetic impurities) are shown in Fig. 1. The Curie temperatures T_C of the samples were determined by magnetization measurements. Further measurements of the magnetic susceptibility of our samples over the temperature range in which the Knight shift has been determined are in progress. A preliminary comparison with susceptibility data published in the literature /3/ indicates a linear relationship between our K_μ values and the bulk susceptibility, $K_\mu = K_0 + \alpha\chi$ at temperatures exceeding T_C by more than 150 degrees. The slope $\alpha \approx 1 \mu\text{KG}/\mu_B$ is nearly the same for the alloys, for pure Pd, and for paramagnetic Ni (for $T > T_C$) /4/.

At lower temperatures K_μ increases more slowly than the susceptibility as T_C is approached, and the stroboscopic signal broadens rapidly. Time differential measurements were employed at temperatures around T_C for a determination of the damping rates. Results for PdFe (3 at%) are presented in Fig. 2. The phenomena observed close to T_C are tentatively ascribed to the presence of slowly fluctuating ferromagnetically coupled regions. Both the observed broadening and the deviation from the linear relation between K_μ and χ in this temperature range are explained by the

same assumption if K_{μ} in these ferromagnetic regions is at least less negative than the extrapolated average value or possibly even positive.

References

- /1/ J.H. Brewer, K.M. Crowe, F.N. Gyax, and A. Schenck, in Muon Physics, edited by V.W. Hughes and C.S. Wu, Vol. 3 (Academic Press, N.Y. 1975), p. 3
- /2/ M. Camani, F.N. Gyax, E. Klempt, W. Rüegg, A. Schenck, H. Schilling, R. Schulze, and H. Wolf, Phys. Lett. 77B, 326 (1978)
- /3/ D.W. Budworth, F.E. Hoare, and J. Preston, Proc. Roy. Soc. A257, 254 (1960); H. Kojima, R.S. Tebble, and D.E.G. Williams, Proc. Roy. Soc. A260, 246 (1961) D. Gerstenberg, Ann. Phys. (Leipzig) 7. Folge, 2, 236 (1959)
- /4/ F.N. Gyax, W. Rüegg, A. Schenck, H. Schilling, W. Studer, and R. Schulze, J. Magn. Magn. Mater. 15-18, 1191 (1980)

3.2 Spin Wave Dispersion Relations in Ordered Fe_3Si

P.v. Blanckenhagen and C. Lin^a

^a*Fellow of the Humboldt Foundation from the Physics Institute, Peking*

The ordered Fe_3Si crystallises in the cubic DO_3 structure and orders ferromagnetically below about 820 K /1/. In the related compound Fe_3Al a strong anomaly of the spin wave dispersion in the [111] direction was observed which has been attributed to an interaction of the spin waves with Stoner excitations /2/. For $\text{Fe}_{0.88}\text{Si}_{0.12}$ it was shown that spin waves exist also above T_c /3/. Hitherto in FeSi alloys magnetic excitation have only been investigated for disordered alloys up to a Si content of 15 % /3,4/.

We have performed neutron scattering experiments in ordered Fe_3Si in order to determine the spin wave dispersion relations and their temperature dependence. The sample had been annealed for 3 days at 1400 K and then slowly cooled down with a speed of 12 degrees per hour. The exact composition of our sample material was $\text{Fe}_{84.7}\text{Si}_{25.3}$. Single crystals with mosaic spreads of 0.4° and 1.5° were used for the neutron scattering experiments. The experiments were carried out on the TAS 1 triple axis spectrometer at the FR2.

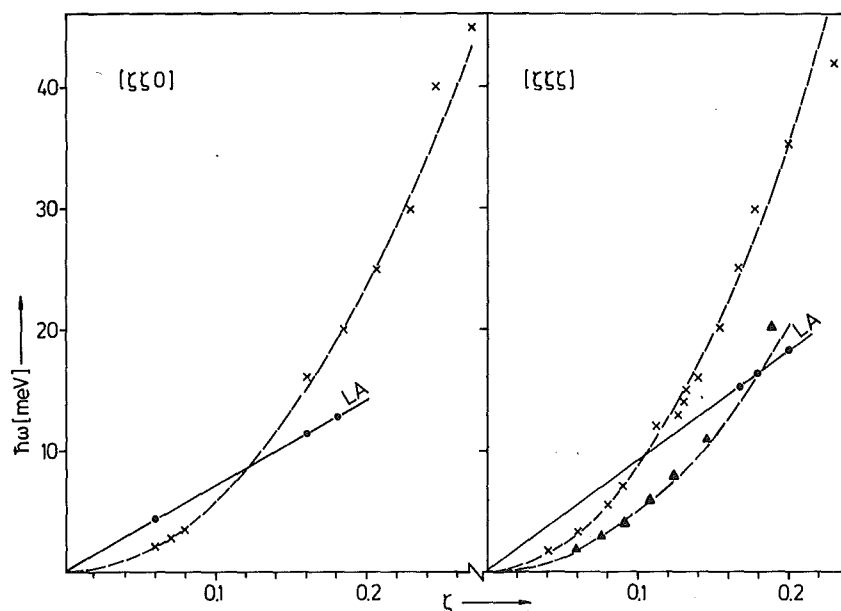


Fig. 1 Spin wave dispersion relations in ordered Fe_3Si in the $[110]$ and the $[111]$ direction at room temperature (x-x) and at 760 K (▲-▲).

The dispersion of the longitudinal acoustic phonons is marked by LA. The dashed lines are the quadratic dispersion relations as calculated with the D value given in the text.

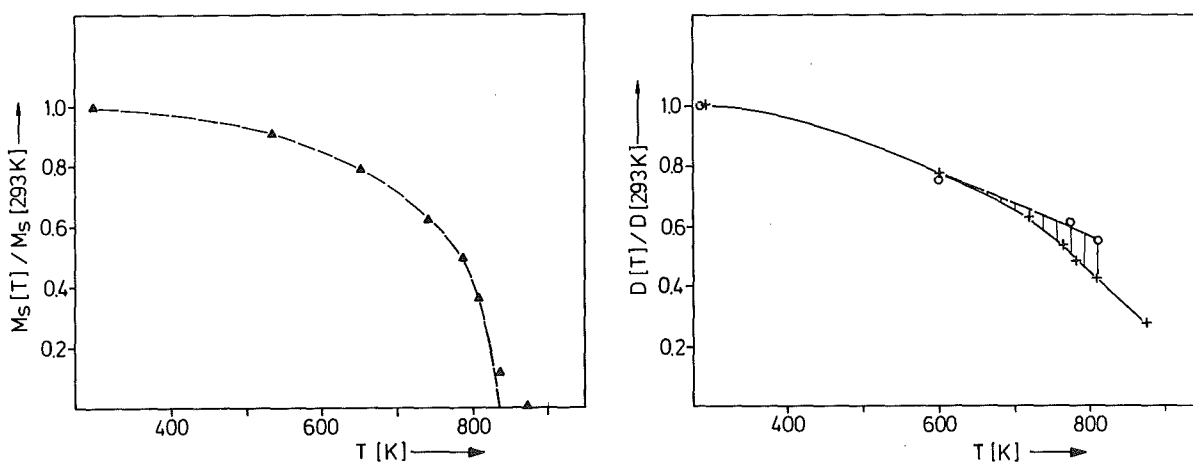


Fig 2 Temperature dependence (a) of the spontaneous magnetization M_s and (b) of the stiffness parameter D (+ : $\hbar\omega=6$ meV, O : $\hbar\omega=20$ meV)

The observed peak positions of the neutron intensity distributions have been corrected for the shift due to the finite resolution of the spectrometer with the aid of a resolution programme which considers the momentum resolution in three dimensions /5/. From the corrected results we obtained the dispersion relations shown in Fig. 1. For room temperature they are described by a dispersion law $\hbar\omega = Dq^2$ with $D = 240 \pm 10 \text{ \AA}^2 \text{ meV}$ for the [110] as well as for the [111] direction. The result for D at room temperature is about 5 % larger than D for a disordered alloy with 12 at% Si [3]. No significant deviations from the quadratic law were observed which could be assigned to interactions with phonons or Stoner excitations.

Fig. 2 shows the temperature dependence of the magnetization derived from the (111) Bragg peak intensity and of the spin wave stiffness constant derived from measurements at different excitation energies. These data indicate that also above T_c spin waves seem to exist in ordered Fe_3Si .

References

- /1/ G. Inden and W. Pitsch, *Z. Metallkd.* 63, 253 (1972)
- /2/ L. Weiss and P. Urwank, in *Neutron Inelastic Scattering Vol. II*, ed. IAEA, Vienna (1978) p. 197.
- /3/ J.W. Lynn, *Phys. Rev.* B11, 2624 (1975)
- /4/ B. Antonini, F. Menzinger, A. Paoletti, and A. Tucciarone, *Phys. Rev.* 178, 833 (1969)
- /5/ L. Pintschovius, private communication

3.3 Spin Wave Dispersion Relation in Partially Ordered Ni_3Mn

P.v. Blanckenhagen and B. Scheerer

J. Magn. Magn. Mat. 13, 116 (1979)

Abstract

The spin wave dispersion relation of partially ordered Ni_3Mn has been measured in the [111] direction by inelastic neutron scattering experiments using the

triple-axis technique. The dispersion curve rises quadratically according to the relation $\hbar\omega = Dq^2$ and the stiffness constant D is about seven times greater than the D value estimated for the disordered (quenched) alloy.

3.4 Antiferromagnetic Long Range Order in $\text{Ni}_{0.65}\text{Mn}_{0.35}$

P.v. Blanckenhagen and T.J. Hicks^a

^a*Guest Scientist on Study Leave from the Department of Physics, Monash University, Clayton, Victoria, Australia*

Disordered Ni-Mn alloys are ferromagnetic up to a critical concentration at about 27 at% Mn /1/. For the Mn-rich alloys on the other hand antiferromagnetic order has been found down to 70 at% Mn /2,3/. Measurements of the hyperfine fields at the Ni sites showed a broad distribution of fields centered at a nonzero value which changes little as the Mn concentration is increased from 2.5 to 35 at% Mn /4,5/. The persistence of the hyperfine fields indicates that some kind of magnetic order exists also beyond 27 at% Mn.

To determine this magnetic order we have started a neutron scattering study of disordered Ni-Mn alloys in the concentration range from 27 to 40 at% Mn. In this report we present results for 30 and 35 at% Mn which indicate that the 35 at% alloy is antiferromagnetic at 4.2 K whilst for the 30 at% alloy no long range magnetic was observed. Alloys are melted in a levitation crucible. They were then homogenized under helium at 1220 K for ten hours and quenched into oil. Spark cut cylindrical specimens of 6 mm diameter were used for the diffraction experiments. The diffraction patterns were obtained using the MAG1 and MAG2 spectrometers at the FR2 with $\lambda=2.4$ and 4.2 \AA , respectively. Fig. 1 shows the MAG1 diffraction patterns of the 30 and 35 at% Mn alloy measured at 7 K and corrected for background. Superimposed on the diffuse scattering from the 35 at% alloy a Bragg peak is indicated at the (110) position.

For the 30 at% Mn alloy there is no indication of a Bragg peak at the (110) position and the shapes of the diffuse peaks at (110) and (100) appear similar. The (110) Bragg peak may be antiferromagnetic in origin. It cannot be due to Ni_3Mn type ordering as that also requires a superlattice peak at the (100) position.

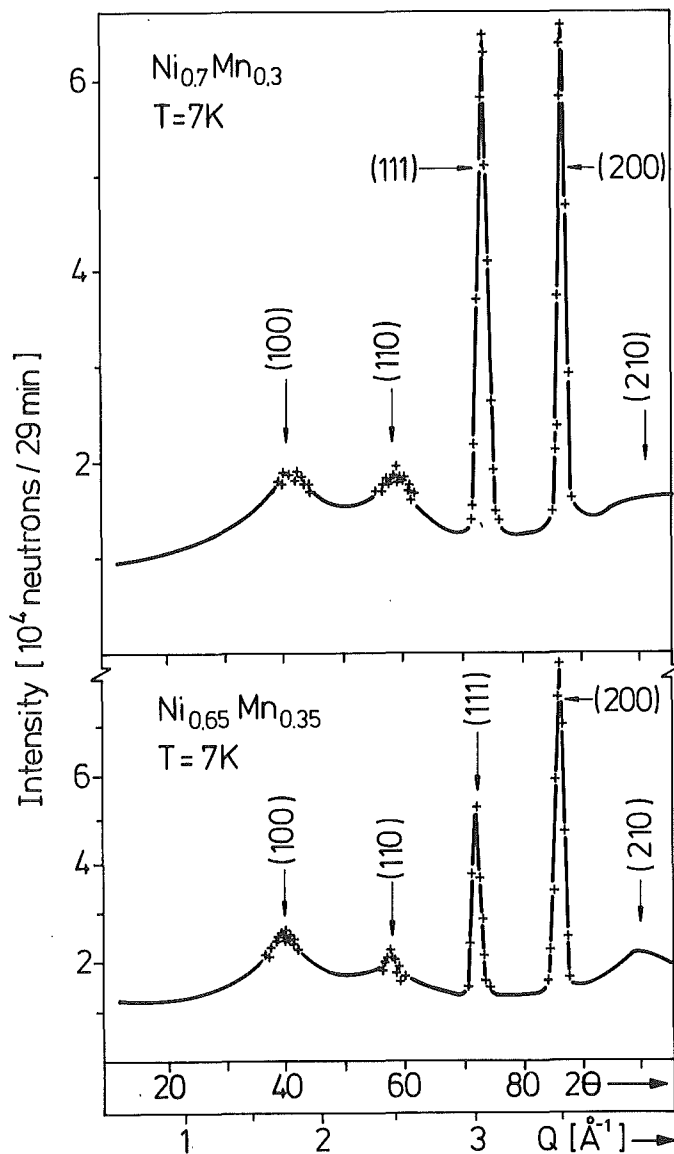
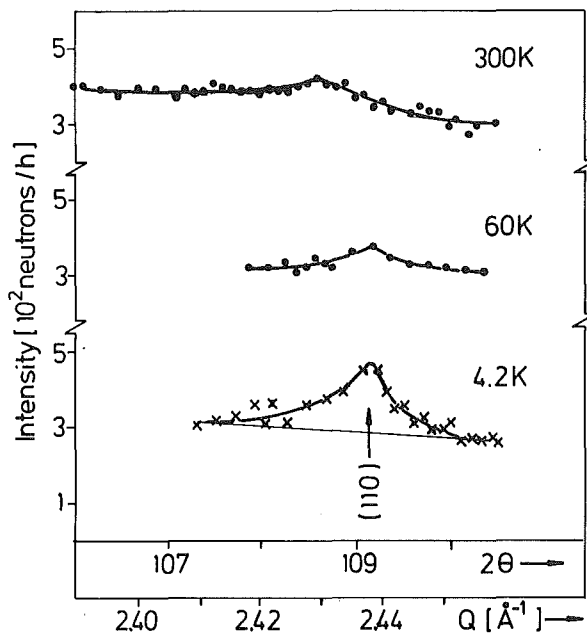


Fig. 1
Diffraction patterns taken at 7 K with $\lambda = 2.4 \text{ \AA}$ for disordered samples with 30 and 35 at% Mn. The ratio of the (111) and (200) peak intensities in the two patterns is different mainly due to texture in the samples.

Fig. 2
Intensity distribution around the (110) position for the 35 at% alloy at different temperatures as measured with $\lambda = 4.2 \text{ \AA}$ and an energy window of 0.15 meV.



To test the proposed antiferromagnetic origin of the (110) peak we took further diffraction patterns at different temperatures and also with improved momentum resolution on the MAG2 spectrometer (at the cold source) in the triple axis mode of operation. In the diffraction pattern for the 35 at% alloy at 4.2 K measured with an energy window of 0.15 meV and with a momentum resolution improved by a factor of 8 the (110) Bragg peak is still evident (Fig. 2). The width of the peak resembles that of the resolution function. The intensity distribution measured at 295 K around the (110) position is much broader indicating the existence of magnetic short range order in this temperature range.

Assuming the collinear antiferromagnetic structure of γ -Mn the average low temperature sublattice moment of the 35 at% alloy was calculated with refer-

ence to the (200) nuclear peak ($\mu=0.65\mu_B$) and also with reference to the diffuse nuclear background ($\mu=0.64\mu_B$). We conclude that the critical concentration for the transition from ferromagnetic to antiferromagnetic order in the disordered Ni-Mn alloys must appear between 27 and 35 at% Mn.

References

- /1/ S.K. Sidorov and A.V. Doroshenko, Fiz. Metal. Metalloved 18, 811 (1964)
- /2/ T.J. Hicks, A.R. Pepper, and J.H. Smith, J. Phys. C1, 1683 (1968)
- /3/ H. Uchisheba, J. Phys. Soc. Japan 31, 436 (1971)
- /4/ J. Göring, Phys. Status Solidi (b) 57, K11 (1973)
- /5/ J. Fink, G. Czjzek, and H. Schmidt, Progr. Rep. IAK I, KfK 2054, 46 (1974)

3.5 Magnetic Order in $Y_6(\text{Fe}_{0.4}\text{Mn}_{0.6})_{23}$

P.v. Blanckenhagen, C. Lin^a, and G. Hilscher^b

^a*Fellow of the Humboldt Foundation from the Physics Institute Peking*

^b*Institut für Experimentalphysik, TU Wien*

Bulk magnetization measurements have shown that the $Y_6(\text{Fe}_{1-x}\text{Mn}_x)_{23}$ system exhibits two critical concentrations where the spontaneous magnetization disappears /1/. The boundary compounds are ferrimagnets whereas in the concentration range $0.4 < x < 0.7$ no spontaneous magnetization has been detected above 4.3 K.

Two models for explaining the magnetic properties of $Y_6(\text{Fe}_{1-x}\text{Mn}_x)_{23}$ have been discussed. Firstly, localized moments with antiferromagnetic coupling were assumed leading to the decrease of the magnetization /2/. Secondly, the Stoner-Wohlfarth band model was proposed in which the disappearance of the spontaneous magnetization is assumed to be due to the decrease of the atomic moments /1/.

In order to get information about the local magnetic order we have performed neutron scattering experiments on $Y_6(\text{Fe}_{0.4}\text{Mn}_{0.6})_{23}$ at various temperatures between 2 and 295 K using the multidetector spectrometer MAG1 with neutrons

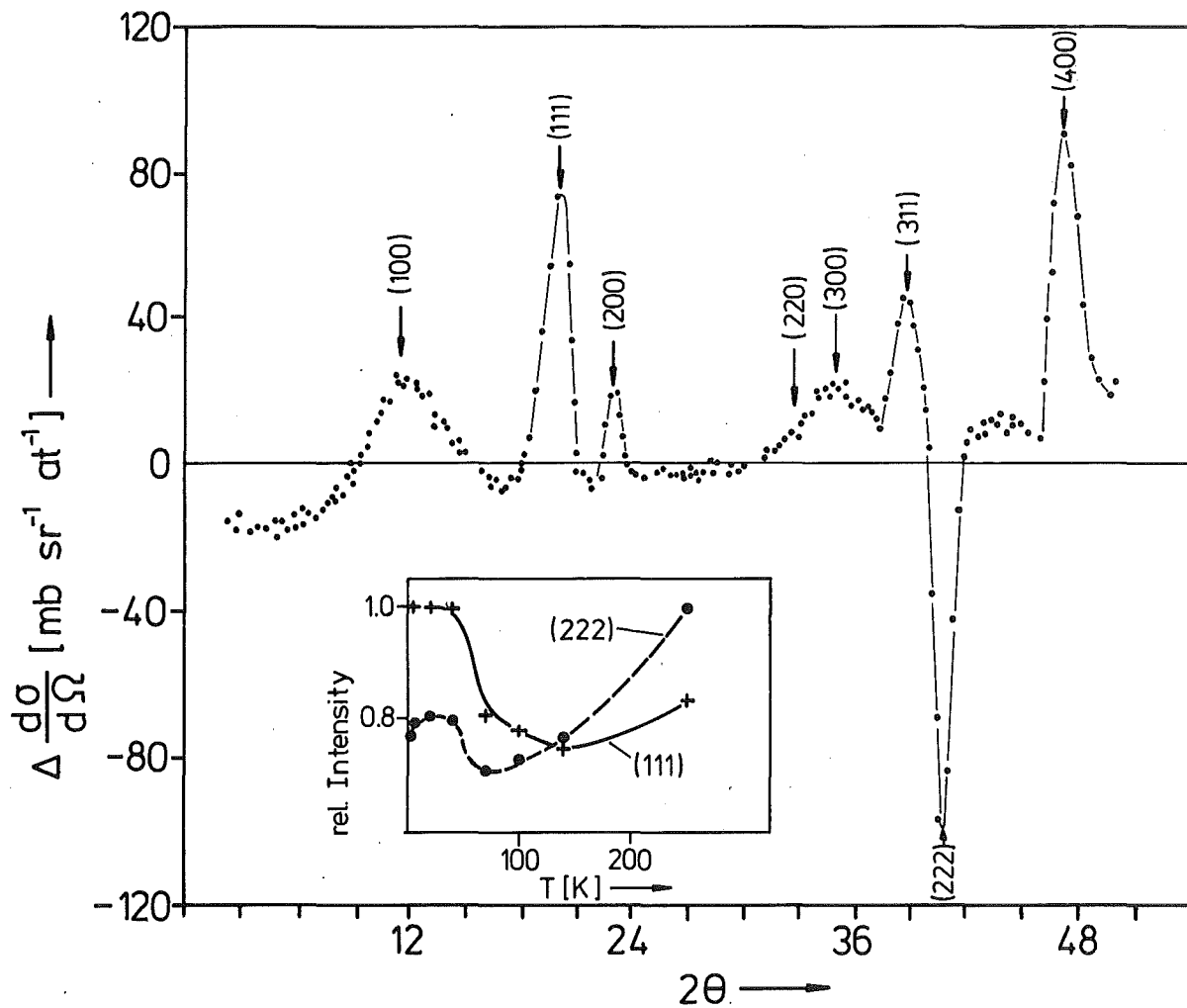


Fig. 1 Difference scattering cross-section calculated from the cross-section measured at 2 K and 250 K. The insert shows the temperature dependence of the (111) and (222) relative peak intensity

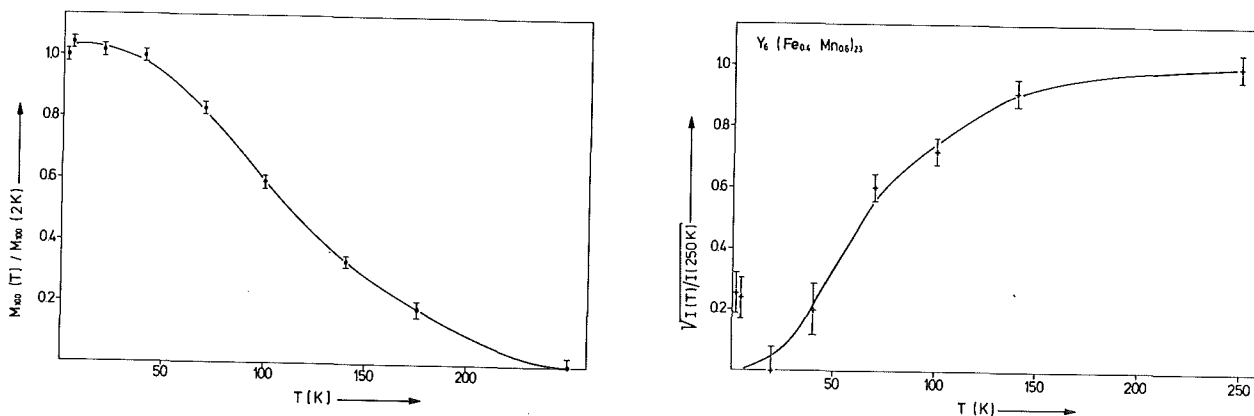


Fig. 2 Temperature dependence of the relative mean magnetic moment derived from cross-section (a) for the diffuse (110) peak and (b) for small scattering angles ($3-6^\circ$)

of 2.4 \AA wavelength. In some experiments a magnetic field up to 3.7 T was applied perpendicular to the scattering plane. Fig. 1 shows a part of the magnetic diffraction pattern obtained from the difference between the scattering cross-sections measured at 250 K and 20 K. Two diffuse maxima appear around the (100) and (300) positions which seem to be due to antiferromagnetic short range order. The relative magnetization corresponding to the diffuse scattering cross-section around the (100) position is shown in Fig. 2a as function of temperature. From the diffuse magnetic cross-section at 4.2 K we estimate an effective magnetic moment per atom of about $0.7\mu_B$. The mean magnetic moment derived from the temperature dependent scattering cross-section measured at small momentum transfers ($Q \approx 0.4 \text{ \AA}^{-1}$) increases with increasing temperature (Fig. 2b) and at 250 K it corresponds to a paramagnetic moment of $0.8\mu_B$ per atom. From the comparison of this value with the moment obtained from the diffuse magnetic scattering at low temperatures ($0.7\mu_B$) we conclude that the interactions causing the antiferromagnetic short range order at low temperatures are weak and are overcome by thermal excitations at temperatures near 250 K.

Besides the magnetic diffuse scattering at superstructure positions there are magnetic contributions to the Bragg peaks, which show a temperature dependence typical for ferrimagnetic order (Fig. 1). Whereas the diffuse peaks remain unchanged by the application of a magnetic field, the Bragg peak intensities are field dependent. From the temperature and field dependence of the intensities of the Bragg peaks we may conclude that there is a contribution due to magnetic scattering from ferrimagnetically correlated moments. The temperature and field dependence of the width of the Bragg peaks gives a lower limit for the correlation length of the ferrimagnetically ordered moments of about 200 \AA .

In conclusion, we suggest that short range antiferromagnetic and ferrimagnetic order with different correlation lengths determine the magnetic properties of $Y_6(\text{Fe}_{1-x}\text{Mn}_x)_{23}$ in the intermediate range of composition.

References

- /1/ G. Hilscher, N. Buis, and J.J.M. Franse; *Physica* 91B, 170 (1977)
- /2/ C.A. Beckmann, K.S.V. Narasimhan, W.E. Wallace, R.S. Craig, and R.A. Butera; *J. Phys. Chem. Solids* 37, 245 (1976)

3.6 The Puzzle of Magnetic Ordering in YbEu Alloys

V. Oestreich, G. Czjzek, H. Schmidt, F. Götz, K. Zlatka^a, K.H. Wienand^b,
and B. Elschner^b

^aGuest scientist from the Jagiellonian University, Cracow, Poland

^bInstitut für Experimentalphysik, TH Darmstadt

Alloys of the paramagnetic rare-earth metal Yb with Eu which for Eu concentrations C_{Eu} below 0.5 have the fcc crystal structure exhibit an unusual sequence of magnetic ordering phenomena. Magnetization measurements /1,2/ have indicated ferromagnetic ordering for low Eu concentrations ($C_{Eu} \leq 0.2$) with a Curie temperature which rises rapidly with C_{Eu} and passes through a maximum value of about 27 K for $C_{Eu} \approx 0.1$. For $C_{Eu} \geq 0.3$, however, no ferromagnetism was found. Instead, the magnetic susceptibility goes through a maximum at low temperatures. Legvold and Beaver /2/ have interpreted these maxima as an indication for the onset of antiferromagnetic order. The Néel temperatures thus defined are for $0.3 \leq C_{Eu} \leq 0.4$ substantially lower than the Curie temperatures found for $C_{Eu} \leq 0.2$ (Table 1).

In dilute alloys ($C_{Eu} \leq 0.2$), the electrical resistivity drops drastically with the onset of magnetic ordering, whereas for samples with $C_{Eu} = 0.3$ and 0.4 the electrical resistivity increases monotonically with decreasing temperature down to 1.5 K, the lowest temperature investigated (Fig. 1). As for bcc alloys with $C_{Eu} \geq 0.5$ antiferromagnetic ordering is again associated with a decrease of the electrical resistivity, these results suggest the absence of any magnetic order in the intermediate range of concentration, i.e. for $0.3 \leq C_{Eu} \leq 0.4$.

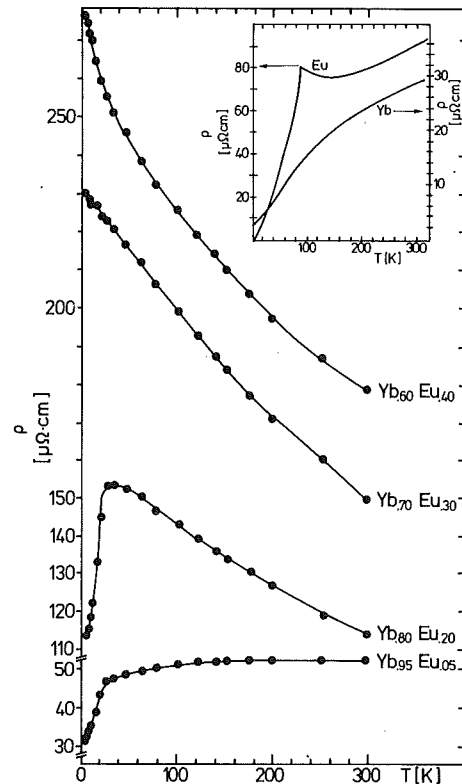


Fig. 1
Specific resistivity from 1.5 K to 300 K of the four YbEu alloys under investigation. The insert shows the specific resistivity of the pure metals /3/.

Table 1 Magnetic ordering temperatures of YbEu alloys as found by different experimental techniques

Sample	Magnetic ordering temperature [K]			Ref.
	from resistivity measurements	from Mössbauer measurements	from magnetization measurements	
Yb _{.95} Eu _{.05}	23±2	23±2	25	/1/
Yb _{.80} Eu _{.20}	22±1	21±2	21	/1/
Yb _{.70} Eu _{.30}	-	11.2±0.2	5	/2/
Yb _{.60} Eu _{.40}	-	14.4±0.1	8	/2/

In order to obtain additional information about the magnetic order occurring in these materials, we have investigated alloy samples with Eu concentrations $C_{\text{Eu}} = 0.05, 0.2, 0.3,$ and 0.4 by ^{151}Eu Mössbauer spectroscopy at temperatures ranging from 1.5 K to 70 K. Resistivity measurements on these samples confirmed the differences of the temperature dependence for the different Eu concentrations shown in Fig. 1.

At 1.5 K, the Mössbauer spectra showed in all samples a well defined hyperfine splitting corresponding to a narrow distribution (width ≤ 1 Tesla) of magnetic hyperfine fields. Significant differences were found in the evolution of the hyperfine spectra with temperature between "ferromagnetic" ($C = 0.05, 0.2$) and "antiferromagnetic" ($C = 0.3, 0.4$) samples.

For the low concentration alloys the spectra at temperatures ≥ 4.2 K could be described only by the assumption of at least two different Eu sites distinguished by different hyperfine fields. This finding indicates a pronounced magnetic inhomogeneity, presumably associated with variations of the magnetic coupling strength, depending upon the local environment. With increasing temperature, the hyperfine fields at all Eu sites decrease gradually, and in addition the weight associated with the low-field component increases. The temperature variation of the resulting average magnetic hyperfine field deviates strongly from that predicted by molecular field theory (Fig. 2a). In the case of Yb_{.95}Eu_{.05} it is very similar to the temperature dependence of the average magnetization found for Yb_{.94}Eu_{.06} /1/ (Fig. 2b). The experimental results are well described by a

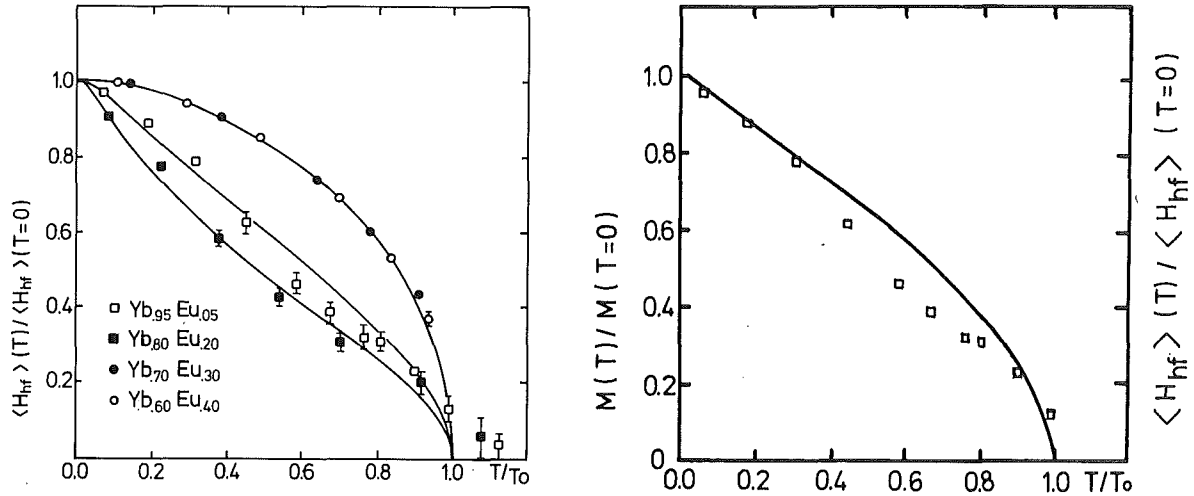


Fig. 2a Temperature dependence of the average magnetic hyperfine fields at ^{151}Eu nuclei. The experimental values for the samples $\text{Yb}_{.70}\text{Eu}_{.30}$ and $\text{Yb}_{.60}\text{Eu}_{.40}$ are compared with a Brillouin function with $S = 7/2$. For $\text{Yb}_{.95}\text{Eu}_{.05}$ and $\text{Yb}_{.80}\text{Eu}_{.20}$ a modified model as described in the text has been fitted to the experimental data.

- 2b The temperature variation of the magnetization of $\text{Yb}_{.94}\text{Eu}_{.06}$ (—) reported by Unterreiner and Elschner /1/ compared with that of the average hyperfine field in $\text{Yb}_{.95}\text{Eu}_{.05}$ (\square).

phenomenological, modified molecular field model involving a temperature dependent coupling constant $\lambda = \lambda_0 + \alpha \cdot (T - T_0)$, (see Fig. 2a) similar to the results found in alloys $\text{Gd}_x\text{Ce}_{1-x}\text{Ru}_2$ /4/. The ordering temperatures T_0 obtained from a least-squares fit of the modified molecular field model to the experimental data agree well with those determined by measurements of the magnetization and of the electrical resistivity (Table 1).

For the samples $\text{Yb}_{.7}\text{Eu}_{.3}$ and $\text{Yb}_{.6}\text{Eu}_{.4}$, on the other hand, the Mössbauer spectra are at all temperatures described by a single component with a narrow distribution of magnetic hyperfine fields centred at an average value whose temperature dependence follows a Brillouin function for $J = 7/2$ (Fig. 2b). The well defined ordering temperatures deduced from the temperature dependence of the hyperfine field are higher than the temperatures of maximum susceptibility (Table 1).

The results can be rationalized by the assumption of dominantly ferromagnetic interactions between Eu moments at distances larger than the nearest-neighbour distance and an antiferromagnetic coupling of nearest neighbours. The rapid rise of the Curie temperature at very low Eu concentrations indicates an exchange-enhanced susceptibility of the Yb host. This leads to predominantly ferromagnetic

correlations between Eu moments in dilute alloys with a finite correlation length evidenced by the anomalous temperature dependence of the spontaneous magnetization and of the average hyperfine field as well as by the magnetic inhomogeneity observed in the Mössbauer spectra. At higher Eu concentrations, the increasing number of Eu neighbour pairs leads to a progressive transition to an antiferromagnetic ordering. The differences observed in the electrical resistivity between alloys with ferromagnetic correlations ($C \leq 0.2$) and those with dominant antiferromagnetic ordering ($0.3 \leq C_{\text{Eu}} \leq 0.4$) may be due to the mechanism of coherent interference scattering proposed by Asomoza et al. /5/ to explain similar phenomena in amorphous magnetic alloys.

References

- /1/ K.H. Unterreiner, B. Elschner; Z. Angew. Physik 30, 239 (1970)
- /2/ S. Legvold, J.P. Beaver; Solid State Commun. 31, 717 (1979)
- /3/ M.A. Curry, S. Legvold, F.H. Spedding; Phys. Rev. 117, 953 (1960)
- /4/ K. Ruebenbauer, J. Fink, H. Schmidt, G. Czjzek, K. Tomala; Phys. Status Solidi (b) 84, 611 (1977)
- /5/ R. Asomoza et al., J. Phys. F7, L 329 (1977), and J. Phys. F9, 349 (1979)

3.7 Magnetization of Dwarf Moments in PrGd and PrEu Alloys

F. Götz, G. Czjzek, H. Schmidt, V. Oestreich, and P. Fulde^a

^aMPI für Festkörperforschung, Stuttgart

The results obtained by magnetization measurements and Mössbauer spectroscopy for PrGd and PrEu alloys have been explained tentatively by assuming dwarf moments for the magnetic impurities, i.e. a field-dependent compensation of the impurity moment by an antiparallel polarization cloud induced in the surrounding Pr matrix /1/. The formation of dwarf moments is suggested by the exchange Hamiltonian $H_{\text{ex}}^{\text{A,B}} = -2 J_{\text{ex}} (g_{\text{A}} - 1)(g_{\text{B}} - 1) \vec{J}_{\text{A}} \vec{J}_{\text{B}}$ which in case of the combination A = Pr, ($g_{\text{Pr}} = 4/5$), B = Gd or Eu, ($g_{\text{Gd}} = g_{\text{Eu}} = 2$) leads to antiparallel coupling for positive

J_{ex} . It was, however, not clear a priori whether all features observed in the field dependence of the difference $\Delta M = M_{\text{alloy}} - M_{\text{Pr}}$ between the alloy magnetization M_{alloy} and the magnetization M_{Pr} of pure Pr could be explained by dwarf moments. Therefore we have calculated the zero-temperature magnetization in a simple molecular field model. More elaborate calculations treating magnetic impurities in Pr /2,3/ could not be applied to our problem since only the case of parallel coupling (which leads to giant moments) had been considered by these authors.

The Hamiltonian relevant for the behaviour of the dwarf moments consists of three terms: $H = H_{\text{CF}} + H_{\text{Zeem}} + H_{\text{Ex}}$. The crystal field Hamiltonian H_{CF} for Pr is well known /4/. Gd and Eu are not affected by the crystal field because for both ions the ground state of the 4f shell is an S state. We have assumed Gd impurities not to modify the crystal field on nearby Pr ions. For Eu impurities this assumption may not be valid since the Eu ions differ both in their charge and their radius from the host ions. In the Zeemann term H_{Zeem} we assumed the applied magnetic field to lie in the hexagonal basis plane, corresponding to the actual situation in our magnetization measurements /1/. In H_{Ex} we accounted for exchange interactions between the Gd spins and Pr spins in the first and second coordination shell of the impurities and only first-neighbour Pr-Pr interactions. For these the effective exchange integral J_{PrPr} was adjusted by comparison with the experimentally determined magnetization curve of Pr at 1.5 K in fields up to 6 Tesla. This yielded the value $J_{\text{PrPr}} = 0.475$ meV. The exchange integrals J_{GdPr1} and J_{GdPr2} were varied such as to give best agreement with the experimental values of ΔM , measured at 1.5 K. Treating the exchange interaction by a molecular field approach we converted the Hamiltonian to a sum of single-ion terms. The ground state and the induced moment of the Pr ion in the first and second coordination shell of the impurity were then determined self-consistently. For Pr ions at larger distances the moment values of pure Pr were substituted. Only very dilute alloys were considered with no overlap between the regions which are influenced by the impurities.

First calculations were carried out with two additional simplifications:

- (a) only Pr ions on hexagonal sites in the dhcp lattice were taken into account, since the first excited crystal field level is much lower for these ions than that for ions in cubic sites, and
- (b) in calculating the induced moment of Pr ions only admixtures of the first excited doublet to the ground state were considered.

Even with this highly simplified model, the dependence of ΔM upon the applied field B was qualitatively well reproduced (Fig. 1). For B less than a critical value B_{cr} , the lowest total energy is obtained for a state in which the Gd moments are directed opposite to the applied field. At very low values of B ($\leq 0.1 - 0.5$ Tesla) and for values J_{PrGd} larger than 0.3 meV, however, the magnetization of the dwarf moment (Gd plus first- and second neighbour Pr ions) is positive since the total moment on the Pr neighbours overcompensates the Gd moment. The dwarf moment drops rapidly with increasing B , reaching a value close to $-7\mu_B$ below B_{cr} . For $B > B_{cr}$, the total energy is minimized when the Gd moment is oriented with B , and for $B = B_{cr}$ a sudden change of ΔM from negative to positive values is expected. As a comparison of Figs. 1a and 1b shows, the qualitative traits of the experimental results for ΔM at 1.5 K and of the calculated curve agree very well, but for any reasonable choice of the parameter values J_{GdPr1} and J_{PrGd2} the calculated value for B_{cr} is much higher than the experimental value. We assume that the discrepancy is mainly due to the additional simplification (b) mentioned above. Extended calculations without these simplifications are in progress.

References

- /1/ F. Götz, G. Czjzek, J. Fink, H. Schmidt, V. Oestreich, and P. Fulde; *J. Appl. Phys.* **50**, 7513 (1979).
- /2/ H. Mais, Dissertation, Univ. Saarbrücken (1975)
- /3/ E. Balanovski, *Phys. Rev.* **B21**, 5272 (1980)
- /4/ J.G. Houmann, B.D. Rainford, J. Jensen, and A.R. Mackintosh, *Phys. Rev.* **B20**, 1105 (1979)

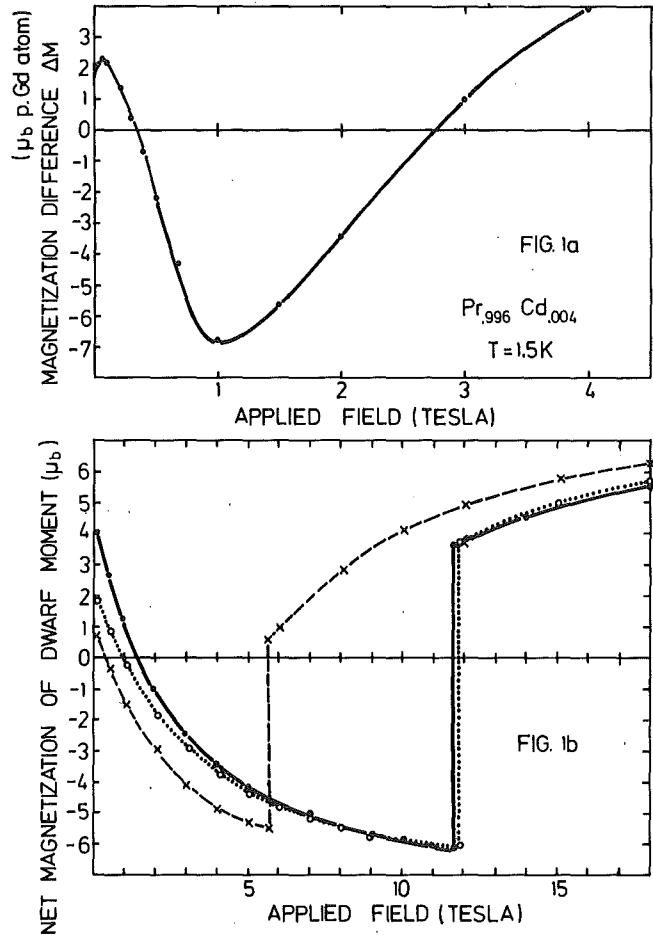


Fig. 1: Additional magnetization due to a Gd moment in a Pr matrix
 (a) experimental result, obtained by subtracting the magnetization of pure Pr from the alloy magnetization
 (b) calculations by a self-consistent mean-field approach
 — two coordination shells, $J_{PrGd1}=0.475, J_{PrGd2}=0$
 --- two coordination shells, $J_{PrGd1}=0.40, J_{PrGd2}=-0.1$
 ... one coordination shell, $J_{PrGd1}=0.475$

3.8 Magnetization of UPd_2Si_2 in a Field of 3.7 T

J. Leciejewicz^a and P.v. Blanckenhagen

^aInstitute of Nuclear Research, Swierk Poland

UPd_2Si_2 and UPd_2Ge_2 are antiferromagnetic with Néel temperatures of 140 K and 150 K, respectively /1/. Powder neutron diffraction patterns taken at different temperatures have shown that the magnetic ordering is given by spin density waves /2/. To prove if this type of order, which is unusual for uranium intermetallics, is stable in applied magnetic fields we have investigated the field dependence of the neutron diffraction pattern. Fields up to 3.7 T were applied normal to the scattering plane. The measurements have been performed with the MAG1 multidetector spectrometer at the FR2 reactor for temperatures of 4, 60, 80, 110, and 150 K.

For UPd_2Ge_2 the nuclear Bragg peak intensities appeared field dependent if the field was applied for the first time after cooling, indicating a strong magnetic anisotropy.

In UPd_2Si_2 the magnetic structure observed at zero field persists up to fields of 3.7 T. The average moment of the uranium ions in UPd_2Si_2 with an applied field of 3.7 T was determined from the intensity of a well resolved magnetic Bragg peak as function of temperature (Fig. 1). The magnitude of the average magnetic moment at 4.2 K is about 20 % larger than in zero field.

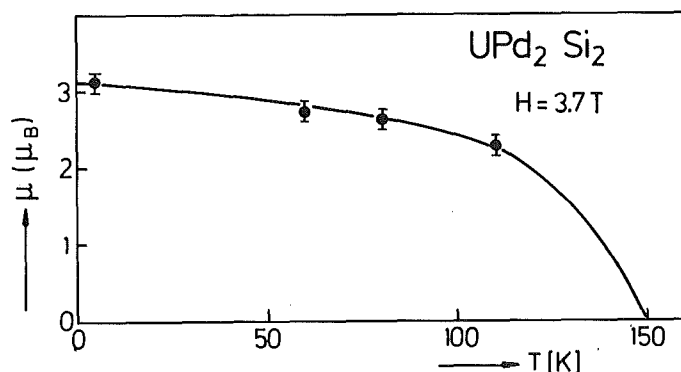


Fig. 1
Temperature dependence of the average magnetic moment of the U ions in an applied field of 3.7 T.

References

- /1/ A. Zygmunt, private communication
 /2/ J. Leciejewicz, H. Ptasiewicz-Bak, and A. Zygmunt, Phys. Stat. Sol. (a) 51, K71 (1979)

3.9 Atomic Coordination and the Distribution of Electric Field Gradients in Amorphous Solids

G. Czjzek, J. Fink, F. Götz, H. Schmidt, J.M.D. Coey^a, J.-P. Rebouillat^a, and A. Liénard^a

^aC.N.R.S., Grenoble, France

to be published in *Phys. Rev. B*

Abstract

The observation of nuclear quadrupole interactions in amorphous solids provides a unique possibility of obtaining information about the angular distribution of local ionic coordinations, complementary to the information about radial distributions deduced from X-ray and neutron diffraction and from EXAFS measurements. In the present paper the relation between ionic coordinations and the distribution of electric field gradients (EFG) is investigated. It is shown that the distribution function $P(V_{ZZ}, \eta)$ of the splitting parameters V_{ZZ} (the electric field gradient) and η (the asymmetry parameter) in general yields zero probability both for $V_{ZZ} = 0$ and for $\eta = 0$. For solids which are isotropic on the average, the distribution function of the components V_{ik} of the EFG tensor depends only on two variables, the invariant functions of the tensor components ($\text{Det}\{V_{ik}\}$ and $\sum V_{ik}^2$). Expressions for these quantities in terms of the radial coordinates of the ions causing the EFG and of the bond angles between pairs of ions are given. For amorphous solids with random ionic coordination an analytic approximation for the distribution function $P(V_{ZZ}, \eta)$ is derived. This function is strongly dominated by the distribution of ions in the first coordination shell. The results are applied to the analysis of Mössbauer spectra of ^{155}Gd in amorphous Gd-Ni alloys.

3.10 Interband Transitions and Core-Level Excitations in 1T-SnS₂ and 1T-SnSe₂ by High Energy Electron Loss Spectroscopy and X-Ray Photoelectron Spectroscopy

R. Manzke^a, J. Fink, G. Crecelius^a, J. Fuggle^a, R. Schöllhorn^b, and M. Campagna^a

^aInstitut für Festkörperforschung, KFA Jülich

^bAnorganisch-Chemisches Institut der Universität Münster

Over the past years there has been an increasing interest in layered materials and intercalates because of their quasi-two-dimensional physical properties and their technical potential. This contribution describes the investigation of the bandstructure and the character of core-level to conduction-band transitions in the semiconducting layer materials 1T-SnS₂ by wave-vector-dependent transmission electron energy-loss spectroscopy (ELS) and by X-ray photoelectron spectroscopy (XPS).

ELS measurements were performed with 50 keV electrons, with 0.5-1 eV energy resolution and with momentum transfer and resolution of $q = 0-1.2 \text{ \AA}^{-1}$ and 0.03 \AA^{-1} , respectively. The dielectric functions as well as the reflectivity and the absorption coefficient were obtained by a Kramers-Kronig analysis of the ELS spectra after subtracting contributions from double scattering. In Fig. 1 we show the density of oscillator strength $df/dE \approx E\epsilon(E)$ of SnS₂ for various momentum transfer values in the direction $\vec{q} \parallel \Gamma M$. For small momentum transfer $q = 0.11 \text{ \AA}^{-1}$ the position of peaks is in excellent agreement with those derived from reflectivity measurements /1/, /2/. Increasing the momentum transfer, we observe a dispersion of the main peaks centered between 5 and 7.5 eV and of the peak at 10 eV. At momentum transfer $\vec{q} \parallel \Gamma M \sim 1 \text{ \AA}^{-1}$ corresponding to the separation of the Γ and the M point in the Brillouin zone additional oscillator strength density is observed at low energies. This can be explained by nonvertical transitions from states at the top of the valence band at the Γ point to those at the bottom of the conduction band at the M point. For SnSe₂ we observe similar spectra which are shifted to lower energy by 1 eV due to the smaller bandgap.

In addition to interband transitions, we identify losses in the ELS spectra corresponding to transitions from the Sn (4d) and Se (3d) core-level to the conduction band (C.B.). In Fig. 2 we present spectra of these transitions taken on SnSe₂ with $q_{\parallel} = 0 \text{ \AA}^{-1}$, i.e. $q \parallel c$ after subtraction of the background. The energy scale is

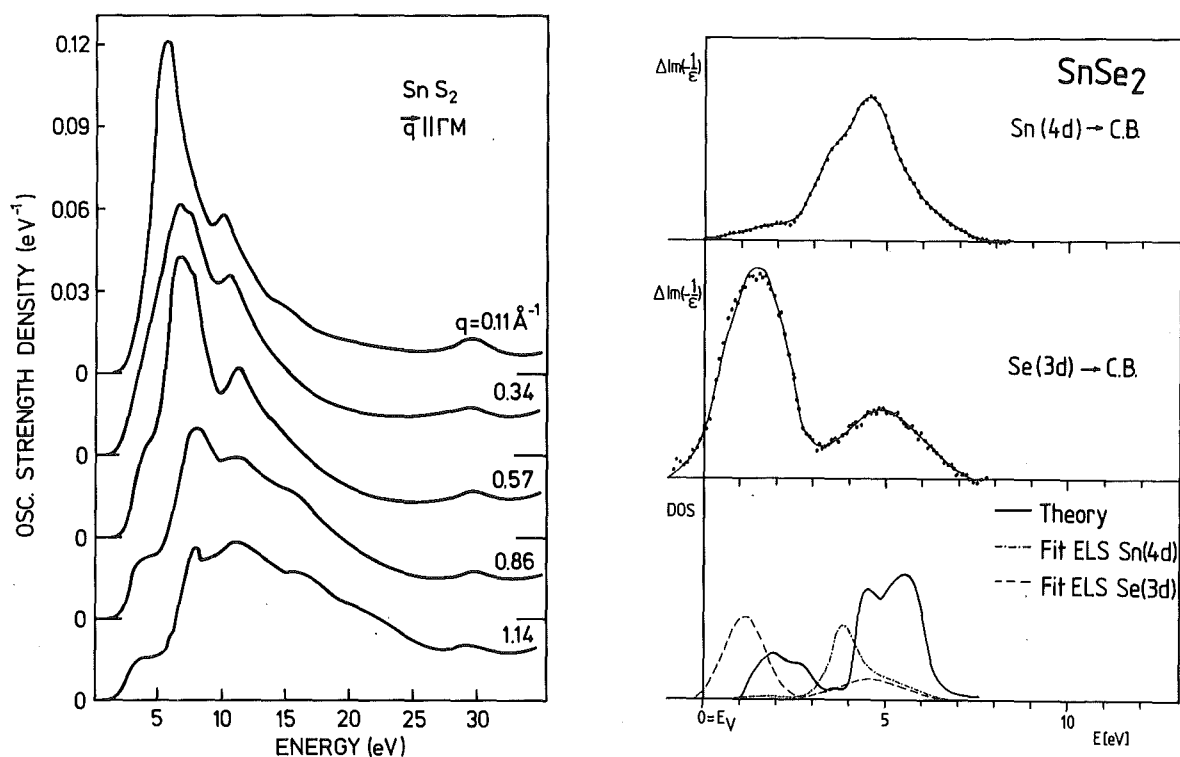


Fig. 1 Wavevector dependent density of oscillator strength for SnS_2

Fig. 2 Sn (4d)-conduction band transition; Se (3d)-conduction band transition; comparison of the derived final states of the core-level transitions with theoretical calculations of the density of states of the conduction band.

shifted by the binding energy, derived from XPS measurements on the same sample, such that the origin corresponds to the top of the valence band (E_V). The spectra have been fitted convoluting a spin orbit doublet, with $d_{3/2}$ and $d_{5/2}$ initial state intensities treated as a free parameter, with a sum of Gaussians describing the final states, taking into account the experimental resolution, a life-time broadening and a phonon broadening of 0.5 eV. The result of the least squares fit is shown as a full line in the spectra. The extracted density of final states is compared in the lower part of Fig. 2 with the theoretical density of states based on empirical pseudopotential bandstructure calculations /3/. As is clearly seen in Fig. 2, the final states are different for the transitions originating from the Sn (4d) and Se (3d) states. This may be due to the difference of the transition matrix elements. The strongly localized core wave functions may be expected to appreciably overlap with conduction band states derived from the particular component atoms under consideration. This overlap is thus supposed to be responsible for the large density of the Sn derived final p states between 4.5 and 5.5 eV in Fig. 2. The same argument holds for the transition between the Se (3d) state to

Se derived states at the bottom of the conduction band. In addition, Fig. 2 shows a downward shift of the observed final states by 1 eV compared with the calculated conduction DOS, which is expected because of the interaction with the core-hole. In SnS_2 this excitonic shift is observed to be of the order of 2 eV, which can be explained by the smaller static dielectric function compared to SnSe_2 . Increasing the momentum transfer q_{\perp} up to 1.1 \AA^{-1} (the total momentum is then perpendicular to the c-axis) both shape and position of our core-C.B. spectra do not change within statistical accuracy. This result indicates that both initial and final states are strongly localized. Thus both matrix element effects and the excitonic nature of the final states play an important role in describing the core-level excitations.

References

- /1/ J. Bordas, J. Robertson, and A. Jakobson, J. Phys. C11, 2607 (1978)
- /2/ Y. Bertrand, G. Leveque, C. Raisin, and F. Levy, J. Phys. C12, 2907 (1979)
- /3/ M. Schlüter and M.L. Cohen, Phys. Rev. B14, 424 (1976)

3.11 The XPS Valence Band Spectra of NbC

H. Höchst^a, P. Steiner^b, S. Hüfner^b, and C. Politis

^aMax-Planck-Institut für Festkörperforschung, Stuttgart

^bFachbereich Physik, Universität des Saarlandes, Saarbrücken

Z. Physik B37, 27 (1980)

Abstract

The x-ray photoemission valence band spectra of NbC have been measured and are compared with the x-ray emission spectra and with the results from band structure calculations. This comparison leads to a large enhancement of the C2p photoabsorption cross section (at $h\omega = 1,487 \text{ eV}$) compared to the value calculated for the free atom.

The effect of the nonmetal vacancy in the valence band can be described very well with vacancy cluster calculations.

4. MATERIALS RESEARCH

4.1 The Influence of Oxygen on the Superconducting Transition Temperature of Quench Condensed Al Films

M. Nittmann^a, P. Ziemann^a, and G. Linker

^aPhys. Institut, Universität Karlsruhe

Al films evaporated from Al_2O_3 crucibles onto substrates held at 4.2 K show strongly enhanced superconducting transition temperatures T_c up to 5.8 K/1/. Similarly, layers evaporated from W boats exhibit enhanced, however lower T_c values of 2.5 K. In previous investigations /2/ it has been shown that in Al films evaporated at RT, oxygen impurities stabilize disorder which is responsible for the enhanced T_c values. A similar stabilization mechanism by impurities may be present in quench condensed films with enhanced T_c values.

In order to test this assumption, Al films have been evaporated from Al_2O_3 crucibles and W boats onto substrates held at temperatures <4.2 K. The oxygen concentration c_o and the depth distribution of oxygen in the layers has been determined by Rutherford backscattering of 2 MeV α particles.

The relationship between oxygen content and T_c in the quench condensed films is shown in Fig. 1 where T_c is plotted vs. c_o . The results from films prepared at RT (closed circles and squares) are included for comparison. For the quench condensed films evaporated from Al_2O_3 crucibles (closed triangles) three important details have been observed:

- (1) all films have very high oxygen contents $c_o > 20$ at%
- (2) T_c decreases steeply with increasing c_o , yielding an extrapolated value of $T_c = 0$ K at $c_o = 33$ at% corresponding to a nominal stoichiometry of Al_2O
- (3) no films could be produced outside the oxygen concentration range of $30 \text{ at}\% \geq c_o \geq 20 \text{ at}\%$ for crucible temperatures between 1400 K and 1800 K

These three facts can be understood if the chemical behaviour of the Al + Al_2O_3 system is considered. In Fig. 2 the partial pressures of this system are plotted vs. temperature /3/. The main component in the vapour is Al_2O ; the oxygen concentration in the vapour was estimated to be 31 at% and 21 at% at temperatures of

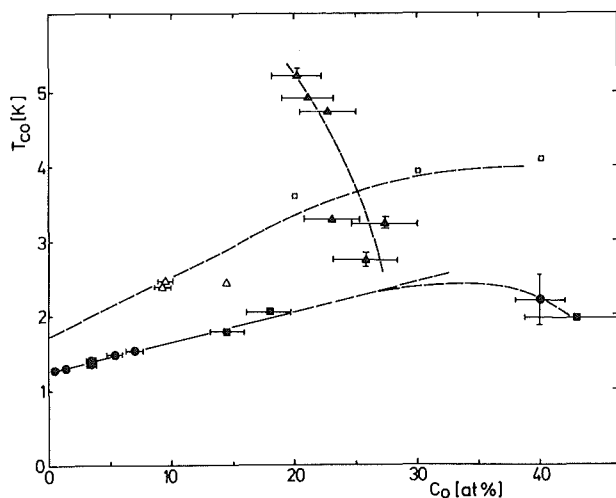


Fig. 1
Superconducting transition temperatures in Al films prepared under different conditions as a function of oxygen concentration (the lines are guides to the eye)

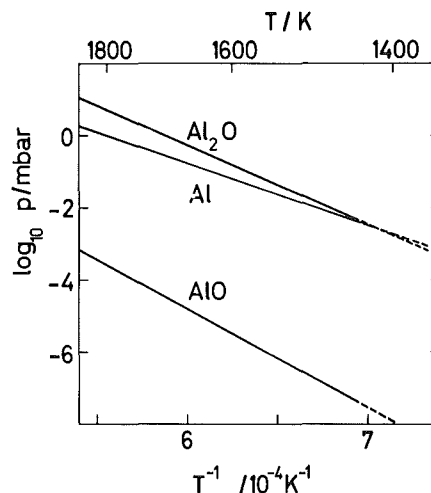


Fig. 2
Partial pressure of the different components present in the vapour of an Al_2O_3 crucible containing molten Al vs. temperature

1800 K and 1400 K, respectively, corresponding to the concentration values experimentally observed in the films.

Thus it is assumed that in the quench condensed films evaporated from Al_2O_3 crucibles the oxygen contamination is due to the reaction $4\text{Al} + \text{Al}_2\text{O}_3 \rightleftharpoons 3\text{Al}_2\text{O}$ in the crucible, and the oxygen is incorporated into the films in form of Al_2O molecules which are unstable at RT.

Quench condensed films evaporated from W boats (open triangles and open squares (data from Buck and Prüfer /4/ in Fig. 1), revealed a totally different behavior compared to that observed for films evaporated from Al_2O_3 crucibles. We assume that here the oxygen is incorporated into the layers in form of O_2 molecules. An extrapolation to $c_{\text{O}}=0$ yields a $T_{\text{C}}=1.8$ K for pure quench condensed Al films.

From this different behaviour it is concluded that a higher degree of disorder is stabilized in quench condensed Al films by Al_2O than by O_2 molecules. This high degree of disorder is thought to be the reason for the observed high T_{C} values.

References

- /1/ G. v. Minnigerode, J. Rothenberg, Z. Phys., 213, 397 (1968)
- /2/ P. Ziemann, O. Meyer, G. Heim, W. Buckel, Z. Phys. B 35, 141 (1979)
- /3/ L. Brewer, A.W. Searcy, J. Am. Chem. Soc., 73, 5308 (1951)
- /4/ V. Buck, G. Prüfer, Verhandl. DPG 15, 395 (1980)

4.2 Redistribution of Cu in Al Single Crystals after Pulsed Electron Beam Annealing

T. Hussain^a, G. Linker, F. Ratzel, and J. Geerk

^aOn leave from Physics Department, University of Dacca, Bangladesh

Recently much attention has been given to study the effect of pulsed electron beam annealing (PEBA) on ion-implanted samples, particularly on implanted semiconductors. The widespread studies in this area were performed mainly on implanted Si. In the most cases a redistribution of impurities has been observed which was explained by rapid diffusion in the liquid phase. This liquid phase can be obtained by choosing appropriate pulse energies which may melt the surface layer deeper than the implanted ion range.

In comparison to implanted semiconductors little work has been performed on implanted metals using pulsed beam techniques. Recently, the redistribution of Cu in polycrystalline and single crystalline Al has been reported using laser beams /1/. A redistribution of Cu in polycrystalline Al was observed while no change of the Cu-profile has been found in the case of a single crystal even after

a laser pulse of 4.1 J/cm^2 . The lack of impurity redistribution is apparently due to the higher reflectivity of the single crystal which diminishes the amount of absorbed energy thus preventing the formation of the liquid phase.

Here, we report the results of the depth distribution and lattice location measurements for high dose Cu implanted ($2.3 \times 10^{16} \text{ Cu}^+/\text{cm}^2$, 140 keV) Al single crystals of $\langle 110 \rangle$ orientation subjected to PEBA. The implantation was performed along a random direction and at room temperature. An average electron

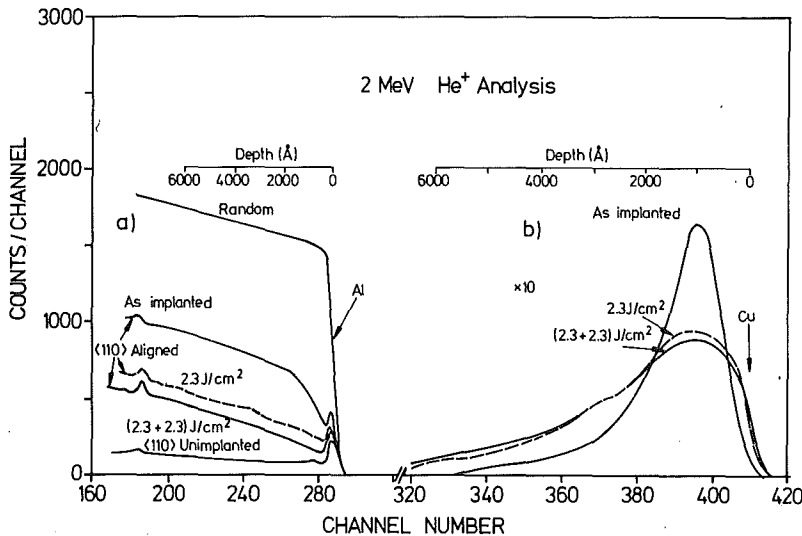


Fig. 1
 $\langle 110 \rangle$ aligned and random backscattering spectra before and after PEBA from a Cu implanted Al single crystal.

energy of 22 keV and pulse duration of 300 nsec were used for annealing at a deposited energy of 2.3 J/cm^2 . The analysis of the Cu distribution and lattice site determination was performed before and after PEBA by 2 MeV He^+ ion channeling-backscattering measurements.

The random and $\langle 110 \rangle$ aligned backscattering spectra before and after PEBA are shown in the left part of Fig. 1. The right part of Fig. 1 shows the respective random distributions of Cu. A significant change in the dechanneling yield and in the distribution of Cu have been observed after a pulse with $\sim 2.3 \text{ J/cm}^2$. After a second pulse with similar e-beam energy a further reduction of the dechanneling yield has been observed. However, only small changes in the Cu profile have been detected. The reduction in the peak concentration and the broadening of the Cu profile suggest that significant diffusion of Cu has occurred. Neither surface segregation nor loss of Cu have been observed in any case.

An improvement of substitutional lattice site occupation of Cu in Al was also observed. This improvement was accompanied by the redistribution of the Cu while the peak concentration has been reduced from 2.3 at% to 1.3 at%. Fig. 2 shows angular scans before (a) and after PEBA (b). For the as implanted sample a substitutional fraction of about 40% was observed. After PEBA with 2.3 J/cm^2 , the substitutional fraction has increased to about 82%.

At the energy of 22 keV, the electrons could penetrate into the material up to a depth of about $3.7 \mu\text{m}$. The estimated surface temperature was $\sim 1400^\circ\text{C}$ which is well above the melting point of Al.

From the above results, we conclude that the Cu atoms redistribute in the melt without loss. The crystal regrowth takes place by liquid phase epitaxy.

Reference

- /1/ G. Della Mea and P. Mazzoldi, in *Laser Solid Interactions and Laser processing*; S.D. Ferris, H.J. Leamy and J.M. Poate (Eds.), AIP, New York, p 212 (1978)

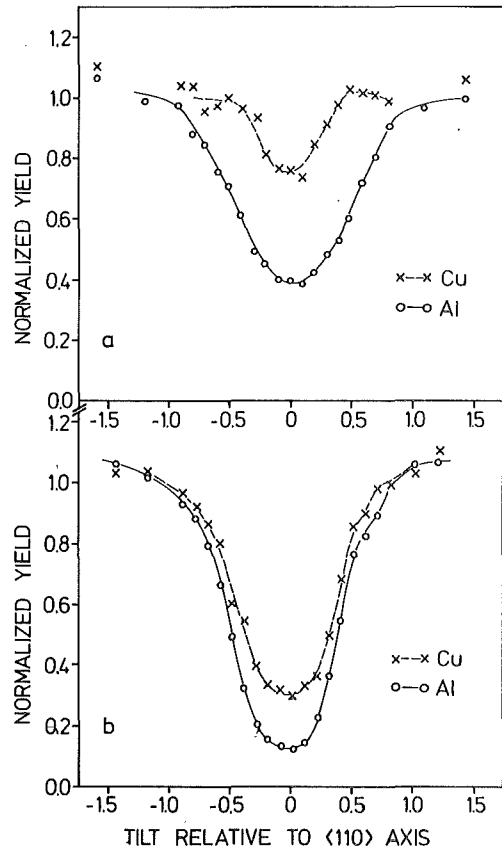


Fig. 2
Angular scans across $\langle 110 \rangle$ for as-implanted (a) and after PEBA (b)

4.3 Dependence of Defect Structures on Implanted Impurity Species in Al Single Crystals

T. Hussain^a and G. Linker

^aOn leave from Physics Department, University of Dacca, Bangladesh

Nucl. Instrum. Methods 168, 317 (1980)

Abstract

Aluminium single crystals have been implanted with Ca and Ga ions. Energy dependent channeling and backscattering experiments for disorder analysis together with lattice site determination have been performed with $^4\text{He}^+$ ions in the energy range of 1.0 - 3.0 MeV. A high substitutional fraction of 87 % and disorder consisting mainly of extended defects (dislocations) has been detected for Ga implanted crystals. For Ca implanted samples local distortions of the Al host lattice and an interstitial distribution of the impurities have been observed. The different kinds of damage correlate with previously observed different changes of the superconducting transition temperature in ion implanted Al layers.

4.4 Low Temperature Self-Ion Irradiation of Pure and Granular Aluminium-Films

P. Ziemann^a, O. Meyer, G. Heim^a, and W. Buckel^a

^aPhysikalisches Institut der Universität Karlsruhe

Z. Physik B35, 141 (1979)

Abstract

Al-films, evaporated at room temperature under different oxygen partial pressures, were irradiated with self-ions (500 keV, Al^{++}) at low temperature (<7 K). The observed increase of the resistivity and of the superconducting tran-

sition temperature T_c depends strongly on the oxygen content c_o present in the layers. A qualitative different behaviour of the above quantities was found for different fluence ranges of the bombarding ions. For high fluences in all cases an oxygen stabilized disorder state was obtained with corresponding T_c -increases between $\Delta T_c = 0.2$ K for the purest films ($c_o \leq 0.5$ at%) and $\Delta T_c = 1.2$ K for films with $\langle c_o \rangle = 40$ at%. The annealing behaviour of the irradiated films is also dependent on the oxygen content c_o .

4.5 Search for the Solubility Limit of Arsenic in Silicon

A. Tuross^a, J. Geerk, M. Kraatz, and F. Ratzel

^aOn leave from Institute of Nuclear Research, Warsaw, Poland

Extensive research has been performed over the past few years on the use of pulsed laser and electron beams for removing radiation damage and introducing the dopants into electrically active lattice sites /1,2/. The mechanism of pulsed beam annealing is due to the surface melting and subsequent rapid crystal regrowth. The time scale of heating and cooling is so fast that the impurity solubility in molten layer can persist in the solid. Thus, it is possible to incorporate impurity concentrations well in excess of the equilibrium solid solubility limits.

The aim of this work was the search for the limit of solubility of As in Si by combining the ion implantation and the pulsed electron beam annealing (PEBA) techniques. The silicon wafers of $\langle 111 \rangle$ orientation were implanted with 100 - 300 keV As ions up to the fluence of $2.6 \cdot 10^{17}/\text{cm}^2$. Fig. 1a shows the backscattering spectra for an unannealed sample implanted with $1.2 \cdot 10^{17} \text{As}/\text{cm}^2$ at 100 keV. In spite of the very high dose of As the silicon yield of the aligned spectrum does not reach the random level. This is due to the stopping power changes associated with the very high concentration of impurity atoms (~ 20 at%) and is also visible in the random spectra. The effects of a single electron pulse ($1.2 \text{ J}/\text{cm}^2$) are shown in Fig. 1b. The aligned yields for Si and As are strongly reduced. This can be interpreted as a conversion of the amorphous layer via liquid phase epitaxy to a single crystal accompanied by the massive incorporation of dopants into substitutional positions. The substitutional fraction of As ($\sim 7 \cdot 10^{21} \text{ at}/\text{cm}^3$) exceeds by the

the factor of more than 20 the equilibrium solid solubility limit.

In order to increase the As concentration several samples were implanted with $2.6 \cdot 10^{17}$ at/cm² at 300 keV. In spite of the very high initial As concentration (~ 25 at%) the As substitutional fraction did not exceed the value of $6 \cdot 10^{21}$ at/cm². Even after PEBA with energy of 2.3 J/cm² the Si and As minimum yields were higher than 10 % and 45 %, respectively. Also

the angular scans across $\langle 111 \rangle$ direction were performed. This is shown in Fig. 2. The As dip is much narrower than that for Si which indicate that the implanted atoms are slightly displaced (~ 0.2 Å) from the silicon lattice sites. One notes that the halfwidth of the silicon dip (0.78°) is significantly smaller than the value obtained for the perfect crystal (0.92°). This is apparently due to the host lattice distortion produced by the strains related to the massive incorporation of As atoms in the nearly substitutional sites.

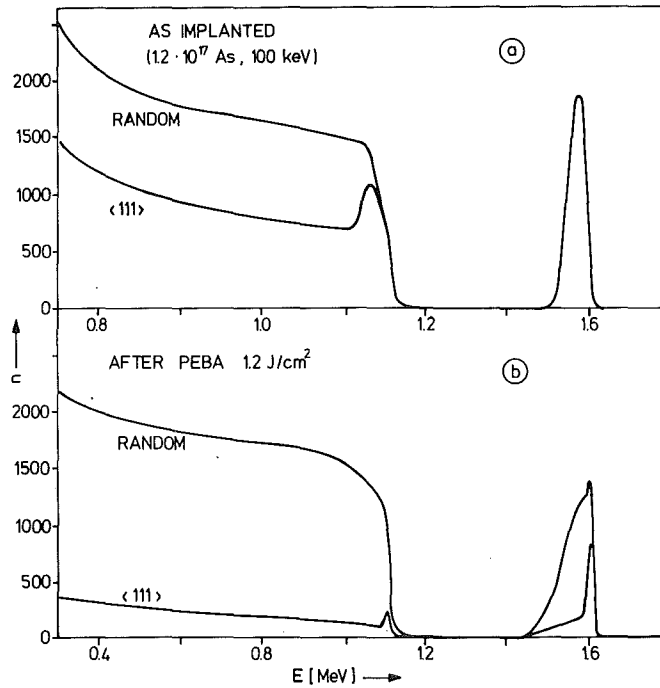


Fig. 1
Random and aligned backscattering spectra of 2 MeV ⁴He ions for arsenic implanted silicon before (a) and after PEBA (b)

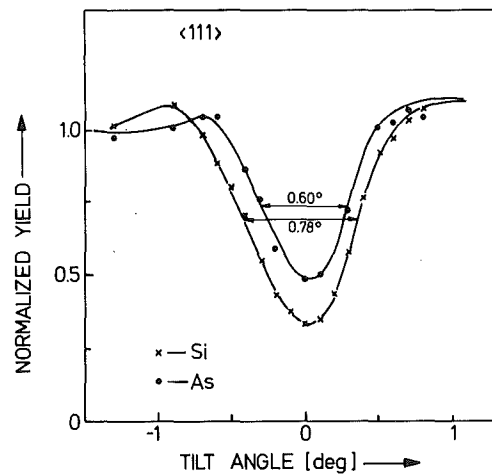


Fig. 2
Angular scans for arsenic implanted silicon ($2.6 \cdot 10^{17}$ /cm², 300 KeV) after PEBA with 1.8 J/cm²

References

- /1/ E. Rimini (ed.): Proc. Laser Effects in Ion Implanted Semiconductors, Catania, (1978)
- /2/ E.F. Kennedy, S.S. Lau, I. Golecki, J.W. Mayer, J.A. Minucci, A. Kirkpatrick, Radiat. Eff. Lett., 43, 31 (1979)

4.6 Channeling Study of Pt Implanted Al_2O_3 and MgO Single CrystalsA. Tuross^a, Hj. Matzke^b, and O. Meyer^aOn leave from Institute of Nuclear Research, Warsaw, Poland^bEuropean Institute for Transuranium Elements, Karlsruhe

There has been considerable interest in recent years in the catalytic activity of platinum implanted monocrystalline insulating oxides /1/. This interest has led us to investigate the damage produced by ion bombardment, its annealing behavior, possible impurity migration and impurity lattice location in Pt-MgO and Pt- Al_2O_3 systems.

MgO and Al_2O_3 single crystals, of $\langle 100 \rangle$ and $\langle 11\bar{2}0 \rangle$ orientations, respectively, were implanted with 30 keV Pt-ions up to a fluence of $1.10^{16}/\text{cm}^2$. During bombardment, the crystals were tilted 20° away from the main axis to avoid channeling of the Pt-ion beam.

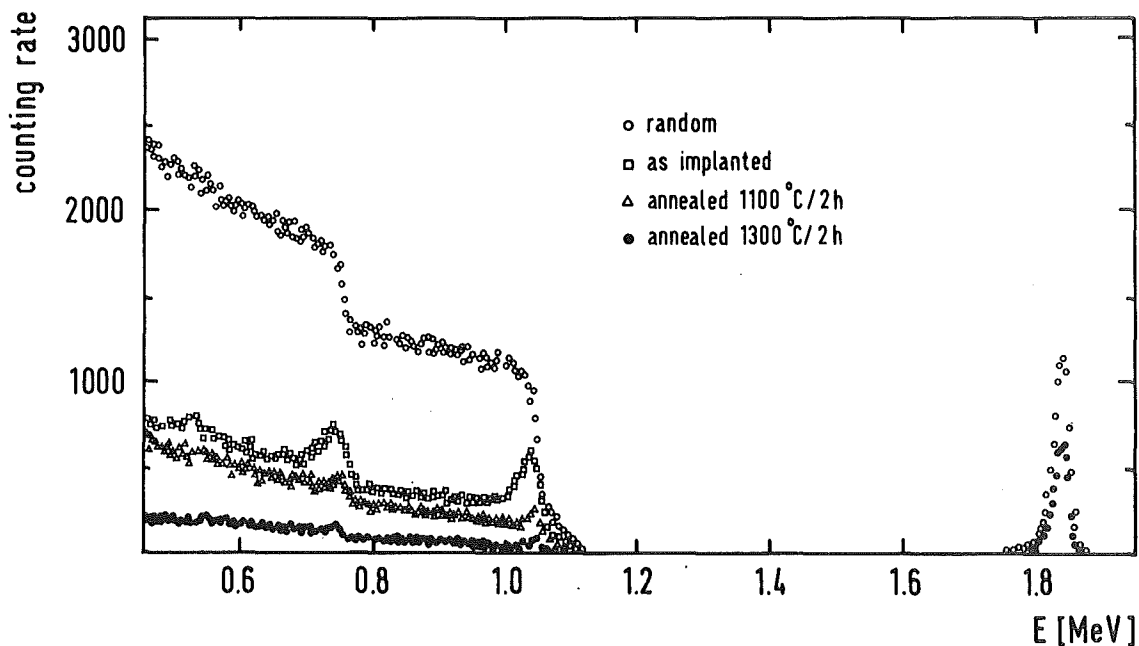


Fig. 1

Rutherford backscattering spectra for 2 MeV $^4\text{He}^+$ ions from Pt-implanted MgO single crystals in random or aligned directions following different annealing treatments.

The influence of the thermal annealing on the channeling spectra of 2 MeV He^+ -ions for MgO crystals is shown in Fig. 1. For the as-implanted sample a pronounced disorder peak is observed close to the surface and extends about 300 Å into the substrate. However, it did not reach the random level. The data for the minimum yield show clearly that the residual disorder decreases with increasing annealing temperature. Complete recrystallization was obtained after 2 hours annealing at 1300°C. With respect to the Pt lattice location, no substitutional lattice position for as implanted samples could be observed. A substitutional fraction of 30 % Pt was first observed after annealing at 900°C/2h. With increasing annealing temperature, the substitutional fraction reached 50 % at 1300°C. It is worth noting that the depth distribution of the impurity does not vary with the annealing temperature, thus leading to the conclusion that there is no significant thermal diffusion of Pt into MgO single crystals. However, after annealing at 1500°C, almost complete outdiffusion of Pt was observed.

The detailed study of the lattice position of Pt performed by means of the angular scans reveals some extraordinary features (Fig. 2): the half-angle of the Pt dip is much broader than that of the host and is close to the value characteristic for Pt single crystals. This is apparently due to the coherent precipitation of Pt atoms in the MgO matrix.

Pt implanted Al_2O_3 single crystals behave in a different manner. No regular lattice position of Pt in the hcp structure of Al_2O_3 was found, neither for as-implanted nor for thermally annealed samples. A substantial outdiffusion of Pt took place during annealing at 1500°C. Complete damage removal of the host crystal was observed after annealing at 1300°C.

References

/1/ P. Rabette, A.M. Deane, A.J. Tench, M. Che, Chem. Phys. Lett. 60, 348 (1979)

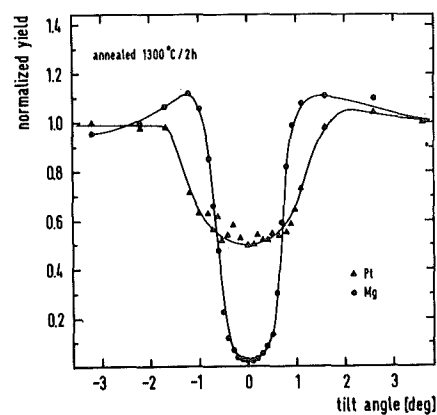


Fig. 2
Angular scan through the $\langle 100 \rangle$ direction of Pt-implanted MgO. The impurity shows a much broader critical angle than the host.

4.7 Lattice Location of Pb and Au in Fe Single Crystals

H. Alberts^a, A. Tuross^b, and O. Meyer

^aOn leave from Physics Department, University of Pretoria, South Africa

^bOn leave from Institute of Nuclear Research, Warsaw, Poland

The influence of ion implantation on the aqueous corrosion of pure iron is currently being studied /1/. It has been found that Pb depresses the corrosion rate whereas Au enhances it. The aim of our work was to study the correlation between the lattice position of implanted species and the corrosion behaviour of Fe.

Iron single crystals of $\langle 111 \rangle$ orientation were implanted with Pb⁺⁺ and Au⁺⁺ at an energy of 400 keV to fluences of $1 \cdot 10^{15}$ ions/cm² and $1 \cdot 10^{16}$ ions/cm², respectively.

The channeling and backscattering experiments were performed with 2 MeV ⁴He ions. In order to determine the impurity lattice sites angular scans along both $\langle 100 \rangle$ and $\langle 111 \rangle$ directions were made. Fig. 1 shows typical angular scans along the $\langle 100 \rangle$ axis for an Au implanted sample. The substitutional fraction of almost 100% has been found for an as implanted case (Fig. 1a). The number of Au atoms occupying substitutional lattice positions remains constant during thermal annealing up to 500°C in an isochronal annealing cycle (100°C steps, 30 min.)

Further increase of the annealing temperature reduces the substitutional fraction to 20 % at 900°C (Fig. 1b). In the same annealing cycle a progressive damage removal of the host crystal was observed. The minimum yield decreased from 36 % for an as implanted sample to 8 % after annealing at 900°C.

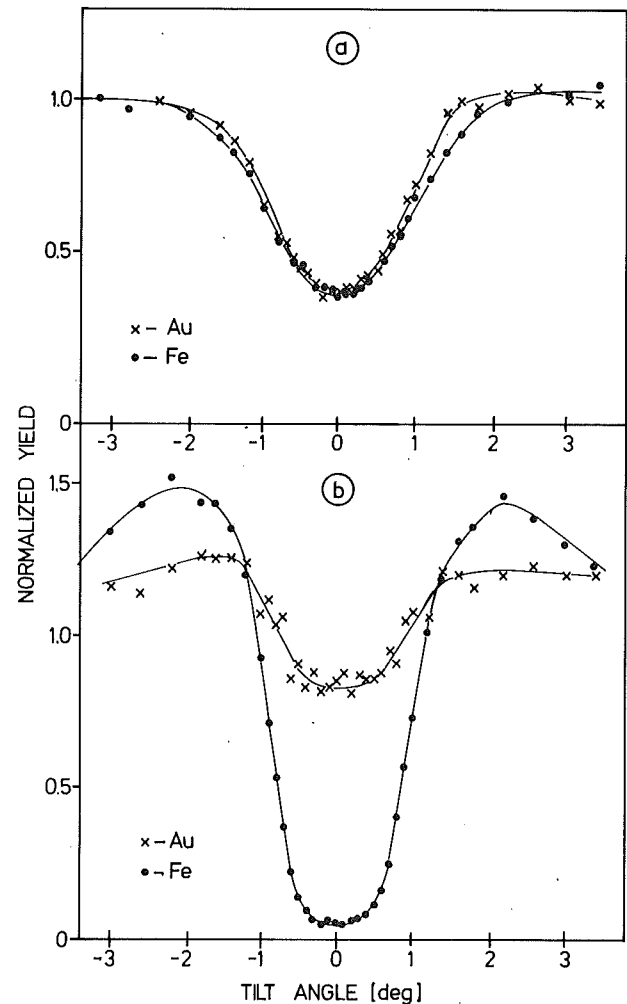


Fig. 1
Angular scans along $\langle 100 \rangle$ axis for Au implanted Fe crystal:
a) as implanted
b) after annealing 900°C/30 min.

The substitutional fraction of Pt amounts to 85 % for an as implanted sample and remains constant for all annealing temperatures up to 700°C. The annealing characteristic of Pb implanted Fe crystals is similar with respect to the damage removal of the host. However, the impurity behaviour is different. Since in both cases no impurity diffusion was observed it can be concluded that the rejection of Au atoms from substitutional positions may be due to their mobility. This may lead to a short range migration followed by the precipitation in the form of small clusters. The thermal stability of Pb atoms positions is apparently due to the low diffusion coefficient of Pb in Fe.

Reference

- /1/ H. Ferber, H. Kasten, G.K. Wolf, W. Lorenz, H. Schweickert; Corrosion Science (in press)

4.8 Investigation of Structural Distortions in Ion Implanted Molybdenum Layers

G. Linker and M. Kraatz

It has been reported previously that the implantation of chemically active ions like e.g. N, P, S into evaporated Mo-layers leads to an enhancement of the superconducting transition temperature T_c up to 9.2 K depending on implantation temperature /1,2/. The maximum T_c value was independent on the implanted ion species, thus the T_c increase was thought to be due mainly to distortions of the host lattice stabilized by the implanted impurity atoms.

In this contribution results are reported from a study of structural distortions in implanted Mo layers as a function of impurity concentration. Mo layers with thicknesses in the range of 100 - 150 nm have been homogeneously implanted with N and P ions at RT and at liquid nitrogen (LN) temperature. X-ray intensity measurements have been performed with a Guinier thin film diffractometer before and after implantation. The intensity data have been analysed with the help of a modified Wilson plot where the intensities of the lines from the implanted samples are referred to those before implantation. A similar procedure has been applied previously for the analysis of implanted niobium layers /3/.

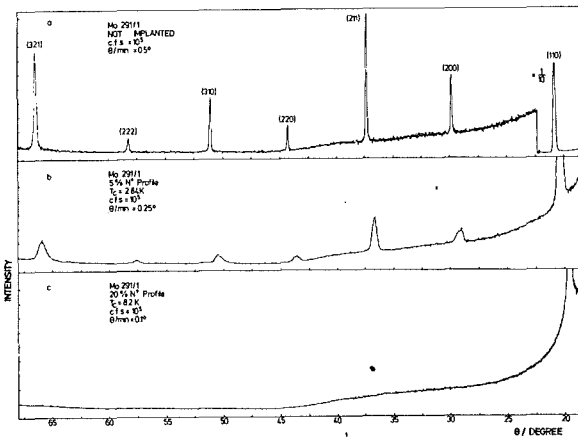


Fig. 1
X-ray diffraction spectra from nitrogen implanted Mo layers (5 and 20 at%) compared to the spectrum of the unimplanted layer

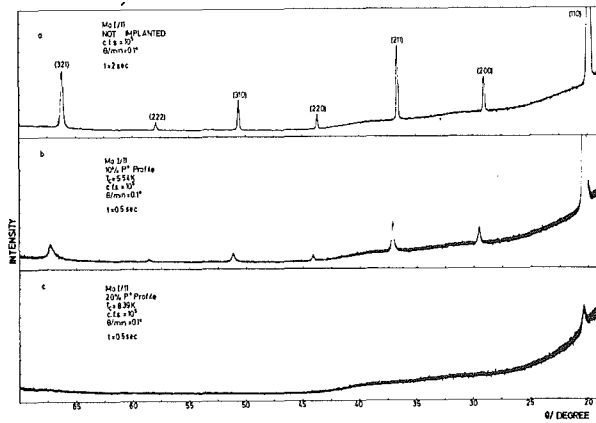


Fig. 2
X-ray spectra of a phosphorus implanted Mo layer (10 and 20 at%). A spectrum from an unimplanted layer is included for comparison

X-ray spectra of the layers before and after implantation of N and P at LNT are shown in Fig. 1 and 2. The common feature for both ions is a considerable intensity decrease for moderate impurity concentrations and a disappearance of all line structure, indicating amorphization of the layers, for concentrations causing the maximum T_C increase. Determination of the lattice parameter a_0 has shown differences for N and P. In the initial slope of disordering a_0 increases continuously with growing N concentration while for P a decrease of the lattice parameter has been observed. Also the intensity data analyses indicate different defect structures for N and P with increasing impurity concentration. Wilson plots for these two ions are shown in Fig. 3 and 4.

For nitrogen the characterization of the plots are increasing slopes of the straight lines fitted through the data points with relatively small axial section values on the $\ln(I/I_0)$ -axis. From this behaviour a defect structure consisting of small atomic displacements from the ideal lattice sites is suggested. Average displacement values μ estimated from the slopes are indicated in Fig. 3.

The plots for phosphorus, in contrast to the results from nitrogen, reveal high intersection values of the straight lines on the $\ln(I/I_0)$ -axis. This lack of intensity partially is due to loss of material by sputtering in the implantation process. The main effect however may be explained by amorphization of parts of the material.

In conclusion the results show that in implanted Mo-layers the maximum T_C phase, is amorphous independent on ions species (N or P). The amorphization of the material as a function of impurity concentration, however, depends on ion species. For

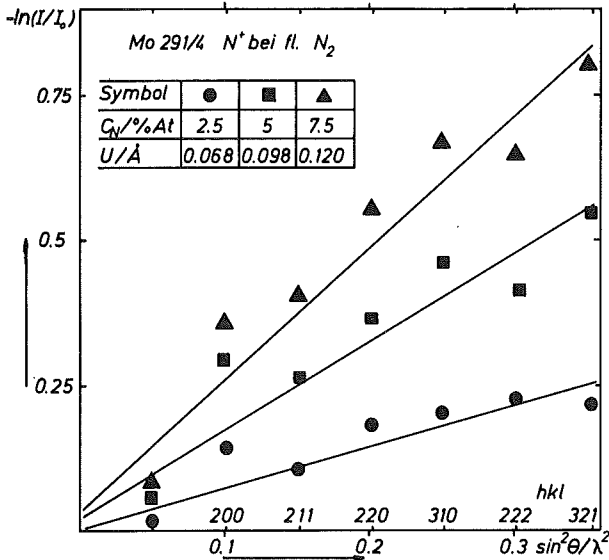


Fig. 3
Wilson plots for a nitrogen implanted Mo layers with concentration and displacement values indicated in the figure

nitrogen a continuous process with growing atomic displacements was observed while for phosphorus the amorphization process is thought to be heterogeneous. Here parts of the material are amorphized, and with growing impurity concentration either the number of amorphous regions or the size of these regions is increasing.

References

- /1/ O. Meyer, Inst. Phys. Conf. Ser. 28, 168 (1976)
- /2/ G. Linker, O. Meyer, Sol. State Commun. 20, 605 (1976)
- /3/ G. Linker, Progr. Rep. IAK I, KFK 2881, 91 (1979)

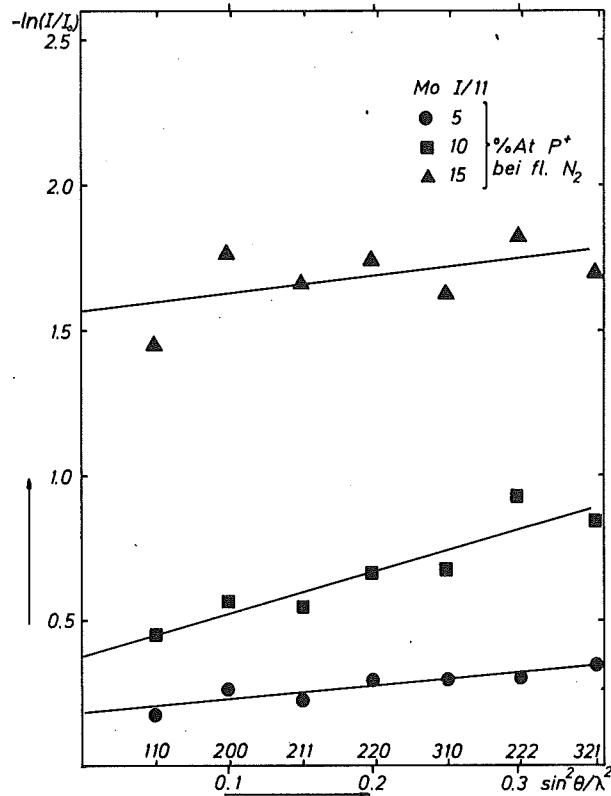


Fig. 4
Wilson plots of a phosphorus implanted Mo layer for three different concentration values

4.9 Pulsed Electron Beam Annealing of Ion Implanted Vanadium Single Crystals

H.W. Alberts, O. Meyer, J. Geerk, and F. Ratzel

The annealing behaviour of radiation damage in ion-implanted vanadium single crystals was found to be dependent on ion dose and the formation of a disordered layer /1/. The disordered layer, which was of polycrystalline nature, was observed to form after implantation of high doses of various ions (Se, In, Bi, Cs $> 10^x$ ions/cm²) or after furnace annealing of low dose implanted ions (Cs, Bi $> 10^{16}$ ion/cm²). At temperatures above 1000°C a break up of this layers accompanied with a loss of the implanted ions and a complete recrystallization of the material was observed.

In this study the Rutherford backscattering and channeling technique was used to examine the damage annealing effects with a pulsed electron beam (PEBA).

Vanadium single crystals have been implanted with low doses of Ga ($1.3 \cdot 10^{16}$ Ga⁺/cm²) and Se ions ($1.1 \cdot 10^{16}$ Se⁺/cm²). Energy dependent channeling and backscattering analysis with ⁴He ions in the energy range between 1.5 and 3 MeV has been performed on the Se implanted sample. From the damage-induced change of the dechanneling yield $\Delta(d\chi/dz)$, the product $\sigma_d \cdot N_s$ is determined (σ_d =dechanneling cross section, N_s =number of defect/cm²). This product is found to be proportional to the square root of the analyzing beam energy, indicating that dislocations are the most prominent defects /2/.

In a first experiment, isochronal annealing studies of a Se implanted sample were performed at temperatures up to 950°C. Annealing was found to occur mainly in a sharp stage at temperatures above 800°C, in accordance with previous results for low dose Se implants ($5 \cdot 10^{15}$ Se⁺/cm²) /1/.

In a second experiment the Ga and Se implanted samples were treated with electron pulses about 100 nsec in width and with pulse energy densities between .35 and 2.3 J/cm². In Fig. 1 the <111>-aligned spectra are shown for the virgin crystal (A), after implantation of Se(B) and after treatments with electron pulses with increasing pulse energy densities (C-F) from .35 to 1.8 J/cm² as indicated in the figure. With increasing energy density up to 2.3 J/cm² a slight decrease of the dechanneling rate is noted. The decrease of the product $\sigma_d \cdot N_s$ with increasing pulse energy density is presented in Fig. 2. At energy densities above about 1 J/cm² a broad peak appeared in the channeled spectra in the range of implanted ions. With increasing pulse energy the peak height increases until the random level is reached (spectra No. F in Fig. 1).

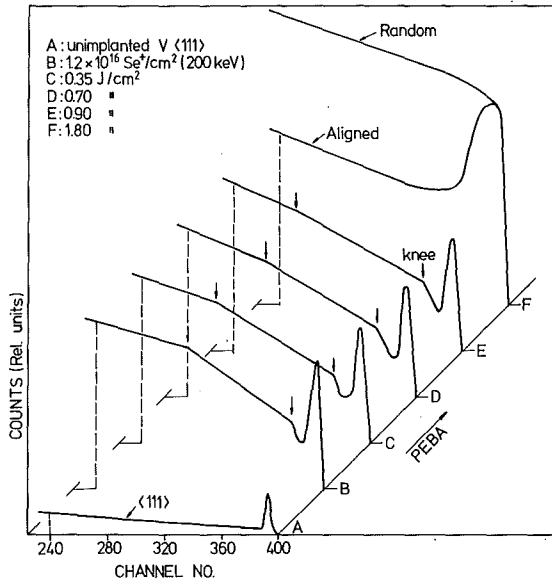


Fig. 1
 $\langle 111 \rangle$ aligned backscattering spectra from a virgin V single crystal (A) and from the crystal implanted with $1.2 \cdot 10^{16} \text{Se}^+/\text{cm}^2$ (200 keV) (B). In addition aligned spectra are shown after various PEBA treatments with energy densities from .35 to 1.8 J/cm^2 (C-F).

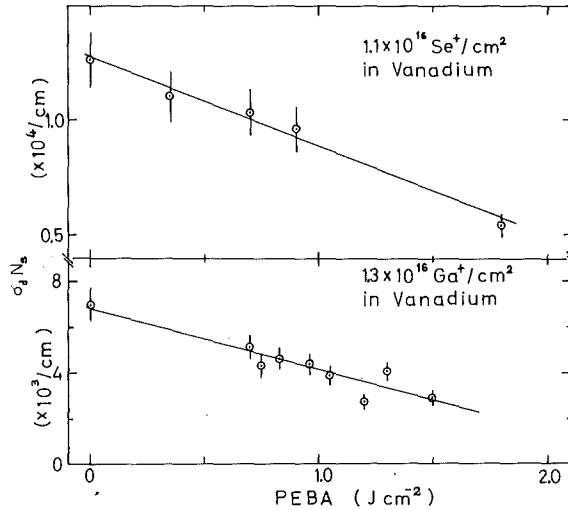


Fig. 2
 Decreases of $\sigma_{\Delta} \cdot N_s$ for Se and Ga implanted vanadium crystals with increasing pulse energy density.

This can be interpreted that a completely disordered layer is formed in the region of implanted Se and Ga. In contrast to the furnace annealing results of Ref. /1/, no indication could be found from thin film X-ray analysis that this layer is of polycrystalline nature. We conclude that these disordered layers produced by PEBA are of finegrain microcrystalline structure or completely amorphous.

References

- /1/ M. Gettings, O. Meyer, and G. Linker, Radiat. Eff. 21, 51 (1974)
 /2/ Y. Quéré, Phys. Status Solidi 30, 713 (1968)

4.10 Dechanneling Cross Section for Defect Clusters in Cu Single Crystals

O. Meyer and B. Larson^a

^aOak Ridge Natl. Laboratories, Solid State Division

Channeling and backscattering of energetic light ions is widely used as a quick tool to obtain a qualitative knowledge on the amount and the depth distribu-

tion of disorder in metals. The dependence of the dechanneling cross section σ_D and the analysing beam energy will provide additional insight into the nature of defects /1/. To determine absolute numbers for σ_D , comparative studies with other techniques (X-ray- or TEM-analysis) on identical samples have to be performed.

We used a Cu-single crystal whose surface was partly damaged by about $10^{12} \text{Ni}^+/\text{cm}^2$ at 17 MeV, having a mean projected-range of 2.5 μm .

The damaged region was carefully analysed with x-ray diffraction techniques. The total density of clusters was found to be $1 \cdot 10^{17}/\text{cm}^3$ with an average cluster diameter of 22 \AA ($7.2 \cdot 10^{16}$ voids/ cm^3 plus $2.8 \cdot 10^{16}$ interstitial clusters) /2/.

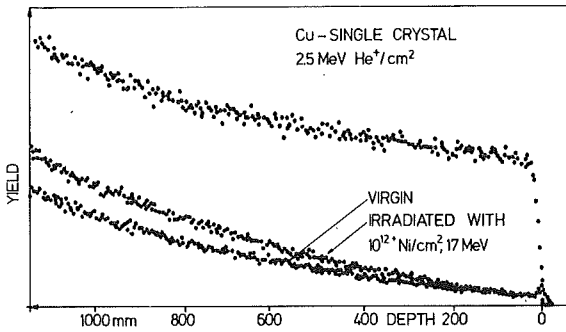


Fig. 1
Random and aligned backscattering spectra from a Cu single crystal, partly damaged with $10^{12} \text{Ni}^+/\text{cm}^2$ at 17 MeV.

In Fig. 1 the aligned spectra from the nonirradiated and the irradiated parts of the Cu-crystal are shown. The damage clusters cause an increase in the dechanneling rate $\Delta(d\chi/dz)$ ($d\chi/dz$ after irradiation minus $d\chi/dz$ before irradiation) which is proportional to $\sigma_D \cdot N_S$ with the relationship $\sigma_D N_S = \Delta(d\chi/dz) / (1 - \chi_{\min})$. N_S is the number of defect clusters/ cm^2 and χ_{\min} is the minimum yield. Assuming that the defect clusters are homogeneously distributed in depth, σ_D values as measured for various beam energies are summarized in Table 1.

Table 1 Minimum yield values, difference of the dechanneled fraction and dechanneling cross sections as a function of the analyzing beam energy.

E[MeV]	χ_{\min}	$\Delta(d\chi/dx) [\text{cm}^{-1}]$	$\sigma_D [\text{cm}^2]$
2.5	0.06	$1.76 \cdot 10^3$	$1.87 \cdot 10^{-14}$
2.0	0.06	$2.06 \cdot 10^3$	$2.2 \cdot 10^{-14}$
1.5	0.055	$2.9 \cdot 10^3$	$3.07 \cdot 10^{-14}$
1.0	0.06	$3.9 \cdot 10^3$	$4.15 \cdot 10^{-14}$
0.5	0.065	—	—

σ_D is found to increase by about a factor of two with decreasing beam energy. The σ_D -value at two MeV He ion energy is in good agreement with a value measured previously for 2 MeV He damage in Au single crystals /3/. There a value of $\sigma_D = 2.3 \cdot 10^{-14} \text{cm}^2$ was determined under the assumption that all of the dechanneling is due to clusters detected by TEM. σ_D was found to be about a factor of 5 smaller than the geometrical cross section of the clusters with an average cluster diameter

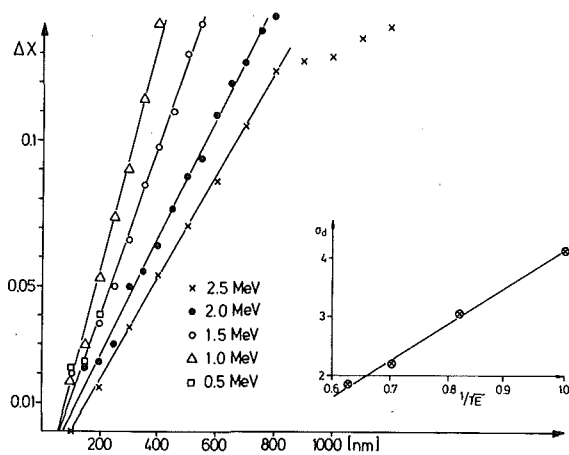


Fig. 2
Difference of the dechanneled fraction $\Delta\chi$ (with and without Ni-damage) as function of depth. The energy dependence of the dechanneling cross section is given in the inset of Fig. 2.

of 38 Å. Here with an average diameter of 22 Å as measured by x-ray analysis, σ_D is found to be only a factor of 2 smaller than the geometrical cross section. This means that the defect clusters are not as transparent to the beam as estimated from the results in Ref. /3/.

The value of the dechanneling cross section σ_D is found to be proportional to $1/\sqrt{E}$ (see inset of Fig. 2).

This result is not understood at present as for dislocations and voids a \sqrt{E} and a E^0 dependence respectively is expected /1/. A $1/E$ dependence is calculated for interstitial atoms /1/.

References

- /1/ Y. Quéré, Phys. Status Solidi 30, 713 (1968)
- /2/ B.C. Larson, J. of Appl. Crystallography 8, 150 (1975) and unpublished results
- /3/ K.L. Merkle, P.P. Pronko, D.S. Gemmell, R.C. Mikkelson, and J.R. Wrobel, Phys. Rev. B8, 1002 (1973)

4.11 Temperature-Dependant Channeling Studies on NbC-Single Crystals

R. Kaufmann and B. Scheerer

In the refractory compound NbC the superconducting transition temperature strongly depends on the C-content /1/. In searching for an explanation for this dependence the question arises about structural distortions near the C-vacancies. Suitable experiments to obtain some information about static displacements or distortions are temperature-dependant channeling measurements on NbC-single crystals.

For the presented channeling experiments NbC-single crystals with C/Nb-ratios of 0.89 and 0.80 were used. The composition has been determined by chemical

analysis. The channeling measurements were performed along the $\langle 110 \rangle$ -axis where the characteristics of the NaCl-structure are separated Nb- and C-strings. A low temperature-two-axis-goniometer allowed to collect data at temperatures of 295 K, 78 K, and 8 K /2/. 2 MeV-He-particles have been used to investigate the Nb-sublattice with Rutherford-backscattering and 1.27 MeV-deuterons for investigations of the C-sublattice with the $^{12}\text{C}(d,p)^{13}\text{C}$ -nuclear reaction.

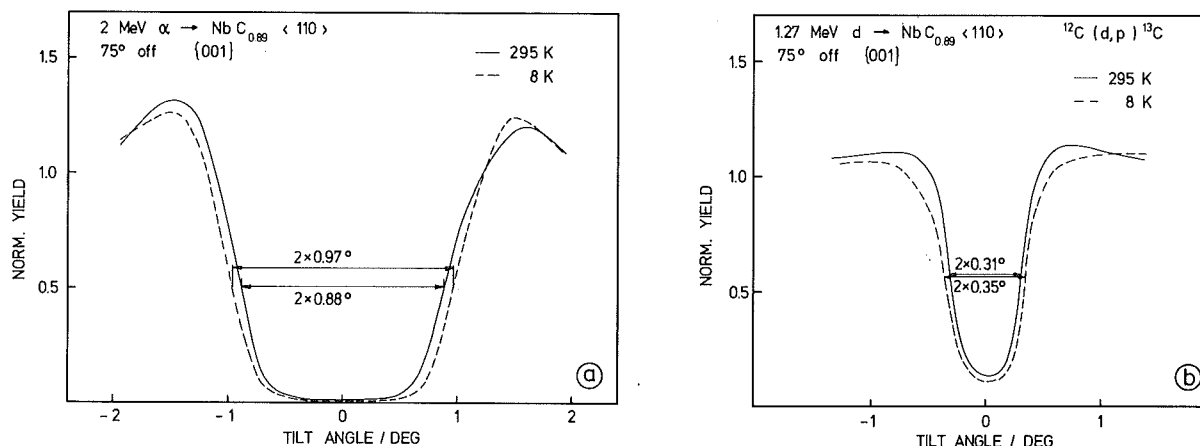


Fig. 1a, 1b
Angular scans through $\langle 110 \rangle$ for the Nb- and the C-sublattices, respectively, at temperatures of 295 K and 8 K.

Typical angular scan measurements are shown in Fig. 1a and 1b for a $\text{NbC}_{0.89}$ - single crystal at temperatures of 295 K and 8 K. The scan at 78 K (not shown) is very similar to that at 8 K. The angular half widths and the minimum yield values are shown in the following table 1:

T	Nb-sublattice		C-sublattice	
	Ψ 1/2/deg	χ_{\min}	Ψ 1/2/deg	χ_{\min}
295 K	0.88 ± 0.02	0.022 ± 0.002	0.31 ± 0.02	0.16 ± 0.01
8 K	0.97 ± 0.02	0.016 ± 0.002	0.35 ± 0.02	0.09 ± 0.01

The values for the Nb-sublattice are recorded in a depth region between 100 and 500 Å below the surface whereas for the C-sublattice this depth region is 2000 Å. The tilt plane for the values shown in the table was 75° off $\{001\}$. In addition angular scans were taken through other tilt planes showing differences in the half widths of up to 0.07° and in the shape of the shoulders. Therefore the exact knowledge of the orientation of the tilt plane is important especially when results from different crystals are compared.

To investigate to what extent the values presented in table 1 are influenced by possible lattice distortions scans were performed in a $\text{NbC}_{0.80}$ -single crystal.

along the same tilt plane. The measured half-widths agree with the values obtained for the case of $\text{NbC}_{0.89}$. Also the minimum yield values for the Nb- and the C-sublattices reached the values of the crystals with higher C-content. From these results it can be concluded that although the $\text{NbC}_{0.80}$ has a higher C-vacancy concentration possible lattice distortions seem to be in the same order of magnitude.

The experimental values have been compared to results from computer simulations. For that purpose a Monte-Carlo program was used based on the binary collision model with the Molière-approximation for the ion-atom interaction potential /3/. Also the electronic stopping behaviour and the scattering of the beam due to ion-electron-collisions have been taken into account. The mean vibrational amplitudes for the simulation of uncorrelated lattice vibrations were used calculated on the basis of a double-shell-model with force constants derived from inelastic neutron scattering experiments /4/. Static contributions of $u_{\text{Nb}}^{\text{stat}} = u_{\text{C}}^{\text{stat}} = 0.06 \text{ \AA}$ were added to the dynamical values of $u_{\text{Nb}}^{\text{dyn}} = 0.057 \text{ \AA}$ and $u_{\text{C}}^{\text{dyn}} = 0.05 \text{ \AA}$ in order to achieve agreement between experimental and calculated results as is shown in Fig. 2.

These values for static contributions to the atomic displacements seem quite reasonable. However, further experiments with NbC crystals of higher carbon content have to be performed in order to obtain more information about the defect structure caused by C-vacancies in NbC-crystals.

References

- /1/ A summary is given by L.E. Toth: Refractory Materials, Vol. 7, Academic Press (1971)
- /2/ R. Kaufmann and F. Ratzel, this report
- /3/ R. Kaufmann and O. Meyer, Rad. Eff. 40, 97. (1979).
- /4/ J.L. Feldmann and E.F. Skelton, Phys. Lett. 49A, 127 (1974)

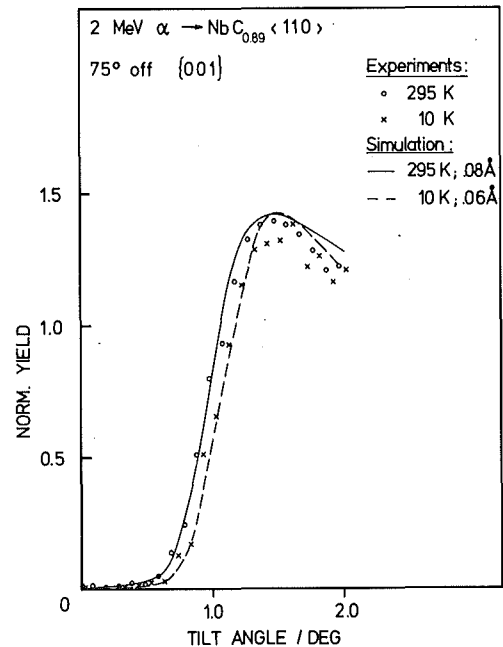


Fig. 2
Comparison of measured and calculated angular scans for the Nb-sublattice at 295 K and 8 K.

4.12 On the Effects of ^3He Implantation in NbC Single Crystals

R. Kaufmann, A. Tuross^a, and M. Kraatz

^aOn leave from Institute of Nuclear Research, Warsaw, Poland

Recently, Geerk /1/ has demonstrated that the superconducting transition temperature, T_c , of $\text{NbC}_{0.89}$ can be increased by the implantation of light elements at a temperature of 920°C . After the implantation of 60 keV He ions at a fluence of $8.8 \cdot 10^{16}$ at/cm² T_c increased from 4 K to 9.7 K.

In order to investigate the mechanism of the T_c enhancement lattice location studies have been carried out. Implantation parameters as reported in /1/ have been used. Only instead of ^4He ^3He ions have been implanted. This makes it possible to perform the lattice location experiments by means of the $^3\text{He}(d,p)^4\text{He}$ nuclear reaction.

This nuclear reaction has a peak cross-section of about 70 mb/sr at an incident deuteron energy of 450 keV. In order to obtain such low energy deuterons in the van de Graaff accelerator the D_2^+ molecular beam of 900 keV was used. The 13.5 MeV reaction-product protons were observed at an angle of 165° with a silicon surface barrier detector with 1 mm depletion layer and 450 mm^2 active surface area. In order to avoid distortion of the spectra due to the very high intensity of backscattered deuterons the detector was covered by an aluminized mylar foil of 12 μm thickness with a few pin-holes. Thus, the majority of backscattered deuterons was stopped in the foil whereas the much more energetic protons do

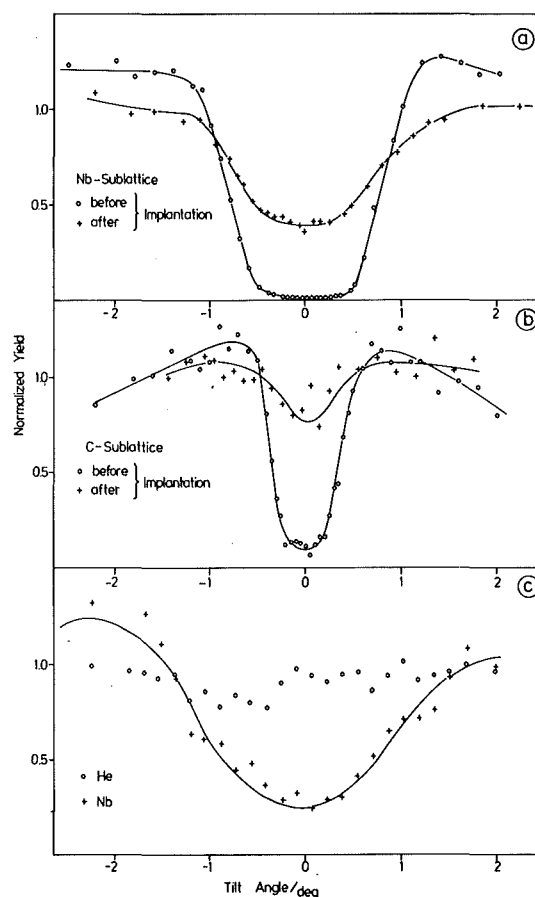


Fig. 1
Angular scans along $\langle 110 \rangle$ direction for NbC single crystal

- a) Nb-sublattice before and after He implantation
- b) C-sublattice before and after He implantation
- c) ^3He yield curve and the corresponding Nb dip

not suffer any significant energy loss. The alignment of the $\text{NbC}_{0.89}$ crystal could be performed by monitoring backscattered deuterons from Nb and simultaneously the ^3He distribution by recording the high energy reaction product protons. The effects of the implantation on the Nb- and C-sublattices were investigated by backscattered deuterons and the $^{12}\text{C}(d,p)^{13}\text{C}$ reaction, respectively. The incident deuteron energy was 1.27 MeV.

Angular scans along the $\langle 110 \rangle$ direction were made before and after the implantation. The spectra from the aligned crystal showed well distinguished damage peaks at a depth corresponding to the mean range of the implanted atoms. The energy windows for the angular scans were positioned at this depth. The angular yields for Nb- and C-sublattices are shown in Figs. 1a and 1b. The minimum yield for Nb increased from 0.02 for the unimplanted to 0.40 for the implanted sample. However, the half-width of the dip did not change. For the C-sublattice the minimum yield increased by the factor of 9. The important narrowing of the dip was also observed. Fig. 1c shows the ^3He and Nb angular yields as measured with the 450 keV deuteron beam. The ^3He yield curve does not show any angular dependence indicating the random distribution of the implanted ^3He in the crystal.

The observed increase of T_c after the ^3He -implantation cannot be attributed to the preferential lattice site occupation by the implanted species. Further investigations should therefore deal with the analysis of the produced defect structures.

Reference

- /1/ J. Geerk, in: Ion Beam Modification of Materials, J. Gyulai, T. Lohner, E. Pasztor (Eds.), Budapest (1978), p. 2035

4.13 Pulsed Laser Beam Treatment of NbN Single Crystals

O. Meyer, B.R. Appleton^a, C.W. White^a, and B. Scheerer

^a*Oak Ridge Natl. Lab. Solid State Division*

Carbon and nitrogen ion implantation into non-stoichiometric refractory metal carbides and nitrides was found to improve the superconducting properties if radiation damage is properly annealed. Because of the important role of defects

for the superconducting properties of these materials we studied the effect of short high power laser pulses on a NbN single crystal with the surface normal to the $\langle 111 \rangle$ crystal direction using the ion channeling and backscattering technique.

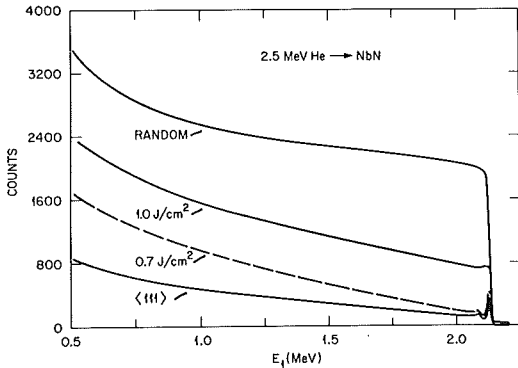


Fig. 1
Random and $\langle 111 \rangle$ aligned spectra from 2.5 MeV He ions, backscattered from a NbN single crystals. $\langle 111 \rangle$ aligned spectra are shown prior and after treatment with laser pulses of .7 and 1 J/cm² energy density.

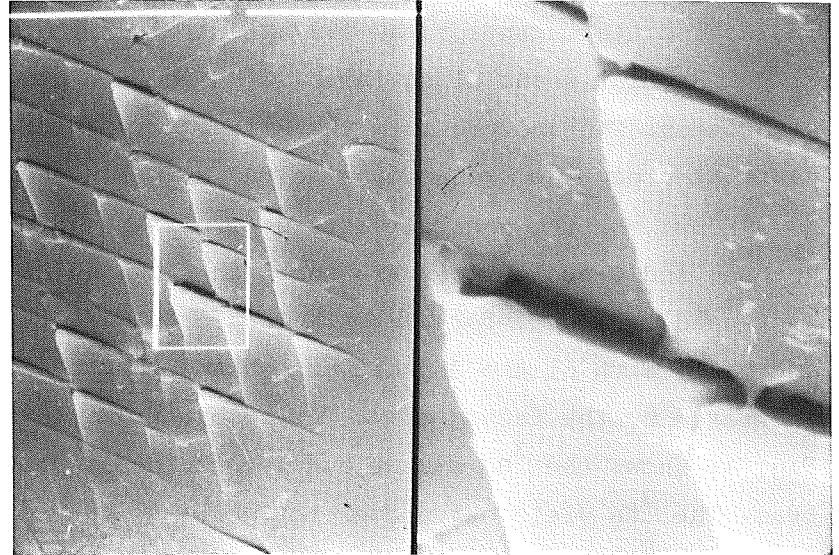


Fig. 2
SEM analysis (2500 X and 12500 X) of NbN single crystal after irradiation with a laser pulse of 1.5 J/cm² energy density.

Fig. 1 shows 2.5 MeV He ion spectra from NbN for random orientation and various $\langle 111 \rangle$ -aligned spectra before and after laser irradiation with single pulses of $15 \cdot 10^{-9}$ sec duration and at energy densities of .7 and 1 J/cm². With increasing energy density the dechanneling rate $d\chi/dz$ is found to increase. From angular scan curves it was observed that while the minimum yield χ_{\min} strongly increased, the critical angle was not much influenced after laser irradiation. The minimum yield χ_{\min} as well as the slope, $d\chi/dz$, were found to be independent on the analysing beam energy between 1 and 2.5 MeV. These results indicate that the laser induced defect structure are possibly stacking faults and microcracks. At 1.5 J/cm² the surface became heavily damaged as can be seen from the Scanning Electron Microscope pictures in Fig. 2. Triangular strips of material fracture and peel away from the $\langle 111 \rangle$ surface with edges along $\langle 111 \rangle$ planes. The strips that lift off are uniform in thickness of about 80 nm. Similar effects have been observed for TiC /1/ and the following mechanism for this appearance was proposed: The heated surface sheat expands but simultaneously will be constrained by the bulk. The compressive strain will cause plastic flow in the hot surface layer. On cooling the

surface layer contracts more than the bulk and will be in a state of tension. Tensile stresses will be relieved by brittle fracture as the temperature is below the brittle-ductile transition temperature. The tensile stresses in the surface layer are relaxed by upward bending of the strips.

The laser beam energy density of 1.5 J/cm^2 is a factor of 5 less than that used to anneal NbN and NbN-C films /2/.

References

/1/ T.J. Bastow, M.E. Packer, N. Gane, *Nature* 222, 27 (1969)

/2/ B.R. Appleton, C.W. White, B. Stritzker, O. Meyer, I.R. Gavalier, A.I. Braginski, and M. Ashkin, in: AIP-Conf. Proc. Laser-Solid-Interaction Boston, C.W. White and P.S. Peercy (Eds.), Academic Press (1980)

4.14 Preparation of TiN- and ZrN-Single Crystals with Different Nitrogen Content

Th. Wolf

For the measurement of the elastic and superconducting properties of refractory metal nitrides some samples of TiN and ZrN were prepared.

As starting materials rods of pure titanium and zirconium with a diameter of 12-13 mm were used. The samples were slowly pulled and simultaneously rotated through a RF-coil in a nitrogen atmosphere of 20 bar (Fig. 1).

By careful heating it could be achieved that only the inner part of a rod melted whereas the surface remained solid because of its higher nitrogen content. The nitrogen diffusing through the surface layer is dissolved in the melt and mixed before the crystal growth process starts. This results in relatively homogeneous samples. The nitrogen content of the rods depends on the velocity of pulling and on the growth temperature. The growth rates were between 8 and 17 mm/h, the temperatures between 2620 K and the melting points of the compounds. Below 2670 K in the case of TiN, and 3000 K in the case of ZrN the temperature could be measured with a filament pyrometer. Above these temperatures the evaporation of the nitrides became appreciable and only relative temperatures could be measured with a chopper ratio pyrometer after calibration with a filament pyrometer at lower temperatures. After zone melting the rods were cut by the spark erosion technique and analyzed

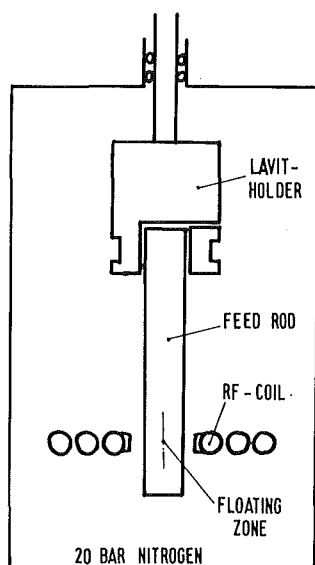


Fig. 1
Experimental assembly of the crystal growing device

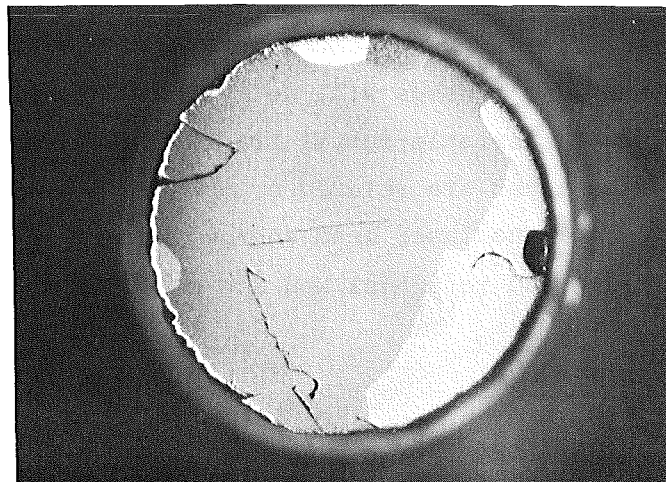


Fig. 2
Cross section of ZrN prepared at 3240 K.
The diameter is 12 mm.

metallographically and chemically. Individual crystals were almost 9 mm in diameter (Fig. 2). The chemical analysis gave $\text{TiN}_{0,68}$ for samples prepared at 2990 K and $\text{ZrN}_{0,79}$ for samples prepared at 3200 K. Further preparations and investigations are still in progress.

4.15 Elastic Properties of Polycrystalline TiN, ZrN, and HfN

Th. Wolf

For the investigation of the elastic properties of IV-a transition metal nitrides large polycrystalline samples were prepared by the hot-pressing method. This method is described in detail by Brundiers /1/.

As starting materials nearly stoichiometric powders of TiN, ZrN, and HfN with a particle diameter of 8 - 44 μm were used. The powders were hot-pressed in a nitrogen atmosphere between two graphite dies with an inner diameter of 26 mm at temperatures ranging from 1900 K to 2800 K and under pressures up to 500 kp/cm^2 . The hot-pressing device was evacuated and filled with nitrogen several times before heating. In table 1 the conditions of preparation are listed. There T means the sintering temperature, p the pressure of the dies, t the duration of the sintering and ρ the pycnometric density of the samples. As can be seen in the table,

Table 1 List of conditions of preparation for the different samples

Sample	T[K]	p[kp/cm ²]	t[h]	ρ [g/cm ³]
TiN	2070	500	2.5	4.56
TiN	2270	500	1.0	4.91
TiN*	2470	500	0.75	5.14
TiN	2770	500	0.75	5.32
ZrN	1970	500	6.0	6.92
ZrN	2120	500	3.0	7.02
ZrN*	2270	500	2.0	7.10
ZrN	2420	500	1.0	7.09
ZrN	2570	500	0.5	7.07
HfN	1870	400	9.0	10.13
HfN	2070	500	2.5	13.12
HfN*	2270	500	1.0	13.10
HfN	2570	500/200	0.25/0.25	12.87
HfN	2770	380	0.5	13.08

Table 2 Elastic moduli, Poissons' ratios, and Debye temperatures

Sample	TiN	ZrN	HfN
Young's Modulus $\times 10^{11} \left[\frac{\text{N}}{\text{m}^2} \right] \pm 3\%$	4.14	3.75	3.41
Shear Modulus $\times 10^{11} \left[\frac{\text{N}}{\text{m}^2} \right] \pm 1\%$	1.70	1.50	1.35
Bulk Modulus $\times 10^{11} \left[\frac{\text{N}}{\text{m}^2} \right] \pm 2\%$	2.44	2.49	2.40
Poisson's Ratio $\pm 3\%$	0.218	0.249	0.263
Debye Temperature θ_{E1} [K]	880	657	462

the highest density was in general obtained at the highest temperature, however, the chemical composition may not be optimal. After removal of the carbon containing surface layer the samples were about 20 mm in diameter and 4 - 10 mm in thickness.

The elastic constants of TiN, ZrN, and HfN were determined on the samples marked (*) in table 1 at room temperature by measuring the velocities of ultrasonic pulses with the pulse-echo-overlap method /2/. The samples were polished so that their front and back faces were parallel within 0.2 % of their separation dis-

tance. A quartz-oscillator-receiver was attached to one side of the specimen to measure the transit time of the ultrasonic pulses. The quartz crystals used were X-cut for the longitudinal measurements and Y-cut for the transverse measurements. Their resonant frequencies were between 9 - 24 MHz.

The elastic moduli, Poisson's ratio and the Debye temperature were calculated assuming the validity of Debye's approach to the isotropic medium /3/ (table 2). These data are preliminary. Porosity corrections after determination of the lattice constants and chemical analysis may lead to minor changes.

References

- /1/ G.D. Brundiers, KfK 2161 (1975)
- /2/ May, IRE National Conv. Rec. 6, 134 (1958)
- /3/ O.L. Anderson, J. Phys. Chem. Solids 24, 909 (1963)

4.16 The Effect of Temperature and Nitrogen Content on the Electrical Resistivity of Ta(C,N) and U(C,N)

H. Matsui^a, Hj. Matzke^b, H. Schneider^c, C. Politis

^a*Dep. of Nuclear Engineering, Nagoya University, Japan*

^b*European Institute for Transuranium Elements, CEC, Karlsruhe*

^c*Institut für Material- und Festkörperforschung, KfK*

KfK 2993 B (1980)

Abstract

The electrical resistivity, ρ , of carbonitrides and nitrides of tantalum and uranium was measured as function of temperature. At room temperature, ρ increased with increasing nitrogen content and with the concentration of constitutional non-metal vacancies.

4.17 Nb₇Si - A New Type of High T_c Superconductor

Ernst L. Haase, R. Smithey, and O. Meyer

In the course of a systematic investigation of the Nb₃Si and Nb₃Ge_{1-x}Si_x systems, we have identified a new cubic high T_c-phase and were able to show that one of the high T_c-samples reported by Dew-Hughes and Linse /1/ also shows this new phase, but no detectable amount of A15-Nb₃Si /2/.

The samples were prepared partly by coevaporation, but mostly by sputtering onto hot (780-900°C) sapphire substrates. T_c was measured resistively by the four point method. The lattice parameters (a₀) were determined with a thin film Guinier camera with Seemann-Bohlin focussing. In the evaluation of the data the stresses were taken into consideration /3/. Identification and separation from the competing Nb, Ni₃P, Ti₃P, Cr₅B₃, and Si₃Mn₅ phases was facilitated by using both Cu-Kα₁ and Cr-Kα₁ radiation. The formation of the Nb₇Si phase with high T_c and high residual resistance ratio is facilitated by addition of Be in the sputtering process. The Be-content was measured using the ⁹Be(d,α) reaction.

Be, however, is not significantly incorporated into the Nb₇Si phase, as there is no correlation between Be-contents and the lattice parameter. In Be-rich samples the a₀-value of the Cr₅B₃ phase is decreased. When this phase is not present, the Be diffuses into the substrate leading to the formation of chrysoberyl (BeAl₂O₄), as shown by its x-ray pattern. The Be appears to enhance the mobility of the atoms during the growth of the films, thus reducing the amount of defects.

Fig. 1 shows on the left hand side T_c vs. a₀ for A15-Nb₃Si /4/ and on the right hand side the same for samples containing the Nb₇Si phase. It is obvious that the A15-Nb₃Si and the Nb₇Si phases lie on two distinct curves. The triangular point with a T_c of 17.7 K stems from a sample prepared by an explosion technique /1/. For this sample a₀ was determined using CrKα₁ radiation /2/. Probably the 19 K sample prepared by essentially the same technique by Pan et al. /5/ also has to be assigned to the Nb₇Si phase. Also the 17.1 K sample prepared by Somekh and Evetts /6/ evidently better fits the Nb₇Si rather than the A15 assignment (Fig. 1).

Even our purest Nb₇Si samples contain Nb-precipitations of 20-30 %. Hence the determination of the Si-contents by Rutherford backscattering needs a correction, so far based on the intensity of the Nb-lines on the x-ray films. The corrected Si-content lies in the range of 8 - 13 at% Si leading to the nominal Nb₇Si assignment. The negative slopes of the curves in Fig. 1 imply an increasing T_c

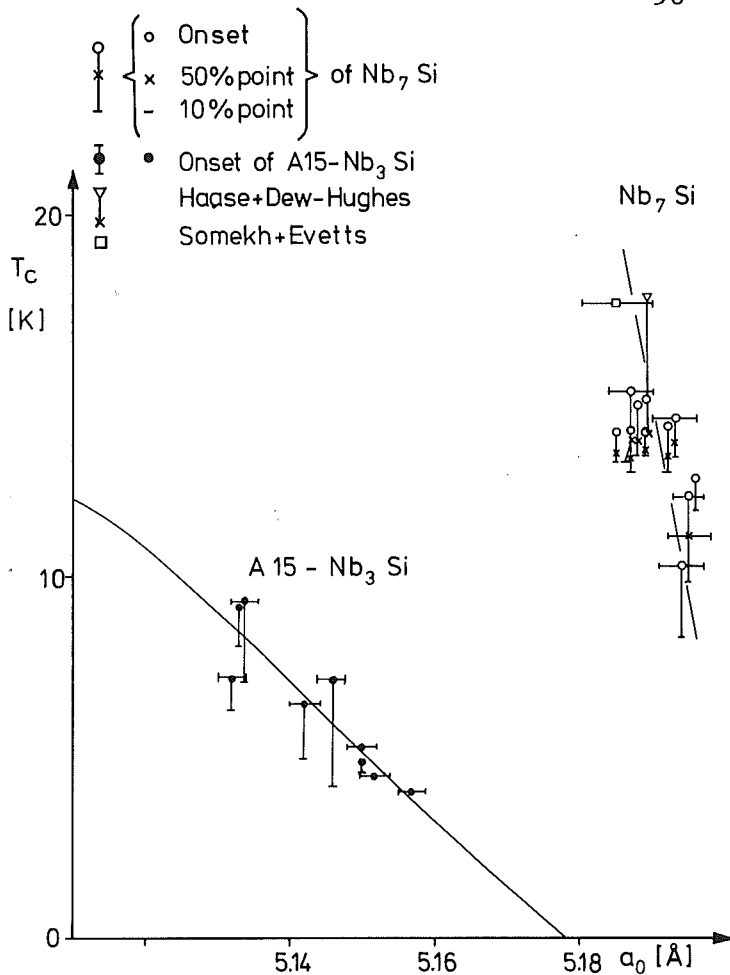


Fig. 1
 T_C vs. lattice parameter a_0 for A15-Nb₃Si on the left side and for Nb₇Si on the right side. The onsets are shown as circles, the transition midpoints as crosses and the 10 % points as bars. The 19 K point can not be shown as its a_0 is unknown.

Nb₃Ge and Nb₃Si values of at best 3 and 1.4 are observed, the Nb₇Si films have values up to 14.8. As the new phase was also observed for Nb₇Ge_{0.7}Si_{0.3}, it is likely to exist, at least in metastable form, in other related systems.

References

- /1/ D. Dew-Hughes and V.D. Linse, J. Appl. Phys. 50, 3500 (1979)
- /2/ E.L. Haase and D. Dew-Hughes, to be published
- /3/ E.L. Haase, Progr. Rep. IAK I, KfK 2670, 100 (1978)
- /4/ E.L. Haase, I.G. Kubeis, R. Smithey, and O. Meyer, Progr. Rep. IAK I, KfK 2881, 116 (1979) and to be published
- /5/ V.M. Pan et al., JETP Lett. 21, 228 (1975)
- /6/ R.E. Somekh and J.E. Evetts, IEEE Trans. Magn. Mag-15, 494 (1979)

with decreasing Nb-contents, as expected on account of the larger Nb-radius.

Unlike for the other phases observed in the Nb-Si system, there appears to exist no proto-structure type for the Nb₇Si phase. Thus its lattice parameter is taken to be the smallest that is needed to fit all observed lines, but could of course be larger by multiples of $\sqrt{2}$. The strongest observed lines are the 211 and 611 reflections. The intensity pattern is distinctly different from that of A15-Nb₃Si thin films. In particular the 311 line, which is forbidden for A15, is consistently observed.

Another noticeable difference is the residual resistance ratio. While for A15

4.18 Increase of the Superconducting Critical Temperature of A15 Mo₃Ge Thin Films by Heavy Ion Irradiation

M. Lehmann^a, E.L. Haase, and G. Saemann-Ischenko^a

^aPhysikalisches Institut der Universität, Erlangen-Nürnberg, D-8520 Erlangen

The critical temperature of A15 compounds decreases with increasing lattice disorder. The probably dominant reason for these effects is the degradation of the electronic density of states (DOS) at the Fermi level E_F . In the undamaged material E_F is situated in a peak of the DOS which becomes broadened and is lowered with increasing lattice disorder due to the finite lifetimes of electronic states /1/. A15 phase Mo₃Ge, however, with $T_C = 1.45$ K shows a different behaviour. By means of α -particle irradiation T_C could be enhanced to about 6 K /2/. In the present experiment the correlations between the superconducting properties and the fluence especially in the high fluence range was investigated.

The samples were 4600 Å - 7000 Å thick films sputtered onto 750°C hot sapphire substrates. The resistive T_C 's of the samples were between 1.40 K and 1.63 K with resistance ratios $1.29 \leq R(273K)/R(10 K) \leq 1.53$, the widths of the superconducting transitions T_ϕ were 50 mK to 200 mK. The x-ray analysis showed A15 structure with a lattice parameter $a_0 = 4.940$ and less than 20 % precipitates of Mo.

The irradiation took place at the Erlangen low temperature irradiation facility at $T_{irr} < 20$ K. The mean range of 20 MeV ³²S projectiles in Mo₃Ge is 3.8 μm, so the samples were homogeneously damaged and not doped with sulphur.

Fig. 1 shows the variation of T_C with fluence and during an isochronal annealing program at the end of the irradiations. T_C increases and reaches a maximum of 6.5 K at 3×10^{15} S⁴⁺-ions cm⁻². At higher fluences the midpoint of the superconducting transition decreases faster than its onset so that T_ϕ increases to 1.34 K - 1.95 K until T_C has dropped to 4 K. At 3.5 K T_ϕ of the samples before and after passing the maximum of the T_C change is nearly the same (≤ 350 mK).

As the displacement cross-sections of Mo₃Ge and Nb₃Ge are equal for the same projectile (20 MeV S) a comparison of the T_C -fluence correlation can be made. In Nb₃Ge T_C decreases from 20 K to a saturation value $T_C^{sat} = 4.0$ K which is reached at 3×10^{15} cm⁻². This means that in both materials a change in the behaviour of T_C , saturation or passing the maximum, occurs at the same fluence. The A15 lattice constant increases with increasing T_C (Fig. 2), the intensity of the diffraction lines decreases indicating increasing lattice disorder. Even after the highest fluence

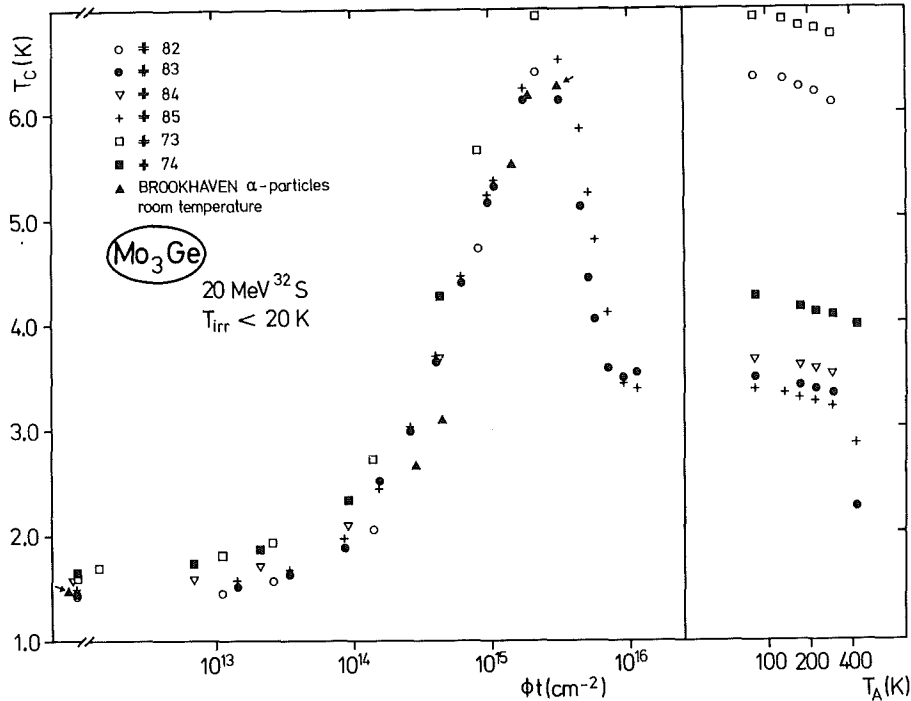


Fig. 1 Variation of the critical temperature T_C with fluence ϕt (left) and annealing temperature T_A of isochronal annealing cycles at the end of irradiation (right). The triangles show the Brookhaven data for 300 K α -particle irradiation.

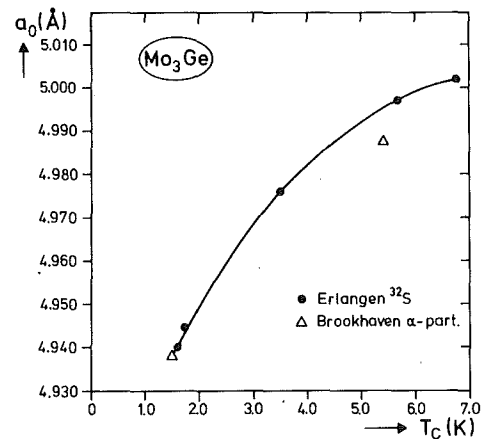


Fig. 2 Correlation between the critical temperature T_C and the lattice parameter a_0 determined with a Seemann-Bohlin X-ray diffractometer for thin films.

the lowest three A15 lines are still present, but a determination of the lattice parameter is no longer possible. The change in lattice parameter up to the maximum in T_C ($\frac{\Delta a_0}{a_0} = 1.26\%$) is greater than in other A15 compounds ($\leq 1.0\%$ (Nb_3Ge)). The diffraction pattern of Mo is not changed in intensity but the lines become asymmetric towards lower lattice parameters ($3.145 \text{ \AA} \rightarrow 3.140 \text{ \AA}$) which indicated radiation induced vacancies in the Mo precipitations, but no significant recoil-induced Ge contamination, which would lead to a a_0 increase.

From the measurement of the slope of the critical magnetic field $\left. \frac{dH_c2}{dT} \right|_{T=T_c}$ and the electrical resistivity the electronic specific heat or DOS at the Fermi level $N(E_F)$ can be derived /3/. Our data show a strong increase of $N(E_F)$ with T_c up to the maximum and then a decrease with decreasing T_c .

In undamaged Mo_3Ge E_F is situated in a valley between two peaks of the DOS /4/. Lattice disorder causes a broadening of the DOS peaks and $N(E_F)$ as well as T_c increase. At high fluences ($>3 \cdot 10^{15} \text{ cm}^{-2}$) T_c decreases either because of the further smearing of the structures in the DOS or, as $\left. \frac{dH_c2}{dT} \right|_{T=T_c}$ points to, because E_F is shifted over the maximum of the broadened peak, as the number of electronic states has to be conserved.

References

- /1/ P. Müller, G. Ischenko, H. Adrian, J. Bieger, M. Lehmann, E.L. Haase, Proc. of the 3rd Int. Conf. on Superconductivity in d- and f-Band Metals, San Diego, USA (1979), Plenum Press, New York, (1980) p. 369
- /2/ M. Gurvitch, A.K. Ghosh, B.L. Gyorffy, H. Lutz, O.F. Kammerer, J.S. Rosner, M. Strongin, Phys. Rev. Lett. 41, 1616 (1978) and private communication
- /3/ H. Wiesmann, M. Gurvitch, A.K. Ghosh, H. Lutz, O.F. Kammerer, M. Strongin, Phys. Rev. B17, 122 (1978)
- /4/ T. Jarlborg, J. Phys. F9, 283 (1979)

4.19 . Investigations of the Defect Structure of Proton-Irradiated Nb_3Ge -layers

W. Stocker, G. Linker, M. Kraatz, O. Meyer, B. Krevet^a, and F. Wüchner^a

^a*Institut für Technische Physik, KfK*

The influence of irradiation with Ar- and He-ions on the superconducting transition temperature and the structure of Nb_3Ge -layers has been reported recently /1/. In this contribution we present results from similar experiments performed with proton irradiation. Due to the small energy transfer to the lattice atoms it was expected that the protons produce less damage and a different defect structure than heavy ions. By comparing with the previous data it was hoped to

isolate the special defect responsible for the T_C -decrease.

Nb_3Ge -layers with thicknesses of about 500 nm were irradiated with various fluences ($5 \cdot 10^{16}$ – $4 \cdot 10^{17}$ ions/cm²) of 300 KeV H^+ -ions at room temperature. At this energy the protons penetrated the layers and came to rest in the substrate. The structure of the Nb_3Ge -layers before and after irradiation has been investigated by x-ray diffraction measurements employing a Guinier thin film diffractometer. For the analysis of the x-ray diffraction intensities a modified Wilson-plot has been used. In this procedure the $\ln(I/I_0)$, where I_0 and I are the intensities of the single lines from a sample before and after irradiation, respectively, is plotted vs. $\sin^2\theta/\lambda^2$ (θ = Bragg angle, λ = wavelength).

The data can be described to a good approximation by straight lines. This is illustrated in Fig. 1 for various fluences.

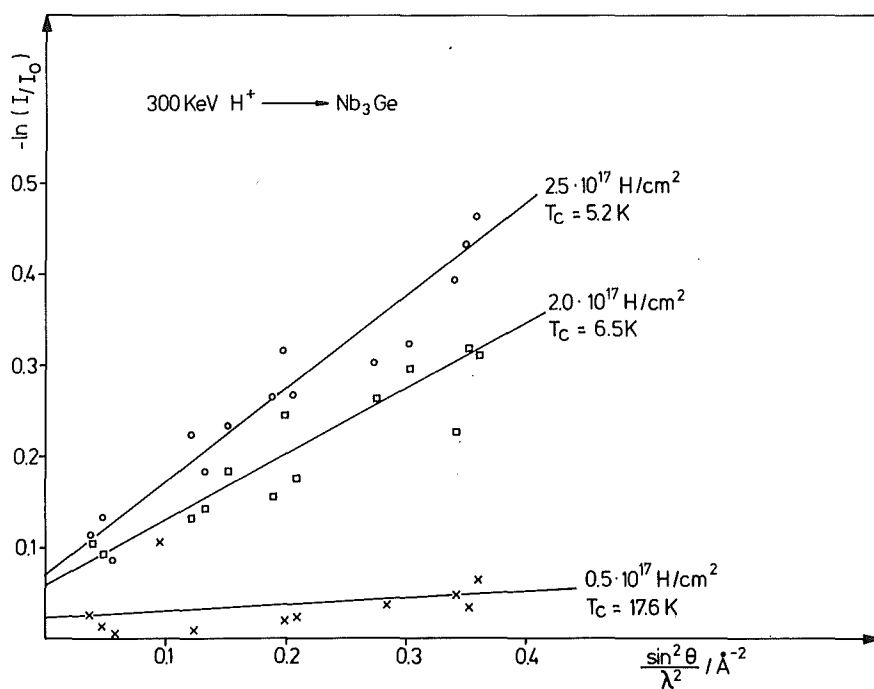
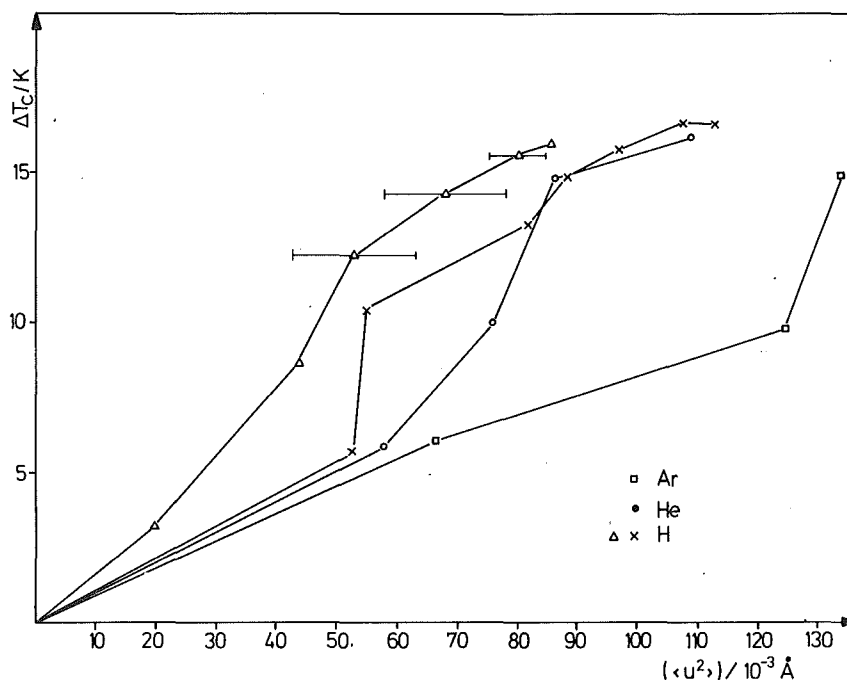


Fig. 1
 $\ln(I/I_0)$ as a function of $\sin^2\theta/\lambda^2$ with the H^+ ion fluence as a parameter.

The slopes of the least square fit straight lines correspond to $-8\pi^2\langle u^2 \rangle$ where $\langle u^2 \rangle^{1/2}$ can be interpreted as mean static displacements of the atoms from their ideal lattice sites. In our analysis we could not distinguish within the accuracy of our experimental results between contributions to $\langle u^2 \rangle$ from A(Nb) and B(Ge) atoms, respectively. With increasing proton fluences the mean displacements of the atoms were found to increase. A similar behaviour has also been observed for He- and Ar-irradiation /1/.

In Fig. 2 the static displacements are plotted vs. the difference of the T_C -values before and after irradiation, ΔT_C , together with the results from Ar- and He-irradiation /1/. For similar T_C -values the mean displacements for proton

Fig. 2
 ΔT_C as function of
 the static displacements for H^{+-} , Ar^{++} -
 and He^{+-} -ion irradiations.



irradiation are smaller than for Ar-irradiation. However, within the errors of the analysis they are not much different from the values obtained for He-ions irradiation.

With He- and especially with Ar-irradiations in addition to the static displacements inhomogeneous damage like amorphous zones was produced which also may influence the results of the quantitative determination of the u -values /1/. The axial section values on the $\ln(I/I_0)$ axis are a direct measure for the amorphous regions in the irradiated material. The axial section values in Fig. 1 are much smaller than previously reported /1/ for He- and Ar-irradiation. Due to the smaller mean energy transfer of protons to the lattice atoms, besides other types of defects, small static displacements are preferentially produced. A strong decrease of the 510, 310, and 220 line intensities with fluence is also observed, indicating the presence of site exchange defects. A quantitative analysis is in progress.

Reference

/1/ J. Pflüger, O. Meyer, Solid State Commun. 32, 1143 (1979)

4.20 X-Ray Diffraction Studies on He- and Ar-Irradiated Nb₃Ge Thin Films

J. Pflüger and O. Meyer

Solid State Commun. 32, 1143 (1979)

Abstract

We have performed measurements of relative integrated x-ray intensities in order to study the influence of radiation damage on the A15 structure of superconducting Nb₃Ge. With increasing He- and Ar-ion fluence an increase of the "temperature factor" and the lattice parameter has been observed in the fluence region where the depression of the superconducting transition temperature T_c was found to occur. Both parameters do not uniquely depend on the decrease of T_c . Further a decrease of the total relative x-ray intensity is found for particle fluences in the saturation region of T_c . The results are interpreted in terms of static atom displacements statistically distributed in the irradiated volume.

4.21 The Superconducting Transition Temperature of Bulk Samples of the Niobium-Germanium A15-Phase after Implantation of Ge, Si, O, and Ar Ions

J. Geerk

Solid State Commun. 33, 761 (1980)

Abstract

Bulk material of Nb₃(Ge_{0.8}Nb_{0.2}) with A15 structure and a superconducting transition temperature T_c of 6.5 K has been implanted with Ge, Si, Ar, and O ions and subsequently annealed at high temperatures. After annealing between 700 and 750°C the Ge implanted samples showed a strong increase in T_c up to 16.2 K. With Si ions only a T_c of 13 K was obtained, with Ar and O ions T_c remained below 9 K. From x-ray measurements carried out on high T_c Ge implanted samples it could be

concluded that the implanted surface layer grows up to a high degree epitaxially on the single crystallites of the bulk material. The lattice constant a_0 of the implanted film was reduced by 0.02 \AA with respect to the bulk material. This reduction in a_0 is stronger than expected from the transition temperature of the implanted surface layer.

4.22 The Defect Structure of Irradiated Nb₃Al Films

U. Schneider, G. Linker, and M. Kraatz

The superconducting transition temperature T_c of A₃B-compounds with A15 structure is strongly depressed by radiation damage. Three kinds of defect models which may be responsible for this depression are discussed in the literature. These models are: amorphous regions, antisite defects and static displacements /1,2,3/.

In this contribution we have investigated the influence of ion irradiation on T_c and the defect structure of sputtered Nb₃Al layers.

The films have been irradiated with 300 keV protons and 700 keV N⁺⁺-ions with fluences in the range of $1 \cdot 10^{15}$ - $6 \cdot 10^{17} \text{ H}^+/\text{cm}^2$ and $1 \cdot 10^{13}$ - $1 \cdot 10^{16} \text{ N}^{++}/\text{cm}^2$, respectively.

X-ray diffraction measurements have been performed with a thin film Guinier diffractometer. The intensities were analysed using a modified Wilson-plot /4/. In an usual Wilson-plot the structure factors F_{hkl} determined from the measured data are referred to calculated values. Here a modified procedure has been used, i.e. the intensities I_D from the bombarded samples have been compared to the intensity I_0 of the unbombarded layer.

This procedure yields $\ln \frac{I_D}{I_0} = -2B \frac{\sin^2 \theta}{\lambda^2} + \text{const}$ where $B = 8\pi^2 \cdot \langle u^2 \rangle$, θ is the glancing angle, λ is the wavelength and $\langle u^2 \rangle$ is the mean square displacement of the atoms perpendicular to the reflecting plane.

In the Wilson-plot, due to the different categories of structure factors existing in the A15 structure, the data from these different classes were treated separately.

These categories are:

- (1) F_{hkl} with contributions from A-atoms only,
- (2) F_{hkl} with contributions from A- and B-atoms.

In the second category a subdivision into further types can be made:

- (a) $F_{hkl} \propto (f_A - f_B)$
- (b) $F_{hkl} \propto (f_B + 3f_A)$
- (c) $F_{hkl} \propto (f_B - 3f_A)$
- (d) $F_{hkl} \propto (f_A + f_B)$

Due to the different atomic numbers of Nb and Al ($Z_{Nb}=41$, $Z_{Al}=13$), lines from category 2a are clearly detected in the unbombarded sample.

These lines are highly sensitive to anti-site defects, while for the other lines less or no sensitivity to lattice-site disorder is expected.

Figures 1a and 1b show modified Wilson-plots, where the data are divided into five groups as indicated above.

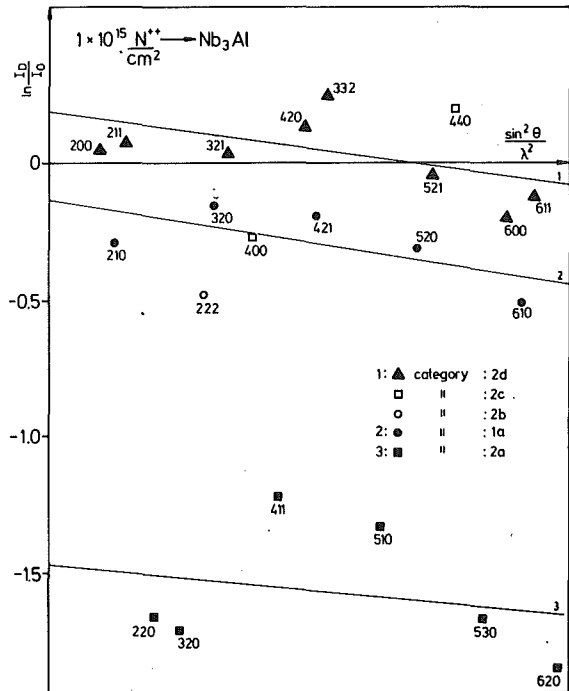
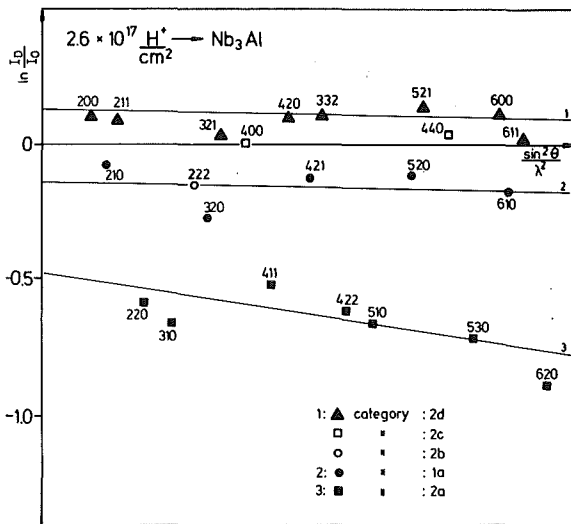


Fig. 1

Modified Wilson-plots for Nb_3Al layers irradiated with a) $2.6 \cdot 10^{17} H^+/cm^2$, 300 keV, and b) $1 \cdot 10^{15} N^{++}/cm^2$, 700 keV.

(1) The most significant result deduced from Fig. 1 is the strong intensity decrease for the lines of category 2a indicating substantial site-exchange disorder.

(2) Lines with $F_{hkl} \propto f_A$ show a smaller effect of intensity decrease than those mentioned above while for lines with F_{hkl} of category 2b/d almost no effect on the intensity could be detected.

Another result of the Wilson-plots are slopes of the straight lines fitted

through the data points of the different structure factor types.

For the example shown in Fig. 1a/b these slopes are significant though in other samples due to the large scatter of the points of category 1a no such clear result emerged.

To quote some results we restrict to slopes of those lines originating solely from diffraction from chain atoms. In the T_c vs. fluence region where T_c starts to saturate, for the static displacements a value of about $\sqrt{u^2}=0.05 \text{ \AA}$ for nitrogen and $\sqrt{u^2}=0.02 \text{ \AA}$ for protons has been estimated.

References

- /1/ C.S. Pandé, Solid State Commun. 24, 241 (1977)
- /2/ A.R. Sweedler, D.G. Schweitzer, G.W. Webb, Phys. Rev. Lett. 33, 168 (1974)
- /3/ O. Meyer, B. Seeber, Solid State Commun. 22, 603 (1977)
- /4/ G. Linker and M. Kraatz, Progr. Rep. IAK I, KfK 2881, 91 (1979)

4.23 Superconducting Properties and Structure of Ion Bombarded Nb Layers

G. Linker

Radiation Effects 47, 225 (1980)

Abstract

The influence of ion bombardment on the superconducting transition temperature T_c and the structure of thin evaporated niobium layers has been investigated as a function of ion species and layer purity. Irradiation through pure layers with neon ions and fluences of typically 10^{16} ions/cm² leads to relatively small T_c decreases ($\Delta T_c \sim 0.5 \text{ K}$), while in oxygen contaminated layers larger effects depending on oxygen concentration are observed. Homogeneous implantation of chemically active impurities (nitrogen, oxygen) also drastically depresses T_c reaching the

detection limit of 1.2 K at a concentration of 15 at% N. The T_c depressions correlate with a lattice parameter expansion of the Nb bcc structure at a rate of about 0.1 % per 1 at% impurity.

4.24 Channeling Measurements in He-Irradiated V_3Ge -Single Crystals

O. Meyer, R. Kaufmann, B. Appleton^a, and M. Chang^a

^a*Oak Ridge Natl. Lab. Solid State Div.*

Defect originated static displacements of atoms with average displacement amplitudes in the order of 0.05 to 0.1 Å have been detected with the channeling technique and with x-ray diffraction in damaged V_3Si , Nb_3Sn , and Nb_3Ge . It may be speculated that this defect structure is correlated with lattice instabilities observed for the high- T_c V_3Si and Nb_3Sn superconductors. In order to test this speculation, channeling measurements have been performed in He-irradiated V_3Ge -crystals with a low T_c -value of 6 K. As the B-atom is heavier than the A-atom in V_3Ge , this material is well suited to study the question if there are small atomic displacements not only in the A-atom but as well in the B-atom sublattice using the backscattering and channeling technique.

A V_3Ge -single crystal was irradiated and analyzed in situ using a 2 MeV He-beam. During irradiations the beam was scanned (in x-y direction) across the crystal surface and a beam current of $4\mu A/cm^2$ was used for 1 to 4 h irradiation time. The analysis was performed in about 15 min. using a beam current of $0.3\mu A/cm^2$.

In Fig. 1 the random and $\langle 100 \rangle$ aligned backscattering spectra using 2 MeV He-ions as the analysing beam are shown. He-ions backscattered from Ge-atoms are well separated in energy from those backscattered from V-atoms. The $\langle 100 \rangle$ aligned spectrum after irradiation with $2 \cdot 10^{17} He/cm^2$ is also given in Fig. 1. Angular scans were taken using an energy window as indicated in Fig. 1.

Angular scan curves from the virgin and the irradiated crystal are shown in Fig. 2. A narrowing in the critical angle $\Psi_{1/2}$ and an increase of the minimum yield χ_{min} is clearly visible after irradiation with $2 \cdot 10^{17} He^+/cm^2$ (2 MeV). A Monte Carlo computer program /1/ has been used to calculate the angular scan cur-

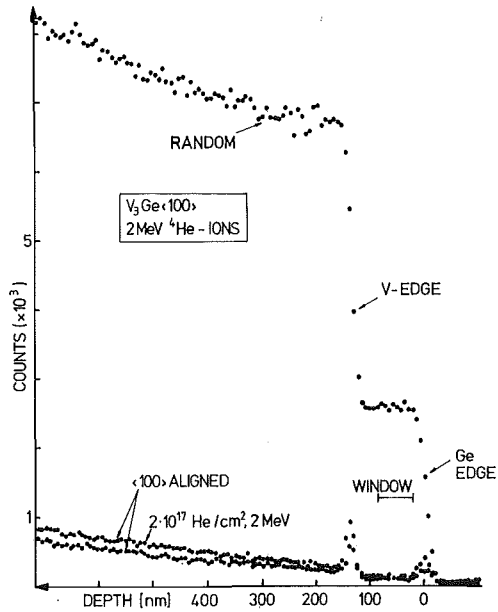


Fig. 1
Energy spectra of 2 MeV ^4He ions backscattered from a V_3Ge single crystal. Included are the $\langle 100 \rangle$ aligned backscattering spectra before and after irradiation with $2 \cdot 10^{17} \text{He}/\text{cm}^2$ at 2 MeV.

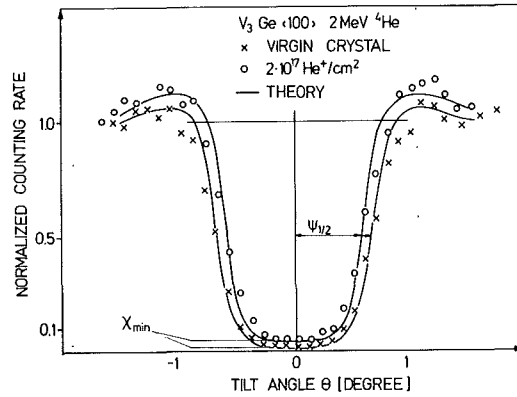


Fig. 2
Normalized angular yield curves before (X) and after (O) irradiation with $2 \cdot 10^{17} \text{He}^+/\text{cm}^2$ at 2 MeV. Calculated angular yield curves are included as solid lines.

Table 1 Decrease of T_c in thin V_3Ge films /2/, decrease of $\Psi_{1/2}$ and increase of χ_{\min} as a function of He ion fluence. Calculated values are included in the last column.

FLUENCE [He/cm ²] 2 MeV	T_c V ₃ Ge-Films Ref.2 [K]	$\Psi_{1/2}$ Ge-Rows [°]	χ_{\min} Ge-Rows [%]	THEORY	
				$\Psi_{1/2}$ [°]	χ_{\min} [%]
0	6	.69±0.01	2.9±.2	.68	2.2±.5
2x10 ¹⁶	4.5	.66	3.9		
6x10 ¹⁶	3	.63	4.8		
2x10 ¹⁷	1.2	.61	5.0	.60	3.6
ANNEAL $T_A=800^\circ\text{C}$ 5 min		.67	3.0		

ves before and after irradiation with He-ions. The best agreement with the measured results after irradiation was obtained by assuming an average static displacement amplitude of 0.06 \AA of all atoms from their lattice sites. The decrease of T_c in thin V_3Ge -films as a function of He-fluence was measured previously /2/. These data together with the measured decrease of $\Psi_{1/2}$ and the increase of χ_{\min} with fluence are summarized in table 1. It may be noted that the decrease of T_c

occurs in the same fluence region where the shape of the angular scan curve is found to change. Annealing at 800°C for 5 min leads to a partial recovery of the crystal.

From these results we conclude that static displacements are a common defect structure for A15 type material with relative small T_c -values and that both the A-atom sublattice as well as the B-atom sublattice are equally distorted.

References

- /1/ R. Kaufmann and O. Meyer, Rad. Effects 40, 97 and 161 (1979)
- /2/ J.M. Poate, R.C. Dynes, L.R. Testardi, and R.H. Hammond, Phys. Rev. Lett. 37, 1308 (1976)

4.25 The Influence of Light- and Heavy-Ion Irradiation on the Structure, Resistivity, and Superconducting Transition Temperature of V_3Si .
A Comparative Study

O. Meyer and G. Linker

J. Low Temp. Phys. 38, 747 (1980)

Abstract

Channeling and x-ray diffraction measurements on Kr- and He-irradiated V_3Si single crystals and films reveal different damage levels for fluences in cases where the superconducting transition temperature T_c has been reduced by the same amount. This indicates that only special defect structures are responsible for the T_c -reduction mechanism. In the fluence region where T_c is decreasing, T_c correlates with residual resistivity ρ_0 , independent of the kind of irradiation. However, at particle fluences where T_c saturation occurs, different saturation values of ρ_0 are observed. The exponential decrease and the saturation of T_c with fluence are explained by a similar behavior of ρ_0 versus fluence in the damage production and saturation processes. The increase of the lattice parameter is not uniquely dependent on the decrease of T_c , but also on the amount of damage present.

4.26 Pulsed Laser Annealing of V_3Si -Single Crystals and Thin Films

O. Meyer, J. Thompson^a, B.R. Appleton^b, and C.W. White^b

^aUniversity of Tennessee, Knoxville

^bOak Ridge National Laboratory, Solid State Division

Non-equilibrium techniques such as evaporation, sputtering, chemical vapor deposition and splat-cooling have been successfully used for the preparation of high T_c superconductors. Extremely rapid heating (melting) by irradiation with a laser pulse and subsequent cooling (crystallization) may also be a useful technique in this respect.

V_3Si single crystals, cut normally to the $\langle 100 \rangle$ and $\langle 110 \rangle$ crystal directions and V_3Si films, sputtered onto heated sapphire substrates, have been irradiated with pulses ($15 \cdot 10^{-9}$ sec duration) from a Q-switched Ruby laser. The $\langle 110 \rangle$ single crystal has been damaged near the surface by implanting $4 \cdot 10^{16} \text{ He}^+/\text{cm}^2$ at 300 KeV. In addition in V_3Si films which were partly damaged with $1.50 \cdot 10^{16} \text{ B}^{++}/\text{cm}^2$ at 300 KeV, a Xe-marker was implanted into the surface of the films. Ion backscattering and channeling has been used to analyse laser treated samples. T_c was measured resistively.

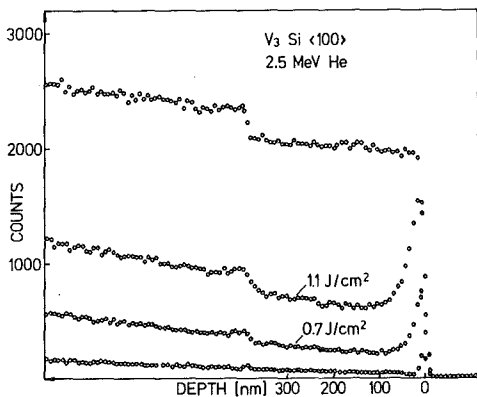


Fig. 1
Random and $\langle 100 \rangle$ -aligned backscattering spectra from V_3Si single crystal before and after irradiation with laser pulses of 0.7 and 1.1 J/cm^2 .

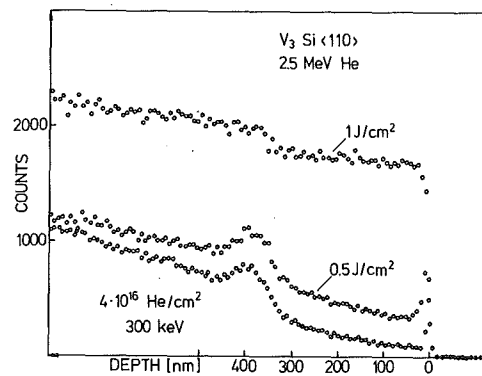


Fig. 2
 $\langle 100 \rangle$ -aligned backscattering spectra from He-implanted V_3Si single crystal before and after irradiation with laser pulses of 0.5 and 1 J/cm^2 .

In Fig. 1 $\langle 100 \rangle$ aligned backscattering spectra are shown before and after irradiation with laser pulses of 0.7 and 1.1 J/cm². The dechanneling yield is found to increase with increasing energy density of the laser pulse. Further a surface peak appears, indicating the formation of a strongly disordered surface layer. The dechanneling rate was found to be independent of the analysing beam energy. Similar results are presented in Fig. 2 for a $\langle 110 \rangle$ oriented V₃Si single crystal preimplanted with 4·10¹⁶ He⁺/cm² at 300 KeV. The enhanced dechanneling yield and the defect peak due to displaced lattice atoms at the end of the He-ion tracks are clearly visible. With increasing laser energy density the dechanneling increases and channeling is no longer observed for an energy density of 1 J/cm². At 1.5 J/cm² the surface became heavily damaged and irregular flaking of the surface layer was observed. For energy densities above about 2 J/cm² surface melting occurred. The molten zone did not recrystallize epitaxially on the bulk single crystal. A possible explanation why the $\langle 110 \rangle$ direction is more sensitive to laser pulse than the $\langle 100 \rangle$ crystal direction is based on the fact that the likely glide systems in V₃Si probably are $\langle 100 \rangle \{010\} /1/$. In $\langle 100 \rangle$ orientation the resolved shear stress on the three slip system would be zero whereas in $\langle 110 \rangle$ orientation two glide systems are activated. For temperatures above 1200°C plastic deformation of V₃Si single crystals has been observed /1/. In the surface layer heated by the laser pulse thermal stresses may cause glide motion. Upon cooling mechanical stresses will build up and will lead to surface flaking and microcracks at laser energy densities above 1.5 J/cm².

In order to study if T_c would recover after laser annealing, damaged V₃Si films have been irradiated with laser pulses as function of energy density. The results of this study are summarized in Fig. 3. T_c recovery was observed to occur at energy densities above .5 J/cm². At 1 J/cm² the film started to peel off the sapphire substrate. Therefore a cumulative deposition of pulses was used which leads to some improved recovery. Irradiation of undamaged V₃Si-layers did not influence T_c for energy densities up to 1 J/cm².

References

- /1/ S. Mahjan, J.H. Wernick, G.Y. Chin, S. Nakahara, and T.H. Geballe, Appl. Phys. Lett. 33, 972 (1978)

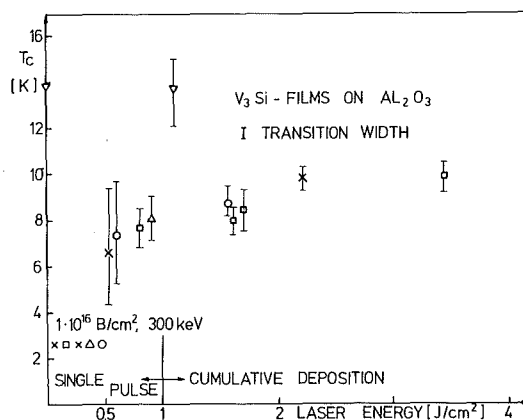


Fig. 3 Superconducting transition temperature T_c of damaged V₃Si films vs. E, the cumulative laser energy density.

4.27 Preparation of YB_6 -Powder Samples

B. Scheerer and F. Gompf

In /1/ we pointed out that the superconducting compounds LaB_6 and YB_6 are chemically very similar. Since their difference in the electronic density of states at the Fermi surface is not large enough to explain their large difference in T_c /2/ (LaB_6 : $T_c = 0.45$ K, YB_6 : $T_c = 7.2$ K) phonon softening is expected to play an important role in the enhancement of T_c . We gave preliminary results of lattice vibrations deduced from neutron inelastic scattering experiments but especially for YB_6 these results suffered under bad statistics due to the high absorption cross section of B-10.

In order to prepare YB_6 with B-11 enriched B we prepared in the first step powder samples with the natural B-isotope-mixture.

Only little literature is known which describes the preparation of single phase YB_6 . Because most of these descriptions and documentations are very superficial and partly contradictory, we had to carry out extensive experiments to produce YB_6 .

Yttriumhexaboride is prepared by reaction of $\text{Y}_2\text{O}_3 + 15\text{B} \rightarrow 2\text{YB}_6 + 3\text{BO}$ at temperatures between 1900-2000 K /3/.

As starting material amorphous boron-powder with 97 % purity and yttrium-oxide-powder with 99,98 % purity and a grain < 100 mesh was used.

The primary handling of the material is important for successful sample preparation. Since the powder mixture tends to become lumpy and thus inhomogeneous, it was repetitively mixed and pressed through a fine sieve.

The powder is then pressed to rods with a diameter of 10 mm.

The result is very sensitive on sample dimensions and density. The pressure with which the homogeneously mixed sample is prepared was found to be an important parameter. We found it to be favourable that the sample is pressed with a pressure not higher than $2 \cdot 10^5$ Pa in order to make it possible for BO to escape easily from the heated sample later on.

The pressed powder rods were placed in a tungsten crucible which was lined with a thin tantalum sheet, and heated in an RF-furnace under vacuum. The best results from a series of variations in temperatures and pressures are given in table 1.

The superconductive transition temperature of our samples lies between 4.7 and 6.1 K, where the best samples are purely single phase after a thin layer is scraped from their outside.

Table 1

Powder Sample			Reacted Sample					
Pressure [Pa]	Thickness [mm]	Weight before	[g] after	React.Temp. [K]	React.Time [min]	Pressure [Pa]	T _c [K]	% YB ₆ phase
2·10 ⁵	3	1.000	0.713	1900	30		5.7	> 95
2·10 ⁵	1.5	0.509	0.356	1900	30		6.1	> 97
2·10 ⁵	3	0.994	0.719	1900	15		5.0	≈ 90
2·10 ⁵	1.5	0.543	0.393	1900	15		5.6	≈ 90

References

- /1/ F. Gompf, Progr. Rep. IAK I, KfK 2670, 17 (1978)
- /2/ A.J. Arko, G. Crabtree, J.B. Ketterson, F.M. Mueller, P.F. Walch, C.R. Windmiller, Z. Fisk, R.F. Hoyt, A.C. Mota, R. Viswanathan, D.E. Ellism, A.J. Freeman, and J. Rath, Int. J. Quantum Chem. Symp. 9, 569 (1975)
- /3/ R.M. Manelis et al., Sov. Powder Metall. and Metal Ceramics 43, 904 (1960)

4.28 Mean Free Path of Electrons in Rhenium Films

A. ul Haq and O. Meyer

When the thickness t of a metal film becomes comparable in magnitude with the mean free path l of electrons the film boundaries impose a geometrical limitation called size effect on the motion of conduction electrons. This effect is discussed in the literature /1/ and the relevant equations describing the resistivity ρ_F of the film for the limiting cases are given as under /1/:

$$\text{for } \gamma = (t/l) \geq 1: \quad \rho_F = \rho_B + \{3\rho_B \cdot (1-P)\} / 8\gamma \quad (1)$$

$$\text{and for } \gamma \ll 1, P < 1: \quad (\rho_F t)^{-1} = (0.75/l \cdot \rho_B) \cdot \{(1+P)/(1-P)\} \cdot \{(\ln l + 0.4228) - \ln t\} \quad (2)$$

where P is defined as the fraction of electrons scattered elastically from the boundaries ($P = 0$ for complete diffuse scattering) and ρ_B is the resistivity of the bulk material at RT. Following the procedures described in /1/ we have determined l values for single crystalline Re films.

Re was evaporated in UHV onto heated polished single crystal sapphire at substrate temperatures of 1300 K (which was measured at the Mo substrate holder)

with a constant evaporation rate of $3 \text{ \AA}/\text{sec}$. Film thickness, homogeneity and impurity content were analysed by Rutherford backscattering of $2 \text{ MeV } ^4\text{He}$ ions. The resistivities of films at room temperature (300 K) and liquid He temperature (4.2 K) were measured by the standard four point method. We have prepared 20 single crystalline films under the conditions mentioned above, in the range of $190 - 850 \text{ \AA}$ with a residual resistivity ratio of 2 - 15. The measured resistivities at 300 K and 4.2 K as a function of film thickness are presented in Fig. 1a and 1b, respectively.

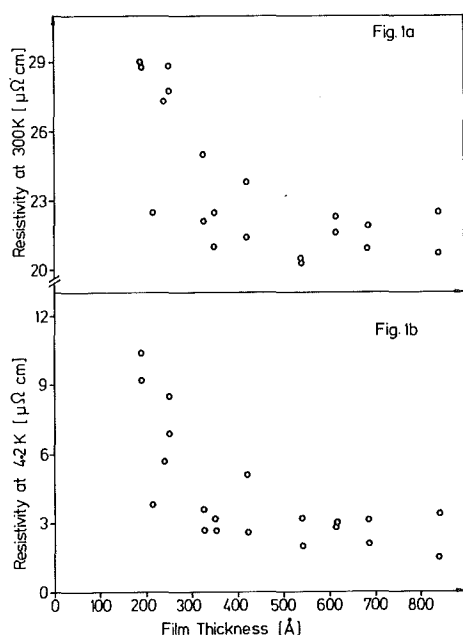


Fig. 1
Film resistivities as a function of film thickness

For film thicknesses $t \leq 500 \text{ \AA}$ the resistivities at room temperature deviate from the resistivity of the bulk material. Since the product ρ_B is temperature independent, one would estimate from our measured resistivities a value of $l = 12000 \text{ \AA}$ at 4.2 K. The deviations in ρ_F from the constant value of measured resistivities, however occur at $t \approx 300 \text{ \AA}$ indicating that P is close to 1. For $P=1$, the size effect would disappear.

Equation (1) can only be applied successfully for RT data, which gave a value of $\rho_B = 18.4 \pm 1 \mu\Omega\text{cm}$, showing a good agreement with the literature values /2/ and the product $l \cdot (1-P) = 269 \pm 31$. To get an idea for the value of P , equation (2) was applied on this data and $P=0.5$ and $l = 943 \pm 260 \text{ \AA}$ was estimated. Using this value of $P=0.5$, equation (1) gave $l = 538 \pm 62 \text{ \AA}$ which is also in agreement with Fig. 1a.

Fitting the equation (2) for the low temperature data shown in Fig. 1b, we get $l(4.2 \text{ K}) = 62240 \pm 270 \text{ \AA}$ and $P = 0.989$. This value of l is larger by a factor of 5 compared to the value of l determined from $P \cdot l$ (as given above). However, it is in a good agreement with the results of Schreiber /2/ who calculated $l \approx 34000$ to 55000 \AA from measured resistivity ratios for bulk Re.

References

- /1/ H. Mayer, Physik der dünnen Schichten, Wissenschaftliche Verlagsgesellschaft, Stuttgart (1955), K.L. Chopra, Thin Film Phenomena, McGraw-Hill Book Co., New York (1969)
- /2/ R. Schreiber, Ph. D. Thesis, Rice University (1974)

4.29 Disorder Analysis in Argon Implanted Rhenium Single Crystals

E. Friedland^a, A.ul Haq, and M. Kraatz

^a*Department of Physics, University of Pretoria, South Africa*

Backscattering and channeling of energetic ions has widely been used as a tool for the detection of disorder in implanted and irradiated single crystalline targets /1/. The dependence of the dechanneling cross section on the analysing beam energy can be used for the determination of defect structures /2/. Here we report our results from energy dependent channeling measurements in Re single crystals implanted with Ar ions at 720 KeV. It was very difficult to prepare the surface of the Re crystals in such a way so that it can be used directly for channeling. After the usual treatments as polishing the crystals did not show any channeling effect. The crystals were then annealed at different temperatures up to 1700°C and were found to be useful for channeling in the regions of two to three mm in diameter.

The sample has been implanted with 10^{13} , 10^{14} , 10^{15} , 10^{16} , and $4 \cdot 10^{16}$ Ar⁺⁺/cm² at 720 KeV and channeling measurements have been performed after each implant with the analysing ⁴He beam energy in the range of 1 to 2.5 MeV. The energy spectra using a two MeV He beam are shown in Fig. 1. Within 400 Å from the surface, a damage peak is formed and the peak area is seen to increase with increasing Ar fluence. At depth below 400 Å in the region of implanted Ar ions (with a mean projected range of 1800 Å) an increase of the dechanneling rate $d\chi/dz$ is observed for the fluences above 10^{15} Ar⁺⁺/cm².

The dependence of the dechanneling rate on the beam energy was measured for fluences

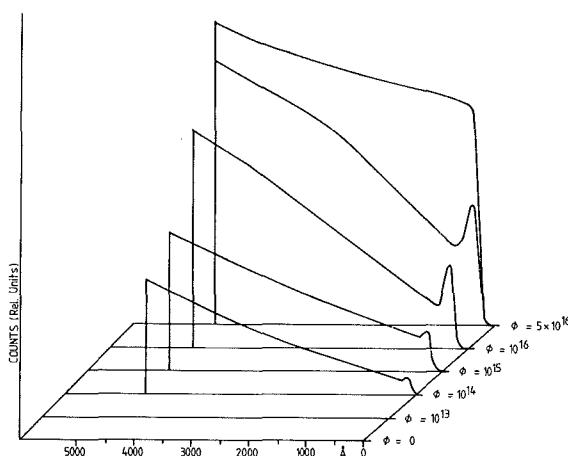


Fig. 1
Aligned and random spectra for backscattering from Re single crystal implanted at RT with various doses of 720 KeV Ar⁺⁺ions.

of 10^{15} , 10^{16} , and $5 \cdot 10^{16}$ $\text{Ar}^{++}/\text{cm}^2$ in the region between 600 and 1800 Å and was found to be independent of the beam energy. The surface damage peak, however, was found to increase with the square root of the beam energy. From these observed energy dependences one may conclude that the surface peak is due to Re atoms, randomly displaced from their lattice sites and possibly stabilized by impurities, whereas the dechanneling in the region below the surface peak (400 - 2000 Å) may be caused by stacking faults.

The sample was annealed in the following annealing sequence: 1 hour at 800°C , 2 hours at 800°C , 1 hour at 1000°C , and 10 min at 1720°C . After each annealing step backscattering spectra were taken and the results are

shown in Fig. 2. After annealing at 800°C the surface peak is reduced by 66 % while annealing at 1000°C did not cause any change. The surface damage peak disappeared completely after annealing at 1720°C , however, no change in the dechanneling rate due to stacking faults is observed.

References

- /1/ J.W. Mayer, L. Eriksson, and J.A. Davies, Ion Implantation in Semiconductors, Academic Press, New York, (1970)
- /2/ Y. Quéré, Phys. Status Solidi 30, 713 (1968)

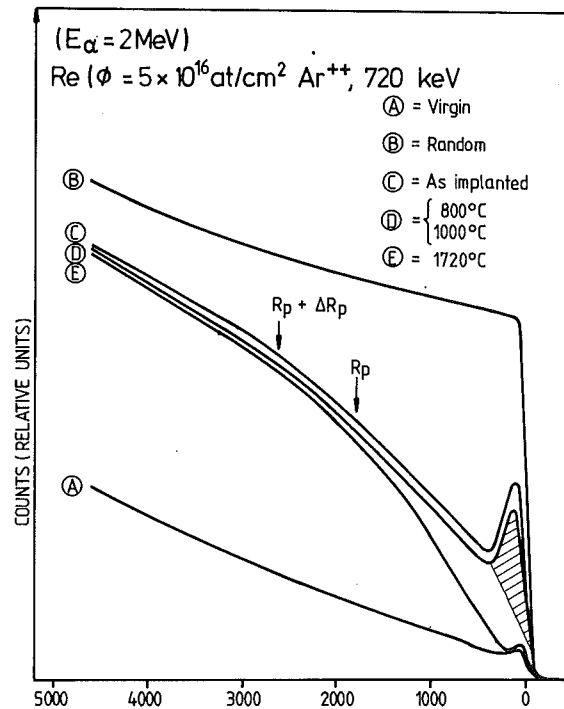


Fig. 2
 Effect of annealing on the aligned spectra of Re single crystal implanted at RT with $5 \cdot 10^{16} \text{at}/\text{cm}^2 \text{Ar}^{++}$ (720 KeV).

4.30 Rhenium Nitride Formation by Nitrogen Implantation in Rhenium

A. ul Haq, O. Meyer, and M. Kraatz

The solubility of nitrogen in rhenium at room temperature and above 400°C is very small. Hahn and Konrad /1/ have succeeded in obtaining a face centered cubic rhenium nitride ($a=3.9 \text{ \AA}$), $\text{ReN}_{0.43}$ by reaction of Ammonia with NH_4ReO_4 or ReCl_3 at $300 - 350^{\circ}\text{C}$. Matthias and Zachariasen /2/ have measured the superconducting transition temperature T_c of $\text{ReN}_{0.43}$ between 4 - 5 K, and crystallite sizes in the range of 20 - 26 \AA from the x-ray line broadening.

We have prepared rhenium nitride through homogeneous implantation of nitrogen (using three different energies 50 KeV, 110 KeV and 300 KeV, calculated /3/ from L.S.S theory /4/) in rhenium thin layers (thickness $\approx 1900 - 2100 \text{ \AA}$) at various substrate temperatures. After each implantation the resistivity ρ , residual resistivity ρ_0 , T_c , lattice parameters a , c , and stress in films was measured. T_c was measured resistively, lattice parameters a and c were calculated using Seeman-Bohling geometry for x-ray diffraction powder method and information about stresses in films have been obtained by a modified method of Feder and Berry /5/.

Fig. 1 shows the changes in $\Delta\rho_0 (= \rho_0^{\text{Impl}} - \rho_0^{\text{Unimpl}})$ and T_c as a function of at% of N^+ in rhenium. Up to 5 at% N^+ , the increase in $\Delta\rho_0$ is accompanied with an increase of the cell volume, T_c and stress. At 9 at% N^+ , a 10 times increase in stress is observed which is accompanied with the appearance of some new x-ray lines in addition to the well known lines from Re. These lines do not belong to the known cubic rhenium nitride $\text{ReN}_{0.43}$. This may be a new superconducting rhenium nitride whose structure has not been established until now.

Similarly at 41 at% N, the increase in stress is related with the formation of cubic face centered rhenium nitride, $\text{ReN}_{0.43}$. Homogeneous Ar^+ implantation using three different energies shows that the increase in ρ_0 which is due to defects and chemically inactive impurities is about $40 \mu\Omega\text{cm}$ at 35 at% of Ar^+ . As

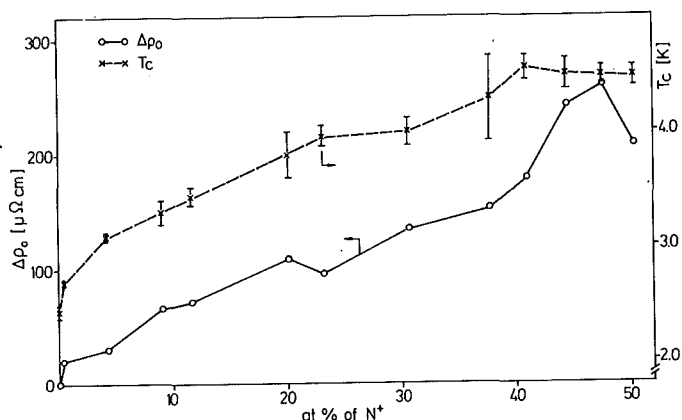


Fig. 1
 $\Delta\rho_0$ and T_c as a function of at% N^+ in Re-film

such the increase in ρ_0 after nitrogen implantation may be due to the appearance of new Re-nitride phases. The T_c at 9 at% N^+ is 3.2 - 3.4 K and at 42 at% N^+ , T_c is 4.4 - 4.6 K. The increase of stress in the Re layer may facilitate the formation of the rhenium nitride phases.

In further experiments 6 -12 at% N^+ was implanted at 500 K, 300 K, and 78 K. At 500 K no indications of rhenium-nitride phase are observed. However, at 300 K and 78 K extra lines related to new rhenium nitride phase are observed which is in agreement with the above mentioned results. After implantation at 78 K a T_c value of 3.6 - 4.0 K is observed which is slightly higher than the value observed for the room temperature implantation.

References

- /1/ Hahn and A. Konrad, Z. anorg. Allgm. chem. 264, 178 (1951)
- /2/ B.T. Matthias and W.H. Zachariasen, J. Phys. & Chem. of Solids 7, 98 (1958)
- /3/ G. Linker, Progr. Rep. IAK I, KfK 2357, 86 (1976)
- /4/ J. Linhard, M. Scharff, H.E. Schiott, Mat. Fys. Medd. Dan. Vid. Selsk. 33, 4 (1961)
- /5/ R. Feder and B.S. Berry, J. Appl. Cryst. 3, 372 (1970)

4.31 Transport Properties, Electronic Density of States and T_c in Disordered A15 Compounds

P. Müller^a, G. Ischenko^a, H. Adrian^a, J. Bieger^a, M. Lehmann^a, and E.L. Haase

^aPhysikalisches Institut der Universität Erlangen-Nürnberg, D-8520 Erlangen

Proc. 3rd Intern. Conf. on Superconductivity in d- and f-Band Metals, San Diego (1979): Academic Press, New York (1980), p. 369

Abstract

The emphasis of this work is the investigation of the effects of defects in order to check the idea of universal behavior of A15 Compounds (J.M. Poate et al., 1975, A.R. Sweedler, 1978, G. Ischenko et al., 1978) and their transition into the metallic glass phase at high degrees of disorder. The main point of interest is not

the study of defect structures, but the well defined variation of sample parameters by the irradiation induced defects as a continuous sample preparation procedure of the same sample. Because of the high Rutherford dislocation cross section, fast heavy ions are the best tool to achieve this within a short irradiation time.

4.32 Changes of Superconducting Properties and Electrical Resistivity of Amorphous Compounds by Means of Low Temperature Heavy Ion Irradiation

J. Bieger^a, G. Saemann-Ischenko^a, H. Adrian^a, M. Lehmann^a, P. Müller^a,
L. Söldner^a, E.L. Haase, and C.C. Tsuei^b

^aPhysikalisches Institut der Universität Erlangen-Nürnberg, Western Germany

^bIBM Thomas J. Watson Research Center, Yorktown Heights, New York

Proc. of the Nato Advanced Study Institute on Liquid and Amorphous Metals, Zwiesel, Germany, September 1979, to be published

Abstract

Thin films of Nb₈₀Si₂₀ and Nb₇₅Ge₂₅ were irradiated ($T_{irr} \leq 20$ K) with 20 MeV sulphur ions up to fluences of 10^{16} cm⁻² and subsequently annealed up to room temperature. Irradiation enhances T_C by about 0.5 K. In the case of Nb₇₅Ge₂₅ ρ decreases by 1.5 % and dH_{C2}/dT by 15 %. Annealing at room temperature nearly restores the initial values of T_C and ρ . The dH_{C2}/dT vs. T_C curves for irradiation and annealing are almost identical for weakly irradiated samples, whereas a pronounced difference is observed after high dose irradiation. Comparison is made with heavy ion irradiation of crystalline A15 - Nb₃Ge.

4.33 Single Crystal Preparation of TiN, ZrN, HfN, VN, and NbN by Chemical Vapor Deposition

H.-J. Schmidt and Th. Wolf

Superconducting single crystals of 4a nitrides TiN, ZrN, HfN, and 5a nitrides VN, NbN have been prepared using the chemical vapor deposition (CVD) process. The reaction follows the universal equation $\text{MeCl}_x + \frac{1}{2} \text{N}_2 + \frac{x}{2} \text{H}_2 \xrightarrow{T} \text{MeN} + x \text{HCl}$. Small amounts (<1ppm) of oxygen and humidity affect:

1. the deposition process (e.g. crystal growth).
2. the vaporization of the halogenides due to the formation of various oxides or oxihalogenides with lower vapor pressures and
3. the properties of the products (superconducting transition temperature T_c , etc.)

In the case of liquid TiCl_4 the experimental design previously reported was used /1/. In the vaporization process of liquid VCl_4 disproportionation and formation of oxides was observed. A gas cleaning system was fitted therefore between the carrier gas (H_2 and N_2) and VCl_4 vaporizer to avoid oxygen and water contaminants.

The solid ZrCl_4 , HfCl_4 , and NbCl_5 was vaporized directly in the reaction tube in front of the r.f. heated molybdenum susceptor. The halogenides were heated with a temperature controlled oil filled outer tube.

The reaction tube was filled with the molybdenum susceptor and in the case of solids halogenides with the halogenides in a glove box with 6n argon atmosphere.

The CVD parameters, the superconducting transition temperatures measured inductively, and typical lattice parameters are listed in the following table.

Because of the coexistence of different Me-N-compounds in a narrow temperature range /2/ the deposition temperature of VN and NbN was carefully controlled.

In the system N-N needles of the fcc δ -phase with a maximum length of 2 mm have been obtained. In the system Nb-N the gray non-superconducting ϵ -phase has been obtained at temperatures below 1570 K.

Substrate	Gas flow of (N ₂ , H ₂) [l/h]	Vaporization temperature [K]	Deposition temperature [K]	T _c [K]	ΔT _c [K]	Lattice parameter [Å]
TiN	2	293-295	1470-2270	6,0	0,04	4,2400±0,0005
ZrN	2	494	2070	10,55	0,15	4,5786±0,0008
HfN	2	489	1770	7,0	0,3	4,522 ±0,002
VN	3-10	323-353	1470-1570	9,7	0,2	4,133 ±0,004
NbN	6-10	353-403	1570-1670	15,2	0,3	4,383 ±0,002

References

/1/ C. Politis, Th. Wolf, H. Schneider, Proc. of the Intern. Conf. on Chemical Vapor Deposition, 1979

/2/ R. Kieffer, D. Fister, E. Heidler, Metall 26, 128 (1972)

4.34 Determination of Stresses in Materials by Neutron Diffraction

L. Pintschovius and V. Jung

Most materials of technical use contain considerable stresses as a result of rapid cooling and/or cold working. These stresses are superposed to those produced by a load and therefore often restrict the strength of a work-piece. A common method for the investigation of stresses is based on the determination of the associated strains by high precision measurements of d-spacings by x-ray diffraction. However, this method has an important drawback caused by the small penetration depth of x-rays: Stresses can be investigated at the surface only. This restriction can be overcome by successive etching of the sample. However, etching of surface layers can lead to uncalculable changes of the stresses and, of course, it is a destructive method.

Another way to avoid the shortcoming mentioned above is the use of neutrons instead of x-rays: Neutrons can penetrate more than 10 mm of steel or 50 mm of aluminium. However, this advantage has to be paid for by severe drawbacks: (i) The intensity of available neutron sources is much lower than those of x-ray sources.

This is of particular importance in our case because the need for a good resolution in real space does not allow to use the full-size of the neutron beam. (ii) The resolution of conventional neutron diffractometers is inferior to those of x-ray diffractometers. (iii) Neutron beam time is much more expensive than x-ray beam time.

To explore the capability of neutron diffraction for the investigation of stresses in spite of the inherent drawbacks we used the set-up outlined in Fig. 1: The neutron beam hitting the sample is confined by a diaphragm just before it to dimensions of 1.30 mm^2 . Likewise the scattered neutrons can reach the detector only by passing through a diaphragm of identical width. The volume actually probed by the neutrons is given as intersection of the incoming and the outgoing beam. Thus the diaphragms control the resolution in real space. To investigate the whole sample it has to be shifted and/or rotated while the diaphragms are kept fixed. In conventional diffractometers scans are performed at constant wavelength by varying the scattering angles θ and 2θ . In our case this would cause small shifts of the probed volume during the scan. In order to avoid such shifts, θ and 2θ have to be kept fixed and instead of it the neutron wavelength has to be varied. For that purpose we used a triple-axis spectrometer instead of a conventional powder diffractometer which has the additional advantage that the background is greatly reduced by the analyzer system.

For first tests the sample consisted of a sandwich of aluminium and copper sheets. Later we investigated a steel cylinder the surface of which was hardened by a heat treatment, and a plate of aluminium stressed by a bending device. The performance achieved at the R6 spectrometer at the FR2 Karlsruhe can be characterized by the figures listed in table 1. The experimental accuracy

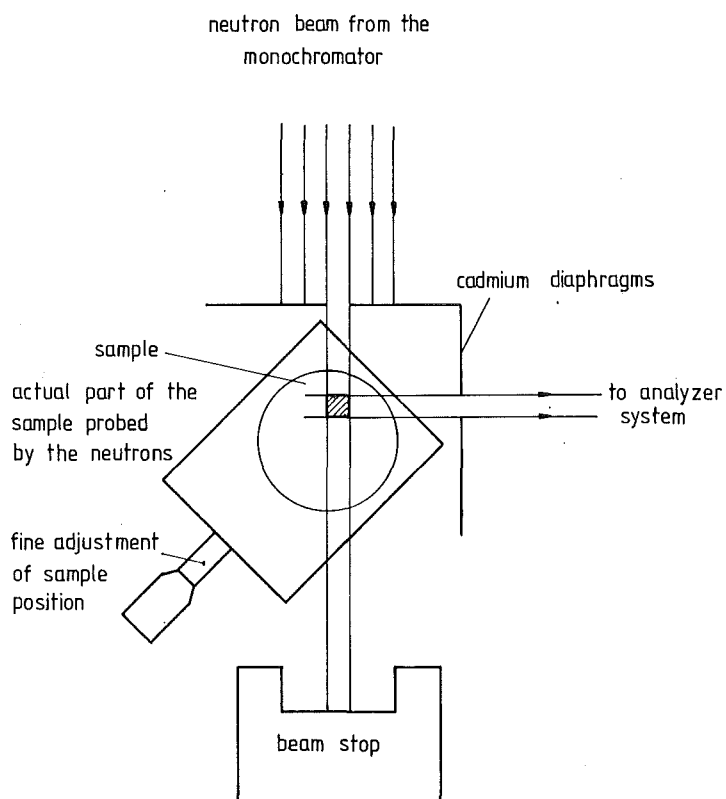


Fig. 1

Set up to determine stresses in materials by neutron diffraction.

$\frac{\Delta d}{d} \approx 1 \cdot 10^{-4}$ gives the lower limit of strains and hence of stresses to be detectable by our method. This value is larger by a factor of about two than that of the x-ray diffraction technique.

Table 1

resolution in real space	:	$1 \cdot 1 \cdot 30 \text{ mm}^3$
linewidth (FWHM) for an unstressed sample	:	$\frac{\Delta d}{d} < 6 \cdot 10^{-3}$
standard deviation of d-spacings	:	$\frac{\Delta d}{d} \approx 1 \cdot 10^{-4}$
maximum penetration depth		
for steel	:	$\approx 10 \text{ mm}$
for aluminium	:	$\approx 50 \text{ mm}$

4.35 Investigation of Stress Induced Phase Transformations in Unstabilized Cr-Ni Steel by the Neutron Diffraction Technique

V. Jung

Phase transformations in stressed Cr-Ni steels as a consequence of swaging and rolling treatment, respectively, were studied in great detail by Bowkett and Harries /1/, mainly by means of x-ray diffraction. In their investigations texture effects have been taken into account by the technique developed by Miller /2/, however, the authors had not performed texture measurements intended to explain the transformation process between the three fcc, hcp, and bcc phases. X-ray diffraction studies on steel samples have the disadvantage of being able to furnish information about phase compositions only up to a material depth of about 30 μm . It was evident that the phase composition to a depth of 7 μm differed greatly from that extending down to 30 μm . Hence, the desire to be able to determine the integral phase composition of bulk specimens. However, this information about the mean phase contributions, averaged over certain specimen volumes being of technical interest, can be obtained only by means of neutron diffraction. This technique also provides valid information with respect to texture for compact volumes.

To transform the fcc structure into a hcp structure not important swaging stresses are necessary because the (111) layers, ABCABC, of the fcc structure are preserved in pairs and slip on each other by 1.46 \AA only in the AB, CA, BC, AB ... groupings /3/. The newly formed hcp structure shows the sequence of ABABAB ... in the [001] direction of the hexagonal lattice, i.e., of the original ABCABC stratification, A and B are transformed into themselves, $C \rightarrow A$, $A \rightarrow B$, $B \rightarrow A$, $C \rightarrow B$, and $A \rightarrow A$ and $B \rightarrow B$. The transformation from the hcp phase has been described by Manganon jr. /4/ and D.S. Lieberman /5/. Renewed sliding of the now individual ABAB ... layers against each other, and simultaneous compaction and elongation, respectively, of all layers to the same extent and in the same direction generates the new bcc structure. The planes produced in this way are indexed (110)-bcc. If the crystallite orientation remains unchanged after each transformation, the three (111)-fcc, (001)-hcp, and (110)-bcc directions were parallel to each other.

Cylindrical specimens of unstabilized 18/8 Cr-Ni steel (0.5 inch ϕ , 4 inch long) were annealed for half an hour at 1050°C and cooled to room temperature for about 12 hours. After this treatment the fcc-specimens were completely free from any texture and without any admixtures of other phases. These specimens were swaged by 2 %; 12.5; 25 % and 47 %. This procedure was performed slowly in order to prevent falsifications of the phase transformation rates from being produced by excessive heating. In order to obtain the fcc, hcp, and bcc phase contributions of these four specimens as a function of the swaging rate in a quantitative way, the (111)-fcc, (101)-hcp, and (110)-bcc reflexes were studied with respect to their intensity ratios for each of these specimens. The respective (111)-fcc, (101)-hcp, and (110)-bcc plane distances hardly differ from each other. For satisfactory separation in the 2θ distribution of these reflexes a neutron wavelength of 3.3 \AA was used. For the first measurement the axis of the specimen (= swaging axis) was always normal to the scattering plane. This means that scattered neutrons will impinge only from those planes ((111)-fcc, (101)-hcp, and (110)-bcc), which are located parallel to the axis of stress. The phase contributions, which are still falsified by texture effects, are shown in Fig. 1. In this diagram the measured result obtained from a specimen of stacked metal sheets made of the same material is plotted, which clearly differs from the results of the other samples because, unlike the cylindrical specimens, texture effects were taken into account in this case.

As a result of swaging and rolling, respectively, the materials so treated exhibit a texture which falsifies the quantitative evaluation of the phase contri-

butions. In addition, phase transformations occur first and preferably at those points where shear stresses parallel to (111)-fcc planes are maximum. Accordingly, texture is generated by two reasons: (1) texture by rolling or swaging without phase transformation effects, (2) texture by phase transformations under preferred angles relative to the direction of swaging, so that the orientation distribution of an original isotropic specimen is distorted. In order to examine these processes in more detail, one-dimensional texture distributions were recorded (ω scans) for all specimens at the (111)-fcc, (101)-hcp, and (110)-bcc reflexes. This was done under the assumption that the cylindrical specimens, for the very reason of their being cylindrical, also exhibit rotational symmetry with respect to texture. This assumption turns false as soon as strain figures emerge on the periphery of the cylinder and the reflex intensity varies on the azimuth at constant ω .

To study textures, the cylinder axes of the specimens were put in the scattering plane and turned around the spectrometer axis in 2.5° steps in the region between $-\pi/2 < \omega < \pi/2$. The neutron detector was always focussed to the maximum of the respective reflex. Fig. 2 shows the results of the ω -scans for the (111)-fcc reflex obtained from the four specimens with 2%; 12.5%; 25%, and 47% swaging. It is striking to note that 2% swaging causes major textures immediately, but with isotropic contributions. Also the distribution of textures around the stress direction ($\omega=0$) is relatively wide. With increasing swaging, the distribution becomes narrower, the isotropic fraction decreasing until, at 47% swaging, shortly before the rupture limit, the isotropic fraction has almost disappeared and the distribution around the

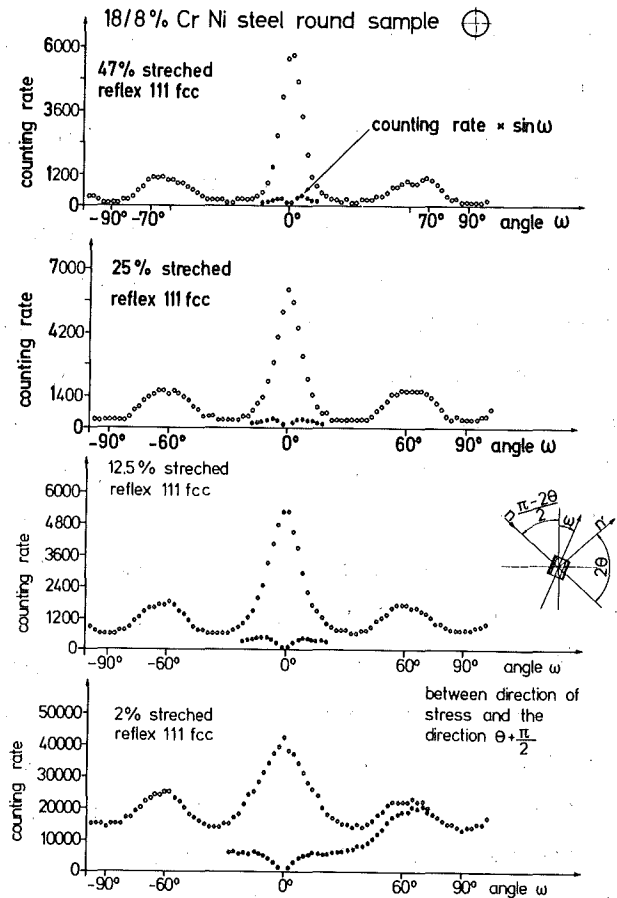


Fig. 2
Peak intensities of the reflex (111)-fcc depending on the angle ω between the direction of stress and the scattering vector for 4 stretching values.

stress- (0° -) direction has a half width of approx. 10° . This means that mainly those areas of the fcc phase have remained untransformed, whose (111)-fcc planes are about normal to the direction of tension and, for this reason, are subject to extremely low shear forces. At $\omega = \pm 70.5^\circ$, the angle to the next (111)-fcc plane, two other peaks are formed, which are slightly broader. For quantitative determination of the relative probability of alignment over the two-dimensional pole figure it is necessary to multiply the one-dimensional distribution by $\sin \omega$. This is indicated by the solid black dots in Fig. 2. For average formation the intensity distribution multiplied by $\sin \omega$ must be integrated over $\Delta\omega$ within the limits of $\pi/2 < \omega < \pi/2$. These averages then must still be corrected with the 2θ half widths of the individual reflexes, because the half width grows with increasing swaging. Obviously, the swaging process causes coarsely crystalline areas to be broken down into more finely crystalline ones.

The values thus obtained for the phase contributions and corrected for texture effects are shown in Fig. 3 together with the results of the specimen of stacked metal sheets already shown in Fig. 1 beside. Now agreement is found be-

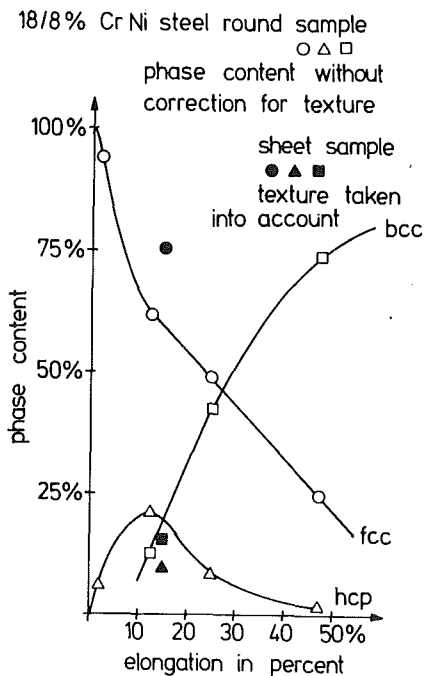


Fig. 1
Phase content without correction for texture (stress direction vertical to the scattering plane). For the sheet sample texture effects are taken into account.

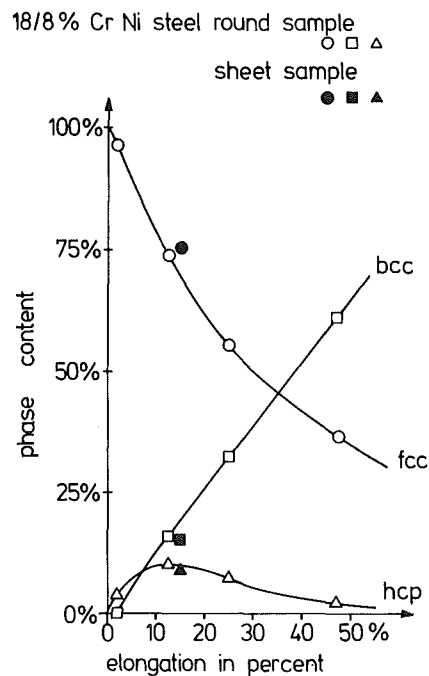


Fig. 3
Phase content in dependence of elongation for cylindric and sheet samples, texture effect are taken into account for all specimens.

tween the results obtained on the cylindrical specimens and the specimen of stacked metal sheets, because now texture effects were taken into account in all specimens. If, in addition, the fact is taken into account that rolling not only causes elongation, but also transverse spread, agreement between cylindrical specimens and stacked specimens is even more convincing. It is evident from the result in Fig. 1 and 3 that only measurements corrected for texture will produce the correct phase contributions. ω scan measurement is indispensable whenever texture effects are to be taken into account.

References

- /1/ M.W. Bowkett and D. Haries; Martensitic Transformations in Cold Rolled En 58 B (Type 321) Austenitic Stainless Steel, AERE-R-9093, Harwell, April 1978
- /2/ R.L. Miller, Transactions of the ASM 61, 592 (1968)
- /3/ Z. Nishiyama, Martensitic Transformation, Academic Press, New York (1978) p.49
- /4/ Pat L. Manganon, jr. and Gareth Thomas, Metallurgical Transactions 1 1577 (1970)
- /5/ D.S. Lieberman, in Phase Transformations, Seminar of the American Society for Metals October 12 and 13, 1968, Metals Park, Ohio, p. 50

5. DATA PROCESSING

5.1 Interactive Function Minimization

W. Abel

An on-line general purpose least square fit program for the analysis of multichannel data has been developed. To process graphical information an IBM/2250-1 graphic display unit is used. The program was primarily written for the evaluation of inelastic magnetic scattering data. However, in order to make the program flexible enough to be easily applicable to related problems, the calling procedure of /1/ may still offer a suitable organizational framework. The non-linear least square fitting part is based on MINUIT/2/, a system of programs for function minimization. The usual approach is to fit a given shape function to a single or multiple peak by minimizing the weighted sum of residuals. Different minimization methods are available which will be briefly outlined in the following.

1. A Monte Carlo search procedure /2/ which is more efficient than the other methods in many dimensions. This procedure may be used at the beginning of a fit or when no reasonable starting point is known.
2. A minimizing routine based on the simplex method of Nelder and Mead /3/, which is very "safe" and should work as well in non-quadratic as in quadratic regions of the shape of the function. It should be noted, that no derivatives of the function to be studied are required.
3. This method of the fit uses Fletchers "switching"/4/ variation of the original Davidon-Fletcher-Powell algorithm /5/. The gradient of the function may be either supplied by the user or estimated by the program. Whereas the simplex method only gives (good) estimates of the diagonal elements, here a full covariance matrix is produced.

The current version of the program is restricted to a maximum of 30 function parameters, of which not more than 15 may be variable. However, a re-dimensioning for larger problems is straightforward. Depending on the behavior of the function or user requirements parameters may be fixed or restored to the variable status between minimization steps by simply selecting an appropriate command

by light pen detect. Furthermore, the allowed values of one or more parameters may be limited to a certain range during the fit. Three kinds of analytical shape functions are provided to the user:

1. Gaussian function
2. Lorentzian function
3. Lines of Lorentzian shape viewed through an instrument, of which the resolution can be approximated by a Gaussian (Voigt profile).

A background continuum may be added as a constant function or higher order polynomial. Unfortunately, the evaluation of the Voigt integral is the dominating time consuming process. This disadvantage has been considerably reduced by writing the Voigt integral in terms of the complex error function /6/. Gautschi has given an algorithm for calculating this function for all arguments to a high accuracy using the method of continued fractions /7/. In case of a convolution the program accepts a resolution peak which is sited on the top of the Voigt profile and for which the height is left free in the fitting process.

For each fit a region in the spectrum must be specified by light pen detect. In this way, the user may vary the number of peaks involved in the current run. Several data corrections may be done before. After completion of a minimization step the final parameter values and their uncertainties together with the estimated distance to the minimum are displayed. Based on the covariance matrix, if it exists, global correlation coefficients are calculated and also displayed on the CRT screen.

References

- /1/ W. Abel, KFK 2481 (1977)
- /2/ F. James and M. Roos, Comput. Phys. Comm. 10, 343 (1975)
- /3/ J.A. Nelder and R. Mead, Comput. J. 7, 308 (1965)
- /4/ R. Fletcher, Comput. J. 13, 317 (1970)
- /5/ R. Fletcher and M.J.D. Powell, Comput. J. 6, 163 (1963)
- /6/ C.J. Batty, S.D. Hoath and B.L. Roberts, Nucl. Instrum. Methods 137, 179 (1976)
- /7/ W. Gautschi, S.I.A.M. J. Numer. Anal. 12, 635 (1969)

5.2 Variable Acceleration and Deceleration Profiles for Stepper Motors

G. Ehret, H. Hanak, and H. Sobiesiak

Most multi-axis-spectrometers are equipped with stepper motors in order to achieve a precise positioning of the desired angles.

Maintaining this high accuracy is difficult since highly variable weights, e.g. half a ton of additional shielding material, or an additional cryostat must be moved.

This results in a permanent shift of the start-stop limit of frequency of the stepper motors. A good stepper motor control must guarantee that the motor exactly executes the number of steps desired. It also must allow to change the acceleration or deceleration ramp in the case that the feed-back (normally via a digitizer) has detected, that the positioning is no longer exact. Thus the feed-back is not actively used, as it would be necessary in a control showing the characteristics of a dc-motor drive: The feed-back is pushed here to the secondary or security level.

We tried to solve the problem very flexible, that is with a program. The following hardware is needed:

1. a computer (DATA GENERAL NOVA) equipped with a BASIC-interpreter-system,
2. a 16 bit output register, and
3. a pulse generator with programmable frequencies in the 1 to 10.kHz region, e.g. the system clock.

We used the following principle:

By subdividing the pulse train of the system clock we directly feed TTL-level into the power amplifier of the stepper motor via a 16 bit output register.

The frequency scheme for the acceleration or the deceleration is computed by the user's BASIC program. Thus the user can easily build any acceleration profile with any high frequency limit. He also is allowed to leave the start-stop-region of speed, pushing the stepper motor into the synchronous mode of rotation. The control always must execute exactly the number of steps desired.

Deceleration is done using the same curvature as for acceleration. Every motor has its own acceleration table, allowing individual moment for each. A 16 bit output register allows simultaneous control of 8 motors.

A problem in acceleration are short movements, where, in the highest slope of acceleration, the movement is switched over into deceleration. We have some

tricks for this case in the program, but it must be stated clearly that this type of movement limits the slope of the acceleration.

The program, written in assembler, is part of the BASIC interpreter-system. It can be used by four subroutine calls:

1. CALL MOTAB (N, FIELD)
 - N motor number $1 \leq N < 8$
 - FIELD table of acceleration
2. CALL MOTOR (N, STEPS)
 - N motor number
 - STEPS number of desired steps (may be positive or negative)
3. CALL MOTEST (X, FIELD)
 - X number of actually running motors
 - FIELD number of steps to be executed for each motor.
4. CALL MOSTOP (N)
 - N number of the motor which is to be forced into decelerating sequence

The system clock of the BASIC interpreter is switched from 10 Hz up to 8 kHz if any motor is to be run. Worst case condition for the system is if all eight motors are well synchronized to run at the highest speed. Even in this very improbable case the new assembler routines needs less than half of the CPU time, leaving enough time for the other control and surveillance purposes.

Reference

- /1/ G. Ehret, H. Hanak, H. Sobiesiak, Proc of the Studiengruppe für Nuklearelektronik p. 10, Bochum 24.-26.3.1980

5.3 A Time-of-Flight Unit for Spallation Source Investigation

G. Ehret, H. Hanak, and H. Sobiesiak

Specification of a time-of-flight unit required for spallation source investigation could not be met by one of two type of devices used in the IAK:

1. Dual ramp ADC for measurements in the keV region of neutron energy because its nonlinearity in time regions above microseconds.
2. Chain of flipflops used in thermal neutron scattering experiments because of their channel-width not below 0.5 microseconds.

We therefore designed a new device /1/ as a card directly pluggable into a NOVA computer. This unit has the following characteristics:

1. Channel-width of 100 up to 25600 nanoseconds with increments of 100 nanoseconds.
2. Able to accept one count per channel in each sweep, thus the highest instantaneous counting-rate is 10 MHz at smallest channel-width.
3. Long term stability is controlled by a quartz.
4. Four input pathes are available.

All software for the control and data manipulation of the device has been added to our BASIC interpreter system of the NOVA computers. This gives a very versatile and easy-to-change data acquisition and data handling facility.

The device has been used at CERN (Geneva), SIN (Villigen), and at SATURN (Saclay) to the following purposes:

1. Determination of the defocussing in a resonant cavity by the incoming pulsed beam of particles to be accelerated. Measurements were done by determination of the time-distribution of those neutrons knocked out of the wall of the cavity /2/.
2. Investigation of the neutron time structure in H₂O and D₂O moderator-reflector systems for an optimized spallation neutron source /3/.

References

- /1/ G. Ehret, H. Hanak, H. Sobiesiak, Proc. of the Studiengruppe für Nuklearelektronik, p. 4, Bochum 24.-26.3.1980
- /2/ S. Cierjacks, W. Kühn, to be published
- /3/ G.S. Bauer, W.E. Fischer, F. Gompf, M. Küchle, W. Reichardt, and H. Spitzer, to be published.

6. DEVELOPMENT OF INSTRUMENTS .

6.1 Fast Neutron Yields from Spallation Targets

F. Gompf and W. Reichardt

In the frame work of the feasibility study of a neutron spallation source we determined the angular dependence and the integral yields of fast neutrons for different target geometries and target materials. The measurements were carried out at the cyclotron of the SIN (Schweizerisches Institut für Nuklearforschung) with a proton beam of 590 MeV.

For these measurements we constructed a long counter (LC) which is shown in Fig. 1. The central BF_3 counter (20 inches active length, 1 inch diameter, depleted to 11% ^{10}B) is surrounded by a satellite BF_3 counters (4 inches active length, 1 inch diameter, enriched to 96% ^{10}B) which are placed at different depth (10, 15, 20, and 25 cm) in the polyethylene core of the LC. With the help of a 20th Century precision long counter (PLC) /1/ we calibrated our LC with monoenergetic neutrons up to 17 MeV at the Van-de-Graaff accelerator of our institute. As with increasing depth of the satellite counters their efficiencies approach a linear dependence on energy a rough estimate of the mean neutron energy \bar{E} can be obtained. A convenient

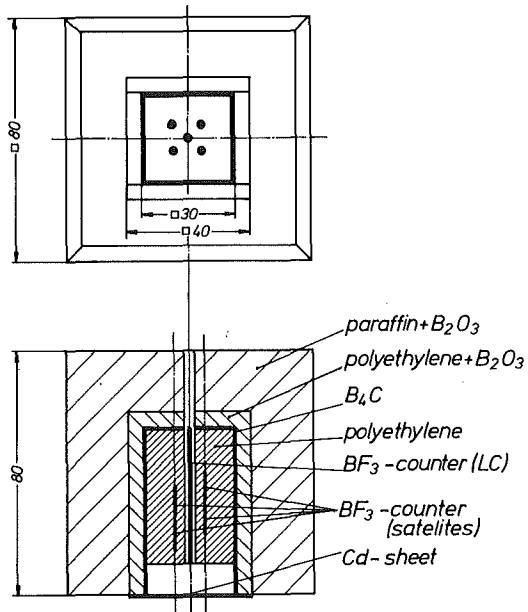


Fig. 1
Longcounter (dimensions in cm)

way to extract \bar{E} from the counting rates of the satellite counters is obtained by an extrapolation technique demonstrated in Fig. 2 for a fission spectrum $Q(E) = e^{-E} \sinh \sqrt{2}E$ with $\bar{E} = 3.25$ MeV.

The target materials tested were Pb, PbBi and U. Most measurements were carried out perpendicular to the proton beam in a distance of 2 meters. For the calculation of integrated fast neutron yields a number of targets were measured

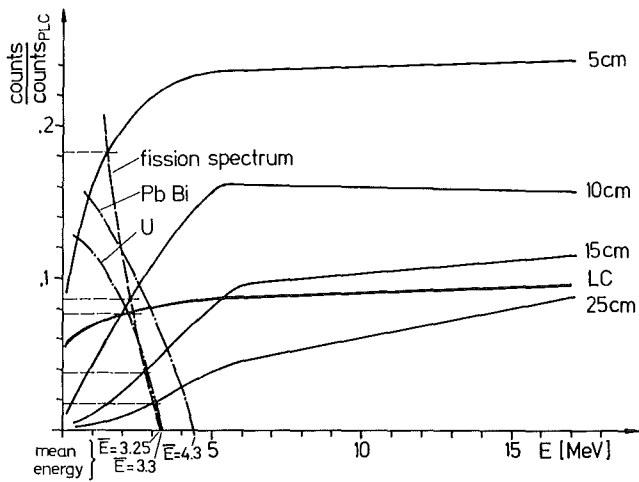


Fig. 2
Calibration curves for the longcounter and satellite counters (for explanation of \bar{E} values see text).

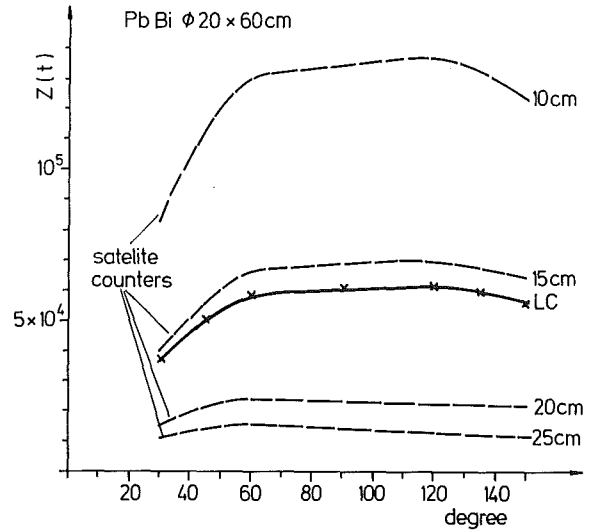


Fig. 3
Angular dependence of neutron intensities for a PbBi target

under 30° , 45° , 60° , 90° , 120° , 135° , and 150° . A typical example is shown in Fig. 3. If the intensities of the four satellite counters (dashed lines) are added up and divided by 4 (xx in Fig. 3) we nicely reproduce the angular dependence of the LC (solid line). For different target geometries some of the results are listed in Tab. 1 (for a more detailed description see /2/).

Table 1: Relative Intensities for different target geometries and target materials

	Target (dimensions in cm)	2m, 90 degree	integral
cylindrical	1. PbBi 20 ϕ x 60	<u>1</u>	<u>1</u>
	2. PbBi 15 ϕ x 60	.96	.97
	3. Pb 15 ϕ x 40	.96	
	4. U 15 ϕ x 30	1.95	1.88
plateshaped	b h l		
	5. Pb 10x 50x 60	1.46	
	6. Pb 10x 30x 60	1.23	
	7. Pb 10x 20x 60	1.16	
	8. U 10x 10x 30	1.75	
9. U 10x 30x 30	2.37		

As to be expected Pb and PbBi targets of the same geometry give identical (Target 2 / Target 3), while U is a factor of 2 better than Pb (Target 2 / Target 4 or Target 6 / Target 9). All other effects are rather small except the difference between target 8 and 9 which is caused by the size of the target with the larger part outside of the proton beam acting as a reflector.

The mean energy \bar{E} was extrapolated by the above mentioned method and roughly gave $\bar{E} = 4.3$ MeV for the PbBi target and 3.3 MeV for the U target. The shift of \bar{E} for Uranium towards smaller energies is caused by the "softer" fission spectrum which makes up about half of the intensity.

From the integrated intensities the number of fast neutrons Q_p per proton was calculated according to $Q_p = \frac{Z_{LC}}{Z_p} \cdot \frac{4\pi R_{eff}^2}{\eta_{LC}}$, with Z_{LC} being the counting rates of the LC and Z_p the number of protons per second, R_{eff}^2 the effective distance between the target and the LC (see /2/) and η_{LC} the efficiency of the LC. For the PbBi target (15 cm diameter, 60 cm long) we get $10.7^n/p$ and for the U target (15 cm diameter, 30 cm long) we get $20.6^n/p$. Since the neutron cross section become rather small above 50 MeV the LC is rather inefficient for neutrons above this energy. Therefore the numbers for the neutron yields do not include contributions from energies between 50 MeV and 600 MeV. The same refers to the data for the mean energies.

To study the influence of higher proton energies on these results, LC measurements have been carried out at SATURNE with 600, 800 and 1100 MeV. The evaluation of these data is underway and will be reported in the near future.

References

- /1/ G.P. Massand.; Central Bureau for Nuclear Measurements, Rep. No. Eur 4783e (1972)
- /2/ F. Gompf, W. Reichardt; unpublished paper

6.2 Moderator Studies for Spallation Targets

F. Gompf, W. Reichardt, M. Kühle^a, G. Bauer^b, and Spitzer^b

^aInstitut für Neutronenphysik und Reaktortechnik

^bInstitut für Festkörperforschung, Jülich

We report about measurements of the integrated thermal neutron flux J_{th} emanating from the surface of hydrogenous moderators at spallation targets. The experiments were performed at a 590 MeV proton beam of the SIN cyclotron and at the synchrotron SATURNE with proton energies of 600, 800 and 1100 MeV. Thermal neutrons were recorded by a "thin" BF_3 counter with $1/v$ sensitivity which was placed several meters from the moderator surface. The counter was heavily shielded by B_4C . In most cases a Cd frame defined a radiating surface of 10 cm x 10 cm. This area seems to be a reasonable choice with regard to a spallation neutron source.

In the course of our investigations the influence of a great number of parameters and configurations on the thermal neutron intensity was studied:

1. Proton energy (590, 800, 1100 MeV)
2. Material of the target (Pb, PbBi, Pb diluted by structural materials, U)
3. Shape of the target (cylinders, slabs in order to simulate a target wheel)
4. Position of moderator relative to the target (in particular SLAB-WING geometry)
5. Material of the moderator (CH_2 , H_2O)
6. Dimensions of the moderator
7. Influence of reflector (CH_2 , Be, Pb)
8. Influence of extraction channels (grid of holes or grooves in the moderator surface).

Experimental details and results of the measurements at SIN can be found in Ref. /1/. Results of the experiments at SATURNE will be described in a forthcoming report.

References

- /1/ F. Gompf and W. Reichardt; unpublished paper
- /2/ F. Gompf et al.; unpublished paper

6.3 On the Actual State of the 250 keV Electron-Energy-Loss Spectrometer

J. Fink, G. Crecelius^a, R. Manzke^a, P. Johnen^a, and F. Schmidt^a

^aInstitut für Festkörperforschung, KFA Jülich

In this contribution we report on the actual state of the construction of a 250 keV Electron Energy-Loss Spectrometer. The details of design and of electron optical calculations have been described in /1/ and /2/ already.

Fig. 1 shows a top view of the electron energy-loss spectrometer. The electrons emitted by a tungsten dispenser cathode (T) pass a spherical deflection monochromator (M). By a zoom lens (Z1) and an accelerator tube (AT) the electron beam is focussed onto the sample (S). Electrons scattered by a given scattering angle are deflected into the decelerating electrode (DT) and, after passing the zoom lenses (Z2), they are analyzed in energy by a spherical deflection analyzer (A) and detected by an electron multiplier (D).

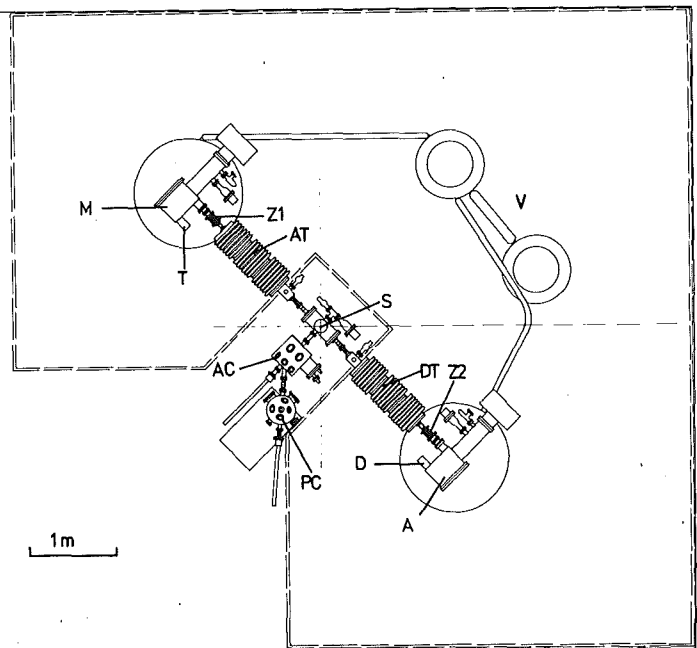


Fig. 1
Schematic drawing of the electron energy-loss spectrometer

Analyzer and monochromator are at 250 keV potential generated by the voltage supply (V) whereas the sample

is on ground potential. Thus it is possible to change sample under ultra high vacuum conditions. The samples are prepared in a preparation chamber (PC) by evaporation on thin carbon substrates. By a transfer mechanism the samples are transferred to an analyzing chamber (AC). The composition of the sample is analyzed by Auger spectroscopy and by ion surface scattering (inelastic Rutherford scattering). Contaminated surfaces can be cleaned by ion etching. After the analysis the samples are transferred by a transfer mechanism to the sample position in the electron energy-loss spectrometer (S).

The sample is located on a XYZ manipulator which is provided with a refrigerator and a heater assembly to vary the temperature of the sample between 20 and 900 K. The actual state of the electron energy-loss spectrometer is shown

in Fig. 2. In the foreground the chamber for the monochromator and electron optics as well as the ion pump for this chamber both mounted on insulating tubes can be seen. The electron optics will be tested after completion of the control electronics. The acceleration and deceleration tubes are not assembled until now. In the center of the picture the sample chamber (S) and in the background the housing for the analyzer can be seen.

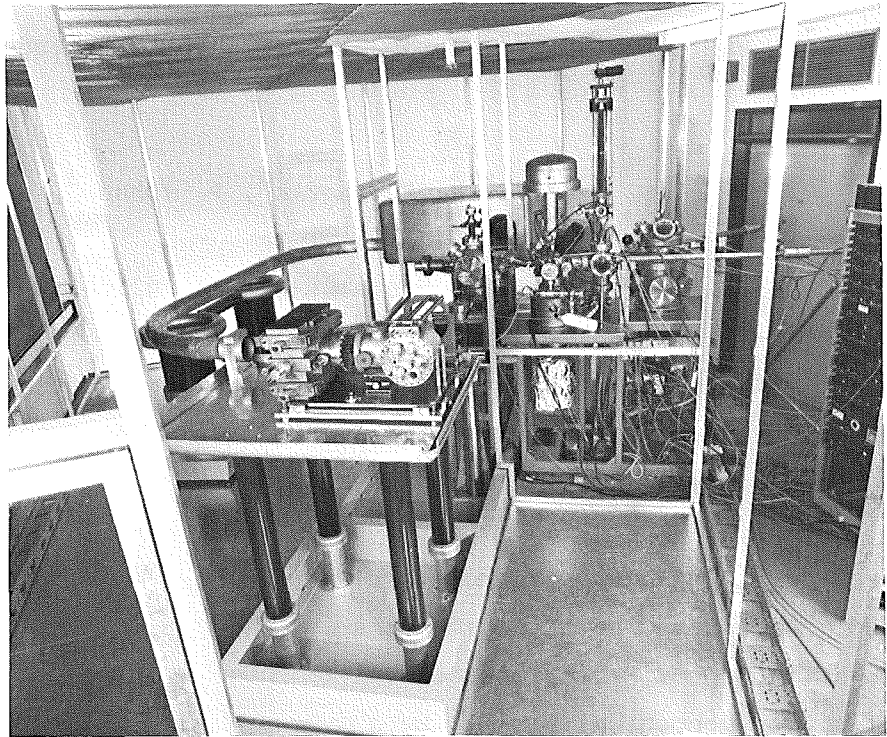


Fig. 2
Actual state of the electron energy-loss spectrometer

On the right the sample preparation chamber and the analyzing chamber both manufactured by Leybold-Heraeus is built up. The Auger spectrometer and the ion surface scattering equipment was tested on Cu and on AuAg samples.

References

- /1/ J. Fink, G. Crecelius, R. Manzke, P. Johnen, and F. Schmidt; Progr. Rep. IAK I, KFK 2881, 148 (1979)
- /2/ J. Fink and E. Kisker; Rev. Sci. Instrum., in press

6.4 A Low Temperature UHV Two-Axis-Goniometer for Channelling Experiments

R. Kaufmann and F. Ratzel

For temperature dependent channelling experiments a low-temperature goniometer working under UHV-conditions in the temperature range down to 10 K has been constructed. Therefore a He-cryostat was built as a two-axis-goniometer. One de-

degree of freedom for crystal rotation was obtained by tilting the whole cryostat insert which serves as a liquid-He-container about the vertical axis. This motion acts as the tilt angle in a channelling experiment. The other degree of freedom is the rotation of the sample about the beam axis which is performed by a UHV rotary feed through via a rod and a worm gear. The precision of the vertical rotation is $\pm 0.02^\circ$. The rotation about the beam axis fulfils the requirements of channelling measurements with a precision of $\pm 0.2^\circ$.

The cooling of the sample was attained with the help of a hollow Cu-block connected to the bottom of the liquid He vessel as shown in Fig.1. The inside of this block is partly filled with liquid He. In the lower part of this Cu block a UHV bearing is mounted to perform the rotation of the sample holder which is pressed against the Cu block to achieve a good thermal contact. To reduce the friction and to increase the thermal conduction a thin sheet of indium is put between the sample holder and the Cu block. The temperature is controlled by a germanium resistor at the side of the Cu block. This resistor has been calibrated with another resistor which for the calibration procedure was placed on the sample holder at the sample position in exactly the same manner as the sample during the measurement. Thermal screening is per-

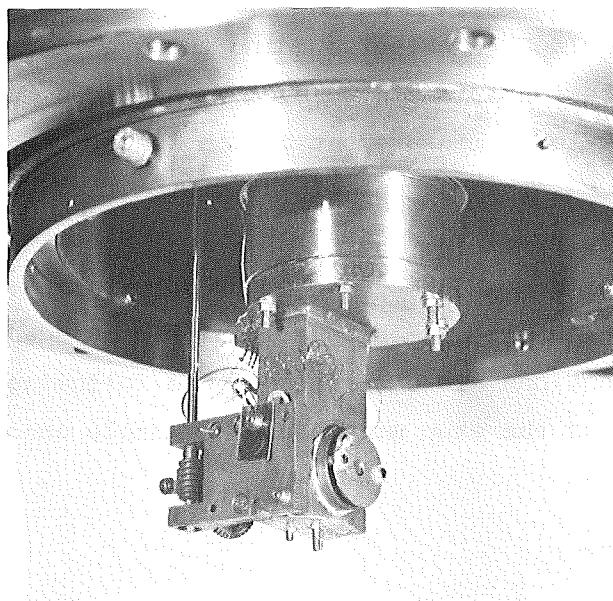


Fig. 1
Liquid He-vessel with the mechanism for the rotation about a direction normal to the sample surface.

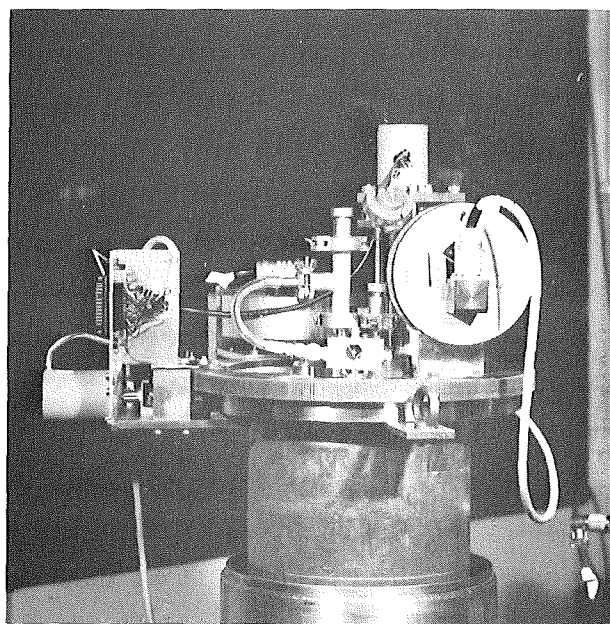


Fig. 2
Arrangement of the step motors and the angle encoders.

formed by a Cu cup mounted onto the He vessel and a second cup connected to the liquid N₂ tank surrounding the whole cryostat insert. Secondary electron suppression is achieved by a Faraday cup mounted to the He vessel. In order to allow for a measurement of the ion current the sample is electrically isolated.

The motions of the goniometer are controlled by a NOVA 3 minicomputer equipped with a CAMAC system. The rotations are performed by step motors controlled by CAMAC step motor drivers and the absolute positions are measured by angle encoders being multiplexed by a CAMAC input/output register. Software functions are described in the following contribution of this report. The set up of the step motors and the angle encoders is shown in Fig. 2.

6.5 A Program System for Computer-Controlled Channeling Measurements

R. Kaufmann

The existing on-line data processing system developed for measuring nuclear reaction and backscattering spectra at the Van-de-Graaff-accelerator /1/ has been modified and extended in order to perform computer controlled channelling measurements. The program system has been adapted to goniometers with a maximum of three axes driven by four phase step motors through CAMAC-step motor controllers as reported e.g. in /2/. The absolute position of the goniometer is indicated by angle encoders in the 13 bit-Petherick-code. This information is multiplexed and transferred to the computer via a CAMAC-input-/output-register. Computer control is performed by a NOVA 3 minicomputer with 128 KByte memory and two 10 MByte disk drives. For communication with the program system a Silent 700 ASR and a video terminal (with TV-display and light pen) and a single bit control unit are available.

Since the resolution of the angle encoders at the goniometer is less than necessary for channelling experiments counting of the steps of the motors between the encoder marks must still be used for exact positioning.

At the present time the following routines are available for control of a goniometer:

- I. Positioning via single bit switches and display of the actual position and spectrum on the TV-screen.
- II. Determination of the absolute position after adjustment with a laser beam.
- III. Positioning by input of a desired angle via teletype.
- IV. Routine for angular scans; parameters: angular increment, number of steps, number and values of energy windows. The measured values are displayed on the TV-screen and listed at the SILENT.
- V. Routine for angular scans through given channel positions; additional parameters: channel position and angle between tilt plane and the plane beam direction and detector position.
- VI. Recording of spectra for fixed angle positions and charges.
- VII. Recording of random spectra for fixed tilt angle and rotation around a direction normal to the sample. During this rotation over a given angle range the goniometer stops 100 times and acquisition is performed for a present charge.
- VIII. Simultaneous display of several angular scans with one or more energy windows.
- IX. Plot of angular scans on a CALCOMP 565 plotter.

References

- /1/ M. Conrad; Progr. Rep. IAK I, KfK 2670, 133 (1978)
- /2/ R. Kaufmann and F. Ratzel, this report.

6.6 Determination of the Superconducting Transition Temperature of Thin Layers by the Inductive Method

U. Schneider and J. Geerk

A sample holder has been constructed for the determination of the superconducting transition temperature T_c using the inductive method. Fig. 1 shows a superconducting layer in a magnetic field perpendicular to the sample. The field strength at the location of the layer equals zero and is small in the surrounding area. An alternating magnetic field from a primary coil cannot induce a magnetic flux into a flat shaped sensor coil located directly upon the layer.

Fig. 2 shows the arrangement of the primary and the sensor coil. The primary coil is conically shaped in order to obtain an optimum signal strength in the sensor coil, which is located above the primary coil. Both coils are fixed to the sample holder and the sample surface is placed directly onto the coils.

The position of the sample can be varied such that T_c can be determined on different regions of the layer, avoiding cutting the sample.

The magnetic field of the primary coil is varied with 970 Hz thus inducing a voltage of about 1 mV in the sensor coil. This signal is amplified in a lock-in amplifier and recorded on the y-scale of an x-y-plotter. The temperature detected by a germanium resistor is recorded on the x-scale.

Using a cryostat transition temperatures down to 1.2 K can be determined.

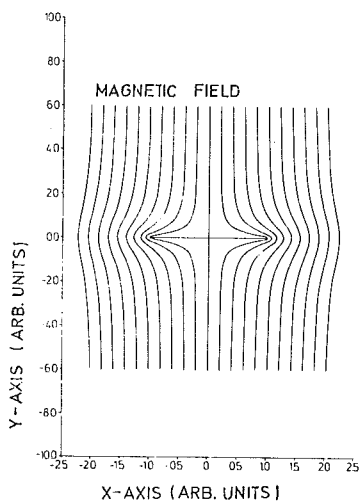


Fig. 1
Influence of a superconducting layer on the magnetic field perpendicular to the layer.

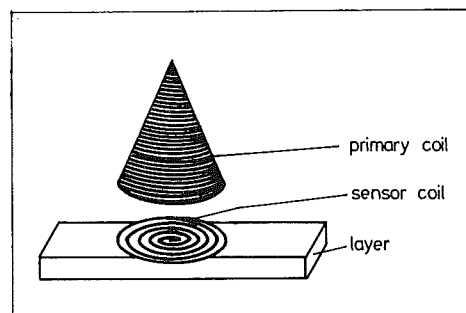


Fig. 2
Arrangement of the primary coil, pick-up coil, and the sample. The coils and the layer are in direct contact with each other.

7. PUBLICATIONS, CONFERENCE CONTRIBUTIONS, AND SEMINARS

7.1 PUBLICATIONS

Appleton, B.R.; White, C.W.; Stritzker, B.; Meyer, O.

Ion implantation and laser annealing of high T_C superconducting materials
in: White, C.W.; Peercy, P.S. (Eds): Laser- and Electron-Beam Processing of
Materials, Academic Press, New York (1980)

Bara, J.J.; Stadnik, Z.M.; Czjzek, G.; Fink, J.; Oestreich, V.; Schmidt, H.
 ^{57}Fe and ^{61}Ni Moessbauer effect investigations of nickel ferrite-aluminates
J. Phys. (Paris) Colloque C-1, 41, 173 (1980)

*Bassalleck, B.; Haase, E.L.; Klotz, W.D.; Takeutchi, F.; Ullrich, H.; Furic, M.;
Sakamoto, Y.*

Two-neutron emission in the absorption of stopped pions on lithium isotopes
Phys. Rev. C 19, 1893 (1979)

*Bieger, J.; Saemann-Ischenko, G.; Adrian, H.; Lehmann, M.; Müller, P.; Söldner, L.;
Söldner, L.; Haase, E.L.; Tsuei, C.C.*

Changes of Superconducting Properties and Electrical Resistivity of Amorphous
Compounds by Means of Low Temperature Heavy Ion Irradiation
in: Liquid and Amorphous Metals, Lüscher, E., Coufal, H., eds., Sijthoff &
Noordhoff, Alphen aan den Rijn, The Netherlands, p. 665 (1980)

Blanckenhagen, P. von; Scheerer, B.

Spin-wave dispersion relation in partially ordered Ni,Mn
J. Magn. Magn. Mater. 13, 116 (1979)

Bohnen, K.P.; Kobbelt, M.; (Eds.)

Progress Report. Teilinstitut Nukleare Festkörperphysik des Instituts für
Angewandte Kernphysik. 1.6.1978 - 31.5.1979
KfK-2881 (Oktober 1979)

Bohnen, K.P.; Ying, S.C.

Selfconsistent study of surfaces of simple metals by the density matrix method:
(100)- and (110)-surfaces of Na, K, Rb and Cs
Phys. Rev. B 22, 1806 (1980)

Brusetti, R.; Coey, J.M.D.; Czjzek, G.; Fink, J.; Gompf, F.; Schmidt, H.

The role of the lattice at the metal-semimetal transition in nickel sulphide
J. Phys. F 10, 33 (1980)

*Czjzek, G.; Fink, J.; Goetz, F.; Schmidt, H.; Rebouillat, J.P.; Lienard, A.;
Coey, J.M.D.*

An investigation of amorphous Gd-Ni alloys by Moessbauer spectroscopy
J. Phys. (Paris) Colloque C-5, 40, 245 (1979)

Geerk, J.

The superconducting transition temperature of bulk samples of the Nb-Ge A15-phase after implantation of Ge, Si, O and Ar ions

Solid State Commun. 33, 761 (1980)

Götz, F.; Czjzek, G.; Fink, J.; Schmidt, H.; Oestreich, V.; Fulde, P.

Magnetic interactions in PrEu and PrGd alloys

J. Appl. Phys. 50, 7513 (1979)

Guth, H.

Strukturuntersuchungen an dem eindimensionalen Li-Ionenleiter β -Eukryptit (LiAlSiO_4) mit Hilfe von Neutronenbeugung

Dissertation, Univ. Karlsruhe 79, KfK-2851 (September 1979)

Guth, H.; Heger, G.

Temperature dependence of the crystal structure of the 1 dim. Lit-conductor β -eucryptite (LiAlSiO_4)

Proc. of the Internat. Conf. on Fast Ion Transport in Solids, Lake Geneva, Wisc., USA, May 21-25, 1979. Amsterdam: North Holland, Publ. 1979. p. 499

Heger, G.; Weitzel, H.; (Eds.)

Nukleare Festkörperforschung am FR2: Ergebnisbericht 1978/79 der externen Arbeitsgruppen

KfK-2911 (Dezember 1979)

Höchst, H.; Steiner, P.; Hüfner, S.; Politis, C.

The XPS valence band spectra of NbC

Z. Phys. B. 37, 27 (1980)

Hofmann, P.; Politis, C.

The kinetics of the uranium dioxide - zircaloy reactions at high temperatures

J. Nucl. Mater. 87, 375 (1979)

Hussain, T.; Linker, G.

Dependence of defect structures on implanted impurity species in Al single crystals

Nucl. Instrum. Methods 168, 317 (1980)

Jung, V.

Anwendung des Cyclobahn-Prinzips auch ohne Linearmotor

Archiv für Eisenbahntechnik (AET). Schriftenreihe zur Ergänzung der Zeitschrift ETR-Eisenbahntechnische Rundschau, 34, 67 (1979)

Jung, V.

Der Individualverkehr darf nicht mehr Vorrang vor dem öffentlichen Nahverkehr haben
Nahverkehrs-Praxis, 28, 178 (1980)

Kaufmann, R.; Meyer, O.

Computer simulation of channelling measurements on V_3Si single crystals

Radiat. Eff. 40, 97 (1979)

Kaufmann, R.; Meyer, O.

Computer simulation of channelling measurements in He-irradiated V_3Si single crystals

Radiat. Eff. 40, 161 (1979)

Kuhs, W.F.; Heger, G.

Neutron diffraction study of Cu_6PS_5Br at 293 K and 473 K

Proc. of the Internat. Conf. on Fast Ion Transport in Solids, Lake Geneva, Wisc., USA, May 21-25, 1979. Amsterdam: North Holland, Publ. 1979. p. 233

Kótal, E.; Nagy, T.; Meyer, O.; Gyulai, J.; Révész, P.; Mezey, G.; Lohner, T.; Manuaba, A.

Diffusion measurement of implanted Sb into Si, using SiO_2 encapsulation

Radiat. Eff. 47, 27 (1980)

Linker, G.

Superconducting properties of ion bombarded Nb layers

Radiat. Eff. 47, 225 (1980)

Mereiter, K.; Preisinger, A.; Hiebl, K.; Mikenda, W.; Guth, H.; Heger, G.

Hydrogen bonds in Schlippe's salt, $Na_3SbS_4 \cdot 9H_2O$ and $Na_3SbS_4 \cdot 9D_2O$: diffraction and spectroscopic studies in the temperature range of 75 K to 295 K

Z. Kristallogr. 150, 215 (1979)

Meyer, O.

Superconductivity

in: Hirronen, J.K. (Ed.): Ion Implantation. Treatise on Materials Science and Technology, Vol 18. Academic Press, May 1980

Meyer, O.; Linker, G.

The influence of light- and heavy-ion irradiation on the structure, resistivity and superconducting transition temperature of V_3Si . A comparative study

J. Low Temp. Phys. 38, 747 (1980)

Nägele, W.; Blanckenhagen, P. von; Heidemann, A.

Spin dynamics of amorphous $Al_2Mn_3Si_3O_{12}$ spin glass

J. Magn. Magn. Mater. 13, 149 (1979)

Narasimham, A.V.; Roth, S.; Renker, B.; Käfer, K.; Buerkin, J.

Elastic constants of UAl_2 . Temperature and magnetic field dependence

Phys. Stat. Sol. (a), 57, K75 (1980)

Nielsen, O.H.; Weber, W.

Lattice dynamics of group IV semiconductors using an adiabatic bond charge model

Computer Phys. Commun. 18, 101 (1979)

Nielsen, O.H.; Weber, W.

Displacement correlations in covalent semiconductors

J. Phys. C 13, 2449 (1980)

Oestreich, V.

Supraleitung und ihre Anwendungsmöglichkeiten
Physik in unserer Zeit 11, 6 (1980)

Pflüger, J.; Meyer, O.

X-ray-diffraction studies on He- and Ar-irradiated Nb₃Ge thin films
Solid State Commun. 32, 1143 (1979)

Politis, C.; Wolf, Th.; Schneider, H.

Preparation, characterization and superconducting properties of TiN and TiC_xN_y
single crystals prepared by chemical vapor deposition
in: Sedgwick, T.O.; Lydtin, H. (Eds.): Chemical Vapor Deposition, 7. Internat.
Conf., Los Angeles, USA, October 14-19, 1979. Princeton, N.J.: Electrochem. Soc.
p. 289 (1979)

Prechtel, J.; Kalus, J.; Luescher, E.; Pintschovius, L; Ghosh, R.

Measurement of mode Grüneisen parameters in Si
Phys. Stat. Sol. (b) 93, 653 (1979)

Press, W.; Renker, B.; Schulz, H.; Böhm, H.

Neutron scattering study of the one-dimensional ionic conductor β-eucryptite
Phys. Rev. B 21, 1250 (1980)

Rietschel, H.

Die Rolle von Kristallstruktur und Kristalldynamik in der Supraleitung
Fortschr. Mineral. 57, 18 (1979)

Rietschel, H.; Winter, H.

The role of spin fluctuations in the superconductors Nb and V
Phys. Rev. Lett. 43, 1256 (1979)

Scheerer, B.

Preparation of NbN single crystals. Solid compounds of transition elements
KfK-2815 (Juni 1979)

Scheerer, B.

Preparation of NbN single crystals
J. Cryst. Growth 49, 61 (1980)

Schmatz, W.

Zur Bedeutung von intensiven Neutronenquellen für Streuexperimente
KfK Nachrichten 11(4), 56 (1979)

Schommers, W.

Structural and dynamical behavior of α-AgI
Vashishta, Muncy (Eds.): Fast Ion Transport in Solids, Conf., Lake Geneva, Wisc.,
USA, May 21-25, 1979. Amsterdam: Elsevier 1979. p. 625

Schommers, W.
Structure and dynamics of superionic conductors
Phys. Rev. B 21, 847 (1980)

Weber, K.
Kollimator für Neutronen
Patent, DE-AS 28 39 570 (17.1.1980)

Weber, W.; Rödhammer, P.; Pintschovius, L.; Reichardt, W.; Gompf, F.; Christensen, A.N.
Phonon anomalies in Vn and their electronic origin
Phys. Rev. Lett. 43, 868 (1979)

Ziemann, P.; Meyer, O.; Heim, G.; Buckel, W.
Low temperature self-ion irradiation of pure and granular aluminium-films
Z. Physik B 35, 141 (1979)

7.2 CONFERENCE CONTRIBUTIONS AND SEMINARS

Bara, J.J.; Stadnik, Z.M.; Czjzek, G.; Fink, J.; Oestreich, V.; Schmidt, H.
 ^{57}Fe and ^{61}Ni Mössbauer effect investigations of nickel ferrite-aluminates
 Internat. Conf. on Mössb. Spectr., Portoroz, Yugoslavia, September 10-14, 1979

Bieger, J.; Müller, P.; Nölscher, C.; Soldner, L.; Linker, G.; Meyer, O.
 Änderung der normal- und supraleitenden Eigenschaften von Nb_3Al durch Gitterdefekte
 Verhandl. DPG (VI) 15, 432 (1980)

Bieger, J.; Haase, E.L.; Tsuei, C.C.
 Changes of superconducting properties and electrical resistivity of amorphous
 compounds by means of low temperature heavy ion irradiation
 Seminar, Nato Advanced Study Institute on Liquid and Amorphous Metals,
 Zwiesel, Germany, September 10-23, 1979

*Bieger, J.; Ischenko, G.; Adrian, H.; Lehmann, M.; Müller, P.; Söldner, L.;
 Haase, E.L.; Tsuei, C.C.*
 Changes of superconducting properties and electrical resistivity of amorphous
 compounds by means of low temperature heavy ion irradiation
 Internat. Advanced Course on Amorphous and Liquid Metals, Zwiesel,
 September 2-15, 1979

*Bieger, J.; Adrian, H.; Lehmann, M.; Müller, P.; Sämann-Ischenko, G.; Söldner, L.;
 Haase, E.L.; Tsuei, C.C.*
 Änderung supraleitender Eigenschaften und des elektrischen Widerstandes amorpher
 Verbindungen nach Tieftemperatur-Bestrahlung
 Verhandl. DPG (VI) 15, 433 (1980)

Blanckenhagen, P. von;
 Neutronenstreuexperimente zur Spin-Dynamik in Festkörpern
 Seminar, Univ. Kaiserslautern, November 12, 1979

Blanckenhagen, P. von; Lin, C.; Hilscher, G.
 Magnetische Nahordnung in $\text{Y}_6(\text{Mn}_x\text{Fe}_{1-x})_{23}$
 Verhandl. DPG (VI) 15, 268 (1980)

Blanckenhagen, P. von; Lin, C.
 Spin wave dispersion in ordered Fe_3Si
 Internat. Conf. on the Physics of Transition Metals, Leeds, GB, August 18-22, 1980

Bohnen, K.-P.
 Selbstkonsistente Berechnung von elektronischen Oberflächeneigenschaften von
 Metallen mit Hilfe der Dichte-Matrix-Methode
 Seminar, KFA Jülich, IFF, July 13, 1979

Bohnen, K.-P.

Density-matrix methods

Conference on the Calculation of Atomic Positions at Solid Surfaces, Gif-sur-Yvette, May 5-6, 1980

Bohnen, K.-P.; Ying, S.C.

Selbstkonsistente Berechnung elektronischer Oberflächeneigenschaften von Metallen mit Hilfe der Dichte-Matrix-Formulierung

Verhandl. DPG (VI) 15, 737 (1980)

Brunsmann, U.; Fischbach, J.U.; Frenzl, O.; Egle, H.; Kraatz, M.

Untersuchungen zur Nachweisgrenze extrinsischer Photoleitungsdetektoren

Verhandl. DPG (VI) 15, 183 (1980)

Christensen, A.N.; Gompf, F.; Pintschovius, L.; Reichardt, W.; Rödhammer, P.; Scheerer, B.

Lattice dynamics of the nitrides of vanadium and niobium

Solid Compounds of Transition Elements, 6. Internat. Conf., Stuttgart, June 12-16, 1979

Creceilius, G.; Manzke, R.; Campagna, M.; Fink, J.; Schöllhorn, R.

Wellenvektorabhängige Elektronen - Energieverlustspektroskopie an SnS_2 und SnSe_2

Verhandl. DPG (VI) 15, 193 (1980)

Ehret, G.; Hanak, H.

Totzeitfreie Multiskalare Spektren

Frühjahrssitzung Nukleare Elektronik, Bochum, March 24-26, 1980

Ehret, G.; Hanak, H.; Sobiesiak, H.

Variable Anfahr- und Abbremskurven für Schrittmotore unter BASIC für Mini- und Mikrorechner

Frühjahrssitzung Nukleare Elektronik, Bochum, March 24-26, 1980

Ehret, G.; Hanak, H.

Schieberegistereinsatz bei mittelschnellen Flugzeitanalysatoren

Frühjahrssitzung Nukleare Elektronik, Bochum, March 24-26, 1980

Geerk, J.

Kurzzeittempern oberflächennaher Bereiche mit gepulsten Elektronenstrahlen

Seminar, KFA Jülich, IFF, October 1979

Götz, F.; Czjzek, G.; Fink, J.; Schmidt, H.; Oestreich, V.; Fulde, P.

Magnetic interactions in PrEu and PrGd alloys

Joint Intermag - MMM Conference, New York, USA, July 17-20, 1979

Gompf, F.; Lannin, J.; Reichardt, W.

Phonon spectra of amorphous red and orthorhombic black phosphorus

Annual Conf. of the Condensed Matter Division of the European Physical Society,
Antwerpen, B, April 9-11, 1980

Haase, E.L.; Khubeis, I.G.

Measurement of oxygen depth profiles in thin layers and bulk materials

Ion Beam Analysis, 4. Internat. Conf., Univ. Aarhus, Dänemark, June 25-29, 1979

Haase, E.L.; Khubeis, I.G.; Meyer, O.

Systematische Untersuchung des Nb₃Si Systems

Verhandl. DPG (VI) 15, 430 (1980)

Haq, A. ul; Meyer, O.

Der Einfluß von Strahlenschädigung und Ionenimplantation auf die Übergangstempera-
tur zum Supraleiter, T_C und die Struktur von Re-Schichten

Verhandl. DPG (VI) 15, 398 (1980)

Hussain, T.; Geerk, J.; Linker, G.

Improvement of lattice site distribution of Ga atoms implanted into Al after
pulsed electron beam annealing

Verhandl. DPG (VI) 15, 342 (1980)

Hussain, T.; Linker, G.

Dependence of defect structures on implanted impurity species in Al single
crystals

Ion Beam Analysis, 4. Internat. Conf., Univ. Aarhus, Dänemark, June 25-29, 1979

Jung, V.

Investigation by neutron diffraction of phase transitions in stressed austenitic
CrNi steel

5. European Crystallographic Meeting, Kopenhagen, August 13-17, 1979

Kaufmann, R.; Meyer, O.

Computer simulation of channelling measurements in carbon-implanted NbC-single
crystals

Ion Beam Analysis, 4. Internat. Conf., Univ. Aarhus, Dänemark, June 25-29, 1979

Köhler, K.; Geserich, H.P.; Christensen, A.N.; Politis, C.

Reflexionsmessungen an TiN_x und TiN_xO_{1-x}

Verhandl. DPG (VI) 15, 156 (1980)

Kuhs, W.F.; Heger, G.

Neutron diffraction study of the Cu⁺⁺-conductor Cu₆PS₅Br at 293 K and 473 K

5. European Crystallographic Meeting, Kopenhagen, August 13-17, 1979

Lehmann, M.; Sämann-Ischenko, G.; Adrian, H.; Bieger, J.; Müller, P.; Nölscher, C.; Söldner, L.; Linker, G.; Meyer, O.

Änderung der normal- und supraleitenden Eigenschaften von Nb₃Al durch Gitterdefekte

Verhandl. DPG (VI) 15, 432 (1980)

Meyer, O.

Anwendung von Ionenstrahlen zur Herstellung und Untersuchung supraleitender Materialien

Seminar, Universität Erlangen, July 5, 1979

Meyer, O.

Radiation damage in Al₅ superconductors

Seminar, Oak Ridge Natl. Lab. Solid State Div., December 13, 1979

Meyer, O.

Anwendung der Channelling-Technik in der Materialforschung

Seminar, Universität Frankfurt, Inst. für Kernphysik, May 22, 1980

Meyer, O.

Ionenimplantation und Supraleitung

Seminar, Universität Karlsruhe, Physikalisches Inst., June 2, 1980

Müller-Vogt, G.; Wolf, Th.

Crystal growth and characterization of transition metal nitrides prepared by chemical vapor deposition

2. European Conference on Crystal Growth, Lancaster, September 10-15, 1979

Müller, P.; Ischenko, G.; Adrian, H.; Bieger, J.; Lehmann, M.; Haase, E.L.

Transport properties, electronic density of states and T_C in disordered Al₅ compounds

Superconductivity in d- and f-Band Metals, 3. Internat. Conf., San Diego, Calif., USA, June 21-23, 1979

Nägele, W.; Blanckenhagen, P. von

Spin relaxation in the amorphous spin glass Al₂Mn₃Si₃O₁₂

Internat. Conf. on Magnetism, München, September 3-7, 1979

Nittmann, M.; Ziemann, P.; Buckel, W.; Linker, G.

Der Einfluß von Sauerstoff auf die Übergangstemperatur abschreckend kondensierter Aluminium-Schichten

Verhandl. DPG (VI) 15, 395 (1980)

Oestreich, V.; Czjzek, G.; Götz, F.; Schmidt, H.; Latka, K.; Wienand, K.H.

Magnetische Ordnung in kubisch-flächenzentrierten Eu-Yb-Legierungen

Verhandl. DPG (VI) 15, 274 (1980)

Oestreich, V.

Magnetic ordering in YbEu-alloys

Seminar, Institute of Nuclear Physics, Krakow, April 16, 1980

Oestreich, V.

A new state in sodium nitroprusside: properties and mysteries

Seminar, Jagellonian University, Krakow, April 17, 1980

Oestreich, V.

Magnetic properties of rare earths: the YbEu-alloy system

Seminar, University of Warszawa, April 24, 1980

Politis, C.

Phase relationships and properties in the Nb-N and Ta-N system

Solid Compounds of Transition Elements, 6. Internat. Conf., Stuttgart, June 12-16, 1979

Politis, C.; Wolf, Th.; Schneider, H.

Preparation, characterization and superconducting properties of TiN and TiC_xN_y single crystals prepared by chemical vapor deposition

Chemical Vapor Deposition, 7. Internat. Conf., Los Angeles, USA, October 14-19, 1979

Reimers, W.; Hellner, E.; Treutmann, W.; Heger, G.

Investigation of the magnetic phase diagram of the NiAs-type system

$(Mn_{1-x}Cr_x)_{1+\delta}Sb$ ($0 \leq x \leq 1$)

Neutron Scattering and Magnetism, Internat. Conf., Jülich, August 29-31, 1979

Riehle, F.; Wolf, Th.

Zur elektronischen Struktur von polykristallinem Ti, TiC, TiN und TiO

Verhandl. DPG (VI) 15, 288 (1980)

Rietschel, H.; Winter, H.

The role of spin fluctuations in the superconductors Nb and V

Seminar, KFA Jülich, IFF, November 16, 1979

Rietschel, H.

Supraleitung und Spinfluktuationen

Seminar, Gesamthochschule Duisburg, December 12, 1979

Scheerer, B.

Preparation of NbN single crystals

Solid Compounds of Transition Elements, 6. Internat. Conf., Stuttgart, June 12-16, 1979

Schell, G.; Winter, H.; Rietschel, H.

The Eliashberg function and the superconducting T_C of transition metal hexaborides

Superconductivity in d- and f-Band Metals, 3. Internat. Conf., San Diego, June 21-23, 1979

Schmatz, W.

Magnetic diffuse and small angle scattering

Neutron Scattering in Biology, Chemistry and Physics, Meeting, London,
September 26-27, 1979

Schmatz, W.

Forschungsprogramm über Hartstoffe am Institut für Angewandte Kernphysik des
Kernforschungszentrums Karlsruhe

Seminar, KFA Jülich, IFF, January 16, 1980

Schmatz, W.

Neutronenspallationsquelle

Seminar, Univ. Tübingen, January 23, 1980

Schommers, W.

Neuere Ergebnisse zur mikroskopischen Beschreibung fester Elektrolyte

Seminar, Univ. Göttingen, July 23, 1979

Steiner, P.; Höchst, H.; Hüfner, S.; Politis, C.

The electronic structure of HfC_xN_y and NbC_x compounds obtained from x-ray excited
photoelectron spectra

Solid Compounds of Transition Elements, 6. Internat. Conf., Stuttgart,
June 12-16, 1979

Turos, A.

Pulsed electron annealing of high-dose arsenic implanted silicon

Seminar, Technische Hochschule Aachen, April 10, 1980

Vogt, K.; Reichardt, W.; Prandl, W.

Soft-Mode-Verhalten und Zentrale Komponente in K_2SnCl_6

Verhandl. DPG (VI) 15, 136 (1980)

Weber, W.

Recent calculations of phonon spectra of transition metals and compounds

Superconductivity in d- and f-Band Metals, 3. Internat. Conf., San Diego,
June 21-23, 1979

Weber, W.

Elektronische Bandstruktur und Gitterdynamik in Übergangsmetallen

Verhandl. DPG (VI) 15, 422 (1980)

Winter, H.; Schell, G.; Rietschel, H.

The Eliashberg function and the superconducting T_c of transition metal hexaborides

3. International Conf. on Superconductivity in d- and f-band metals, San Diego, 1979

Wolf, Th.

Herstellung von TiN, TiC und TiC_xN_y - Einkristallen und deren Charakterisierung
Gesellschaft für Kristallwachstum und Kristallzüchtung, Karlsruhe, March 20, 1980

8. LIST OF THE NEUTRON SPECTROMETERS AT
THE FR2 AT KARLSRUHE OPERATED BY THE
IAKI

- DIF 1 : Four circle diffractometer, $\lambda = 1.020 \text{ \AA}$
- DIF 2 : Two circle diffractometer, $0.7 \text{ \AA} \leq \lambda \leq 2.6 \text{ \AA}$
- DIF 3 : Two circle diffractometer, $\lambda = 1.338 \text{ \AA}$
- DIF 4 : Four circle diffractometer, $\lambda = 0.920 \text{ \AA}$ or 2.418 \AA
- DIF 5 : Four circle diffractometer, $\lambda = 0.895 \text{ \AA}$
-
- TAS 1 : Three-axis spectrometer, $13 \text{ meV} \leq E_0 < 120 \text{ meV}$
- TAS 2 : Three-axis spectrometer, $4 \text{ meV} \leq E_0 < 55 \text{ meV}$
-
- TOF 1 : Time-of-flight spectrometer with Fermi-chopper,
140 detectors, thermal neutrons
- TOF 2 : Time-of-flight spectrometer with rotating crystal,
60 detectors, cold neutrons
- TOF 3 : Time-of-flight spectrometer with Fermi-chopper,
120 detectors, thermal neutrons
- TOF 4 : Time-of-flight spectrometer with rotating crystal,
6 detectors, cold neutrons
-
- MAG 1 : Spectrometer for diffuse scattering, 40 detectors,
thermal neutrons
- MAG 2 : Multipurpose spectrometer, 40 detectors, cold neutrons.

9. STAFF MEMBERS (June 1, 1980)

Head of Institute: W. Schmatz

Professional Staff

Blanckenhagen, P.v.	Haase, E.L.	Nücker, N.	Rietschel, H.
Bohnen, K.-P.	Heger, G.	Oestreich, V.	Schmidt, H.
Czjzek, G.	Jung, V.	Pintschovius, L.	Schmidt, H.-J.
Fink, J.*	Kobbelt, M.	Politis, C.	Schommers, W.
Geerk, J.**	Linker, G.	Reichardt, W.	Suck, J.-B.***
Gompf, F.	Meyer, O.	Renker, B.	Weber, W.

Technical Staff

Abel, W. ⁺	Hanak, H. ⁺	Roller, H. ⁺	Sobiesiak, H. ⁺
Ehret, G. ⁺	Kraatz, M.	Scheerer, B.	Weber, K.
Ernst, A. ⁺	Ratzel, F.	Schreiber, H. ⁺	
Ewert, D.	Richelsen, H. ⁺	Smithey, R.	

Visiting Scientists

Alberts, H.W.; Guest from South Africa	Yeh, C.T.; Guest from the Rep. of China
Baumgartner, O.; Guest from Austria	Lin, C.; Guest from the Rep. of China
Friedland, E.; Guest from South Africa	Mayer, W.H.; Guest from Marburg
Guth, H.; Guest from Marburg	Schweiß, P.; Guest from Frankfurt
Hussain, T.; Guest from Bangladesh	Turos, A.; Guest from Poland

Research Students

Aker, E. ⁺⁺	Kieselmann, G. ⁺⁺
Bletzer, H. ⁺⁺	Kloska, M. ⁺⁺
Geibel, C. ⁺⁺⁺	Krauss, W. ⁺⁺
Götz, F. ⁺⁺⁺	Schell, G. ⁺⁺
Härdle, H. ⁺⁺	Schneider, U. ⁺⁺
Haq, A. ul. ⁺⁺	Steinmann, G. ⁺⁺
Kaufmann, R. ⁺⁺	Stocker, W. ⁺⁺

*On leave of absence at KFA, Jülich

⁺Member of infrastructure

**On leave of absence at Bell Lab., N.J.

⁺⁺Universität Karlsruhe

***On leave of absence at ILL, Grenoble

⁺⁺⁺Universität Heidelberg